A Thesis Submitted for the Degree of PhD at the University of Warwick

Permanent WRAP URL:

http://wrap.warwick.ac.uk/156454

warwick.ac.uk/lib-publications

Nanostructured Copper Electrodes for Organic Photovoltaics

By

Philip Bellchambers
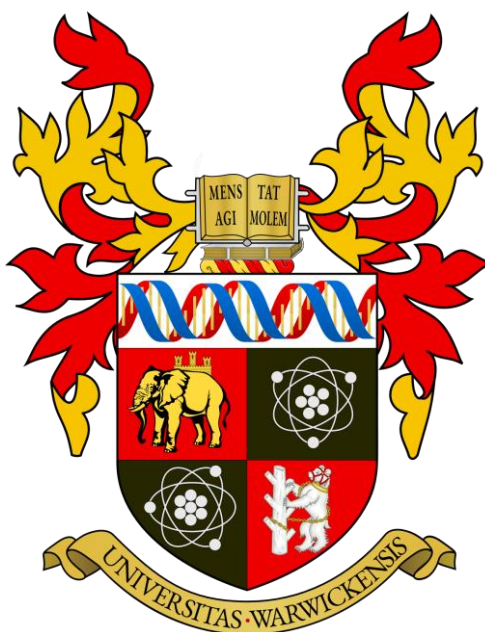
A thesis submitted in partial fulfilment of the requirements for the degree of Doctor of Philosophy in Chemistry.

Supervisor: Professor Ross A. Hatton

Department of Chemistry, University of Warwick

January 2021

Table of Contents

Acknowledgements

Firstly, I would like to thank my PhD supervisor Professor Ross Hatton for his tutelage and patience, and the EPSRC for this opportunity. I would not have developed the skills, knowledge or confidence I have without Ross' input. I would also like to thank all my friends in the Hatton group past and present, and in MAS, for your excellent company and kind help.

Last but one I would like to thank my parents, without them I would not be the person I am, for their unwavering love and support. Finally, to my partner Sophie, thank you for the inspiration and company on this journey.

Declaration

This thesis is submitted to the University of Warwick in support of my application for the degree of Doctor of Philosophy. It has been composed by myself and has not been submitted in any previous application for any degree.

The work presented (including data generated and data analysis) was carried out by the author except in the cases outlined below:

Data collection for X-ray photoelectron spectroscopy was conducted by Dr Marc Walker at the University of Warwick XPS Facility; the analysis was performed in collaboration.

Data collection and analysis for X-ray diffraction and Small-Angle X-ray diffraction were conducted by Dr David Walker and Dr Steven Huband respectively at the University of Warwick X-ray RTP.

The preparation of patterned silicon wafers by photolithography, as described in Chapter 4, was conducted by Corinne Maltby in the School of Engineering, University of Warwick.

Data collection for transmission electron microscopy was conducted by Dr Houari Amari (STEM, Chapter 5) and Steve Hindmarsh (TEM, Chapter 6).

Parts of this thesis have been published by the author and a full list follows.

List of Publications

[1]   P. Bellchambers, J. Lee, S. Varagnolo, H. Amari, M. Walker, R. A. Hatton, Elucidating the Exceptional Passivation Effect of 0.8 nm Evaporated Aluminium on Transparent Copper Films, *Front. Mater.* **2018**, *5*, 71.

[2]   P. Bellchambers, M. Walker, S. Huband, A. Dirvanauskas, R. A. Hatton, Enhanced Oxidation Stability of Transparent Copper Films Using a Hybrid Organic-Inorganic Nucleation Layer, *ChemNanoMat.* **2019**, *5*, 619.

[3]   P. Bellchambers, S. Varagnolo, C. Maltby, R. A. Hatton, High-Performance Transparent Copper Grid Electrodes Fabricated by Microcontact Lithography for Flexible Organic Photovoltaics, *Submitted.*

[4]   H. J. Pereira, P. Bellchambers, R. A. Hatton, Nano-structured copper: Retarding oxidation without electrical isolation (Review), *Submitted.*

Abstract

This thesis focuses on the development of high-performance copper (Cu) based transparent electrodes for application in organic photovoltaics (OPVs). Laboratory-scale OPV devices are typically supported on costly and brittle indium tin oxide (ITO) coated glass substrates which serve as the transparent electrode. There is however near universal consensus in the community that for the commercialization of OPVs a flexible, lower cost alternative to ITO is needed. To date transparent electrodes based on silver (Ag) nanowires, grids and optically thin planar films are considered the most viable alternatives. However, Ag is as costly as indium and so offers little advantage over ITO glass in this respect. Cu is an attractive alternative to Ag, with comparable electrical conductivity at $< 1\%$ of the material cost. Historically however, Cu has been overlooked due to its lower stability towards oxidation in air and its stronger absorption of visible and near infra-red light.

The first results chapter of this thesis focuses on the development of a high-performance Cu grid electrode fabricated using microcontact printing, which is an unconventional method of patterning metal films that has been little explored for this application. Using a low-toxicity single component etchant and a printed mask of monolayer thickness flexible Cu grid electrodes with simultaneously $> 90\%$ transparency and $< 10\ \Omega\ \text{sq}^{-1}$ sheet resistance are realised - comparable to ITO on glass. Additionally the grid line width achievable using this approach is $20\times$ narrower than possible using conventional printing methods, which reduces or eliminates the requirement for a PEDOT:PSS conductive polymer interlayer.

A remarkably effective approach to passivating Cu without electrically isolating it, first reported by Hutter *et al.* (*Adv. Mater*, 2013, 25, 284–288), is to cap the Cu with 0.8 nm of aluminium (Al) by simple thermal evaporation. In the second results chapter it is shown that a slab-like 8 nm thick Cu film capped with an 0.8 nm Al capping layer and perforated with ~6 million apertures per cm^2 using photolithography exhibits a sheet resistance increase of less than 1% after 2 years in ambient air. The reason for this remarkable stability is elucidated for the first time: Namely, spontaneous segregation of the Al to grain boundaries in the polycrystalline film Cu results in ternary oxide plugs at those sites most vulnerable to oxidation.

Cu does not adhere strongly to glass and plastic substrates, and so there is a need to develop ways to seed the growth of dense films of < 10 nm thickness of low roughness and concomitant improved stability. The third results chapter describes the development of a hybrid seed layer for the fabrication of robust, optically thin Cu films on glass and plastic substrates that outperforms the best alternative. The hybrid layer is based on a combination of molecular and inorganic (Al) layers.

The final results chapter applies the insight from the second results chapter to develop novel bilayer electrodes of copper/tin and copper/zinc which improve with *in-situ* oxidation, which represents ongoing work.

The four results chapters are prefaced with an introduction chapter which outlines the relevant background literature and theory and is followed by chapters summarizing the methods and techniques used in this thesis.

List of Acronyms and Abbreviations

AFM	Atomic Force Microscope
APS	ammonium persulfate
APTMS	3-aminopropyl(thrimethoxysilane)
at. %	Atomic Percentage
BE	Binding Energy
BHJ	Bulk Heterojunction
C_{60}	Buckminster Fullerene
CB	Conduction Band
CdTe	Cadmium Telluride
CO_i8DFIC	2,2-[[4,4,11,11-tetrakis(4-hexylphenyl)-4,11-dihydrothieno[2,3:4,5]thieno[2,3-d]thieno[2,3:4,5]thieno[2,3:4,5]pyrano[2,3:4,5]thieno[2,3:4,5]thieno[3,2-b]pyran-2,9-diyl]bis[methylidyne(5,6-difluoro
c-Si	Crystalline Silicon
DIO	1,8-diiodooctane
EDXS	Energy-Dispersive X-ray Spectroscopy
ETL	Electron Transport Layer
FF	Fill Factor
FoM	Figure-of-Merit
FWHM	Full Width at Half Maximum
GISAXS	Grazing Incidence Small-Angle X-Ray Scattering
GIXRD	Grazing Incidence X-ray Diffraction
HDT	hexadecanethiol
HOMO	Highest Occupied Molecular Orbital
HTL	Hole Transport Layer
ICP	Inductively Coupled Plasma

IPA	Isopropyl Alcohol
IR	Infrared (Light)
ITIC	3,9-bis(2-methylene-(3-(1,1-dicyanomethylene)-indanone))-5,5,11,11-tetrakis(4-hexylphenyl)-dithieno[2,3-d:2',3'-d']-s-indaceno[1,2-b:5,6-b']dithiophene
ITO	Indium Tin Oxide
J	Current Density
J_{sc}	Short Circuit Current Density
k_B	Boltzmann Constant
KE	Kinetic Energy
LUMO	Lowest Unoccupied Molecular Orbital
MM	Mixed Molecular Adhesive Layer (MPTMS:APTMS)
M_{pp}	Maximum Power Point
MPTMS	3-mercaptopropyl(trimethoxysilane)
NFA	Non-Fullerene Acceptor
OPV	Organic Photovoltaic
PBDB-T	Poly[(2,6-(4,8-bis(5-(2-ethylhexyl)thiophen-2-yl)-benzo[1,2-b:4,5-b']dithiophene))-alt-(5,5-(1',3'-di-2-thienyl-5',7'-bis(2-ethylhexyl)benzo[1',2'-c:4',5'-c']dithiophene-4,8-dione)]
$PC_{60}BM$	[6,6]-Phenyl-C61-butyric acid methyl ester
$PC_{70}BM$	[6,6]-Phenyl-C71-butyric acid methyl ester
PCE	Power Conversion Efficiency
PDMS	Polydimethylsiloxane
PEDOT:PSS	Poly(3,4-ethylenedioxythiophene) Polystyrene Sulfonate
PEI	Polyethylenimine
PEN	Polyethylene Naphthalate
PET	Polyethylene Terephthalate
PID	Proportional Integral Derivative

PTB7-Th / PCE10	Poly[4,8-bis(5-(2-ethylhexyl)thiophen-2-yl)benzo[1,2-b;4,5-b']dithiophene-2,6-diyl-alt-(4-(2-ethylhexyl)-3-fluorothieno[3,4-b]thiophene-)-2-carboxylate-2-6-diyl)]
PV	Photovoltaics
QCM	Quartz Crystal Microbalance
RMS	Root Mean Square
R_{series}	PV Series Resistance
R_{sh}	Sheet Resistance
R_{shunt}	PV Shunt Resistance
SAM	Self-Assembled Monolayer
SEM	Scanning Electron Microscopy
Si	Silicon
STEM	Scanning Transmission Electron Microscopy
T	Temperature
T_{AVG}	Average Transmission (400 – 800 nm)
TCE	Transparent Conductive Electrode
TEM	Transmission Electron Microscope
TFOCS	tridecafluoro-1,1,2,2-tetrahydrooctyl-1-trichlorosilane
UHV	Ultra-High Vacuum
UV	Ultraviolet (Light)
UV/Vis	UV-Visible (Spectroscopy)
V	Voltage
VB	Valence Band
V_{oc}	Open Circuit Voltage
wt. %	Weight Percentage
XPS	X-ray Photoelectron Spectroscopy
XRF	X-ray Fluorescence

ZnO-nps	Zinc Oxide Nanoparticles
θ	Take-off Angle (XPS)
λ	Inelastic Mean Free Path
Φ	Work Function
q	Charge Magnitude
r	Vector Distance
w	Depletion Region Width
%T	Transmittance
Φ_{height}	Energetic Barrier
Φ_M	Metal Work Function
Φ_S	Semiconductor Work Function
E_F	Fermi level
V_L	Vacuum Level
ε_0	Vacuum Permittivity
ε_r	Dielectric Constant
μ-CP	Microcontact Printing

1   <u>Introduction</u>

A global population increase of 2 billion people by 2050,[1] coupled with an improving standard of living, continues to rapidly increase our demand for energy. As countries develop this increasing energy appetite has historically been sated by coal or gas power stations. There is a growing global industrial and political recognition that this model is unsustainable and so our reliance on fossil fuels must come to an end to control the increasing casualty rate of global warming. The burning of fossil fuels releases greenhouse gases, which accumulate in the atmosphere leading to an increase in the frequency, intensity and duration of extreme weather and climate events. By the end of the century, regions of the middle east are predicted to become uninhabitable, while a disproportionate decline in productivity in warmer countries is likely to increase migration and conflicts, making this a global problem.[2] A 'conservative estimate' by the World Health Organisation (WHO) of 5,000,000 deaths between 2030 and 2050 as a direct result of climate change through heat-exposure, disease, coastal flooding and childhood stunting does not account for variations in food availability or climate-disruption to health services.[3] Here in the UK for the first time in early 2020 however, energy from wind and solar sources eclipsed that from fossil fuels, which reduced on previous years.[4] This rapid deployment of renewable energy is being driven in large part by the levelized energy cost per kWh of new solar and wind installations falling below that of coal and nuclear energy.[5] The solar resource is a constant and inexhaustible source of free energy, which can be harvested directly using photovoltaics (PV) or indirectly using wind turbines or biofuels. Photovoltaics convert sunlight directly to electricity without any moving parts, emissions or noise and are expected to play a major role in meeting our future energy needs. The average energy density reaching the earth's surface is 198 W/m^2 which importantly peaks in the visible region of the spectrum (Figure 1).[6] Unlike any other mainstream energy generation, photovoltaics are also well matched to point-of-use energy generation for a broad range of applications, from rooftop solar to powering individual internet-connected sensors or devices.
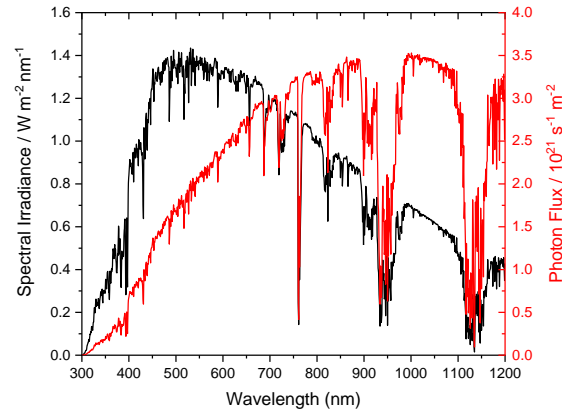
Figure 1: (Red) The photon flux across the visible spectrum (incoming photons). (Black) The available energy, centred in the visible region.

1.1 Solar Technologies

From 2005 to 2016 installed PV capacity in Europe increased from 1.9 to 102 GW, accounting for > 25% of newly installed capacity.[7] Of this > 95% was made up of silicon PV technologies (predominantly crystalline silicon based (c-Si)) with the remainder made up by thin-film technologies including cadmium telluride (CdTe).[8] c-Si PVs dominate the PV market due to a remarkable and continuous reduction in manufacturing cost over the past 30 years, achieved through incremental technological advancements in processing and design (e.g. thinning the Si wafer), improvements in module efficiency to 24.4% and lifetimes over 25 years.[9] There is however room for other complimentary PV technologies.

Emerging thin-film technologies, such as perovskite PV and organic PV (OPVs), aim not only to compete with these efficiencies but also offer other advantages and new applications such as energy payback times below one year, lower materials and fabrication costs, and flexibility for roll-to-roll production. Both perovskite and organic photovoltaics (OPVs) are thin film technologies close to commercial production and compatible with flexible plastic substrates. Both offer low energy payback times due to the very thin light harvesting layers (< 500 nm *vs* 200 µm for c-Si), their low temperature processing and compatibility with printing.[10,11] This enables their application to compliment traditional fixed solar capacity through flexible, lightweight modules which can be installed at point-of-use as building-integrated modules or for transportation. It

also enables semi-transparent modules to be produced, unlike silicon-based cells which utilize a brittle opaque Si wafer of > 100 µm thickness.

1.2 Semiconductors and Electricity Generation

The photovoltaic effect is a property of a material or combination of materials whereby a voltage or electric current is generated upon illumination with light, due to an inter-band excitation of electrons. This effect is the central process in the photoactive layer of all solar technologies. Additional layers of semiconductors in the device facilitate efficient charge extraction from the light harvesting layer to the external circuit. The photovoltaic effect is inherent to semiconductors which have an energy gap between the valence and conduction band edges less than or equal to the energy of incident photons. Therefore, the absorption of a photon of light provides sufficient energy to promote an electron from the edge of the valence band to the conduction band from where it can be harnessed to do work in an external circuit. Semiconductors are, somewhat arbitrarily, defined as those materials with a band gap below 3.2 eV (400 nm, $E = hc/\lambda = 3.11$ eV) and insulators those with a band gap greater than 3.2 eV. In contrast (Figure 2), metals have a partially filled valence band and so are good conductors of electricity.
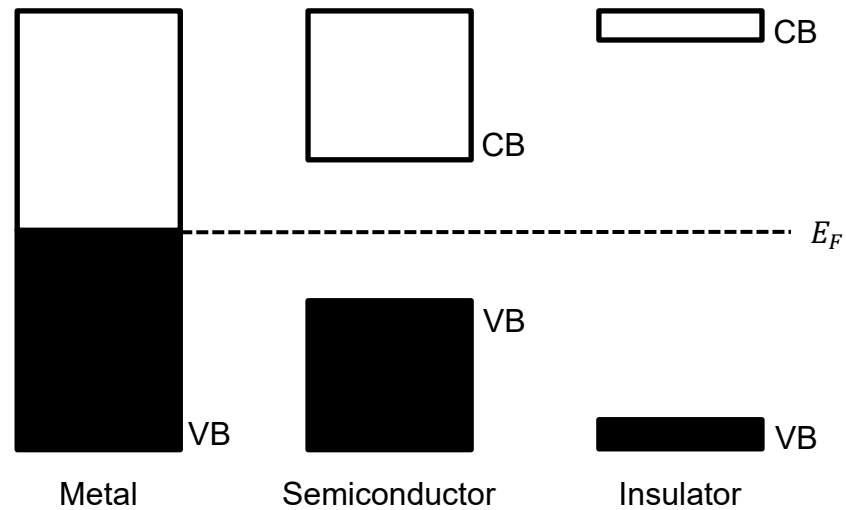
Figure 2: Schematic band structures of a model metal, semiconductor and insulator. Filled bands are depicted in black. The dashed line depicts the Fermi level (E_F). VB and CB denote the valence and conduction bands respectively.

In conventional Si solar cells *p* & *n*-type Si layers form a junction (*p-n* junction) across which there is a depletion region which forms when electrons in the *n*-type region spontaneously diffuse to the *p*-type region until Fermi level alignment (thermodynamic equilibrium) is achieved across the junction, creating a built-in electric field. When the junction is exposed to light of sufficient energy there is the promotion of an electron from the valence band (VB) to the conductance band (CB), leaving a positively charged vacancy in the VB called a hole. The energy of attraction between the electron and hole is smaller than the thermal energy of an electron at room temperature (~ 25 meV), and so both the electron and hole are free to move under the influence of an electric field. The in-built electric field across the junction sweeps the electrons and holes out of the junction in opposite directions before they recombine.

1.2.1 *Metal-Semiconductor interfaces*

A key parameter for understanding metal-semiconductor interfaces is the work function (Φ). In Figure 2 energy bands are depicted in isolation however, in order to understand the energetics at interfaces between materials, the absolute energy of each level must be defined with respect to the vacuum level (V_L). The vacuum level is the energy level at which the electron is at rest, which is the case when the electron is immediately outside the surface of a solid.[12] The Fermi level (E_F) is defined as the energy at which the probability of occupancy of an electron state is 0.5. In a semiconductor without dopants or defect states, E_F is in the middle of the band gap (Figure 3). The work function is defined as the energy required to take an electron from E_F to the V_L and the difference in work function between different materials brought into contact is a key determinant of the energetics at the interface at thermodynamic equilibrium.
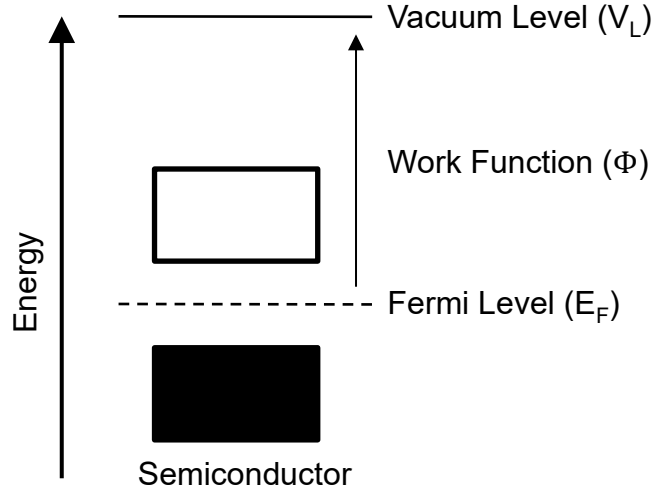
Figure 3: A schematic showing the new terms, vacuum level, work function and Fermi level, superimposed on the previous model.

The position of E_F with respect to the VB and CB edges is determined by the degree and type of semiconductor doping: In a heavily doped *p*-type semiconductor E_F lies close to the edge of the VB. In an intrinsic semiconductor E_F lies centrally between the band edges and in an *n*-type semiconductor E_F is close to the CB edge. In contrast to the case of semiconductors, the E_F of a metal is located within a band (Figure 2) so the band is partially filled.

Metal-semiconductor interfaces can be categorised in one of two ways: An ohmic contact or a Schottky contact.

Ohmic contacts

An ohmic contact is a metal-semiconductor interface with no significant barrier (i.e., ≤ 100 meV) to charge injection from the metal into the semiconductor. When a metal and semiconductor are interfaced the net movement of electrons is from the lower Φ material to the higher Φ material reaching thermodynamic equilibrium once the Fermi levels equalise across the junction, i.e., once the concentration difference and opposed electric field balance. This net migration of electron density has two effects; (a) a depletion (or accumulation) region forms in the semiconductor across which there is a built-in electric field. In the metal the charges are at the surface, as unlike in the case of dopants in a semiconductor charges in a metal are not fixed in space. (b) The energies of the vacuum level, VB and CB change continuously across the depletion region. Contacts are ohmic if

either: (i) Φ_{height} is less than 100 meV; or (ii) the width of the depletion region, w, is sufficiently thin to enable the efficient tunnelling of charges through the barrier which is commonly the case for heavily doped semiconductors.

Scenario (i), where Φ_{height} is $\leq$ 100 meV, is commonly the case when the Fermi level of the metal is closely aligned to an *n*-type semiconductor. As such, no depletion region will form and the barrier to the injection of electrons is equal to the difference between the Fermi level and CB edge of the semiconductor. Scenario (ii) is depicted in Figure 4 (a), where the heavily doped *n*-type semiconductor has a lower Φ than the metal, and so the net movement of electrons is from the semiconductor to the metal to reach equilibrium. The subsequent interface, shown in Figure 4 (b), with a theoretical energetic barrier Φ_{height} to the injection of electrons from the metal to the semiconductor, is ohmic only for heavily doped semiconductors, where the depletion region is very narrow.
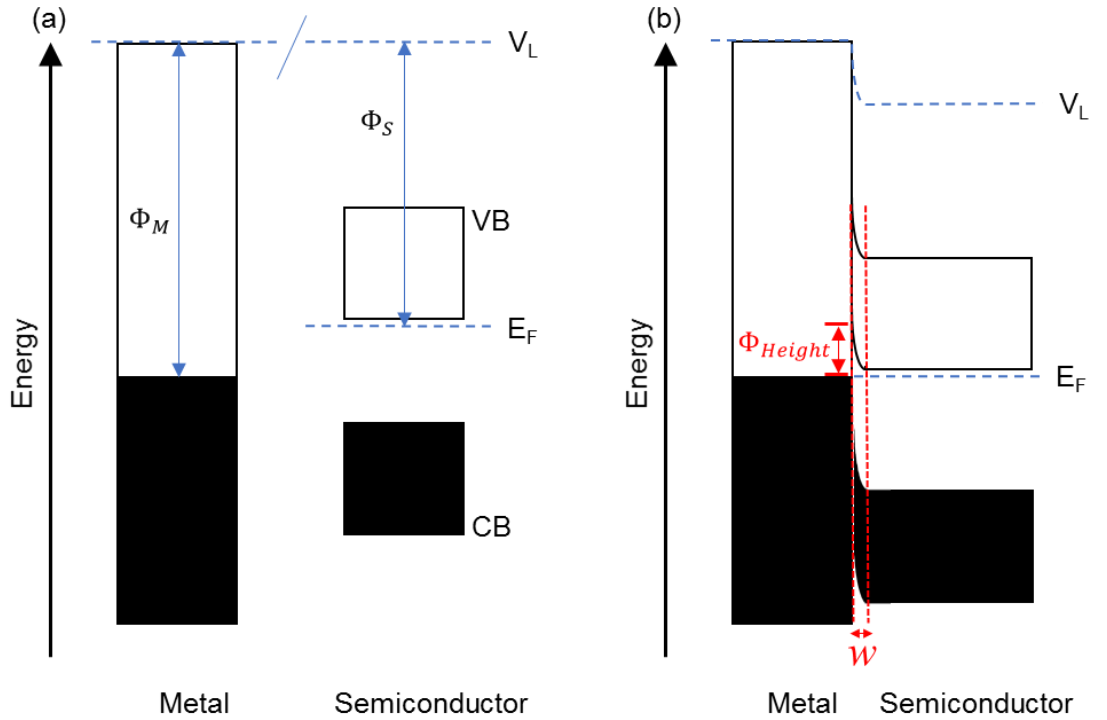
Figure 4: Schematic energy level diagrams of a metal and a heavily doped *n*-type semiconductor before contact (a) and after contact formation (b), with depletion region width *w*.

In the case of metal-organic semiconductor junctions which typically involve undoped organic semiconductors, the energy level alignment across the junction is typically dominated by the formation of an abrupt vacuum level shift associated with a dipole layer at the interface rather than the formation of a depletion region.

Schottky contact

A Schottky contact or Schottky barrier describes an interface with an energetic barrier to charge carrier injection of $\geq$ 100 meV, causing the interface to behave as a diode. By example, in Figure 5, a barrier to the injection of electrons from metal to the *n*-type semiconductor exists with height Φ_{Height}.
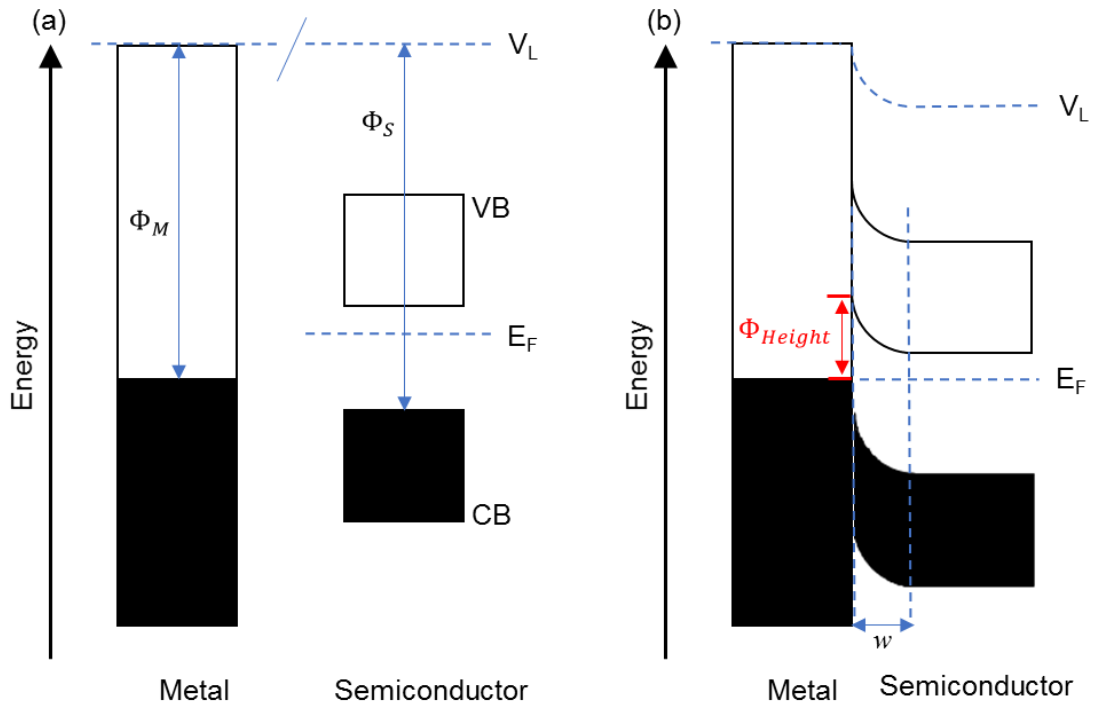
Figure 5: Schematic diagrams of (a) a separate metal and *n*-type semiconductor with Fermi level above that of the metal. (b) metal and semiconductor in intimate contact with depletion region width *w*.

1.3   Organic Photovoltaics: Principles of Operation

In conventional inorganic semiconductors the photogenerated electron/hole pair are well screened from each other by the surrounding lattice due to the large dielectric constant (ε_r), and so the charges are easily separated by the built-in field across the *p-n* junction: That is, the binding energy between the electron and hole is less than the thermal energy of the particles at room temperature of ~ 25 meV (i.e. k_BT, where T is temperature and k_B the Boltzmann constant). The relationship between ε_r and the force of attraction is described by Coulombs law:

Equation 1.

$$F = \frac{q_1 q_2}{4\pi\varepsilon_0\varepsilon_r r^2}$$

Where F is the force of attraction, q_1 and q_2 are the magnitude of the two charges, ε_0 the vacuum permittivity (constant) and r the vector distance between the charges.

In contrast, the conjugated organic molecules used in OPVs to harvest light have a low ε_r and so the binding energy between the photogenerated electron and hole is substantial and cannot be easily overcome using an electric field alone.[13,14] The coulombically bound electron-hole pair is localised on a single molecule or section of conjugated polymer and is called an exciton, shown schematically in Figure 6. These excitons diffuse randomly between many thousands of molecules before relaxing to the ground state. To separate the electron and hole into free charges, which can be collected by the electrodes and used to do work, the exciton on the organic semiconductor must diffuse to the interface with a different organic semiconductor having offset frontier orbital energies (Figure 6, Process 2) where it is possible to split the exciton into an electron and hole. The exciton binding energy in organic semiconductors is typically 0.1 – 0.5 eV and so the offset in frontier orbital energy at the organic heterojunction must be ≥ 0.1 eV. At the organic heterojunction the molecule with the smallest electron affinity and ionisation potential is called the electron donor. The maximum voltage attainable from the OPV device is determined by the difference in energy between the highest occupied molecular orbital (HOMO) of the donor and the lowest unoccupied molecular orbital (LUMO) of the acceptor, and as such the offset should be minimised in order to drive rapid separation without excessive voltage losses.[14] Additionally the time taken for excitons to diffuse to the heterojunction must be less than the time taken for relaxation of

the exciton to the ground state. In organic semiconductors, typical exciton diffusion lengths are in the range of 5-20 nm for an exciton before decaying approximately 0.5 ns after their generation through a range of mechanisms including exciton-exciton annihilation or non-radiative relaxation of the promoted electron.[15] The low exciton diffusion length in organic semiconductors severely limits the thickness of the donor and acceptor domains to 5-20 nm and dictates the subsequent design of all OPVs.[15]
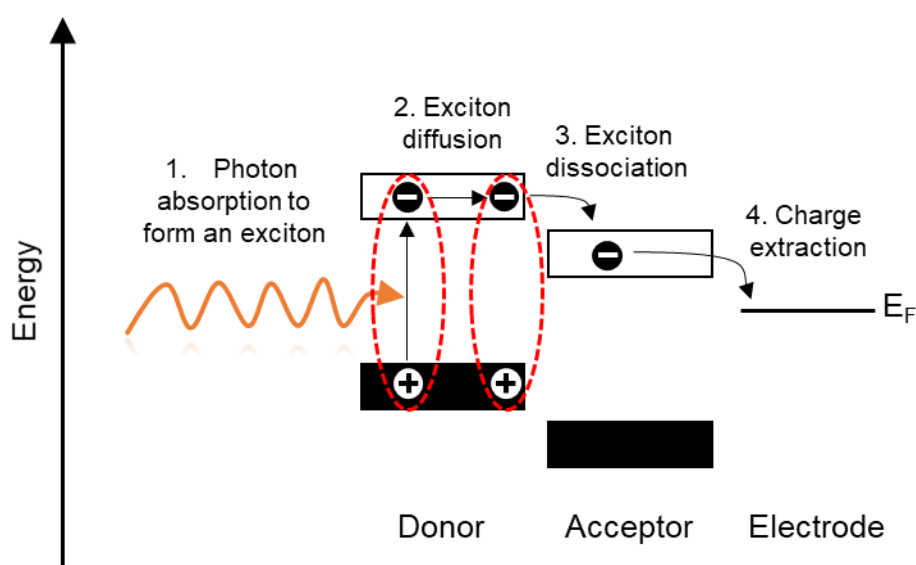
Figure 6: Schematic energy level diagram depicting the basic physical processes in OPVs leading to the extraction of a free charge to the external circuit.

The first heterojunction OPV was reported by *C. Tang,* had ~ 1% power conversion efficiency and was based upon a bilayer of the small molecules copper phthalocyanine and a derivative of perylene which served as the electron donor and acceptor respectively.[16] The low pathlength through both donor and acceptor materials is evident in the optimised 30/50 nm layer thicknesses: Charges generated further from the donor/acceptor interface than the pathlength will decay before separation and not contribute to the photocurrent and so the extra thickness contributes only to the resistance of the device. This device structure was analogous to Figure 7 (a) and provided a model for further development of OPVs based upon these planar thin films up to and beyond the discovery of the bulk-heterojunction (BHJ) in 1995: Figure 7 (b).[17,18]
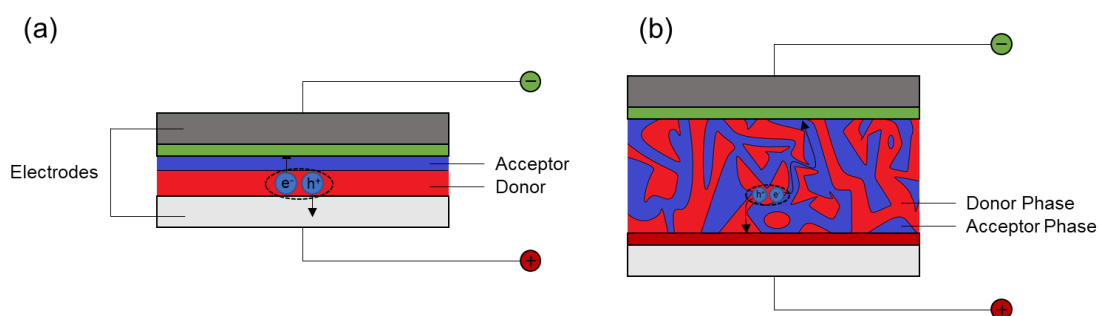
Figure 7: (a) The planar donor/acceptor layers first developed in small molecule OPVs. (b) The modern bulk heterojunction device where donor and acceptor are present as phases in a mixed layer.

The bulk-heterojunction overcomes the limitation imposed by the low exciton diffusion length in organic semiconductors via an interpenetrating blend of a polymeric donor and an acceptor molecule, with distinct donor and acceptor phases spontaneously forming on the scale of 10-20 nm.[19] This heterojunction architecture enables the photoactive layer thickness to be increased up to and beyond 300 nm in modern BHJs so that all of the incident light can be absorbed, despite exciton pathlengths remaining stubbornly low.[20] Thickness-insensitive heterojunctions are key to the transition of OPVs to large scale processing, since it is difficult to fabricate uniform films with precise thickness < 200 nm over a large area. Ensuring light can be absorbed largely on the first pass through the active layer reduces the required precision since device performance is independent of the optical cavity effects discussed later.

In order to minimise electron-hole recombination at the electrodes and so maximise device efficiency, BHJ OPV devices require high selectivity for electrons and holes at each respective electrode, since the donor and acceptor phases both interface with each of the electron and hole extracting electrodes (Figure 7 (b)). To block the possibility of recombination (collision and decay of electron/hole pair) an interfacial layer is added between each electrode and the BHJ such that a barrier to holes exists at the electron extraction electrode and a barrier to electrons at the hole extraction electrode.

1.3.1   An equivalent circuit diagram for a PV device

The charge selective interlayers at the electrode interfaces in an OPV device must have sufficient conductivity to not significantly impede charge extraction. This is reflected in a simplified circuit diagram of an OPV in Figure 8 as a contributor to the resistance labelled R_{series}. The series resistance (R_{series}) represents the total ohmic losses within the device, including the bulk resistance (of the layers), the contact resistance (to the electrodes for charge extraction) and the resistance of the top and rear contacts (electrodes) themselves: An ideal OPV has a series resistance of $0\ \Omega\ cm^{-2}$. An ideal OPV also would be a perfect diode with $R_{shunt} \sim \infty\ \Omega\ cm^{-2}$: A low shunt resistance means that there are paths through the OPV materials along which photocurrent can travel against the intended flow across the junction, rather than being extracted to the external circuit.
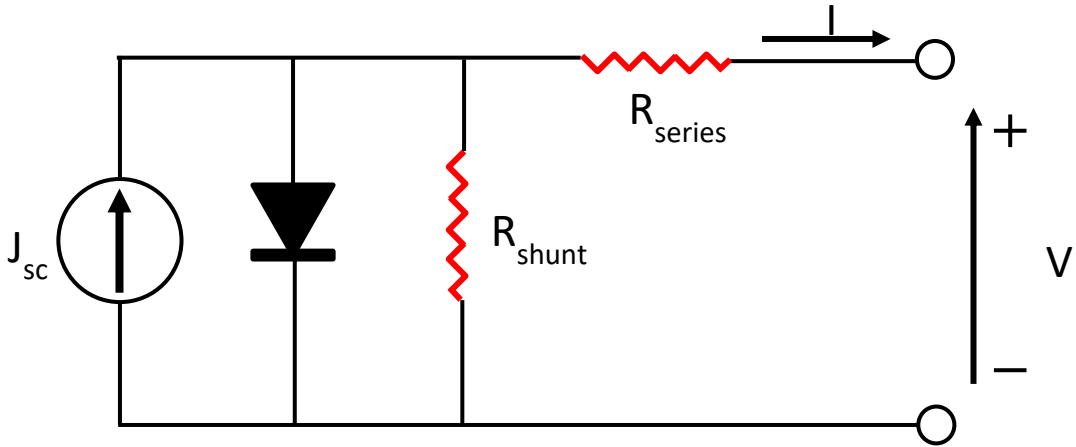
Figure 8: Simplified circuit diagram for a PV device where R_{series} and R_{shunt} are the series and shunt resistances respectively, and J_{sc} represents photocurrent under illumination.

The optimisation of OPV device structure can be described in terms of many factors/parameters, but typically is described by four parameters discussed below when the cell is under simulated solar illumination.

Short circuit current (J_{sc}): J_{sc} is the maximum current from the OPV, at $V = 0$, divided by the active area of the device. Typically, in units of mA cm^{-2}.

Open circuit voltage (V_{oc}): V_{oc} is the maximum potential difference across the electrodes which occurs when $J = 0$, in volts.

Fill factor (FF): FF (unitless) is the maximum power (M_{pp}, Figure 9 (a)) divided by the ideal power out ($J_{sc} \times V_{oc}$). When using the same bulk heterojunction, it reflects well the effects of parasitic resistances: R_{series} and R_{shunt}.

Efficiency (η):

$$\left(\frac{J_{sc} \times V_{oc} \times FF}{Power_{in}}\right) \times 100\%$$
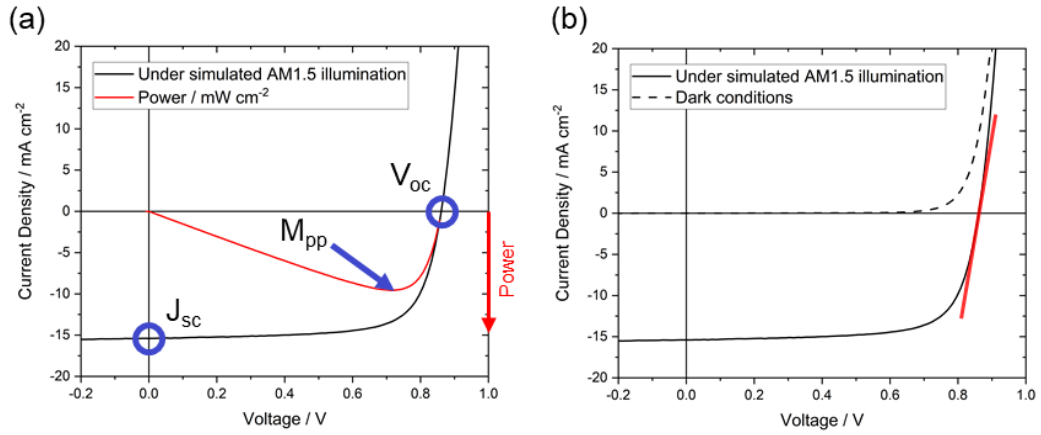
Figure 9: (a) The current response of a model OPV device from this work between -0.2 and 1 V (Black) with the corresponding power curve (Red). In (b) the red line demonstrates how series resistances were estimated and compared between cells produced using different electrodes in this work from the gradient of the curve at $J = 0$.

In Figure 10 (a) the IV characteristics of two comparable structures where in black, the electron extracting electrode has a marginally increased series resistance. The difference in gradient is seen correspondingly to as discussed, and in Figure 10 (b) it is evident how the maximum power point (and so efficiency) is reduced in the cell with higher R_{series}.
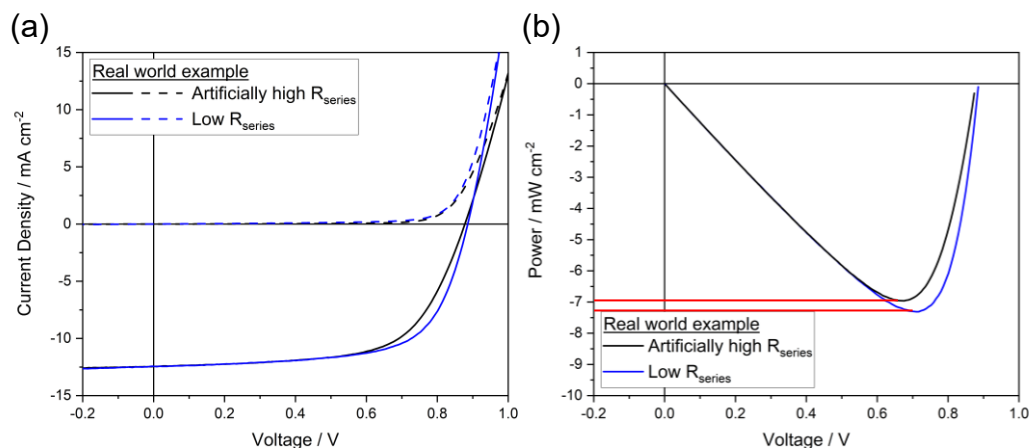
Figure 10: (a) The IV characteristics of two comparable model OPV cells from this work, where (Black) has a significantly raised R_{series} as compared to (Blue). (b) For the same cells, the maximum power output is affected correspondingly.

1.4 Organic Photovoltaics: Materials

In this section some of the most used materials and OPV device architectures reported in the literature are introduced. Figure 11 shows the most common OPV device stack, where the stack refers to the sequential deposition of thin films of material to form the device from the supporting substrate upwards. The majority of OPV devices are designed to be illuminated from the substrate side, and so the substrate electrode and adjacent charge extraction interlayer must be highly transparent to maximise the light intensity reaching the photo-active layer. An 'inverted' OPV device structure (Figure 11) refers to a device in which the extraction of electrons to the external circuit is via the transparent substrate electrode with holes extracted via the highly reflective opaque top electrode. The inverted structure is widely believed to have greater commercial potential due because it puts the high work-function, least reactive electrode materials on the top of the device which is the part of the device most vulnerable to oxidation.[21]
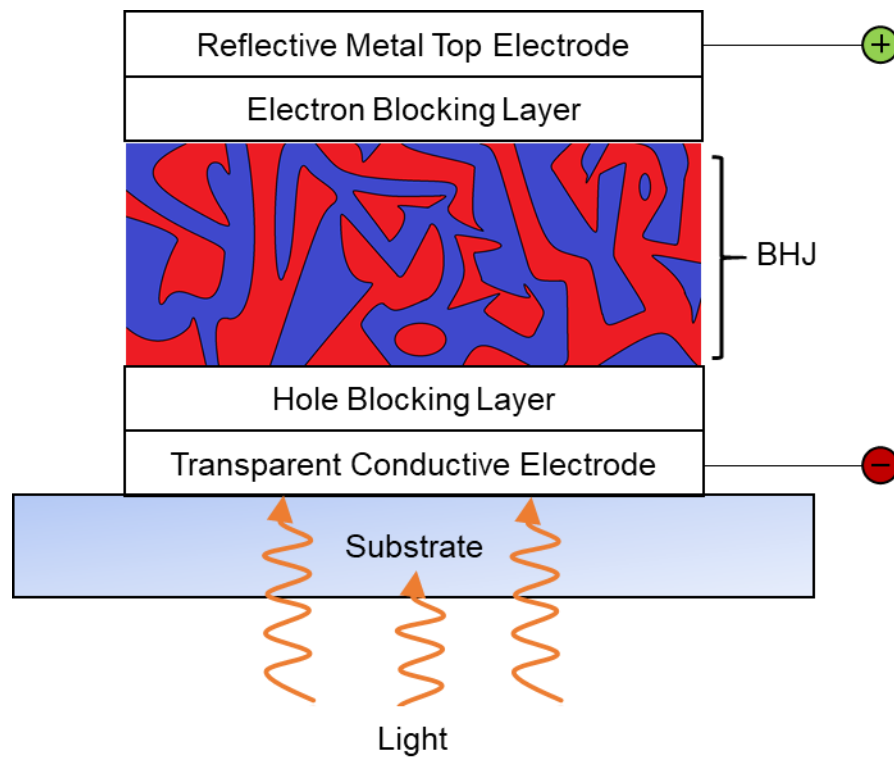
Figure 11: A schematic depiction of the inverted device 'stack' common in OPVs.

1.4.1 Substrates

The majority of research scale OPV devices are supported on glass substrates and are illuminated from the substrate side (Figure 11). Glass is a useful substrate for OPVs as, apart from its high transparency, it has a low surface roughness and is an excellent barrier to H_2O and O_2 ingress which can degrade the BHJ. It is well accepted however that commercial OPVs would be best supported on flexible plastic substrates to enable compatibility with high-throughput roll-to-roll production and applications requiring low weight such as in transportation.[22–24]

The most common transparent plastic substrates for OPVs are polyethylene terephthalate (PET) and polyethylene naphthalate (PEN). Less commonly, polycarbonate, polyethersulfone and polyimide are also used. The choice of OPV charge extraction layers, BHJ materials and the top electrode are largely independent of the substrate choice because all are inherently flexible at the film thicknesses used in OPV devices. The transparent conductive electrode (TCE) material, which is deposited directly on the supporting substrate, can however often require annealing at $> 200°C$ at which

temperature all of the aforementioned plastic substrates suffer low dimensional stability.[25]

1.4.2 *Transparent conducting electrode (TCE)*

To achieve their maximum cost-advantage over other types of PV, it is widely accepted that OPVs must achieve the original vision for continuous printing of the solar cell onto a roll of flexible conductive substrate. Most research into OPV development has typically focused on increasing efficiency, with cell areas < 0.1 cm^2 on rigid glass substrates and with the organic semiconductors deposited using spin.[20,26,27] Significant progress has been made to demonstrate the scalability of OPV production, such as printable top contacts and replacing spin-coating with blade coating.[28] To date, relatively little attention has been given to the development of transparent electrodes matched to the needs of OPVs, which are needed in order to achieve their full commercial potential.

Perhaps the most overlooked trend in high performance OPVs is the continued use of the high cost indium tin oxide coated glass (ITO) as a transparent conductive electrode.[20,26,27] The expense of ITO glass largely derives from the scarcity of indium, and is predicted to rise sharply with increasing demand as indium is currently produced as a by-product of zinc refinement.[29] This cost is compounded by the requirement to sputter ITO, which is a slow process and inherently costly. Additionally the conductivity of sputtered ITO is insufficient to scale OPV cells to cell areas > 0.5 cm^2 without incurring significant electrical losses. In the research laboratory typical cell areas on ITO glass are < 0.1 cm^2,[30,31] and so the parasitic resistance associated with the TCE sheet resistance is not evident in the device characteristics and the high transparency leads to high J_{sc}.

Several solutions have been proposed for replacing ITO glass, each with their own merits and disadvantages. Firstly, ITO can be sputtered directly onto plastic. On glass ITO is typically annealed at $> 300°C$ which simultaneously reduces roughness, reduces the sheet resistance and improves the transparency.[25] This annealing step is not compatible with plastic substrates such as PET or PEN and so the achievable optoelectronic performance is reduced. The brittle nature of ITO also makes ITO on plastic exceedingly difficult to work with, even in the research laboratory, often resulting in devices with macro-scale cracks across the TCE which seriously degrade device performance.[32] Also, analyses of the life-cycle of OPVs using ITO as the transparent

substrate electrode suggest that 50% the fabrication cost of a typical OPV would be contributed from the use of ITO. It is widely considered that although a useful material for many applications, OPVs require a lower cost, highly conductive TCE compatible with roll-to-roll printing which ITO on plastic is not.

Ultra-thin metal films

The simplest alternative to ITO is an optically thin metal film (5-15 nm thick) of one of the most electrically conductive metals; gold (Au), copper (Cu) or most commonly silver (Ag). The relatively low cost (~ 1% of Ag) and abundance of Cu with comparable conductivity makes it an attractive metal choice for a commercial OPV electrode. The higher susceptibility of Cu to oxidation in air however has prevented its widespread use for this application. Importantly ultra-thin metal film electrodes can exhibit surprising robustness and low surface roughness (as in Figure 12) and research in our group,[32–35] and others,[36–42] has shown the promise of this type of electrode to replace ITO in OPVs. Sheet resistances as low as 4 Ω sq^{-1} have been demonstrated for Ag films, which is below that achievable with ITO glass, with comparable transparency.[43] To achieve high transparency ultra-thin metal film electrodes are typically coupled with one or more transparent layer of very well-defined thickness and a refractive index,[35,39,40,44] intermediate between that of the glass and substrate/semiconductor to reduce the reflection at each interface, since most optical losses from thin metal films are due to reflection.[45,46] Thin metal films are inherently malleable due to their low thickness and so are compatible with plastic substrates and roll-to-roll fabrication.[42] To further improve transparency thin metal film electrodes can be patterned with an array of small apertures although this is at the cost of sheet resistance due to the metal removed.[47]
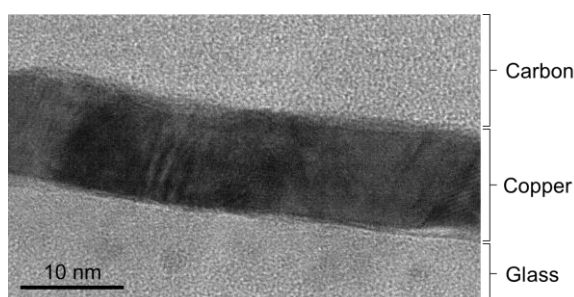
Figure 12: A transmission electron microscope (TEM) image of an example 9 nm thick Cu film on glass from this work.

Nanowires

Another popular approach to transparent electrode fabrication is a network of metal nanowires, typically of Ag but also Cu.[48–51] These electrodes are based on a random array of metal nanowires, typically < 100 nm in diameter and > 10 µm in length, synthesised and processed from solution (Figure 13). The random network of wires can be formed on glass, plastic or directly on an OPV as a top electrode in semi-transparent OPVs (Figure 13)[52] by painting,[53] spray-coating,[54] or drop-coating.[55] Ag nanowires have been shown to match the optical performance of ITO in OPV devices, with similar sheet resistances of 10-100 Ω sq^{-1}.[50,52,56–58] Notably, to collect charges produced in areas between nanowires, nanowire electrodes are typically coated with the high-cost conductive polymer poly(3,4-ethylenedioxythiophene) polystyrene sulfonate (PEDOT:PSS) to span the gaps between nanowires. Although nanowire electrodes have found application as a transparent electrode in other technologies, the high surface roughness and their susceptibility to delamination is limiting for OPVs.[59]
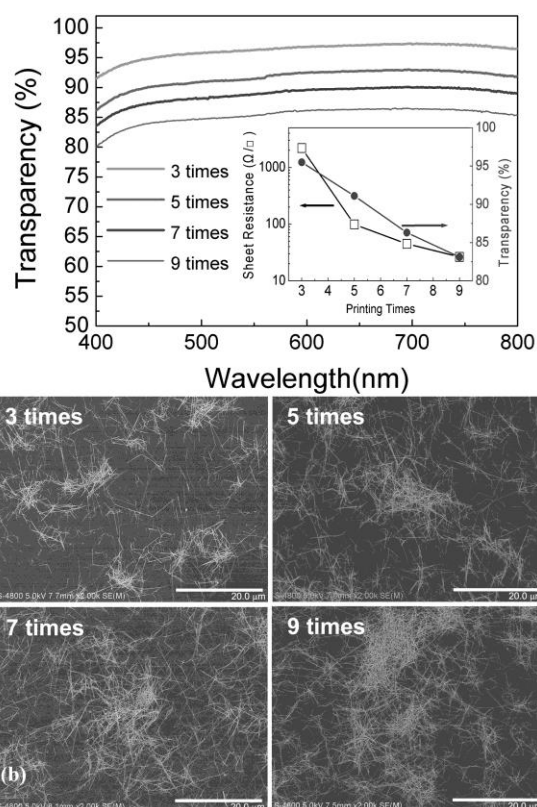
Figure 13: Published in "Inkjet printed silver nanowire network as top electrode for semi-transparent organic photovoltaic devices" by Lu *et al.*[52] The transparency (a) and SEM images (b) of inkjet printed Ag nanowires on PEDOT:PSS:MoO$_3$/Glass surface. The inset

in figure (a) shows the average sheet resistances and transmissions of the Ag nanowire networks of different printing times.

Metal grid electrodes

In many respects metal grid electrodes can be compared to an ordered array of nanowires (Figure 14), with greater line width and without the disadvantage of vulnerable junctions between nanowires. The stability of metal grid electrodes is not often reported in the literature, although it is logical that these differences to nanowire electrodes will improve stability. The ordering of the metal lines in a grid electrode results in less superfluous metal and so enables higher theoretical optoelectronic performance when compared to random nanowire electrodes. Unlike optically thin planar metal electrodes sheet resistances much lower than 5 Ω sq^{-1} are attainable without compromising transparency.
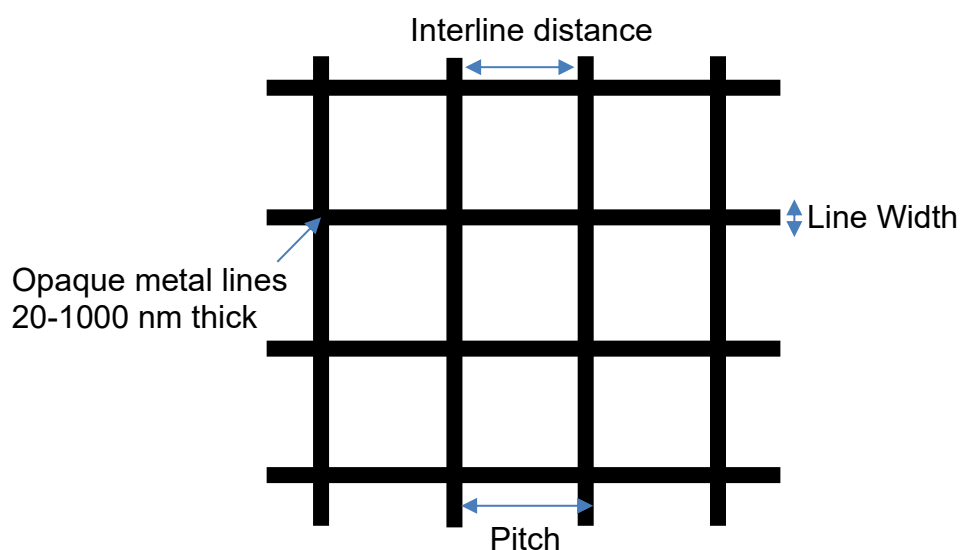
Figure 14: Schematic of a metal grid electrode with the meaning of the dimension terms illustrated.

Metal grid electrodes have been reported with a wide array of patterns, most typically square grids with: metal thickness 0.1 - 2 µm, pitch 150 – 2000 µm and line-width 5 – 200 µm.[60] Notably, since grid lines are opaque a wide range of metals are suitable as compared to optically thin metal film electrodes; with little inherent advantage to using

Ag. Increasing the surface coverage of metal by increasing line width or reducing pitch inevitably reduces the transparency but also reduces the sheet resistance. The sheet resistance can be reduced without changing the transparency by increasing the metal thickness, although this increases surface roughness which can be limiting for OPVs. The effect of changing each of these parameters is summarised in Figure 15.
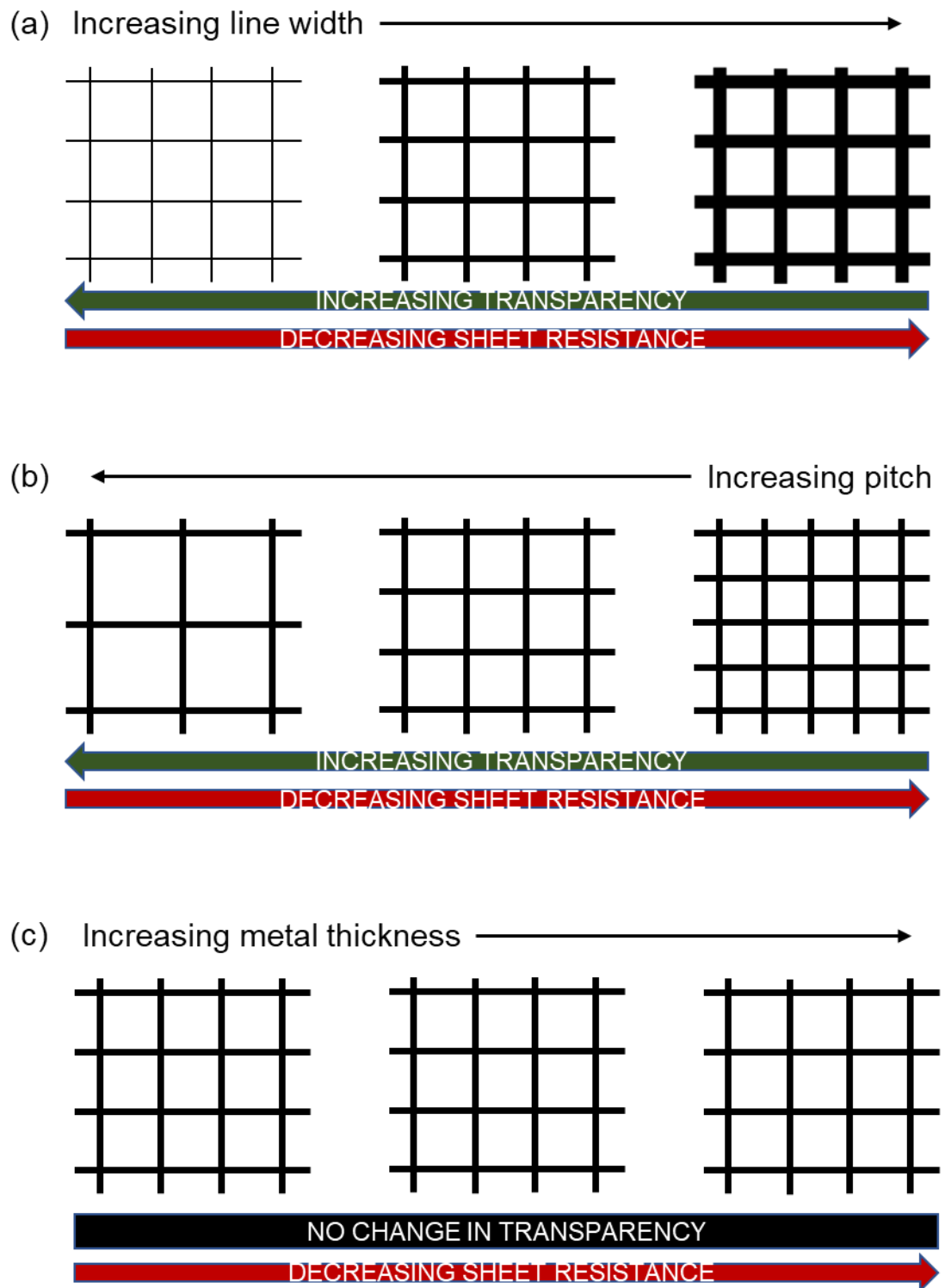
Figure 15: The effect of changing the (a) line width, (b) pitch and (c) metal thickness (z-plane) on both transparency and sheet resistance summarised. Adapted from Lee *et al.*[60]

The importance of the transparent electrode sheet resistance in determining OPV performance is often overlooked in the literature because the small area of most laboratory-scale OPV devices, ~ 0.1 cm^2, means that high electrode sheet resistances can be tolerated without affecting device fill-factor because the total series resistance is low. Thus OPVs based on electrodes with 20 - 30 Ω sq^{-1} are commonplace in the literature.[38,61–63] For practical applications the cell area would need to be ≥ 1 cm^2 at which dimensions an electrode sheet resistance > 10 Ω sq^{-1} results in an unacceptable loss of fill factor. As such it is important not to evaluate the transmittance, or small-scale device performance, in isolation.

The performance of transparent electrodes with different designs and using different materials can be directly compared using the following Haacke Figure-of-Merit (FoM), which is especially important for grid electrodes since it is so easy to change the line width and pitch of the grid (Figure 15) to achieve high transparency at the cost of conductivity:

Equation 2.

$$Haacke \ FoM = \frac{\%T^{10}}{R_{sh}}$$

where %T is the average transmittance 400 – 800 nm and R$_{sh}$ is the sheet resistance. Until this point only the simplest grid design; square grids, has been considered here. As shown in the literature by Muzzillo *et al.* there are small gains to be made in the FoM through optimising the design, particularly with solar cells as equal conductivity in the x and y directions is not required, only the lateral conductivity to a bus bar is important.[64] As the gains in FoM are < 10 % (Figure 16) and the fabrication methods reported in this thesis are capable of producing any of these designs, this aspect will not be a focus of this thesis.
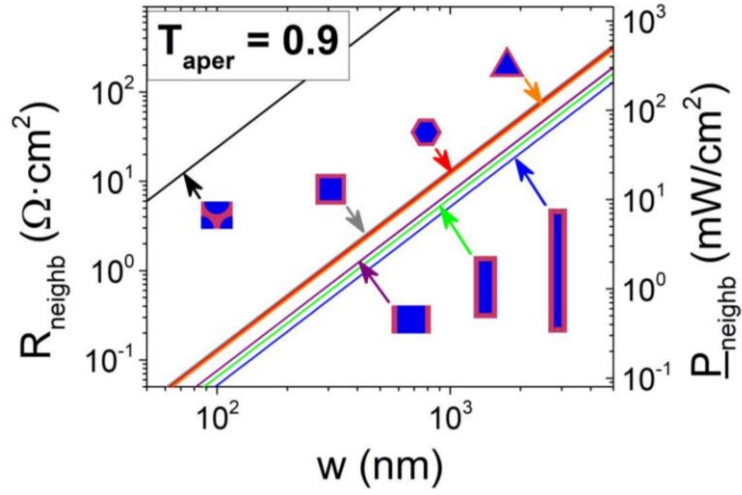
Figure 16: Reproduced from Muzzillo *et al.*[64] Neighbour series resistance versus minimum wire width at constant aperture transmittance of 0.9 for the grating (purple), 4× rectangle (blue), 2× rectangle (green), triangle (orange), hexagon (red), square (grey), and circle (black). Resulting power dissipation density on the right axis was calculated at 40 mA/cm^2.

1.4.3   Bulk-heterojunction materials

All of the OPVs in this work were produced using BHJs, rather than the planar bilayer architectures discussed earlier, to enable simple solution processing, thicker light harvesting films and higher device efficiencies. It is also important to note that, as this thesis focuses on developing the transparent electrode, well understood BHJ materials were used to demonstrate and compare device performance.

35
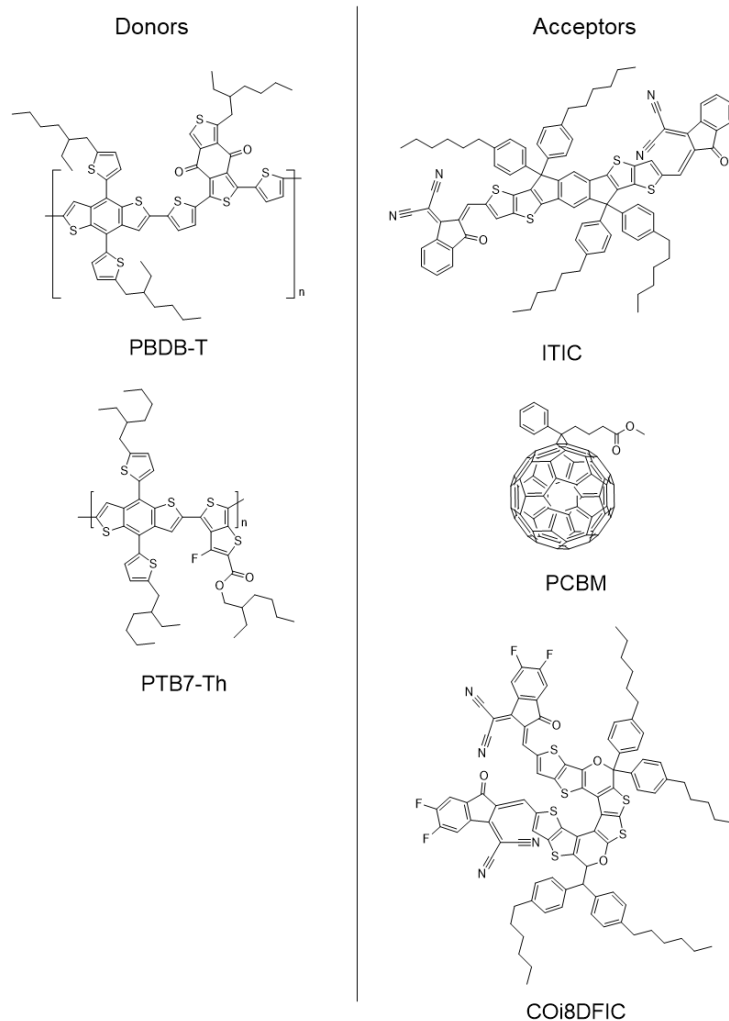
Figure 17: Donor and acceptor molecules used in this work.

Non-Fullerene acceptors

The evolution of polymeric donor materials for OPVs has been largely iterative, with the vast majority of new materials sharing a similar thiophene backbone. A step change in OPV performance was however made with the development of non-fullerene acceptors (NFAs). Until that point OPV donors were universally paired with the electron acceptor $PC_{60}BM$ or $PC_{70}BM$, which are cage fullerenes derivatised to improve solubility (Figure 17). Their success as electron acceptors in BHJs is largely attributed to their isotropic electron transport and propensity to phase separate spontaneously when blended with conjugated polymers to form domains with lengths comparable with the exciton diffusion length (5-15 nm).[65] However, their low absorbance in the visible and near IR spectral range limits their contribution to device photocurrent. Although compatible with many

common polymer donors, the cage structure of PCBM also limits the tunability of the frontier orbitals (HOMO/LUMO) to optimise device performance.

In contrast, the frontier orbital energies of NFAs are highly tuneable and in recent years a wide range of NFAs have been developed based on very different structures. Modular A-D-A type NFAs for example, where an electron rich core is flanked by two electron deficient acceptor moieties are promising replacements for fullerene acceptors in OPVs due to the ease of synthesis and excellent tuneability due to the modular design.[65] A-D-A fused ring acceptors have enabled < 16% power conversion efficiency to be achieved.[26] Other entirely different acceptor classes have also shown promise with perylene diimide based molecular acceptors demonstrating 10.6% efficiency,[66] and all-polymer OPVs (polymeric donor and acceptor molecules) 14.4%.[67] The improved OPV performance with use of these NFAs is due to the increased absorbance and spectral-coverage of these new types of electron acceptors.

PBDB-T/ITIC

The most common donor/acceptor blend used in the research presented in this thesis is PBDB-T, a polymeric donor, and ITIC, a A-D-A type non-fullerene acceptor (Figure 17). This BHJ was chosen for the ease of solution processing, reasonable device power conversion efficiencies (~ 10%) and reliability.[68] PBDB-T is known to be thermally stable up to 160°C in solution and as thin films which enables fast and complete dissolution of the polymer by heating the solution, and removes the need to vacuum dry the film. The large contribution of the acceptor molecule to photocurrent generation is evidenced by the comparison of the reported currents under 1 sun illumination for PBDB-T/PC$_{70}$BM blend (12.80 mA cm^{-2}, 7.45% efficient) and PBDB-T/ITIC (16.80 mA cm^{-2}, 11.21% efficient), and results from the complimentary absorption spectrum; Figure 18.
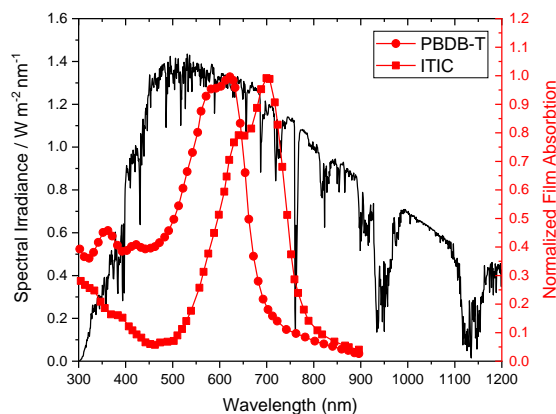
Figure 18: The overlaid spectral irradiance and normalised absorption of PBDB-T and ITIC.

PTB7-Th/PC₇₀BM

PTB7-Th, also commonly referred to as PCE-10 (Figure 17), is one of the most common polymers used in OPVs with 618 literature citations in the period 2013 – 2019 alone (Clarivate Analytics, Web of Science). Together with the fullerene acceptor $PC_{70}BM$ this blend is one of the most intensively researched BHJ systems. Importantly it has also since been demonstrated as part of a 10% efficient OPV processed entirely in air and using doctor-blading to deposit the BHJ, making it an excellent candidate for commercialisation.[69] In this thesis PTB7-Th/$PC_{70}BM$ BHJs are used to demonstrate the relative performance of a range of heterojunction thicknesses, since PTB7-Th has been shown to yield excellent device performance with thicker than optimal BHJ films.[70]

Ternary PTB7-Th/COᵢ8DFIC/PC₇₀BM BHJ system

One key advantage of NFA molecules is the increased spectral coverage they offer, particularly in the near-IR region, and this has led to a range of ternary BHJs being demonstrated where light is harvested by a single layer comprising both donor/acceptor-1/acceptor-2 and donor-1/donor-2/acceptor in separate phases. This approach has many of the benefits of multi-junction OPVs (i.e., tandem cells) with the simplicity of a single light harvesting layer. The PTB7-Th/COᵢ8DFIC/$PC_{70}BM$ BHJ used in the research reported herein is a donor/acceptor/acceptor system absorbing strongly to ~1000 nm, far beyond the PTB7-Th/$PC_{70}BM$ BHJ system (~750 nm), although suffers from poor device stability.

Role of solvent additives

Post-deposition vacuum drying or annealing of the BHJ layer is needed to remove residual solvent and morphology controlling additives such as 1,8-diiodooctane (DIO) which can dramatically reduce the photostability of the BHJ layer.[71] DIO is commonly added to laboratory-scale OPVs to slow evaporation because of its high boiling point (> 300°C), which leads to better phase segregation into donor and acceptor phases and typically improves device efficiency by ~20%.[72] Unfortunately the photostability of these phases is lower than those formed without additives, or using alternative additives, and as such DIO is not expected to be used in commercial OPVs.[73]

1.4.4   *Electron/hole transport layers*

The complex interpenetrating network morphology of BHJs (Figure 7 (b)) results in both donor and acceptor phases contacting both electrodes, necessitating the inclusion of an interfacial layer to selectively extract either e⁻ or h⁺ whilst blocking the other carrier type. In the inverted OPV device structure used throughout this thesis the hole-blocking electron transport layer (ETL) is deposited onto the TCE, and the electron-blocking hole transport layer (HTL) is deposited prior to deposition of the reflective top contact.

By example, Figure 19 depicts the simplified electronic structure for a model OPV device without (a) and with (b) a ZnO electron extraction layer between the electrode and BHJ. Without the ZnO holes can unintentionally be extracted by the Cu electrode. The low-lying valence band of ZnO effectively blocks the transfer of holes to Cu and as such the photocurrent and fill-factor of the OPV device are increased.
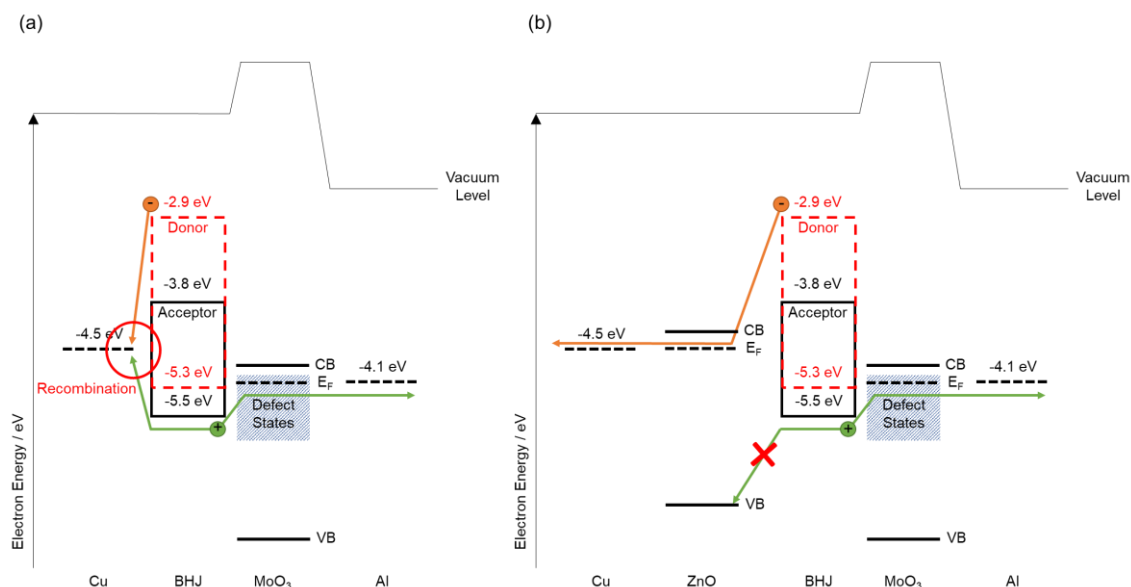
Figure 19: Simplified band structures (Cu,[74] ZnO,[75] ITIC,[76] PBDB-T,[68] MoO$_3$.[77]) for the inverted OPV device structure used in this thesis without (a) and with (b) an ETL (ZnO) to block recombination at the electron extracting electrode (Cu). The overlapping donor/acceptor HOMO and LUMOs are represented by the extent of the dashed red and black boxes respectively.

It is important that the charge extraction interlayers do not degrade device performance by increasing R$_{series}$ significantly and so they are typically much thinner than the BHJ. MoO$_3$, the HTL used for these model OPV devices, is thermally evaporated and so can be deposited reliably as extremely thin (< 10 nm) and compact films which minimises the resistance to hole transfer whilst retaining selectivity for holes. Evaporated MoO$_3$ is a wide band gap semiconductor, *n*-type doped as a result of oxygen lattice vacancies.[77] Holes are transported across the layer through these dense, occupied, defect states in the band gap as depicted in Figure 19. PEDOT:PSS (AL 4083), as opposed to the highly conductive PEDOT:PSS formulation (PH1000) used previously with grid electrodes, is also a commonly used HTL in OPVs and can be solution processed. It cannot easily be deposited however on top of the organic semiconductor layer and as such was not used in the inverted structure here.

In inverted OPVs ZnO is the most widely used ETL. ZnO can be solution processed to form compact thin films of thickness $20 - 50$ nm and have a conduction band edge ideally located for electron extraction (Figure 19) from most electron acceptor

molecules. Wide band gap metal oxides like ZnO can also be used to optimise the optics of OPVs by enabling an optical cavity effect, since the thickness of this layer can be fine-tuned to optimize the light distribution in the device.[39,78] Through the micro-cavity effect the current generated by a BHJ OPV can exceed expectation based on the transmittance of the electrode. In this work the nanoparticulate ZnO interlayer is deposited from a commercial suspension of ZnO nanoparticles by spin coating, although it can also be deposited by blade or spray coating which offer the best compatibility with roll-to-roll processing. ZnO is sufficiently conductive due to the presence of zinc interstitials and oxygen vacancies which render it *n*-type.[79] Together with the deep lying valence band edge at 7.5 eV below the vacuum level, and wide band gap, this makes ZnO one of the most common ETL materials used in OPVs.[75] ZnO can also be deposited from a sol-gel, where precursors are coated from solution before annealing at 180-600°C to drive the reaction of the precursor materials to form ZnO.[80] Using this method a small percentage of the zinc acetate can be substituted by an aluminium source (optimally at ~ 3% concentration) to improve the conductivity by an order of magnitude.[79,81] Experimentally however, the latter method was found to be unsuitable for Cu-based electrodes due to the high annealing temperature in air.

Notably in many of the OPV device experiments reported in this thesis an Al-doped ZnO nanoparticle suspension was used (Sigma Aldrich (SKU 901092)). The level of Al in these ZnO nanoparticles is extremely low and does not have a significant impact on the conductivity of the film. At very low levels Al does however reduce the well-known photo-activation requirement associated with ZnO ETLs: The charge carriers in the thin ZnO nanoparticulate layer can be depleted in reaching thermodynamic equilibrium with the adjacent layers blocking electron transfer.[82] Doping with Al or introducing UV light of energy greater than the ZnO bandgap, which can excite electrons to the ZnO conduction band, increases the carrier density and also may serve to fill trap states within the ZnO bandgap increasing charge mobility.[82,83] Unfortunately, UV light is also detrimental to the stability of many OPV polymers and commercial modules are likely to integrate a UV filter. The effect of the UV photo-activation of ZnO is evident in the series resistance (IV gradient at > 0.8 V in forward bias) of the two dark IV characteristics for a model ZnO-ETL OPV in Figure 20 before (Red) and after (Blue) illumination.
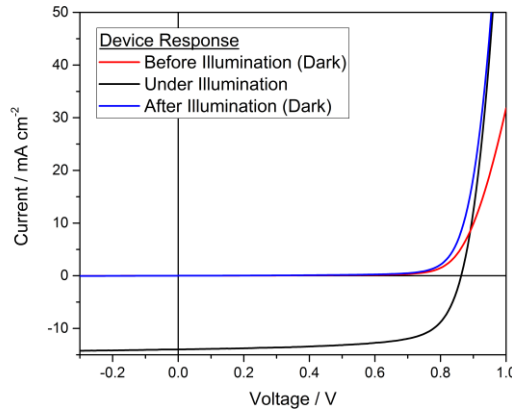
Figure 20: The dark characteristics for a model OPV using an un-doped ZnO electron transport layer before (Red) and after (Blue) illumination (Black).

1.4.5 *Reflective electrode*

Unlike the TCE on the light-facing substrate side of an OPV device, the top contact has no requirement for transparency and so is most commonly a thick metal film (100 - 300 nm) that offers both high conductance and high reflectance. In inverted OPV device structures the opaque top contact extracts holes and so should have a high work function (≥ 5 eV) to minimise any barrier to hole extraction. By using a MoO_3 hole extraction layer it is possible to use lower work function metals such as Ag (Φ 4.3 – 4.7 eV) and Al (Φ 4.2 – 4.4 eV) since Fermi level alignment pins the Fermi level of the electrode to the HOMO of the acceptor and maximises the electric field across the device. Thermally evaporated Al is used here as the top contact and is popular for its low material cost and high morphological stability. In commercial OPV modules Ag is expected to be the metal of choice due to its higher oxidative stability.[84]

The thick metallic top contact must be highly reflective across the visible (400 – 700 nm) and near-IR (700 – 1000 nm) regions because in OPVs the heterojunction is typically too thin to absorb all the incoming light on the first pass.[85] By reflecting light not collected on the first pass through the heterojunction the path length can be doubled by a highly reflective top contact, or multiplied by many times by light trapping between the two electrodes (i.e. the micro-cavity effect).

Top contacts have also been demonstrated made from Ag nanowire networks,[52] and semi-transparent conductive PEDOT:PSS formulations.[86] However, these give no

opportunity for reflection of light so to achieve equivalent performance requires > 2× the BHJ thickness. Both of the latter types of top electrodes are useful for semi-transparent OPV device designs, although the high sheet resistances limits performance at the module scale.

1.5   Cu-based electrodes

Ag nanowires,[87] planar metal films,[44] and metal grid electrodes,[31] are all viable alternatives to ITO or can be used as the top contact in OPVs. However, a cost analysis of the respected model 'freeOPV' structure attributes 33% of the total material cost to Ag:[88] The estimated material cost of a thick Ag top electrode alone is €7.67 / m^2.[89] This demonstrates that to drive wider commercialisation it is necessary to achieve equivalent performance and stability using low-cost materials and processing. Cu is an attractive replacement for Ag in the transparent electrode since the conductivity is equivalent to Ag but at 1% the material cost.[90]

A seed or adhesion layer is an intermediary layer between the substrate and a metal film that facilitates the formation of compact and mechanically robust films of very low metal thickness. Au, Ag and to a lesser extent Cu adhere only very weakly to typical substrate materials,[91,92] and so the atom-atom interactions between condensed metal atoms dominate over atom-substrate interactions. The weak interaction with the substrate enables the diffusion of metal atoms, forming isolated islands which eventually coalesce. Seed layers are especially important for films of thickness < 15 nm as this is close to the percolation threshold thickness of most metal films where initial atomic layers coalesce to a continuous film, and in this region the properties of the film evolve rapidly.[93]

A seed layer binds strongly to the substrate and condensing metal, supressing island growth by binding incoming metal atoms strongly to the substrate so supressing metal atom diffusion. At first, seed layers were typically 1 - 5 nm thick films of germanium, chromium or nickel which are spluttered or evaporated.[94] Unfortunately these metal seed layers absorb light strongly across the visible spectrum and so this parasitic absorbance is detrimental to their inclusion in OPVs.[95]

In the research presented in this thesis thin optically thin Cu films were most typically evaporated onto glass or plastic substrates derivatised with a mixed monolayer of 3-mercaptopropyl(trimethoxysilane) (MPTMS) and 3-

aminopropyl(thrimethoxysilane) (APTMS), as in Figure 21. The molecular seed layer was deposited using a vapor-phase deposition process established by Stec *et al*, which enables the reproducible formation of sub-10 nm thick slab-like Cu films.[34,96] This molecular seed layer is transparent to visible light so does not contribute to parasitic light absorption. APTMS rapidly binds to glass and UV/O$_3$ treated plastic films via hydrogen bonding between the amine end group and hydroxyl groups, which hold the methoxysilane group in close proximity to the surface increasing the likelihood of a condensation reaction between the methoxysilane group and the substrate hydroxyl group to form a strong siloxane linkage (Figure 22 (a)). APTMS bound to the surface also catalyse further reactions through the deprotonation of hydroxyl groups on the substrate forming highly reactive moieties onto which incoming APTMS or MPTMS molecules can covalently bind (Figure 22 (b)).[96–98]
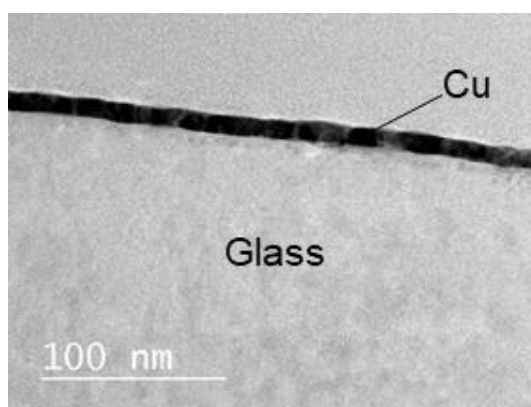
Figure 21: Transmission electron microscope cross-sectional image of a 9 nm Cu film supported on a glass substrate derivatised with a MPTMS/APTMS monolayer.
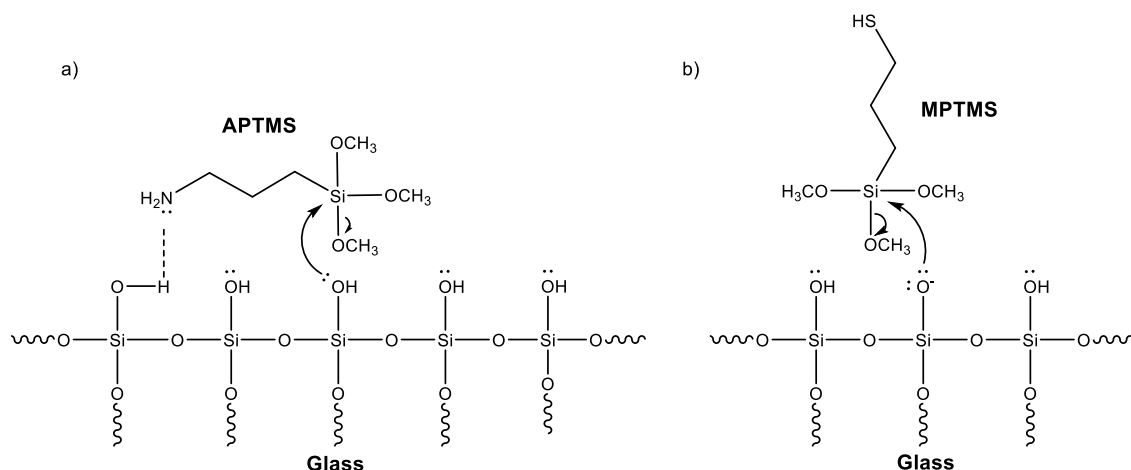
Figure 22: a) The hydrogen-bond facilitated condensation reaction of APTMS to a glass surface. b) The amine-deprotonated hydroxyl moiety reacting with MPTMS.

The amine-Cu bond is weaker than the thiol-Cu bond and so, although high quality Cu films form on APTMS-derivatised substrates, the film stability in water is low which is important because water is often used during the substrate cleaning procedure. To compensate for this MPTMS and APTMS were added in equal quantities to a vial for the solvent-less deposition of the adhesive layer, where cleaned substrates were held at low pressure ($<$ 50 mbar) for 4 hours in close proximity to the liquid phase alkylsilanes as the published protocol.[96] This results in a mixed monolayer of APTMS and MPTMS ~ 1 nm thick at a ratio of 3.4 ± 0.1 : 1 with a dense array of amine and thiol groups exposed.[99] Although typical plastic substrates used for OPVs; namely PET and PEN, do not have native hydroxyl groups to covalently bind with the methoxysilane moiety of MPTMS/APTMS, a 15 minute UV/O_3 treatment results in the formation of surface hydroxyls of sufficient density.[34] The alkylsilane molecular adhesive layer presents a very high density of nucleation sites to the incoming metal and so suppresses metal diffusion at the early stages of film growth enabling the formation of compact and extremely smooth slab-like films of Cu at sub-10 nm film thickness.[96]

1.5.1   *Corrosion of Cu*

The wide variety of applications of Cu has motivated many studies into the kinetics of Cu oxidation in ambient air. This section summarises the findings of those studies focusing

on polycrystalline Cu films (as opposed to single crystal films), which are of most relevance in the current context.

Cu has three thermodynamically stable oxidation states; Cu^0, Cu^+ and Cu^{2+}, with most studies in agreement that at ambient temperature spontaneous reaction of the metal with O_2 and H_2O results in an oxide overlayer on top of the base metal of which the most significant components are Cu_2O and CuO, with a minor component of $Cu(OH)_2$ (Figure 23).[100–104] It is understood that the hydroxide forms a metastable thin intermediary layer of constant thickness, and decays to form the oxide CuO.[100] CuO_2 forms directly when Cu^+ ions react with oxygen adsorbed at the air interface.
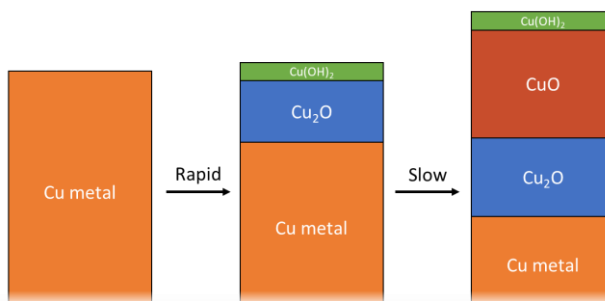
Figure 23: A general model for Cu oxidation where the rapid initial reaction with oxygen at the surface of the film forms a Cu_2O layer. In a parallel mechanism CuO forms slowly through intermediate (metastable) $Cu(OH)_2$ burying the initial Cu_2O oxide.

The formation of oxide layers under ambient conditions on metal surfaces is not in many cases well understood. Whilst a few metals such as Au and Pt do not oxidize and a few form compact self-limiting oxide layers (e.g. Al, Cr), most oxidize continuously. The kinetics of oxidation are affected by environmental factors, such as O_2 concentration, humidity and temperature, as well as material factors such as purity, roughness, thickness and crystallite orientation/structure. This has led to a confusing array of reports about the oxidation of Cu, many with conflicting statements. It is broadly agreed that at elevated temperature ($\geq$ 200°C) Cu metal undergoes a complete oxidation to a mixed oxide of Cu_2O and CuO.[105,106] However there are relatively few reports pertaining to the oxidation of Cu at low temperature ($\leq$ 100°C), which is the relevant temperature range for PVs which operate typically in the 0 - 70°C range.

Those reports pertaining to the ambient oxidation of Cu agree that upon air exposure a Cu_2O layer rapidly forms by reaction between Cu^+ ions and O_2. Platzman *et al.* postulate this reaction is limited by the diffusion of Cu^+ ions, driven by an electric field to the air-oxide interface.[100] Since the potential difference giving rise to the migration to the surface is constant, the electric field strength is attenuated with increasing oxide thickness and the rate of Cu_2O sharply falls after the initial formation. Platzman *et al.* proposed that the oxidation of Cu to Cu_2O is continual, although slow, and occurs alongside the oxidation of Cu^0 to CuO and $Cu(OH)_2$, while other reports show that further formation of Cu_2O after the initial stage is halted by the formation of a CuO overlayer.[107] In other reports, Cu is shown to form a pure Cu_2O overlayer with no CuO formation.[108] The model described by Platzman *et al.* is most consistent with the data presented in this thesis; both in terms of the similar compositional XPS analysis (Chapter 6) and similarities in sample preparation (evaporated polycrystalline Cu).[100,108] It is important to emphasise that any comparison to the literature must be made with caution, since the degree and relative proportions of the different oxidation products are a complex function of a number of factors including ambient humidity and the crystallinity of Cu, but also the surface roughness.

Alongside the rapid formation of Cu_2O, Platzman *et al.* postulate that $Cu(OH)_2$ forms simultaneously as a result of the continual dissociation of H_2O at the oxide-air interface to form hydroxyl ions which react with Cu^+ that have migrated up from the buried metal.[100] $Cu(OH)_2$ is metastable, and the decomposition to form CuO is in dynamic equilibrium with its formation at the surface. The formation of CuO via $Cu(OH)_2$ is rate limited by the dissociation of H_2O, and it is this which results in the susceptibility of thin film polycrystalline Cu, with a high surface area and small crystallites, to the formation of CuO as compared to bulk Cu.[108] The rapid initial formation of Cu_2O upon air exposure slows exponentially over a period of hours to days,[100] so the very slow formation of CuO dominates the long-term oxidation of Cu. This, it is believed, leads to the stratified structure shown in Figure 23.

The common oxides of Cu have a conductivity at least six orders of magnitude lower than the base metal,[100,101,104,109,110] and so surface oxidation of very thin metal films can dramatically reduce the conductance. Indeed the loss of conductance over time can be used as a sensitive measure of the extent of oxidation of thin Cu films, together with the transmission spectra.[74,102] However, the presence of a thin CuO and Cu_2O overlayer (0 – 10 nm) at the Cu surface may not be detrimental to the ability to extract

charge carriers in an OPV because both CuO and Cu_2O are p-type semiconductors with accessible valence band edges for hole transport. Indeed, Zuo *et al.* have shown exceptional performance from an OPV device with a solution processed $CuO/Cu_2O < 10$ nm HTL.[111] Photovoltaics based on a light harvesting Cu_2O/ZnO junction have also attracted sporadic interest since 1970 and achieved $> 6\%$ efficiency.[112,113]

A second possibility arises from the dissociation of O_2 and H_2O and nucleation of oxide growth by defects or grain boundaries in the polycrystalline Cu.[108,114] Initial oxide formation is centred at these nucleation points, which results in island growth. After coalescing into a defined oxide layer, it is postulated that local thinning between crystallites may enable tunnelling across the oxide: It is established for ultra-thin insulating layers below 5 nm, that (inelastic) direct tunnelling through the insulating layer becomes significant.[115,116]

The measurement of Cu film oxidation in ambient air is almost certainly greatly accelerated as compared to *in-situ* oxidation within OPVs, since the sensitivity of the polymeric absorber layers to O_2 and H_2O necessitates encapsulation with a barrier layer.[117] Copper metal nanowires have been shown to effectively passivated by ZnO overlayers in the literature,[48,118] and indeed the sheet resistance of Cu | ZnO films fall over time by doping of the ZnO by Cu.[119] As such the specific rate of oxidation can only be found by experiment *in-situ* and may vary significantly with environmental and structural factors. The oxidation of Cu in air is used throughout this project to compare approaches to improve the stability of the Cu electrode and translated to devices. This approach is taken as the stability of the sensitive organic layers and interfaces to oxidation in OPVs is low compared to Cu metal and as such device studies in air reflect only degradation of the heterojunction.

1.6   Microcontact Printing

Conventionally metal films are patterned using photolithography which is a method for reliably patterning films with features of dimensions > 50 nm in size. It is however complex, low-throughput, costly and poorly compatible with flexible substrates making it poorly matched for OPV fabrication outside of the laboratory.

Microcontact printing (μ-CP) is a soft-lithographic technique with sub-micron resolution, compatible with rapid roll-to-roll printing.[120–123] In μ-CP soft polymeric

replicas are made of a patterned, hard master and inked with a dilute solution of the molecules to be printed (Figure 24, Steps 1-4). Intimate contact between the substrate and stamp leaves a layer of the ink molecule chemically bound to the surface. μ-CP, which was originally developed by Whitesides and coworkers was intended as a direct replacement for replicating features produced by photolithography on a commercial scale. They demonstrated that polydimethylsiloxane (PDMS) stamps inked with a dilute (0.1 - 1 mM) solution of hexadecanethiol (HDT) can be used to print a patterned self-assembled monolayer (SAM) of HDT bound to the surface of a gold film (Figure 24, Steps 5-7). This single molecule thick mask can then be used as a mask for a wet etchant (l M KOH, 0.1 M KCN) to produce features as small as 200 µm: Figure 24, Step 8. In this work, 1-10 cm^2 stamps approximately 1 cm thick were formed, inked and brought into contact by hand as outlined by D. Qin *et al.*[123]
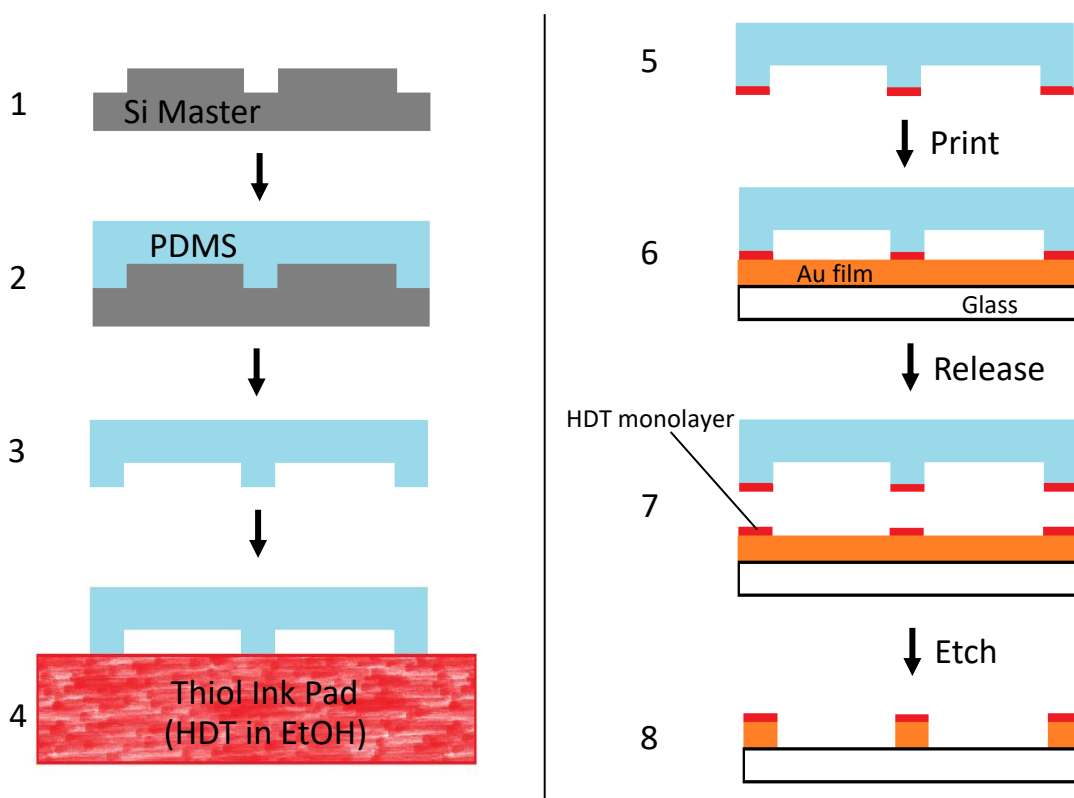
Figure 24: Schematic of the μ-CP/wet-etch system.[124] Steps 1 - 4 describe the forming of a polymeric PDMS stamp from the silicon master, and subsequent inking. Steps 5-8 describe the production of a patterned Au film from the PDMS stamp infused with HDT.

Further work by the Whitesides group, and wider community, has extended the application of μ-CP to patterning metal films of Cu, Ag, and Pd as well as to cell biology. [123,125–130] The reliable minimum feature size has been reduced from 200 μm to 50 nm by using composite polymeric stamps,[131] while additives and specialist resists have are being reported to improve pattern quality and the edge profile of metal features.[132,133] Conceivably, this enables line widths ~ 500× narrower than is possible with conventional printing techniques such as inkjet printing.[134] Until this point it was widely believed that contact times of 1 – 10 s were necessary to produce highly ordered low-defect SAMs, however Helmuth *et al.* demonstrated an optimal contact time (stamp-film) between 1 and 10 ms by increasing the ink concentration.[135] The tolerance of μ-CP to a wide range of contact times, pressure and ink concentation is a result of the high diffusivity of alkanethiols in PDMS. The applicability of the technique to large-scale manufacturing has been enabled by this understanding, with continuous roll-to-roll and automated printing now demonstrated.[120,121]

The initial intended application for micro-contact printing was in microelectronics, for the miniaturisation of electronic devices. Whilst, for the reasons discussed below, the fabrication of such devices is still almost always done using variants of photolithography,[120,136] interest remains for the application of μ-CP in flexible electronics for its high throuput and since photolithography is limited to hard substrates.[137]

In this authors opinion this can be attributed to the weaknesses of the μ-CP technique: The rapid processing can impact pattern quality with deformation of the stamps, contamination of the SAM by uncured PDMS molecules, swelling of the stamps in solvent, lateral spreading of the SAM, and limited edge resolution have all been reported. Distortions or the adverse impact of dust is more common as compared to photolithography,[120,123,132] although this can be minimised through process optimisation (e.g. processing in a clean room, or the use of additives). Microelectronic circuits are however extremely sensitive to as much as a single defect and so μ-CP has not yet proved suitable for the fabrication of electronic circuits. Additionally, photolithography patterning is largely independent of the material to be patterned and so the substrate/film can be coated with primer to improve the wetting and quality of the mask. Conversely in μ-CP the choice of material, ink, stamp construction and processing conditions all affect the quality of the subsequent pattern achieved and need to be optimised for each application.

Defects

The two main factors leading to the imperfect replication of features using μ-CP such as in Figure 9 are the deformation of the polymeric stamps and dust collected during stamping or storage of the stamps. The deformation of the stamps can largely be eliminated through the design of the master, by following the aspect ratio guidelines in Figure 25: If features are separated by too great of a distance and the height of these features on the stamp is too low, as in Figure 25 (c), the stamp can sag and touch the substrate ($H/D < 0.05$). If features on the stamp are too tall and thin as in Figure 25 (b) these can flex.

(Optimal aspect ratio: $0.5 < H/L < 5$, $H/D > 0.05$)
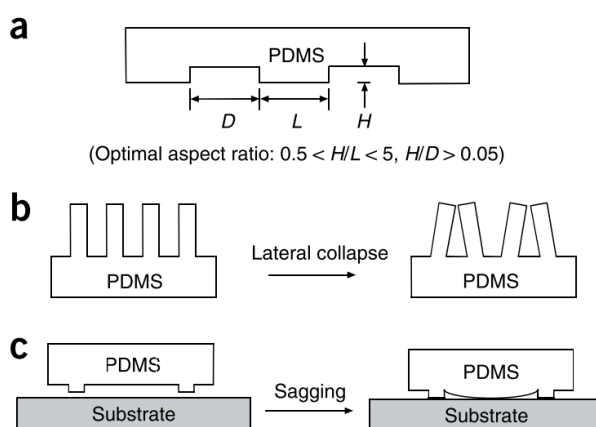
Figure 25: Reproduced from D. Qin *et al.*[123] Schematic depiction of two routes leading to defective μ-CP replication using PDMS stamps, (b) and (c), and guidelines for the master design, (a).

Ink choice

A variety of inks have been used in the literature for the formation SAM masks, including hexadecanethiol (HDT), mercaptoundecanoic acid and octadecylphosphonic acid. These can be broken down into head group, chain length and end group (Figure 26).
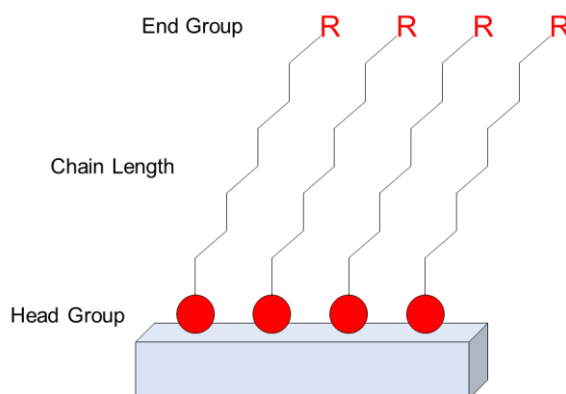
Figure 26: Schematic showing the terms by which the SAM molecule can be defined.

The head group must be matched to the metal in order to bind the monolayer to the metal surface forming a compact monolayer (SAM): For example thiol head groups are the typical choice for the coinage metals Cu, Ag and Au (binding energy 274.5 kJ mol^{-1}).[123,138] Al however presents a native Al_2O_3 surface layer onto which SAMs with a phosphonic acid head group can be formed by μ-CP.[121] Chain lengths are typically > 10 carbons as this ensures the formation of a compact SAM through van-der-waals interactions.[128,139] The end group can be CH_3 as with HDT, or more reactive moieties like carboxylic acids can be used to improve the wetting characteristics of subsequent solution processed layers.[140] Polar or bulky end groups can however affect the packing density of the monolayer. The ink molecule should be dissolved in a volatile and low-residue solvent, such as ethanol, at concentrations 1 – 10 mM for laboratory work or 10 – 50 mM for industrial processing.[120]

Contact dynamics

The reasoning behind this range of concentrations is to control the optimal contact time between inked-stamp and substrate/film. Higher concentrations (10 – 50 mM) reduce the required contact time to ~1 – 10 ms, useful for industrial processing such as compatibility with high speed roll-to-roll processing (Figure 27). At the research scale, since this is hard to control, lower concentrations e.g. 2 mM HDT in ethanol in this work increase the optimal contact time to 1 – 5 s.[120]
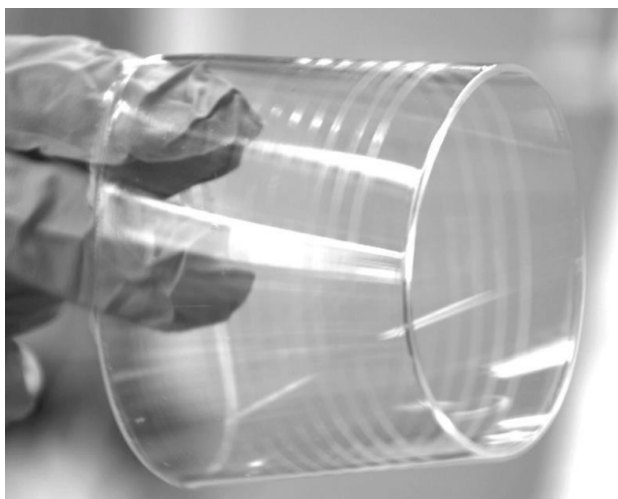
Figure 27: Reproduced from Merian *et al.* showing a cylindrical stamp for roll-to-roll μ-CP.[121]

The optimal contact time is the minimum contact time required to form a complete SAM with a low density of defects. Below this time the SAM will contain pinholes or bare regions which allow the wet etchant to penetrate the mask and undermine the metal film. Above this time molecules can diffuse in the vapour phase or across the surface causing widening of the intended features. The optimal time is unique to each ink, and the following considerations need to be borne in mind:

I.   Experientially, with 2 mM HDT in ethanol as the ink, the widening is small on the scale of the features here (1 – 2 µm).

II. The formation of the SAM is through diffusion of the ink molecule from the bulk PDMS, and as such increasing pressure does not improve the quality of films but spreads the features and can cause damage to the stamp.

III. On the laboratory scale, where flat stamps are used rather than a cylindrical stamp (Figure 27), one common pitfall is trapping air between the stamp and substrate which is evident as 1 – 10 mm diameter regions where all metal is removed after etching. To avoid this, contact should be made from the corner of the stamp as described by Qin *et al.*[123]

Etching

In principle all chemical etchants are compatible with microcontact printing as an ideal SAM will sterically hinder the approach of etchant molecules to the surface of the metal. In addition, the end group can be selected to improve selectivity: For example, the

hydrophobic alkyl chain of HDT for example can reject etchants in aqueous media. In practice although all etchants are slowed by the SAM, the selectivity of the monolayer to etchants and tolerance to defects in the SAM can be improved by using bulky etchants, such as branched polyethylenimine/nitrobenzenesulfonic acid, which are too large to penetrate individual defects in the monolayer. This will increase the contrast between regions of the replica and widen the process window for etching the film.[132]

1.7 References

[1]   United Nations, *World Population Prospects 2019 Data Booklet*; 2019.

[2]   J. Hansen, M. Sato, *Environ. Res. Lett.* **2016**, *11*.

[3]   A. Haines, K. Ebi, *N. Engl. J. Med.* **2019**, *380*, 263.

[4]   Ofgem, Electricity generation mix by quarter and fuel source (GB).

[5]   Lazard.com | Levelized Cost of Energy and Levelized Cost of Storage 2018 **2018**.

[6]   J. T. Kiehl, K. E. Trenberth, *Bull. Am. Meteorol. Soc.* **1997**, *78*, 197.

[7]   A. Jäger-Waldau, *European Commission PV Status Report 2017*; 2017.

[8]   ISE, *Photovoltaics Report*; 2012.

[9]   National Renewable Energy Laboratory (NREL), Champion Photovoltaic Module Efficiency Chart **2019**, 1.

[10]   N. Espinosa, M. Hösel, D. Angmo, F. C. Krebs, *Energy Environ. Sci.* **2012**, *5*, 5117.

[11]   J. Gong, S. Darling, F. You, *Energy Environ. Sci.* **2015**, *8*.

[12]   D. Cahen, A. Kahn, *Adv. Mater.* **2003**, *15*, 271.

[13]   K. M. Pelzer, S. B. Darling, *Mol. Syst. Des. Eng.* **2016**, *1*, 10.

[14]   T. Linderl, T. Zechel, M. Brendel, D. Moseguí González, P. Müller-Buschbaum, J. Pflaum, W. Brütting, *Adv. Energy Mater.* **2017**, *7*, 1700237.

[15]   O. V. Mikhnenko, P. W. M. Blom, T. Q. Nguyen, *Energy Environ. Sci.* **2015**, *8*, 1867.

[16]   C. W. Tang, *Appl. Phys. Lett.* **1986**, *48*, 183.

[17]   G. Yu, J. Gao, J. C. Hummelen, F. Wudl, A. J. Heeger, *Science (80-.).* **1995**, *270*, 1789.

[18]   J. J. M. Halls, C. A. Walsh, N. C. Greenham, E. A. Marseglia, R. H. Friend, S. C. Moratti, A. B. Holmes, *Nature* **1995**, *376*, 498.

[19]   H. Li, G. Sini, J. Sit, A. J. Moulé, J.-L. Bredas, *Energy Environ. Sci.* **2020**, *13*, 601.

[20]   L. Ma, Y. Xu, Y. Zu, Q. Liao, B. Xu, C. An, S. Zhang, J. Hou, *Sci. China Chem.* **2020**, *63*, 21.

[21]   K. Wang, C. Liu, T. Meng, C. Yi, X. Gong, *Chem. Soc. Rev.* **2016**, *45*, 2937.

[22]   M. Välimäki, P. Apilo, R. Po, E. Jansson, A. Bernardi, M. Ylikunnari, M. Vilkman, G. Corso, J. Puustinen, J. Tuominen, J. Hast, *Nanoscale* **2015**, *7*, 9570.

[23]   F. C. Krebs, T. Tromholt, M. Jørgensen, *Nanoscale* **2010**, *2*, 873.

[24]   M. Hoesel, F. C. Krebs, *Large-scale Roll-to-Roll Fabrication of Organic Solar Cells for Energy Production Large-scale Roll-to-Roll Fabrication of Organic Solar Cells for Energy Production. DTU Energy Conversion*; 2013.

[25]   V. Fthenakis, *Third generation photovoltaics*; BoD–Books on Demand, 2012.

[26]   B. Fan, D. Zhang, M. Li, W. Zhong, Z. Zeng, L. Ying, F. Huang, Y. Cao, *Sci. China Chem.* **2019**, 1.

[27]   J. Yuan, Y. Zhang, L. Zhou, G. Zhang, H. L. Yip, T. K. Lau, X. Lu, C. Zhu, H. Peng, P. A. Johnson, M. Leclerc, Y. Cao, J. Ulanski, Y. Li, Y. Zou, *Joule* **2019**, *3*, 1140.

[28]   R. Søndergaard, M. Hösel, D. Angmo, T. T. Larsen-Olsen, F. C. Krebs, *Mater. Today* **2012**, *15*, 36.

[29]   M. Lokanc, R. Eggert, M. Redlinger, *The Availability of Indium: The Present, Medium Term, and Long Term*; 2015.

[30]   M. W. Rowell, M. D. McGehee, *Energy Environ. Sci.* **2011**, *4*, 131.

[31]   L. Mao, Q. Chen, Y. Li, Y. Li, J. Cai, W. Su, S. Bai, Y. Jin, C. Q. Ma, Z. Cui, L. Chen, *Nano Energy* **2014**, *10*, 259.

[32]   H. J. Pereira, R. A. Hatton, *Front. Mater.* **2019**, *6*, 228.

[33]   M. S. Tyler, I. M. Nadeem, R. A. Hatton, *Mater. Horizons* **2016**, *3*, 348.

[34]   H. M. Stec, R. A. Hatton, *ACS Appl. Mater. Interfaces* **2012**, *4*, 6013.

[35] O. S. Hutter, R. A. Hatton, *Adv. Mater.* **2015**, *27*, 326.

[36] D. Ebner, M. Bauch, T. Dimopoulos, *Opt. Express* **2017**, *25*, A240.

[37] S. Lim, D. Han, H. Kim, S. Lee, S. Yoo, *Sol. Energy Mater. Sol. Cells* **2012**, *101*, 170.

[38] D. S. Ghosh, R. Betancur, T. L. Chen, V. Pruneri, J. Martorell, *Sol. Energy Mater. Sol. Cells* **2011**, *95*, 1228.

[39] I. P. Lopéz, L. Cattin, D.-T. Nguyen, M. Morsli, J. C. Bernède, *Thin Solid Films* **2012**, *520*, 6419.

[40] S. Jeong, S. Jung, H. Kang, D. Lee, S. Choi, S. Kim, B. Park, K. Yu, J. Lee, K. Lee, *Adv. Funct. Mater.* **2017**, *27*, 1.

[41] Y. Liu, C.-F. Guo, S. Huang, T. Sun, Y. Wang, Z. Ren, *J. Materiomics* **2015**, *1*, 52.

[42] J. Yun, *Adv. Funct. Mater.* **2017**, *27*, 1606641.

[43] J. Lee, M. Walker, S. Varagnolo, S. Huband, R. A. Hatton, *ACS Appl. Energy Mater.* **2019**, *2*, 5198.

[44] H. Kang, S. Jung, S. Jeong, G. Kim, K. Lee, *Nat. Commun.* **2015**, *6*, 6503.

[45] S. Chhajed, M. F. Schubert, J. K. Kim, E. F. Schubert, *Appl. Phys. Lett.* **2008**, *93*, 251108.

[46] S. Chhajed, D. J. Poxson, X. Yan, J. Cho, E. Fred Schubert, R. E. Welser, A. K. Sood, J. K. Kim, *Appl. Phys. Express* **2011**, *4*.

[47] H. Lu, X. Ren, D. Ouyang, W. C. H. Choy, *Small* **2018**, *14*, 1703140.

[48] Z. Chen, S. Ye, I. E. Stewart, B. J. Wiley, *ACS Nano* **2014**, *8*, 9673.

[49] M. G. Kang, H. Joon Park, S. Hyun Ahn, L. Jay Guo, *Sol. Energy Mater. Sol. Cells* **2010**, *94*, 1179.

[50] T. Sannicolo, M. Lagrange, A. Cabos, C. Celle, J. P. Simonato, D. Bellet, *Small* **2016**, *12*, 6052.

[51] S. Chen, L. Song, Z. Tao, X. Shao, Y. Huang, Q. Cui, X. Guo, *Org. Electron. physics, Mater. Appl.* **2014**, *15*, 3654.

[52] H. Lu, J. Lin, N. Wu, S. Nie, Q. Luo, C. Q. Ma, Z. Cui, *Appl. Phys. Lett.* **2015**, *106*, 093302.

[53] S.-B. Kang, Y.-J. Noh, S.-I. Na, *Sol. Energy Mater. Sol. Cells* **2014**, *122*, 152.

[54] J. Krantz, T. Stubhan, M. Richter, S. Spallek, I. Litzov, G. J. Matt, E. Spiecker, C. J. Brabec, *Adv. Funct. Mater.* **2013**, *23*, 1711.

[55] T. Tokuno, M. Nogi, M. Karakawa, J. Jiu, T. T. Nge, Y. Aso, K. Suganuma, *Nano Res.* **2011**, *4*, 1215.

[56] E. Lee, J. Ahn, H. C. Kwon, S. Ma, K. Kim, S. Yun, J. Moon, *Adv. Energy Mater.* **2018**, *8*, 1702182.

[57] H. G. Im, S. H. Jung, J. Jin, D. Lee, J. Lee, D. Lee, J. Y. Lee, I. D. Kim, B. S. Bae, *ACS Nano* **2014**, *8*, 10973.

[58] C. Mayousse, C. Celle, A. Fraczkiewicz, J.-P. Simonato, *Nanoscale* **2015**, *7*, 2107.

[59] F. Basarir, F. S. Irani, A. Kosemen, B. T. Camic, F. Oytun, B. Tunaboylu, H. J. Shin, K. Y. Nam, H. Choi, *Mater. Today Chem.* **2017**, *3*, 60.

[60] H. B. Lee, W. Y. Jin, M. M. Ovhal, N. Kumar, J. W. Kang, *J. Mater. Chem. C* **2019**, *7*, 1087.

[61] Y.-G. Bi, J. Feng, J.-H. Ji, Y. Chen, Y.-S. Liu, Y.-F. Li, Y.-F. Liu, X.-L. Zhang, H.-B. Sun, *Nanoscale* **2016**, *8*, 10010.

[62] D. Zhao, C. Zhang, H. Kim, L. J. Guo, *Adv. Energy Mater.* **2015**, *5*, 1500768.

[63] W. Zhou, J. Chen, Y. Li, D. Wang, J. Chen, X. Feng, Z. Huang, R. Liu, X. Lin, H. Zhang, B. Mi, Y. Ma, *ACS Appl. Mater. Interfaces* **2016**, *8*, 11122.

[64] C. P. Muzzillo, *Sol. Energy Mater. Sol. Cells* **2017**, *169*, 68.

[65] A. Wadsworth, M. Moser, A. Marks, M. S. Little, N. Gasparini, C. J. Brabec, D. Baran, I. McCulloch, Critical review of the molecular design progress in non-fullerene electron acceptors towards commercially viable organic solar cells.

Chem. Soc. Rev. **2019**, *48*, 1596–1625.

[66]   J. Zhang, Y. Li, J. Huang, H. Hu, G. Zhang, T. Ma, P. C. Y. Chow, H. Ade, D. Pan, H. Yan, *J. Am. Chem. Soc.* **2017**, *139*, 16092.

[67]   T. Jia, J. Zhang, W. Zhong, Y. Liang, K. Zhang, S. Dong, L. Ying, F. Liu, X. Wang, F. Huang, Y. Cao, *Nano Energy* **2020**, *72*, 104718.

[68]   W. Zhao, D. Qian, S. Zhang, S. Li, O. Inganäs, F. Gao, J. Hou, *Adv. Mater.* **2016**, *28*, 4734.

[69]   N. Li, C. J. Brabec, *Energy Environ. Sci.* **2015**, *8*, 2902.

[70]   H. J. Pereira, R. A. Hatton, *ACS Appl. Mater. Interfaces* **2019**, *11*, 43.

[71]   B. J. Tremolet de Villers, K. A. O'Hara, D. P. Ostrowski, P. H. Biddle, S. E. Shaheen, M. L. Chabinyc, D. C. Olson, N. Kopidakis, *Chem. Mater.* **2016**, *28*, 876.

[72]   Y. Zhang, A. J. Parnell, F. Pontecchiani, J. F. K. Cooper, R. L. Thompson, R. A. L. Jones, S. M. King, D. G. Lidzey, G. Bernardo, *Sci. Rep.* **2017**, *7*.

[73]   D. Yang, F. C. Löhrer, V. Körstgens, A. Schreiber, S. Bernstorff, J. M. Buriak, P. Müller-Buschbaum, *ACS Energy Lett.* **2019**, *4*, 464.

[74]   O. S. Hutter, H. M. Stec, R. A. Hatton, *Adv. Mater.* **2013**, *25*, 284.

[75]   J. C. Wang, W. T. Weng, M. Y. Tsai, M. K. Lee, S. F. Horng, T. P. Perng, C. C. Kei, C. C. Yu, H. F. Meng, *J. Mater. Chem.* **2010**, *20*, 862.

[76]   H. Bin, Z.-G. Zhang, L. Gao, S. Chen, L. Zhong, L. Xue, C. Yang, Y. Li, *J. Am. Chem. Soc.* **2016**, *138*, 4657.

[77]   Y. Gong, Y. Dong, B. Zhao, R. Yu, S. Hu, Z. Tan, *J. Mater. Chem. A* **2020**, *8*, 978.

[78]   B. R. Lee, G. E. Park, Y. W. Kim, D. H. Choi, T. G. Kim, *Appl. Energy* **2019**, *235*, 1505.

[79]   J. H. Lee, B. O. Park, *Mater. Sci. Eng. B Solid-State Mater. Adv. Technol.* **2004**, *106*, 242.

[80]   V. Anand, S. Sood, A. Sharma, *AIP Conf. Proc.* **2010**, *1324*, 399.

[81] C.-H. Huang, H.-L. Cheng, W.-E. Chang, M.-S. Wong, *J. Electrochem. Soc.* **2011**, *158*, H510.

[82] Z. Jiang, S. Soltanian, B. Gholamkhass, A. Aljaafari, P. Servati, *RSC Adv.* **2018**, *8*, 36542.

[83] J. Choi, J. W. Jo, F. P. G. de Arquer, Y. B. Zhao, B. Sun, J. Kim, M. J. Choi, S. W. Baek, A. H. Proppe, A. Seifitokaldani, D. H. Nam, P. Li, O. Ouellette, Y. Kim, O. Voznyy, S. Hoogland, S. O. Kelley, Z. H. Lu, E. H. Sargent, *Adv. Mater.* **2018**, *30*, 1801720.

[84] A. Gambhir, P. Sandwell, J. Nelson, *Sol. Energy Mater. Sol. Cells* **2016**, *156*, 49.

[85] S. Babar, J. H. Weaver, *Appl. Opt.* **2015**, *54*, 477.

[86] X. Fan, W. Nie, H. Tsai, N. Wang, H. Huang, Y. Cheng, R. Wen, L. Ma, F. Yan, Y. Xia, *Adv. Sci.* **2019**, *6*.

[87] R. Zhang, M. Engholm, *Nanomaterials* **2018**, *8*, 1.

[88] F. Machui, M. Hösel, N. Li, G. D. Spyropoulos, T. Ameri, R. R. Søndergaard, M. Jørgensen, A. Scheel, D. Gaiser, K. Kreul, D. Lenssen, M. Legros, N. Lemaitre, M. Vilkman, M. Välimäki, S. Nordman, C. J. Brabec, F. C. Krebs, *Energy Environ. Sci.* **2014**, *7*, 2792.

[89] B. Azzopardi, C. J. M. Emmott, A. Urbina, F. C. Krebs, J. Mutale, J. Nelson, *Energy Environ. Sci.* **2011**, *4*, 3741.

[90] R. A. Matula, *J. Phys. Chem.* **1979**, *8*, 1147.

[91] J. Zou, C. Z. Li, C. Y. Chang, H. L. Yip, A. K. Y. Jen, *Adv. Mater.* **2014**, *26*, 3618.

[92] N. Formica, D. S. Ghosh, A. Carrilero, T. L. Chen, R. E. Simpson, V. Pruneri, *ACS Appl. Mater. Interfaces* **2013**, *5*, 3048.

[93] S. Yu, G. Santoro, Y. Yao, D. Babonneau, M. Schwartzkopf, P. Zhang, S. K. Vayalil, P. Wessels, R. Döhrmann, M. Drescher, P. Müller-Buschbaum, S. V Roth, *J. Phys. Chem. C* **2015**, *119*, 4406.

[94] L. Ke, S. C. Lai, H. Liu, C. K. N. Peh, B. Wang, J. H. Teng, *ACS Appl. Mater.*

Interfaces **2012**, *4*, 1247.

[95] K. Zilberberg, T. Riedl, *J. Mater. Chem. A* **2016**, *4*, 14481.

[96] H. M. Stec, R. J. Williams, T. S. Jones, R. A. Hatton, *Adv. Funct. Mater.* **2011**, *21*, 1709.

[97] K. C. Vrancken, K. Possemiers, P. Van Der Voort, E. F. Vansant, *Colloids Surfaces A Physicochem. Eng. Asp.* **1995**, *98*, 235.

[98] K. M. R. Kallury, P. M. Macdonald, M. Thompson, *Langmuir* **1994**, *10*, 492.

[99] H. M. Stec, Metal window electrodes for organic photovoltaics, University of Warwick, 2013.

[100] I. Platzman, R. Brener, H. Haick, R. Tannenbaum, *J. Phys. Chem. C* **2008**, *112*, 1101.

[101] M. O'Reilly, X. Jiang, J. T. Beechinor, S. Lynch, C. NíDheasuna, J. C. Patterson, G. M. Crean, *Appl. Surf. Sci.* **1995**, *91*, 152.

[102] C. Zhong, Y. M. Jiang, D. M. Sun, J. Gong, B. Deng, S. Cao, J. Li, *Chinese J. Phys.* **2009**, *47*, 253.

[103] M. C. Biesinger, *Surf. Interface Anal.* **2017**, *49*, 1325.

[104] J. Li, J. W. Mayer, E. G. Colgan, *J. Appl. Phys.* **1991**, *70*, 2820.

[105] A. O. Musa, T. Akomolafe, M. J. Carter, *Sol. Energy Mater. Sol. Cells* **1998**, *51*, 305.

[106] J. Y. Zheng, T. K. Van, A. U. Pawar, C. W. Kim, Y. S. Kang, *RSC Adv.* **2014**, *4*, 18616.

[107] T. L. Barr, *J. Phys. Chem.* **1978**, *82*, 1801.

[108] C. Gattinoni, A. Michaelides, *Surf. Sci. Rep.* **2015**, *70*, 424.

[109] W. Gao, H. Gong, J. He, A. Thomas, L. Chan, S. Li, *Mater. Lett.* **2001**, *51*, 78.

[110] M. C. Biesinger, L. W. M. Lau, A. R. Gerson, R. S. C. Smart, *Appl. Surf. Sci.* **2010**,

257, 887.

[111] C. Zuo, L. Ding, *Small* **2015**, *11*, 5528.

[112] B. K. Meyer, A. Polity, D. Reppin, M. Becker, P. Hering, P. J. Klar, T. Sander, C. Reindl, J. Benz, M. Eickhoff, C. Heiliger, M. Heinemann, J. Bläsing, A. Krost, S. Shokovets, C. Müller, C. Ronning, *Phys. Status Solidi Basic Res.* **2012**, *249*, 1487.

[113] T. K. S. Wong, S. Zhuk, S. Masudy-Panah, G. K. Dalapati, *Materials (Basel).* **2016**, *9*, 1.

[114] G. Zhou, L. Wang, J. C. Yang, *J. Appl. Phys.* **2005**, *97*, 063509.

[115] J. Maserjian, *J. Vac. Sci. Technol.* **1974**, *11*, 996.

[116] M. Depas, B. Vermeire, P. W. Mertens, R. L. Van Meirhaeghe, M. M. Heyns, *Solid State Electron.* **1995**, *38*, 1465.

[117] J. Ahmad, K. Bazaka, L. J. Anderson, R. D. White, M. V. Jacob, Materials and methods for encapsulation of OPV: A review. *Renew. Sustain. Energy Rev.* **2013**, *27*, 104–117.

[118] P. C. Hsu, H. Wu, T. J. Carney, M. T. McDowell, Y. Yang, E. C. Garnett, M. Li, L. Hu, Y. Cui, *ACS Nano* **2012**, *6*, 5150.

[119] H. J. Pereira, J. Reed, J. Lee, S. Varagnolo, G. D. M. R. Dabera, R. A. Hatton, *Adv. Funct. Mater.* **2018**, *28*, 1802893.

[120] A. Perl, D. N. Reinhoudt, J. Huskens, *Adv. Mater.* **2009**, *21*, 2257.

[121] C. Merian, X. Du, D. Hardt, H. AlQahtani, In *ASME International Mechanical Engineering Congress and Exposition, Proceedings (IMECE)*; American Society of Mechanical Engineers, 2015; Vol. 14–2015.

[122] H. A. Biebuyck, N. B. Larsen, E. Delamarche, B. Michel, *IBM J. Res. Dev.* **1997**, *41*, 159.

[123] D. Qin, Y. Xia, G. M. Whitesides, *Nat. Protoc.* **2010**, *5*, 491.

[124] A. Kumar, G. M. Whitesides, *Appl. Phys. Lett.* **1993**, *63*, 2002.

[125] Y. Xia, X. M. Zhao, E. Kim, G. M. Whitesides, *Chem. Mater.* **1995**, *7*, 2332.

[126] L. B. Goetting, T. Deng, G. M. Whitesides, *Langmuir* **1999**, *15*, 1182.

[127] J. C. Love, L. A. Estroff, J. K. Kriebel, R. G. Nuzzo, G. M. Whitesides, *Chem. Rev.* **2005**, *105*, 1103.

[128] Y. Xia, G. M. Whitesides, *Annu. Rev. Mater. Sci.* **1998**, *28*, 153.

[129] Y. Xia, E. Kim, G. M. Whitesides, *J. Electrochem. Soc.* **1996**, *143*, 1070.

[130] Y. Xia, G. M. Whitesides, *Langmuir* **1997**, *13*, 2059.

[131] T. W. Odom, J. C. Love, D. B. Wolfe, K. E. Paul, G. M. Whitesides, *Langmuir* **2002**, *18*, 5314.

[132] M. Geissler, H. Schmid, A. Bietsch, B. Michel, E. Delamarche, *Langmuir* **2002**, *18*, 2374.

[133] M. Geissler, H. Schmid, B. Michel, E. Delamarche, *Microelectron. Eng.* **2003**, *67–68*, 326.

[134] D. A. Jacobs, K. R. Catchpole, F. J. Beck, T. P. White, *J. Mater. Chem. A* **2016**, *4*, 4490.

[135] J. A. Helmuth, H. Schmid, R. Stutz, A. Stemmer, H. Wolf, *J. Am. Chem. Soc.* **2006**, *128*, 9296.

[136] A. U. Haq, D. Djurdjanovic, *IEEE Trans. Semicond. Manuf.* **2019**, *32*, 320.

[137] E. P. Yalcintas, K. B. Ozutemiz, T. Cetinkaya, L. Dalloro, C. Majidi, O. B. Ozdoganlar, *Adv. Funct. Mater.* **2019**, *29*, 1906551.

[138] Y.-R. Luo, *Comprehensive Handbook of Chemical Bond Energies*; CRC Press: Boca Raton, FL, 2007.

[139] C. Nogues, P. Lang, *Langmuir* **2007**, *23*, 8385.

[140] J. Zou, H. L. Yip, S. K. Hau, A. K. Y. K.-Y. Jen, *Appl. Phys. Lett.* **2010**, *96*, 203301.

2   Experimental methods and equipment maintenance

This chapter details the experimental setup within the laboratory and techniques used to complete the experiments in this thesis.

2.1   Substrate preparation

2.1.1   Cleaning

Airborne dust particles typically range from $1 - 100\,\mu m$ in diameter,[1] or $10 - 1000$ times the typical thickness of the BHJ heterojunction layer in an OPV device. Chapter 1, Figure 8 shows the correlation of OPV performance with R_{shunt}, a measure of alternative pathways through the semiconducting layers where photocurrent can travel against the intended flow across the junction. Dust particles nearly always results in a complete 'short' where current bypasses the junction entirely during IV testing and the solar cell behaves as a resistor. It is therefore essential to work cleanly, efficiently (by minimising time between steps) and to thoroughly clean the substrates prior to film deposition. The cleaning process used can be broken down to the following steps:

1. Ultra-sonication in distilled H_2O and surfactant.
2. Rinsing and further ultra-sonication in distilled H_2O to remove the surfactant.
    I.   If specific 'residue-free' surfactants, such as the Hellmanex III (Hellma GmbH) used here, are not used extra care and boiling water should be used to remove the surfactant.
3. Rinsing and ultra-sonication in acetone.
    I.   This splits opinion in the community as acetone is an exceedingly dirty solvent which can leave a residue.
    II. Experientially I have found this step to give significant improvements in film properties on some substrates.
4. Rinsing and ultra-sonication in isopropyl alcohol (IPA)
    I.   This is a low residue solvent used to prepare samples for deposition.
5. UV/O_3 cleaning, 15 minutes.

UV/O₃ cleaner

The UV/O$_3$ cleaner holds samples in close proximity to a mercury lamp which emits strongly at 185 and 254 nm converting the O$_2$ in the air to ozone (O$_3$). The UV light and O$_3$ break down adsorbed organic contaminants and increase the density of reactive oxygen containing moieties at the surface which can react with airborne water to form surface bound hydroxyl groups on glass. The plastic substrates PET and PEN are partially oxidized/damaged and the reactive O$_3$ similarly results in the formation of surface hydroxyl groups. The static water contact angle is reduced from $> 70°$ to $< 25°$ due to the formation of polar oxygen containing groups.[2]

2.1.2 MPTMS:APTMS deposition

As described and used extensively throughout this thesis a solventless approach to producing a ~ 1 nm thick mixed monolayers (MM) of APTMS:MPTMS at a ratio of 3.4 ± 0.1 : 1 was used. The resultant monolayer presents amine and thiol groups that bind incoming noble metal atoms to the surface.[3] For the solventless approach substrates are held at < 50 mbar for 4 hours (in a desiccator) in close proximity to an open vial with 4 drops each MPTMS and APTMS. APTMS is best kept at $< 5°C$ to slow the polymerisation (evident as an excessive crust around the bottle top) and MPTMS in the glovebox and drops taken out in a sealed vial. Bottles should be dated.

2.2 Spin coating as a model

In spin coating (Figure 1) a small amount of solution is pipetted onto the centre of a substrate, either while the substrate is spinning (spin coating) or when it is stationary and then spun (spin casting).

Figure 1: The Laurell WS-650S06NPP/Lite spin coater used in this work to deposit thin films from solution.

The substrate is rotated at 1000 – 6000 rpm which exerts a centrifugal force on the liquid spreading it outwards, with excess running off the edges. The solvent partially evaporates and leaves a wet film of thickness typically 1 – 20 µm which then dries with continued spinning, leaving a solid film of controllable thickness in the range 5 nm to several microns depending on the solution viscosity and spin speed. The uniformity of film thickness is typically ± 5%,[4] and thickness is controlled through the rotational speed according to Equation 3:

Equation 3.

$$t \propto \frac{1}{\sqrt{w}}$$

where t is film thickness and w the angular velocity. The constant of proportionality is specific to each material, so a calibration curve must be produced.

The biggest drawbacks of spin coating are the extremely low throughput (1 sample at a time, max diameter ~15 cm) and material wastage (typically > 90%). Spin coated films can also suffer from the 'comet' effect where small particulate debris, e.g. dust, causes outward facing streaks where material is not deposited. There is a greater tolerance to dust when films are spin cast (drop then spin) than spin coated (spin then drop).

The spin coating of organic semiconductors is commonplace in OPV research, but universally acknowledged to be used only as a model for other coating/printing

techniques such as blade coating, dip coating or inkjet printing. Spin coating is a simple research model for these techniques as all rely on coating the substrate with a thin, wet, film which is then dried to leave a solid layer. As this thesis focuses on electrode design, spin coating was used.

2.2.1 'Annealing'

The technical definition of annealing is to 'heat (typically metal or glass) and allow it to cool slowly, in order to remove internal stresses and toughen it'. In OPV research, annealing is typically done for one of two reasons:

1. Thin metal film electrodes (5 - 500 nm thick) can be annealed at 120 - 300°C to reduce their sheet resistance. In the literature this is attributed to improved crystallinity by surface melting of the crystallites improving contact resistance,[2] and in this work evidence is seen for the reduction of crystalline stresses which are anticipated to scatter the electron flow.
2. BHJ films and ZnO films immediately after spin coating are annealed to drive off residual solvent and moisture.

In this work, all annealing was done by placing samples on a calibrated hotplate in the glovebox or fume hood.

2.3   The glovebox

Thermal evaporation, spin-coating of organic semiconductors and the fabrication of OPV devices were all performed inside a N_2 filled glovebox (Figure 2). O_2 and H_2O levels were kept at < 2 ppm as gas is circulated within the glovebox through a loop containing both a charcoal filter (to absorb solvent vapours to a capacity of ~ 500 mL) and copper catalyst to actively remove O_2 and H_2O. Devices were transferred in a sealed N_2 filled vessel to a second glovebox with integrated solar cell IV test system.

Figure 2: (Left) and (Right) the two N_2 atmosphere gloveboxes uses in this work for the thermal evaporation of films, spin coating and processing of OPV devices.

2.4   Thermal Evaporation

The principles of thermal evaporation are simple: Under vacuum pressures of 5×10^{-6} – 1×10^{-8} mbar the material to be deposited is heated until it evaporates, or sublimes, and the vapour condenses onto the substrates which are in the line-of-sight. A base pressure range of 5×10^{-6} – 1×10^{-8} mbar is needed to minimize the incorporation of contaminant gases into the deposited film and to achieve the required mean free path length. Contaminant gases significantly degrade the quality of the resultant film: For example, water vapour pins the grain boundaries of metal films, reducing mean crystallite size, and residual O_2 reacts with metal vapour during the deposition and is incorporated into the lattice.[5] The term 'base pressure' refers to the minimum pressure of the system before the evaporation. The measured pressure during evaporation typically increases to $\sim 10^{-5}$ mbar.

During thermal evaporation atoms arriving at the substrate have kinetic energy $<<$ 1 eV and so, unlike sputter deposition, damage to the receiving substrate is minimal unless a chemical reaction occurs.[6] At atmospheric pressure, vapours such as an opened perfume bottle travel in the nm range between collisions, slowing diffusion across the room. In thermal evaporation mean path lengths are of the order of tens of metres and so most particles travel directly from the source to the substrate, evidenced by the shadowing effect of for example the substrate shutter (Figure 3).[6] To reduce variation in thickness

across the substrate area or between samples in different positions in the holder, the sample holder is rotated.

Figure 3: The evaporation chamber (Left) Upper section: substrate/mask bays, substrate shutter and QCMs. (Right) Lower section: Organic sources (central) and obscured thermal sources below.

Commonly metals are thermally evaporated from dimpled tungsten boats, or in this work from aluminium oxide crucibles mounted in a heater as shown in Figure 4, which are resistively heated to 300 - 1600°C. Thermal evaporators can also be used to deposit thin films of small-molecule organic compounds such as C_{60} and bathocuproine which typically evaporate or sublime at < 300°C under high vacuum. The SPECTROS series Kurt J. Lesker vacuum used for this work uses a proportional integral derivative (PID) controller to control the rate to within ± 2%, although this is reliant on accurate calibration. Most commonly materials are evaporated from aluminium oxide crucibles, with the notable exception of Al metal where a BN-TiB$_2$ crucible is the best choice. Al should always be evaporated from a tall crucible so that the lip protrudes from the crucible holder by several mm which prevents the spill over of molten Al, caused by the wetting characteristics.
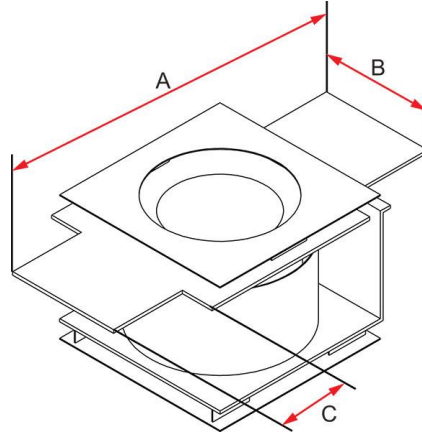
Figure 4: An example of the type of crucible heater used in this work for the thermal evaporation of metals. Reproduced from www.lesker.com.[7]

The evaporation rate is monitored using a quartz crystal microbalance (QCM) which can be sensitive to mass changes of < 1 pg cm^{-2} (~ 0.1 % of a hydrogen monolayer) and so gives the deposition rate to a precision of 0.01 Å s^{-1}.[8] Quartz is a piezoelectric material that can be made to oscillate at a well-defined frequency under applied bias. The resonant frequency of this oscillation is altered by the condensation of material onto the crystal and this can be converted to an equivalent thickness for a particular material provided the Z-ratio (material/quartz mismatch factor) and density for the material being deposited are known. This thickness must be multiplied by the tooling factor which accounts for the difference in position between the quartz crystal microbalance and the sample with respect to the source. The tooling factor is determined for each source material by depositing a nominal 100 nm and measuring the real thickness by step-edge analysis using an atomic force microscope (AFM). This is done through the following equation:

Equation 4.

$$Tooling\ (New) = Tooling\ (Initial) \times \frac{Real\ thickness\ (AFM)}{Thickness\ (QCM)}$$

The tooling factor for key materials is recalibrated periodically, as it is typical for this to drift over time due to for example the build-up of material around the apertures or changes such as new heaters. It is essential for the thermal sources to be loaded into the evaporator chamber in exactly the same position when replaced, because differences in positioning

70

and the angle of the crucible will affect the tooling factor. Experientially, this this limits the accuracy in thickness to $\pm$ 5%.

2.4.1   Adaptations for co-deposition

In 2018 we made several changes to the SPECTROS thermal evaporator to enable the evaporation of metals from two sources simultaneously (i.e., co-deposition) as used in Chapter 6. To achieve independent control an additional transformer and circuit were added along with two additional QCMs in the vacuum chamber. For controlled and independent deposition from two sources two QCMs with mutually exclusive line-of-sight to each source were installed. The first placement of these QCMs transpired to be too close to the thermal sources and experienced interference attributed to the high temperatures, and so QCMs were moved to above the 'chute' seen in Figure 3 and shown schematically in Figure 5.
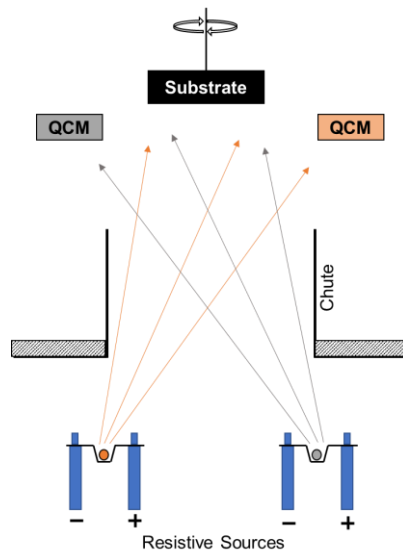
Figure 5: Schematic showing the final Kurt J. Lesker SPECTROS series evaporator chamber configuration for the co-evaporation of metals.

2.4.2   The cryopump circuit

Commonly thermal evaporators use a turbopump to maintain the vacuum in which a spinning turbine propels gas molecules from the chamber. The relatively simple

mechanical design requires relatively little maintenance. However, to reach pressures of $< 5 \times 10^{-8}$ mbar the chamber is connected to a cryopump. In a cryogenic system, like for those with turbopump, a mechanical roughing pump is first used to reduce pressure to $\sim 10^{-2}$ mbar before the vacuum chamber is opened to the cryopump. In the cryopump chamber gases are passed across a series of fins cooled to < 20 K at which temperature the gases condense and are collected. The temperature of these fins is maintained by a closed-loop helium circuit where helium is externally compressed and allowed to expand on the opposite face of the cryopump fins, cooling them.

2.4.3   *Thermal evaporation of Cu: Rules and Recipes*

Vacuum processing, including thermal evaporation, is often believed to be low-throughput and high-cost as on the laboratory scale < 10 substrates at a time are typically individually prepared and loaded to the evaporator. In the packaging industry however, roll-to-roll thermal evaporation of 10-100 nm thick Al films on flexible plastic (for example for crisp packaging) is done at speeds of up to 1000 m/min and so is very low cost; a process directly transferrable to thin Cu films for OPVs. The evaporation of metal films is a well understood metal deposition method for which where film uniformity is dictated by three main parameters: the seed or adhesion layer, the vacuum pressure, and the evaporation rate.

As compared to Au and Ag, both Cu and Al are reactive metals and so better quality films are attained at higher evaporation rates and lower vacuum pressures.[5] Residual gases, particularly H_2O, can dope the metal film causing defects or pin grain boundaries such that smaller crystallites with higher optical scattering and lower lateral conductivity are formed.[5] Thermal evaporation is typically performed in the pressure range of $5 \times 10^{-6} - 1 \times 10^{-8}$ mbar, and it follows that at the lower end of this range and at higher rates (where less time is given for the reaction with residual gases) lower roughness films are produced. Typical thermal evaporation rates are $0.1 - 10$ Å s^{-1}, although throughout this work the evaporation rate was largely fixed at 1 Å s^{-1}.

The data in Figure 6, which was collected in the initial optimisation for Chapter 6, demonstrates the complex factors that affect the stability of optically thin Cu films upon exposure to ambient laboratory air via the evolution of the sheet resistance. The base pressure during evaporation is known to affect the crystallite size of the subsequent

film,[5] and therefore the stability of the Cu film to oxidation. High vacuum pressure results in larger crystallites and therefore a lower density of grain boundaries, which are the part of the film most susceptible to oxidation. Consequently, as is evident in Figure 6 (a), the sheet resistance increases at a lower rate for Cu films deposited under higher vacuum.
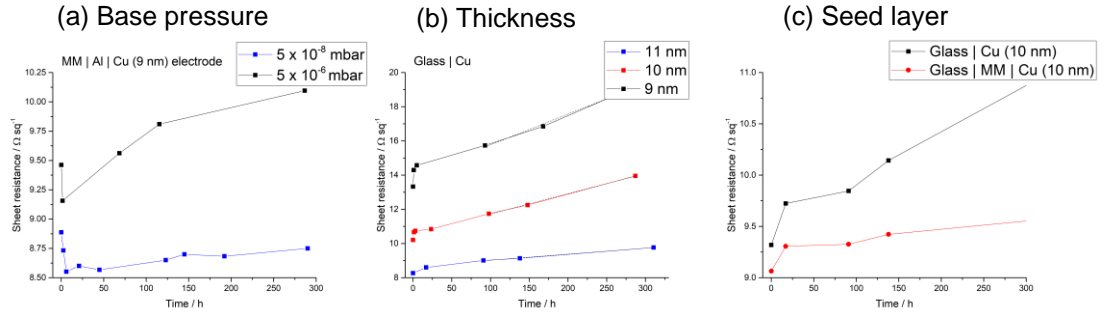
Figure 6: The evolution of sheet resistance as a function of time for optically thin films exposed to air for three different processing conditions: (a) Base pressure; 5 x 10^{-8} mbar (Blue), 5 x 10^{-6} mbar (Black). (b) Metal thickness; 11 nm (Blue), 10 nm (Red), 9 nm (Black). (c) Without seed layer (Black), APTMS/MPTMS derivatised glass (Red). The effect of thickness is summarised in Table 1.

Despite the relatively high adhesion energy of Cu on SiO_2 (glass), nearly twice that of Ag,[9] the same effect as is well known for Ag is seen when Cu films are deposited on an effective seed layer (Figure 6 (c)). The densely packed slab-like polycrystalline film resultant from the higher initial atomic-substrate interaction force during deposition exhibits lower surface roughness (1.44 ± 0.12 *vs* 1.02 ± 0.05 nm root mean square roughness) and less exposed grain boundaries (Figure 7) which is expected to dominate the rate of oxidation. Note that the minimum thickness for the onset of slab-like metal film growth (which is most desirable) can be reduced using a seed layer, known as the percolation thickness.
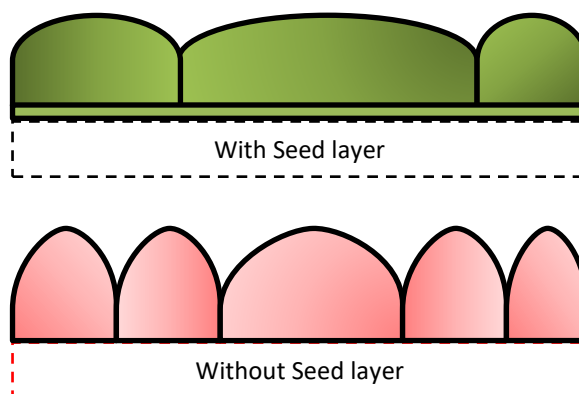
Figure 7: Descriptive diagram showing how morphology, influenced by the effectiveness of the seed layer bonding, can have a significant impact on effective metal thickness for lateral conductivity (sheet resistance).

Interestingly the thickness appears to have a disproportionate effect on the stability of the subsequent film in the 9 – 11 nm range here. It is expected that the 11 nm Cu film on glass would be more stable than 9 nm because the percentage of metal film oxidized is always larger for the thinner film, however the disproportionate difference (Table 1) reflects the subtle difference in the propensity of low-thickness Cu to form a series of 'islands' with far higher roughness than thicker films as crystallites enlarge and are pressured together to form a film.

Table 1: The representative stability (linear fit, 80-320 hours) of a glass | Cu film of varying thickness, as shown in Figure 6 (b).

Thickness (nm)	Gradient (Ω sq^{-1} h^{-1})
9	0.01792
10	0.01184
11	0.00351

2.5   Routine maintenance

The routine maintenance procedures for the glovebox, cryo-system and thermal evaporated are summarised here.

2.5.1   Glovebox

Catalyst Regeneration

The Cu-based catalyst over which the glovebox atmosphere is circulated to actively remove O_2 and H_2O has a limited capacity, after which the O_2 and H_2O levels will steadily rise. At this point the catalyst should be regenerated using a 5% mix of H_2 in N_2 which is passed across the heated catalyst to reduce the oxidized Cu catalyst back to Cu metal.

Charcoal

The 'inert' and contained environment of the glovebox is only maintained if solvent vapour is actively removed. Additionally, if this solvent vapour reaches the Cu catalyst it can permanently 'poison' the Cu metal by irreversible oxidation of the metal. Before the glovebox gas is circulated across the catalyst it is therefore filtered through a densely packed column of activated carbon. This column has a capacity ~ 500 mL and the carbon must be replaced **before** it reaches capacity to avoid damage to the catalyst: Every $1 - 2$ months depending on usage.

Catalyst replacement

The performance of the catalyst will degrade over time, although with proper maintenance the estimated lifetime is 2 - 5 years. If regeneration of the catalyst does not reduce the base O_2/H_2O levels first check for excessive leakage and then consider changing the catalyst. A simple check for excessive leakage is to raise the pressure to 10 mbar and monitor the rate of pressure decay.

Dust filters

Dust is detrimental to OPV fabrication. The manufacturer Mbraun recommend changing the dust filters, which unscrew, every year under regular use.

Rotary Vane Pumps

These require regular (specialist) oil top ups when the meter indicates, and annual exchange of the mist filters.

2.5.2 Cryopump

Regeneration

The cryopump passes gas across a series of cooled fins where the gases condense and are collected. As these build up on the cold fins, the efficiency of the system is reduced. When the base temperature of the cryopump rises above 30 K the pump should be regenerated using the pre-set recipe. The temperature of the cryopump is steadily raised by isolating the helium circuit and the waste valve opened to purge the reservoir before the pump is reset. This takes 24 hours to fully complete.

Helium absorber

The cryopump relies on the expansion of high-pressure, high-purity helium over the fins to cool them. The design of compressors means that they are prone to leaking oil into the helium circuit. To prevent this, compressors contain an 'absorber' (carbon-based filter) in the circuit to remove oil before it passes through the cooled cryopump. This must be changed every 6 months or if the cryopump can be heard to 'grind'.

2.5.3 Thermal evaporator

QCM exchange

The estimated life of each sensor can be found on the control unit under: Sigma Software → File → Sensor Readings → Life (%). For thermal sources crystals with < 30 % life should be changed or those for the organic sources < 70 %.

2.6 Patterning of metal films

2.6.1 Photolithography

Photolithography is the conventional method for the patterning of thin films or bulk wafers. In photolithography samples are coated with a primer and then a thick (1 – 10 µm) polymeric photoresist by spin coating, followed by baking. In this thesis it is used to fabricate Si masters for microcontact printing in Chapter 4 and to pattern Cu films in Chapter 5. The samples are typically processed once with a solid mask to remove the edge beads before processing as follows to produce the pattern:

1. Sample with resist layer aligned and held by vacuum contact close to the featured chromium mask.

2. Exposed to UV light
3. Developed in a proprietary developer solution.
    a. 'Positive' resists replicate the mask pattern in photoresist after developing.
    b. 'Negative' resists switch polarity.
4. Patterning of the metal film by wet or inductively coupled plasma (ICP) etching where the photoresist does not cover the sample.
5. Removal of the photoresist mask with solvents (commonly acetone).

For the patterning of deep (~ 5 µm) trenches to a Si wafer, as in Figure 8, an evaporated Al_2O_3 was required as polymeric resist layers could not withstand the ICP etch. As such, after developing the polymeric resist Al_2O_3 was uniformly evaporated before a solvent lift-off. As a side effect this reversed the polarity of the wafer produced.
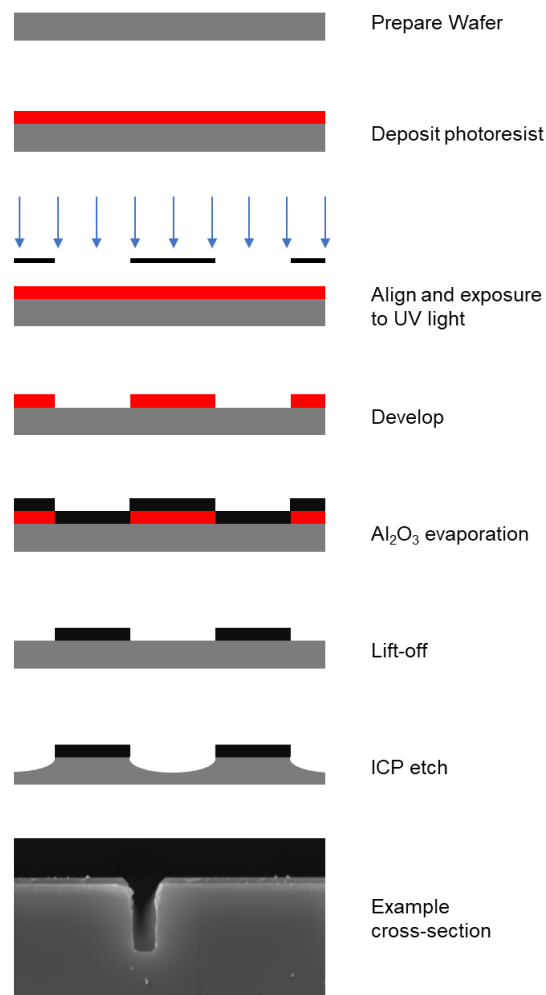
Figure 8: Example photolithographic processing of an Si wafer to produce a series of trenches ~ 5 µm deep for use as a master for microcontact printing.

2.6.2 Microcontact printing

μ-CP is a soft-lithographic technique which can be used to rapidly fabricate multiple replicas of a hard master. The process is discussed in Chapter 1. To reduce the number of defects caused by dust it is sensible to keep the stamps covered in-between uses and always face up. Avoid contact between the patterned surface of the stamp and the work surface or gloves. This is the commonest cause of line breaks, such as in Figure 9, however the low-impact of these defects did not necessitate clean-room processing in this work.

The low impact of defects in the context of transparent electrodes for OPVs, unlike microelectronic circuits in which a single line break can render a device defunct, is attributed to the grid structure which provides alternative routes for the current to take when it meets a defect. This is exaggerated by the high density of lines produced by μ-CP. Experientially, when produced in the ambient laboratory environment (i.e., not a cleanroom) such grid structures suffer in the range of 0 – 1% line breaks (Figure 9).
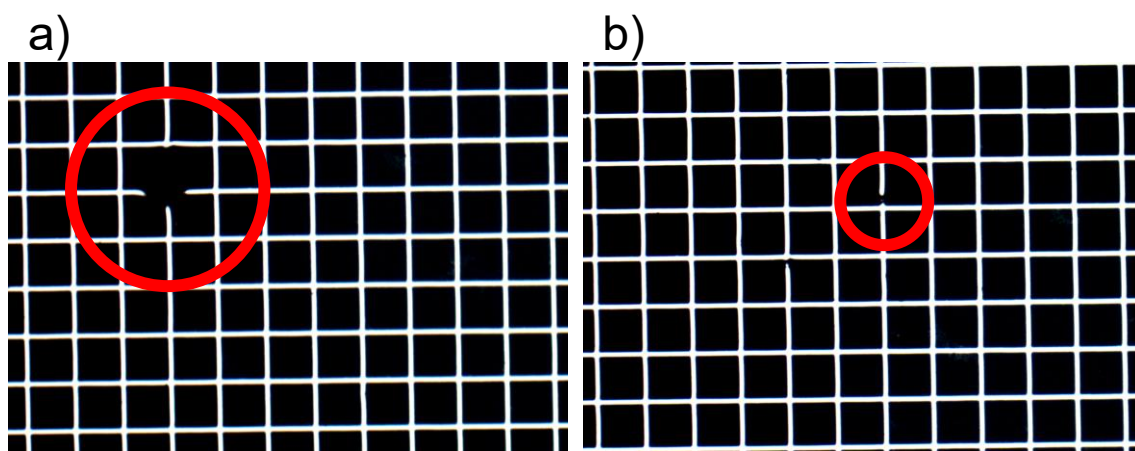
Figure 9: Optical microscope images (reflected light) of two circled defects present on a representative Cu grid produced by μ-CP.

For application as a TCE not only is high contrast between the grid lines and the intervening space needed, but the void should be clear and free of residual metal particles which can cause parasitic absorption and scatter incoming light. As metal thickness increases, requiring higher etchant concentrations or longer etch times, producing clear voids while maintaining continuous grid lines of low roughness becomes increasingly

difficult: All real-life SAMs exhibit partial disorder, which in µ-CP can allow the etchant to slowly penetrate the mask causing at first pitting of the metal surface followed by discontinuity of the lines.[10] An example of this 'process window' is given for a 500 nm thick Cu film in Figure 10, although it should be noted that the process window is far wider for more realistic metal thicknesses (< 200 nm). At t = 3:15 s, the edge resolution of the grid lines is poor, and the void is not clear of particles. t = 3:30 s shows the best compromise between grid definition and voids clear of particles. At t ≥ 4:00 s the metal lines show clear damage, followed by discontinuity.
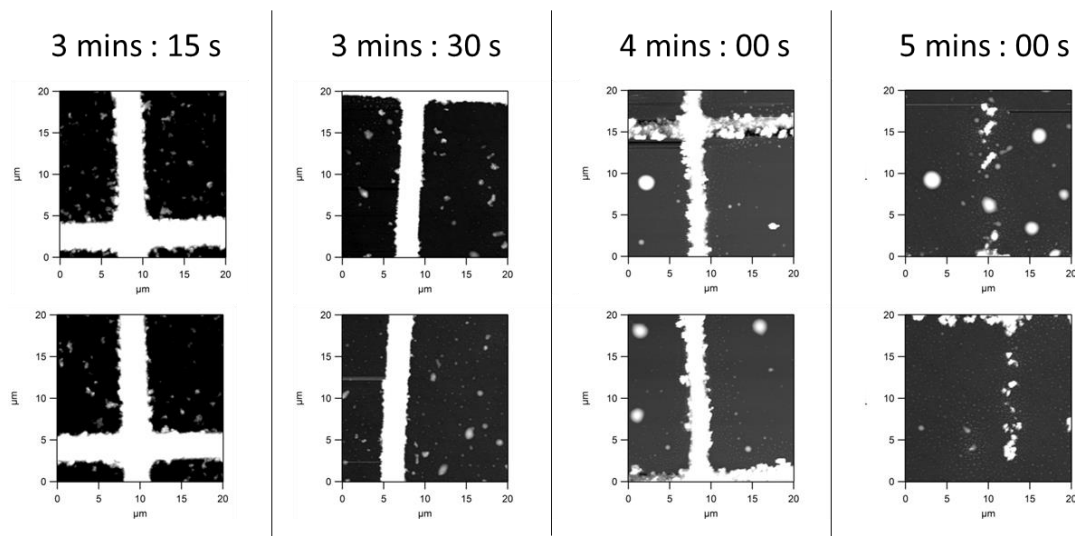
Figure 10: An example of the process window for a 500 nm Cu film with patterned HDT SAM etched in 27 mM aqueous ammonium persulfate. A thick film and weak etchant are used to exaggerate and separate the stages.

When wet etching micron-scale grid structures from planar metal films the following simple steps are useful to estimate when etching is complete:

I. With etching the film (by eye) proceeds from opaque to a semi-transparent film grey in colour, before the grey colour (caused by residual metal nanoparticles) recedes leaving a highly transparent, bright film. At this point etching is relatively complete, although typically the film is left etching for a short additional period to ensure the edge resolution of the grid lines.

II.   At the laboratory scale the ~ 50 mL of etchant does not significantly evolve over the fabrication of 10 – 20 electrodes and so timing the first electrode can inform etching of the set.

III.   After etching, when viewed at an angle under bright white light a diffraction pattern ('rainbow' effect) should be seen indicative of ordered and repeating micron-scale grid lines.

Storage and Reuse

Both the hard silicon master and the polymeric replicas can be reused many times. With proper storage and usage, one master can produce > 10,000 replicas. It was not part of this study to evaluate the limits of this.

The silicon master, in this case with an Al_2O_3 mask still in place, can be silanised by exposure to tridecafluoro-1,1,2,2-tetrahydrooctyl-1-trichlorosilane (TFOCS) vapour (30 mins, < 50 mbar).[11] The resultant highly fluorinated TFOCS monolayer on the surface reduces the adhesion between cast PDMS and the master, so PDMS stamps are easy to remove, increasing the lifetime of the master. The PDMS stamps were used in this work for up to an estimated 500 printings with no noted degradation. The number of printings per stamp is highly dependent on the ink used and care during processing/storage to avoid particulate contamination. 2 mM HDT in ethanol was extremely clean leaving no residue and so the stamp was reused. Whilst determination of the limits of μ-CP was not part of this study, electrodes were printed in sets of 3 – 8 without reinking of the stamp. This is possible because PDMS acts as a reservoir for alkane-thiols such as HDT.[12]

2.7 OPV fabrication and testing

The OPV devices in this thesis are a model to evaluate the performance of Cu-based transparent conductive electrodes in optoelectronic devices. An inverted architecture device structure was used throughout depicted in Chapter 1, Figure 11.

2.7.1 *Fabrication*

For the small-area devices, 0.06 cm^2, 6 devices were fabricated on each substrate as shown in Figure 11. For larger-area devices, 0.6 cm^2, a single device was fabricated on each substrate. The ETL, BHJ and HTL were all deposited over the entire substrate. After deposition the underlying TCE was exposed by cleaning along one edge and conductive silver paint applied to ensure an ohmic electrical connection. The connection to the top contact (Al) was made outside of the area covered by the TCE to avoid short circuiting.
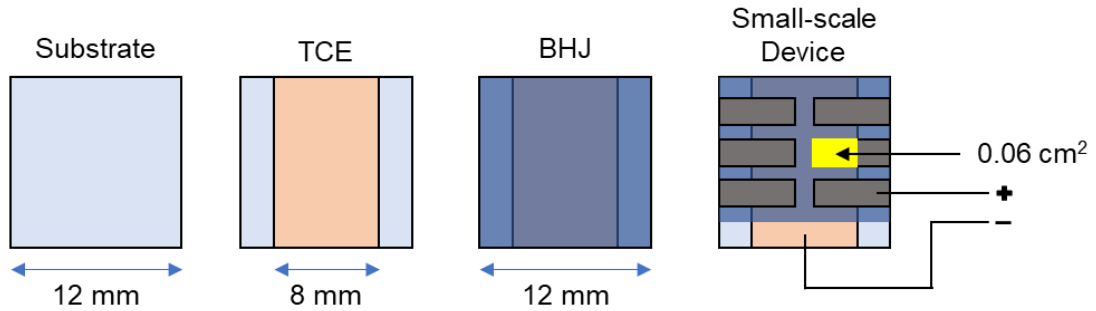
Figure 11: The width of sequentially deposited layers from left to right to form small scale devices.

Conductive PEDOT:PSS (PH1000)

This optional interlayer is included between the TCE and ETL for metal grid structures featuring apertures > 2 µm to efficiently extract electrons from the whole photoactive area. Without additional processing post-deposition, the inclusion of this interlayer even when using a planar ITO reference electrode dramatically reduces the shunt resistance, as evident in Figure 12 from the change in shape/gradient of the IV characteristics. The reduction in shunt resistance is indicative of an additional pathway along which charges can circumvent the junction and flow directly between the electrodes. To avoid the

characteristic gradient of the IV curve as in Figure 12 (Red) the edges of the substrate were cleaned using a sharp razor blade after deposition of PEDOT:PSS.
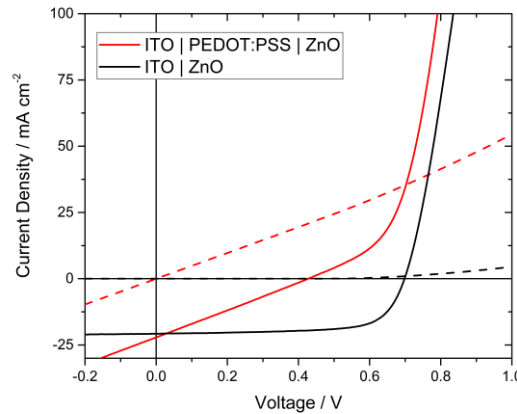
Figure 12: Inverted OPV devices on a planar ITO electrode with and without complete coverage by a conductive PEDOT:PSS interlayer.

The top contact

In the OPV device structures used the top contact was always 8 nm MoO_3 | Al. This well understood combination aligns the Fermi level of the Al electrode to the HOMO of the donor material and so maximises V_{oc}. MoO_3 was evaporated at a constant rate $0.2 – 0.3$ Å s^{-1}. $100 – 150$ nm Al was evaporated at $0.5 – 3$ Å s^{-1} in order to form a top contact with sheet resistance far greater than that of the TCE. Al deposition was started at low rate of $0.5 – 1$ Å s^{-1} for the first 10 nm to minimise damage of the underlying layers and increased after 10 nm. The mask used to produce the individual device pixels (Figure 11) was moved into place using a series of transfer arms under vacuum after deposition of the MoO_3.

2.7.2   OPV testing

Shadow mask

One effect which disproportionately affects small-area OPV performance is photocurrent generated in the BHJ outside the area covered by the top Al contact. The conductivity of the interlayers and BHJ are such that charges can be drawn from hundreds of microns

outside of the area defined by the top contact.[13] The series resistance to transporting electrons and holes from outside the area defined by the metal contact lowers the device FF and V_{oc}.[13] To avoid this effect a shadow mask is used: The device is illuminated through an aperture of precisely defined area smaller than the Al top contact area. This eliminates the generation of photocurrent from outside the intended area, although results in a decrease in V_{oc} (< 0.05 V). This voltage loss is believed to be caused by the incorporation of the surrounding non-illuminated cell area into the IV curve.

Illumination and calibration

For the quantification and comparison of OPV device performance, the simulated solar spectrum needs to closely match that of the intended application; the latitude in particular affects the spectrum since incoming solar radiation is attenuated in specific regions by the absorption of atmospheric gases. In this thesis AM 1.5G, the standard test condition for all photovoltaics (as defined by ASTM International), was used as the simulated spectrum (Figure 13) which closely matches the yearly average spectrum received at sea level in mid-latitude countries.
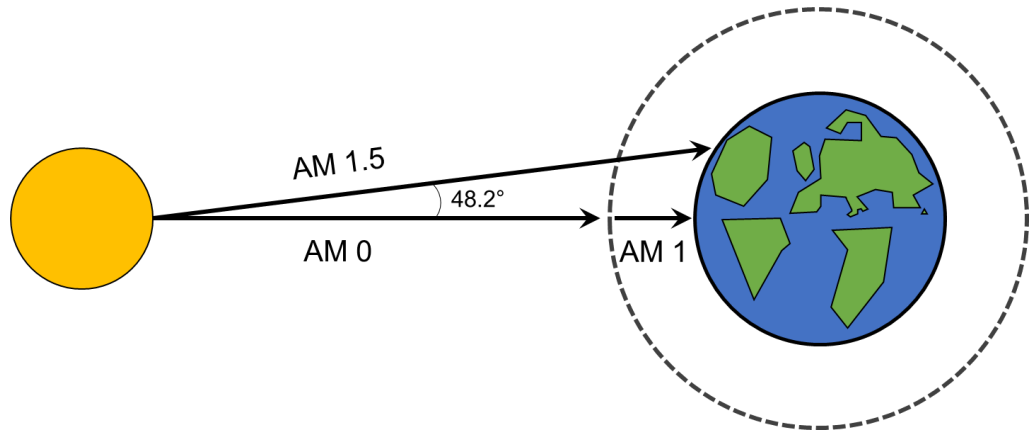
Figure 13: The AM 0, AM 1 and AM 1.5 spectra and the scenario each is used to simulate.

The intensity of the AM 1.5G spectrum is 100 mW cm^{-2} over the solar spectrum, 300 – 2500 nm. To ensure the accuracy of the lamp in the 400 – 800 nm region over which OPVs typically absorb, as opposed to the entire solar spectrum, a calibrated Si reference

cell incorporating a 'window' is utilized. This window is transparent only over the region of interest.

Since the OPV devices produced in this work were not encapsulated, they were tested in a N_2 filled glovebox unless otherwise stated (< 2 ppm O_2 and H_2O): It is universally accepted that commercial OPVs will feature an integrated barrier to O_2 and H_2O. Indeed it is in part the development of improved flexible barrier films that have driven the recent improvement in device lifetime and early commercialisation of OPVs.[14] Although solar cells typically operate at up to 70°C, the close proximity of the device to the lamp during simulated irradiation would be expected to raise the temperature above that in many real-world scenarios.[15]

2.8   Optical simulations

The transmittance of unpatterned optically thin metal films was simulated using the software Essential Macleod Version 9.7 (Thin Film Centre Inc.) assuming ideal homogeneity and uniform thickness. The optical constants, refractive indices (n) and extinction coefficients (k), are either provided in the software database or literature values were used.

2.9 References

[1]   WHO, *Hazard prevention and control in the work environment: Airborne dust*; 1999.

[2]   H. M. Stec, R. A. Hatton, *ACS Appl. Mater. Interfaces* **2012**, *4*, 6013.

[3]   H. M. Stec, Metal window electrodes for organic photovoltaics, University of Warwick, 2013.

[4]   N. Atthi, O. U. Nimittrakoolchai, W. Jeamsaksiri, S. Supothina, C. Hruanun, A. Poyai, *Songklanakarin J. Sci. Technol.* **2009**, *31*, 331.

[5]   K. M. McPeak, S. V. Jayanti, S. J. P. Kress, S. Meyer, S. Iotti, A. Rossinelli, D. J. Norris, *ACS Photonics* **2015**, *2*, 326.

[6]   H. Adachi, K. Wasa, In *Handbook of Sputter Deposition Technology*; Wasa, K.; Kanno, I.; Kotera, H. B. T.-H. of S. T. (Second E., Eds.; William Andrew Publishing: Oxford, 2012; pp. 3–39.

[7]   Kurt J. Lesker Company, Heat Shielded Crucible Heaters.

[8]   A. W. Warner, C. D. Stockbridge, *J. Appl. Phys.* **1963**, *34*, 437.

[9]   K. S. Gadre, T. L. Alford, *J. Appl. Phys.* **2003**, *93*, 919.

[10]   M. Geissler, H. Schmid, A. Bietsch, B. Michel, E. Delamarche, *Langmuir* **2002**, *18*, 2374.

[11]   D. Qin, Y. Xia, G. M. Whitesides, *Nat. Protoc.* **2010**, *5*, 491.

[12]   T. E. Balmer, H. Schmid, R. Stutz, E. Delamarche, B. Michel, N. D. Spencer, H. Wolf, *Langmuir* **2005**, *21*, 622.

[13]   A. Cravino, P. Schilinsky, C. J. Brabec, *Adv. Funct. Mater.* **2007**, *17*, 3906.

[14]   D. Yu, Y. Q. Yang, Z. Chen, Y. Tao, Y. F. Liu, *Opt. Commun.* **2016**, *362*, 43.

[15]   M. Shima, M. Isomura, K. I. Wakisaka, K. Murata, M. Tanaka, *Sol. Energy Mater. Sol. Cells* **2005**, *85*, 167.

3   Analytical Techniques

3.1   Sheet Resistance Measurements

3.1.1   *Mechanics*

Throughout this work the van der Paaw method was used to measure sheet resistance (R_{sh}) of metal and semiconductor films of thickness 3 – 500 nm. A Keithley 2400 source meter was used to apply a 5 mV potential difference between two contacts whilst measuring the current from opposite contacts (Figure 1).
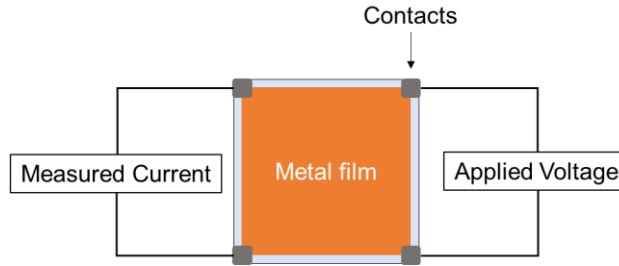
Figure 1: Schematic depicting the experimental setup for the sheet resistance of a metal film by the van der Paaw method.

The van der Paaw method can be used to calculate the R_{sh} using the equation:

Equation 5.

$$e^{\frac{-\pi R_{vertical}}{R_{sh}}} + e^{\frac{-\pi R_{horizontal}}{R_{sh}}} = 1$$

where $R_{vertical}$ and $R_{horizontal}$ are the measured resistances across a film (Figure 1) at right angles to each other. When $R_{vertical} = R_{horizontal}$, as is the case for a square film of uniform thickness and composition, Equation 5 can be simplified as follows to Equation 6:

$$e^{\frac{-\pi R}{R_{sh}}} + e^{\frac{-\pi R}{R_{sh}}} = 1$$

$$R_{sh} = \frac{\pi R}{\ln 2}$$

Equation 6.

$$R_{sh} = \frac{\pi}{\ln 2}\left(\frac{V}{I}\right)$$

where V is the applied voltage (5 mV) and I the induced current (mA) averaged across both directions of measurement. Ohmic contacts are made using silver contact paint (RS PRO Silver Conductive Paint Paint) to ensure negligible contact resistance and reliable measurement. Measurements in this work were made across a minimum of 3 samples.

3.1.2   Outputs and Applications

R_{sh}, in Ω sq^{-1}, is independent of area provided the sample is square and as such is useful to standardise reporting the resistance of thin film electrodes. The resistivity of bulk materials is independent of dimension. This is not the case however for metal films with a thickness $\leq$ the mean free path of electrons in the bulk material ($\leq$ 50 nm) because of the high dependence on the degree of scattering from the top and bottom surfaces of the film when film thickness is reduced below the mean free path. The sheet resistance of thin films also reflects crystallite size, fine morphology (roughness) and the degree of surface oxidation.[1] Indeed, for 5 – 15 nm thick slab-like films, the evolution of the sheet resistance over time provides a sensitive probe of the growth of an oxide surface layer upon exposure to air, since the conductivity of metal oxides are typically orders of magnitude lower than the base metal.[2] The evolution of the sheet resistance in a N_2 atmosphere can also provide information about changing morphology or crystallinity, at ambient temperature.[3]

3.1.3   Limitations

The van der Paaw equation (Equation 5) assumes uniform thickness, homogeneity and isotropic behaviour of the sample. Evaporated metal and organic semiconductor films typically are of low variance in conductance across the area. The van der Paaw equation is however less accurate for spin coated films (e.g. PEDOT:PSS) because this deposition method often leaves an edge bead (border region of increased thickness). The painted silver contacts provide low contact areas (more than an order of magnitude smaller than

sample area) and prevent mechanical damage to the film by the probes. The contacts formed using silver paint are unstable with heating $> 180°C$ and so for heating above this temperature evaporated silver contacts (> 100 nm) thick were used.

Notably the sheet resistance provides information only on macro-scale conductivity. This is often overlooked and as such OPVs in the literature based on large-pitch grid structures can have extremely low macro-scale sheet resistance however the R_{series} resistance seen in the OPV devices remains high. This is attributed to the poor micron-scale conductivity where free charges generated must be extracted over large distances to reach a metal grid line, since the mobility of charges in organic semiconductors is low.[4]

3.2   Atomic Force Microscopy (AFM)

3.2.1   *Mechanics*

AFM is the most widely used variant of scanning probe microscopy, where a sharp probe is rastered across the sample surface and the force of interaction between the tip of the probe and the sample is measured. By keeping the force between the tip and substrate constant by continuous adjustment of the tip along the z-axis via a feedback loop, the force of interaction between tip and surface can be kept constant and a three-dimensional topographic map of the surface can be built up. The cantilever to which the sharp tip is attached can be thought of as a soft leaf spring, and force is measured by the deflection of this spring. A laser beam is reflected from the top face of the cantilever and the change in the angle of deflection as the cantilever flexes displaces the reflected beam on the sensor. This is then fed back to piezoelectric actuators which raise or lower the tip in response. The AFM tip is at the end of a cantilever that is several mm long, however the sharp tip on the underside tapers to typically a $5 - 50$ nm radius. As contact is made only through the tip, which is most commonly made of silicon nitride, it is both extremely sensitive and fragile. The key advantages of AFM are the high spatial resolution, compatibility with practically any material conductive or not, and that a topographical image can be collected alongside other information such as conductivity or variation in surface potential. Whilst the lateral resolution depends on the tip radius, the vertical resolution of AFM is of the order of 1 angstrom and so under ideal conditions can image with atomic resolution.

The described mode of operation is known as contact mode AFM, where the tip is in constant contact with the sample. On soft samples however the tip can drag or stick, while hard samples rapidly degrade the fragile tip. In non-contact mode AFM cantilever is oscillated close to its resonant frequency just above the sample surface and changes in this frequency measured as the tip is rastered above the surface of the sample. Van der Waals forces for example, extending from the surface by 1 – 10 nm, will decrease the resonant frequency of the cantilever. This prevents damage to the tip, however adsorbed fluids (particularly water) which form on most samples can often be indistinguishable from the true surface.

Consequently, tapping mode is used in this work. In tapping mode, the cantilever is oscillated near its resonant frequency, but the driving force is kept constant. The height of the tip is then set such that the tip contacts the sample only intermittently, which reduces the amplitude of the oscillation. An electronic servo maintains a constant height of the tip above the sample while rastering across the surface using the change in oscillation amplitude as the feedback mechanism. In this way tapping mode provides a similar output to contact mode, but with reduced chance of sticking and damage to the tip. In this work an Asylum Research MFP3D instrument was used in tapping mode to image sample topography.

3.2.2   *Outputs and Applications*

AFM images give a topographical map of the surface which is best represented as a 2D map with z-axis data shown through colour as in Figure 2 (a).
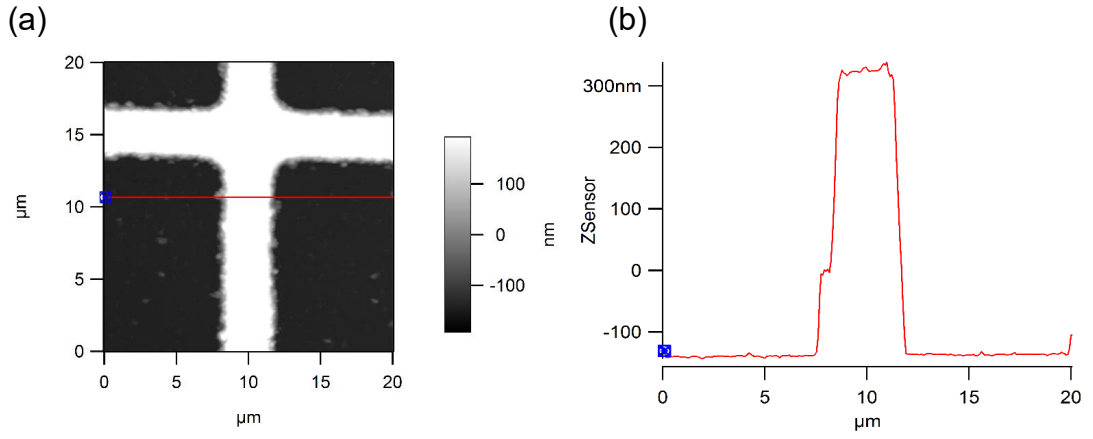
Figure 2: (a) Topographical AFM image of an example ~500 nm thick Cu grid line where the 'furry' substrate-grid edge is caused by metallic 'steps'. (b) Cross-section of the drawn red line.

The thickness of evaporated and spin cast films is measured using the AFM by making a scratch using a needle. A (flattened) topographical map can then be 'binned': Each point can be plotted on a histogram as in Figure 3 (b). If several images are collected at different locations along the scratch, a film thickness can be calculated with precision < 1 nm.
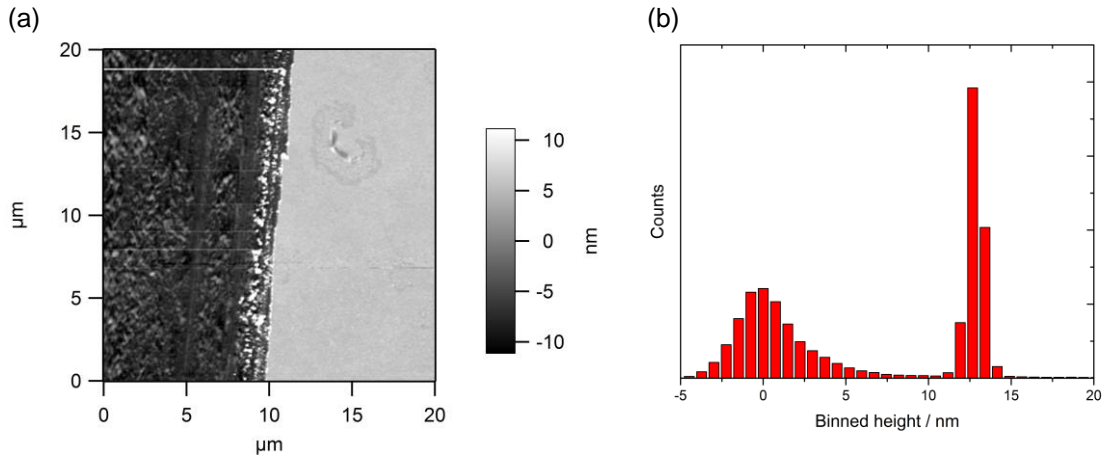
Figure 3: (a) One example AFM image of a scratch through the MM | Al | Cu electrode from which the height difference was calculated by histogram in (b).

The AFM z-axis on the MFP3D instrument (Asylum Research) used here is sensitive to < 0.25 nm, limited by thermal noise, and as such even the surface of 'slab-like' < 10 nm

thick metal films can be probed (Figure 3). Commonly this data is presented as a root mean square (RMS) roughness value, or the square root of the mean of the squared points.

3.2.3 Limitations

The nature of AFM where a physical tip is passed across the sample can lead to the exaggeration or misrepresentation of features. In the simplest case where the surface features are smaller than the tip radius the data acquired using an AFM can be misleading or incomplete, for example the depth of the gap between two adjacent crystallites, as depicted in Figure 4 (a), is not reflected in the path of the tip. Figure 4 (b) also shows a case of a spherical particle on a flat surface which is imaged as being wider than it really is due to the curvature of the tip. Importantly, the 7 nm radius tip was chosen for this work as it enables imaging of the individual crystallites in polycrystalline films of typical width ~ 50 - 100 nm. Figure 4 (c) shows a similar but important case in this work: AFM can give no indication of the undermining of a metal film (i.e. under-etching) due to the directionality of the probe.
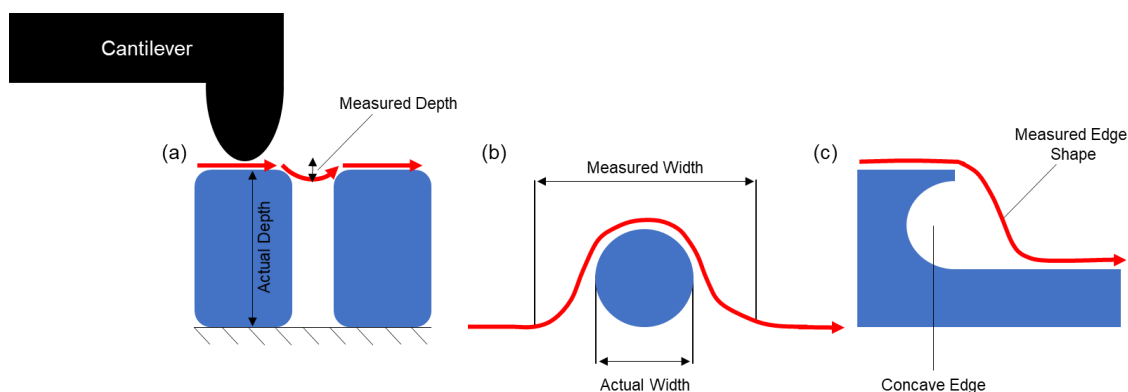
Figure 4: Three cases where AFM misrepresents the physical structure. The red line represents the travel of the tip and cross-section collected by the cantilever of the blue features: (a) Two closely packed features. (b) Spherical particle. (c) Undercut edge.

3.3 UV-Visible (UV/Vis) Spectroscopy

In this work electronic absorption spectroscopy was used to determine the transmittance of the electrodes. Semi-transparent samples can be characterised by four spectra: Linear

transmission spectra (specular transmission), scattered transmission spectra (diffuse transmission), reflection spectra and absorption spectra. The specular transmission spectrum gives the spectrum of light as a percentage of the incident beam which has been transmitted with little variation in momentum. If not mentioned otherwise in this work, the 'transmission spectrum' refers to the specular transmittance. The diffuse transmission spectrum gives the spectrum of light which has been scattered away from the incident beam as it passes through the sample. Reflected light is scattered backwards by the sample and so is not transmitted.

The reflected light is the most significant loss from metal films and, in the simplest case of a single film on a transparent substrate (Figure 5), is the sum of the reflection from three interfaces (red arrows): air-substrate, substrate-TCE and TCE-air. The air-substrate reflection is negligible in commercial optoelectronics due to established anti-reflective coatings, and as such is subtracted by referencing the spectra to that of a clean substrate in this work. Discrete measurement of the diffuse transmission can also be useful because scattered light has a longer path length through the photoactive layers in an OPV and so increases absorption.
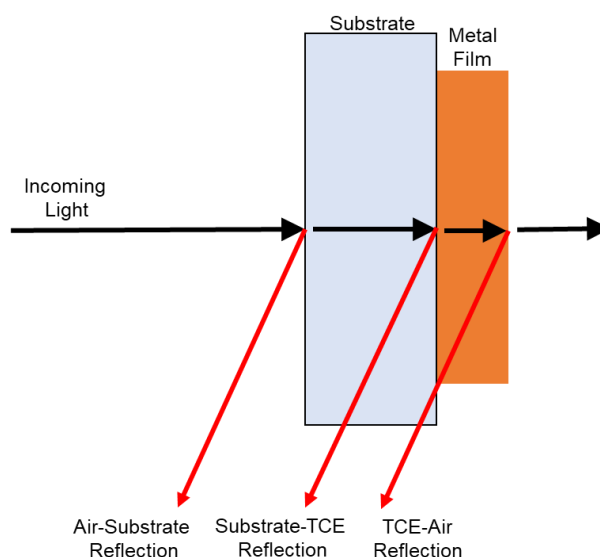
Figure 5: Schematic summarising the main contributions to reflected light for a planar metal film electrode supported on a transparent substrate.

Figure 6 shows the arrangement of optical elements used to measure these spectra. Specular transmission, Figure 6 (a), is the simplest measurement where a narrow detector is used to collect light passing along its original trajectory after transmission through the sample. Total transmission (specular and diffuse transmission) and total reflected light are then collected separately using an integrating sphere to focus scattered light onto a detector as shown in Figure 6 (b) and (c).
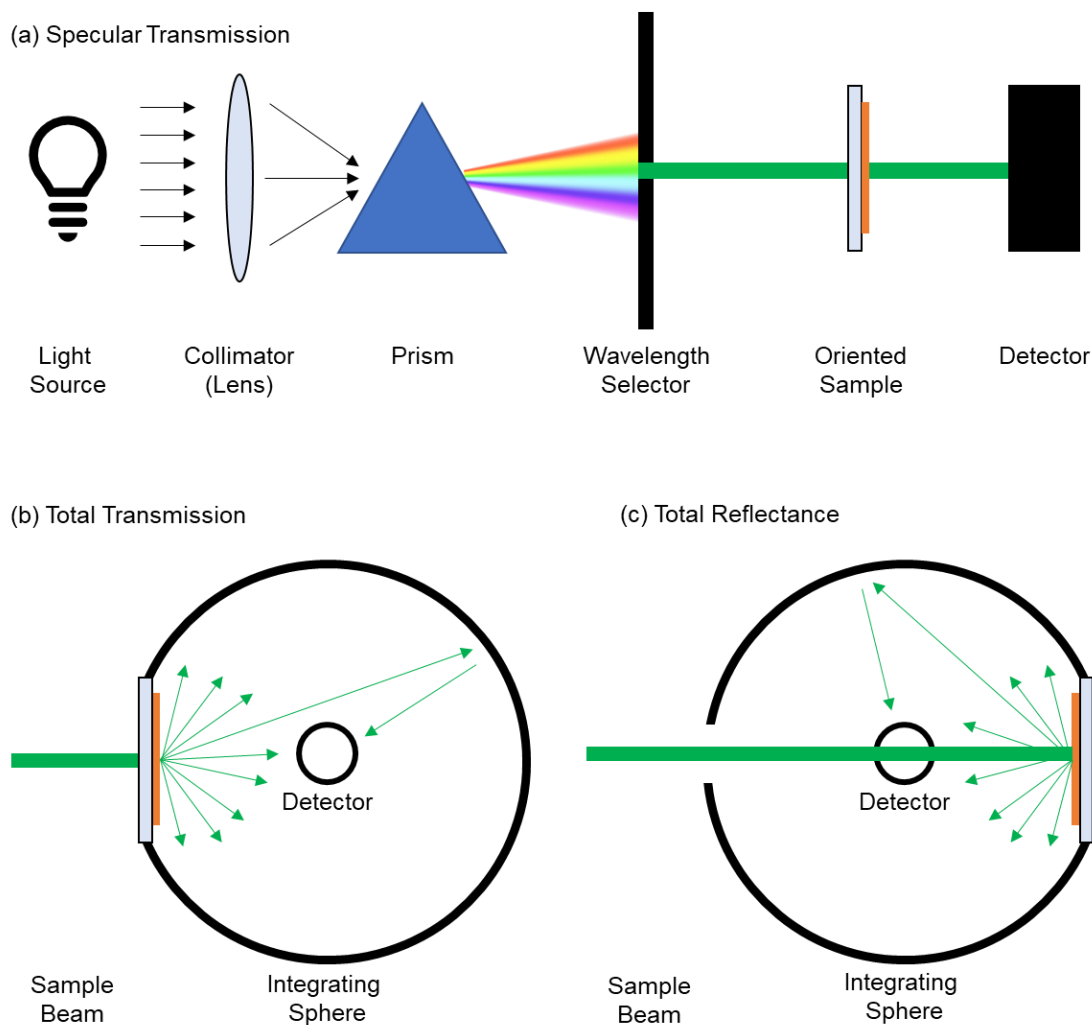
Figure 6: Three UV/Vis spectrometer setups used in this work (a) Complete schematic of a simple UV/Vis spectrometer where specular transmission is the main contribution to intensity. (b) Sample/Detector setup using a total-internal-reflection (integrating) sphere to additionally collect diffuse transmitted light. (c) Sample/Detector setup using an integrating sphere to collect total reflected light.

3.4 Scanning Electron Microscopy (SEM)

The SEM used throughout this work was a Zeiss Supra 55-VP Field Emission SEM, where field emission refers to the generation of electrons in the instrument using a field emission gun. This source of electrons provides a higher spatial resolution and enables lower potentials than traditional hot-filament sources.[5] In SEM a focused beam of electrons is rastered across the sample surface, which interacts with the sample in a number of ways (Figure 7).
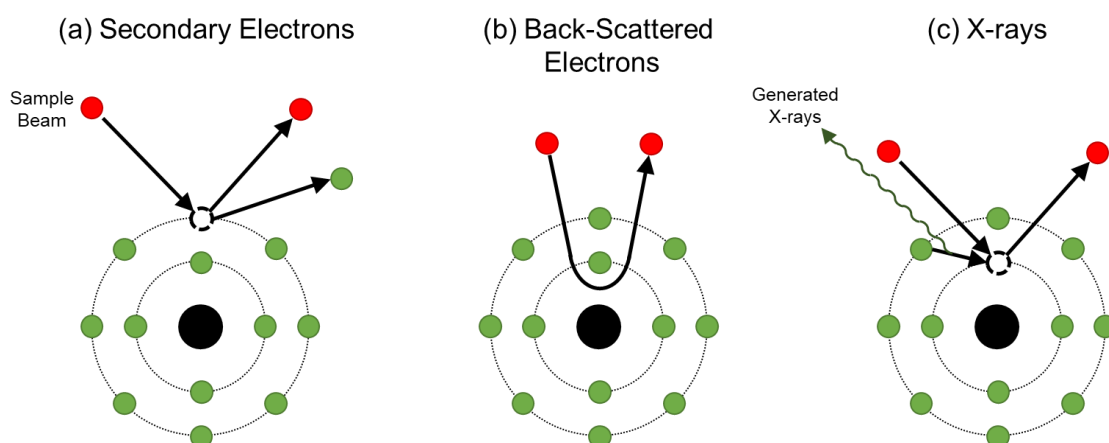
Figure 7: Three common interaction types of the electron beam (sample beam) with atomic nuclei (black circles) and orbitals (grey circles) in the sample to produce measurable outputs: (a) Secondary electron, (b) Back-Scattered Electrons and (c) X-rays.

The emission and detection of secondary electrons (Figure 7 (a)) is the most common mode of SEM imaging. To achieve this the detector is located close to the electron beam origin (in-lens detector) such that secondary electrons are collected directly from the impact zone. The contrast in the image reflects the topography of the sample. With increasing atomic number elements emit increasing high energy back-scattered electrons (Figure 7 (b)) and so contrast in this mode provides information about the elemental composition. More detailed elemental analysis, but without spatial resolution, is commonly achieved using emitted X-rays (Figure 7 (c)) however this was not used in this work since the energies of the X-rays produced by the elements of interest in this thesis overlap (Cu, Zn, Al). SEM imagery has been demonstrated with sub-nanometre resolution,[6] but is more generally limited to 3-5 nm resolution.

In this work SEM was used for the analysis of patterned metal electrodes. By cleanly breaking substrates and mounting the sample at 90° it is also possible to image the cross-section of OPV devices, as in Figure 8.
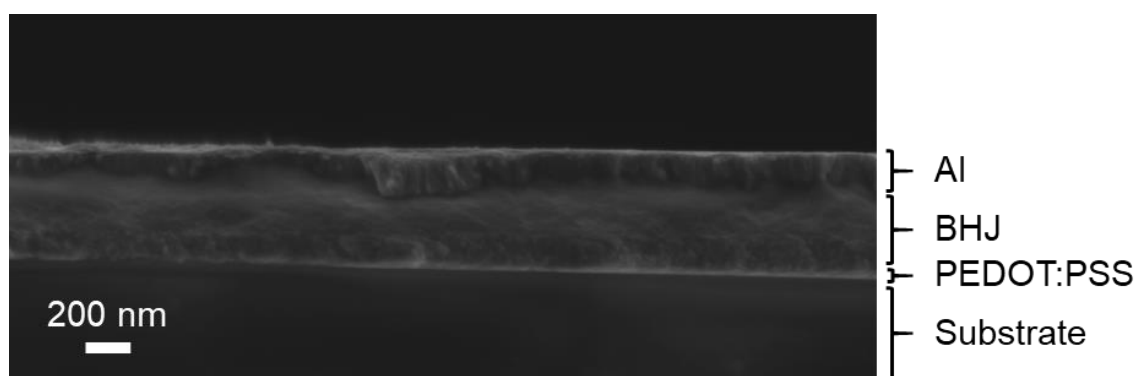
Figure 8: Cross-sectional (side-on) SEM secondary electron image along the edge of a fractured OPV device.

SEM is only compatible with conductive samples, as non-conductive surfaces quickly become charged which distorts the images. Non-conductive samples can be sputtered with metals, typically gold, to enable imaging at the expense of some surface detail. In this work, even the metal oxide layers proved sufficiently conductive for SEM imaging without charging.

3.5 Transmission Electron Microscopy (TEM)

Transmission electron microscopy will be discussed in lesser detail than SEM, due to its similarities with SEM and its lesser utilisation in this work. In TEM, the sample is prepared by cutting a thin (~ 50 nm) cross-section through the film and substrate. The thickness of the sample is chosen to be lower than the mean path length of electrons and so significant beam intensity travels through the sample. The 2D detector is on the opposite side to the incident beam and records the electron beam intensity as a function of position. Image contrast is produced by positional variations in density, atomic number, crystal structure or lost momentum. TEM can achieve atomic resolution and, in many cases, resolution is limited only by the quality of sample preparation.

Alongside the TEM analysis in Chapter 5, energy-dispersive X-ray spectroscopy (EDXS) was used to provide spatially resolved elemental analysis. The X-rays emitted as a result of electron ejection from an inner shell by the incident beam, and the subsequent decay of an outer shell electron (Figure 7 (c)) are imaged by a 2D detector. Each element exhibits a unique electromagnetic emission spectrum at an intensity proportional to the composition, and the elemental analysis can be overlaid on the TEM image.

3.6   Optical Microscopy

In contrast to the sub-nanometre resolution of electron microscopy, optical microscopy resolution is limited to $> 0.2\ \mu m$. Samples are imaged under ambient conditions however, and do not need to be electrically conducting. In this work optical microscopy was used to observe the macro-scale uniformity of patterned electrodes with metal or non-metal features $> 2\ \mu m$ wide, due to the wide field of vision and speed of image collection. Optical microscope images can be collected showing reflected or transmitted light by the sample.

3.7   X-ray Photoelectron Spectroscopy (XPS)

An atom or molecule absorbing an X-ray photon can eject an electron with kinetic energy (KE) equal to the difference between the energy of the photon and the electron binding energy (BE). In XPS, an X-ray source (here Al Kα) of precise emission energy is directed at the sample under ultra-high vacuum and the ejected electrons collected by a detector of work function Φ. Since this means that measured energy will be total energy subtract the difference between the Fermi level of the detector and vacuum level, this gives rise to the following relationship:

Equation 7.

$$KE = hv - BE - \Phi$$

where h is plank's constant (J s^{-1}) and v the frequency of the incident photon (Hz). In this work the detector work function was calibrated using the 3d$_{5/2}$ peak recorded from a polycrystalline Ag sample prior to experiments. When Φ, hv and KE are known, the BE is determined by the element, the orbital from which the electron was ejected and the

chemical environment of the atom from which the photoelectron emanates. Whilst XPS probes core electron shells (which are not involved in bonding) due to the high energy of X-rays, it is sensitive to the chemical environment of the atoms because the valence electrons screen the coulombic force of attraction between the atom nucleus and the ejected electron. Consequently, the binding energy of core electrons is a function of the distribution of valence electrons.

Detected electrons can also be attributed to a separate mechanism of emission known as Auger emission. These electrons are ejected via a secondary process where after the initial ejection of a core electron the relaxation of an electron into this deep lying state releases energy. Typically, this energy is released as a photon, however it can also be transferred to an electron in a shallow state which is then ejected: an Auger electron. Again, the KE of this electron depends on several factors including the element, the orbital from which the electron was ejected and the chemical environment of the source atom. XPS and Auger electron spectroscopy are conducted simultaneously and can give complimentary quantitative information about the chemical environment of the elements making up a sample. In XPS the detected energies are reported as binding energies using Equation **7**, however as Auger electrons are independent of the energy of the initial photon these are typically reported as kinetic energies.

Although the depth penetration of the incident X-rays is relatively large, the mean free path length (λ) of ejected electrons is typically < 10 nm, dependent on the material. For example, the mean free path of ZnO is approximately 2.5 nm,[7] and the depth from which 95% of XPS intensity originates is given by:

Equation 8.

$$3 \times \lambda \times \sin\theta$$

where λ is the mean free path (2.5 nm for ZnO) and θ the take-off angle, or angle of the detector with respect to surface normal. For ZnO, this means that by collecting XPS spectra in subsequent scans with the take-off angles 90, 30 and 15° the spectra represent the upper 7.5, 5.0 and 2.5 nm respectively. Although with stochiometric films such as this no additional information is given, for materials with thin overlayers < 5 nm such as a native oxide this is a useful technique to resolve the thickness and composition of each overlayer. An example of XPS spectra at 3 different take-off angles for the same sample is given in Figure 9.
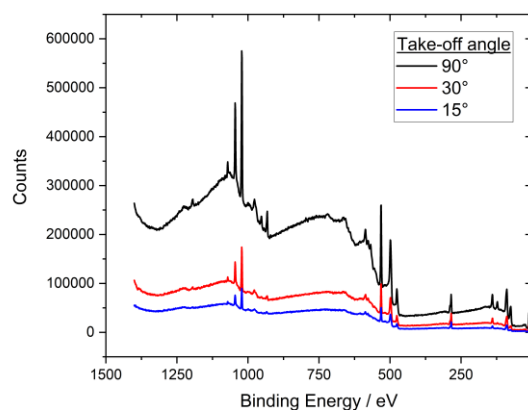
Figure 9: The XPS spectra of the same sample (Cu-based electrode) at three different take-off angles; 90° (Black), 30° (Red) and 15° (Blue).

The sharp peaks rising from the baseline on the spectra in Figure 9 reflect electron emissions at energies pertaining to the element and orbital from which they originate. For example, electrons from the element Cu and 2p orbital have binding energies in the range 925 – 970 eV. The total electrons ejected is independent from the chemical environment, only the BE is affected. This together with a sensitivity of < 1% of a monolayer mean XPS can also be used as a quantitative measure of elemental composition.[8] Although binding energy is dominated by the element and orbital from which the emission occurs, the chemical environment affects the fine structure. This is the most common application for XPS where fine peak structures are assigned by fitting using the extensive available literature of calibrated reference environments for atoms, orbits and chemical environments.

Like SEM, the release of free electrons from the surface of the material cause a charge build-up when the sample is not grounded. Any further electrons ejected have their kinetic energy reduced as they are attracted to the positively charged surface. Unlike SEM however, XPS can be used to probe non-conductive samples also as charging of the surface can be compensated for by neutralising surface charge using a low energy electron source.

3.8   X-ray Fluorescence (XRF)

X-ray fluorescence is a technique complimentary to XPS, providing elemental detail with simpler instrumentation and analysis: XRF analysers are available which are handheld and designed for use in industry. As in Auger electron spectroscopy, an impacting X-ray photon can impart energy to an atom and eject an electron from a deep lying orbital followed by the decay of a valence electron to the deep lying state. In Auger electron spectroscopy this energy is imparted to a third electron which is ejected from the atom. More commonly this energy is released however as X-rays. By shuttering the source X-rays, this intensity or fluorescence can be measured by a detector. The peak position of the resultant energies is used to identify elements present and the integrated area is indicative of the concentration (thickness for high-purity thin films).

3.9   Grazing Incidence X-ray Diffraction (GIXRD)

3.9.1   *Mechanics*

In the classic diffraction experiment, reported by Thomas Young in 1801, photons are directed through two broad slits of width greater than the photon wavelength the photon behaves as a particle maintaining its original momentum; Figure 10 (a). When a photon approaches a slit with width less than the wavelength, it behaves as a wave and is diffracted from the back face of the slit as in Figure 10 (b). Photons travelling through adjacent narrow slits (Figure 10 (c)), exhibit constructive and destructive interference causing a diffraction pattern of repeating intensity.
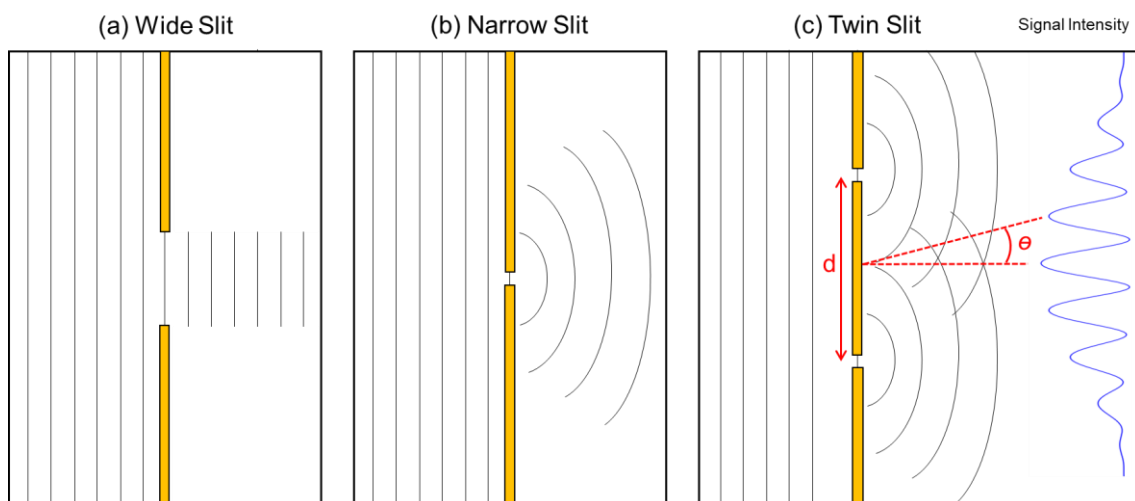
Figure 10: Three example behaviours of photons travelling through a slit behaving as particles where the slit width is greater than the wavelength, a wave when it is narrower and exhibiting an interference pattern where photons pass through adjacent narrow apertures separated by distance d.

In XRD, this phenomenon is exploited on an atomic scale: A monochromatic X-ray source with wavelength of the same order as the distance between atoms in the crystal lattice of the sample. A portion of the X-ray beam is diffracted by the repeating atomic planes producing a diffraction pattern as in Figure 10 (c) which is a function of the distance between atomic planes (d) and the angle of incidence (θ). The angles at which a specific crystal produces constructive interference, resulting in a peak in the XRD spectra, is defined by the Bragg equation:

Equation 9.

$$2d \sin \theta = n\lambda$$

where *n* is a positive integer and λ the wavelength of the incident X-ray. In GIXRD, the incident beam is at a low angle ($< 5°$ above the plane) to sample the surface of the film rather than bulk. A large portion of the incident beam is also reflected at an equal angle to the incident beam above the plane, which carries information utilised in techniques such as small-angle X-Ray scattering.

3.9.2   Outputs and Applications

GIXRD is specifically useful for surface analysis, or in this work the analysis of thin films upon a substrate of no interest due to the low sampling depth. The sharp peaks and low background in Figure 11 also demonstrate the high crystallinity of the example evaporated Cu thin film, as the background level is a result of scattering by amorphous phases.
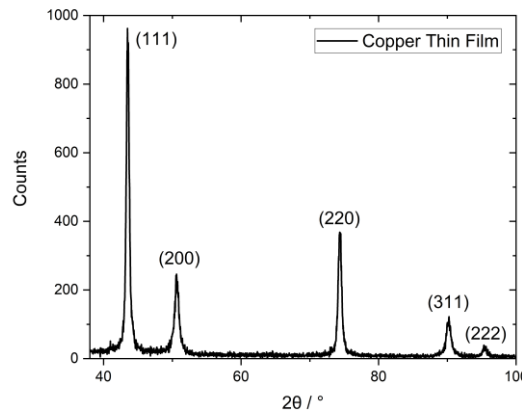
Figure 11: An example GIXRD spectra for a thin Cu film (120 nm) on glass.

The FWHM of peaks in GIXRD reflect particle size, defect density or inhomogeneous crystal strain. The relationship between increasing particle size and the FWHM of the peak results from the relative order of the film increasing, as crystallite boundaries are associated with mismatched crystal planes. Crystal strain, if homogenous such as even compression, will result in a shift in peak position as the angle of constructive interference is shifted. Inhomogeneous strain, such as that caused around a defect site within the lattice, creates however a series of separate partially constructive angles as the crystal planes are bent around the site.

3.9.3   Limitations

The greatest limitations of XRD are inherent in the technique: The material must be crystalline, or polycrystalline, and reference data is required to assign peaks with Miller indices. XRD also only returns information on the crystalline film, for example defects

are only represented as a broadening of the crystal peaks and no information can be directly determined about the chemical composition.

3.10 Small-Angle X-Ray Scattering (SAXS)

3.10.1 Mechanics

In SAXS a collimated X-ray beam is fired at a sample in a transmission setup, with the scattered X-rays recorded by a detector with an angular range of 0.05 - 5° 2θ. Regions with differences in electron density, such as nanoparticles, scatter the X-rays with the scattering angle related to the size of the particle. The larger a particle the smaller the scattering angle.

Similarly to GIXRD, in GISAXS a thin film sample is aligned to the X-ray beam such that the incident angle is extremely low (0.1° to 2°) and close to the critical angle. Below the critical angle the X-ray beam is fully reflected from the surface layer, whereas at the critical angle the beam is refracted and travels nearly parallel to the surface giving an enhanced scattering signal from the thin film. As in SAXS, the X-ray beam is scattered by regions of electron density such as film interfaces, crystallites and surface features. This scattering can be in any direction, which can be analysed with the use of a 2D detector. The scattering in the vertical direction also includes the strong reflected beam so is typically blocked by a beamstop to protect the detector.

3.10.2 Outputs and Applications

The size of features, such as crystallites in a thin metal film can be determined from the scattering angle of the X-rays. Through a simplified model, such as that developed by Shun Yu *et al.* for thin films close to the percolation threshold,[9] this pattern can be predicted and information decoded such as the average particle size, packing, and film roughness. In this work crystallites were modelled as cylindrical protrusions from the sample surface.

3.10.3 Limitations

The scattering of X-rays in a SAXS measurement requires a contrast between the electron density of the region of interest and the surrounding matrix. As such for closely packed

crystallites in a polycrystalline metal film, SAXS intensity is believed to be derived largely from the exposed roughness at the surface of the film. For thin films it should be determined separately, for example using TEM, that the surface topology reflects the bulk of the film as is the case for metal films of single crystallite thickness.

3.11 References

[1]   G. Govindaraj, *Phys. status solidi* **1989**, *113*, 113.

[2]   O. S. Hutter, H. M. Stec, R. A. Hatton, *Adv. Mater.* **2013**, *25*, 284.

[3]   H. M. Stec, R. A. Hatton, *ACS Appl. Mater. Interfaces* **2012**, *4*, 6013.

[4]   D. A. Jacobs, K. R. Catchpole, F. J. Beck, T. P. White, *J. Mater. Chem. A* **2016**, *4*, 4490.

[5]   J. Pawley, *Scanning* **1997**, *19*, 324.

[6]   L. Y. Roussel, D. J. Stokes, I. Gestmann, M. Darus, R. J. Young, In *Scanning Microscopy 2009*; SPIE, 2009; p. 7378.

[7]   L. G. Mar, P. Y. Timbrell, R. N. Lamb, *Thin Solid Films* **1993**, *223*, 341.

[8]   C. Y. Lee, P. Gong, G. M. Harbers, D. W. Grainger, D. G. Castner, L. J. Gamble, *Anal. Chem.* **2006**, *78*, 3316.

[9]   S. Yu, G. Santoro, Y. Yao, D. Babonneau, M. Schwartzkopf, P. Zhang, S. K. Vayalil, P. Wessels, R. Döhrmann, M. Drescher, P. Müller-Buschbaum, S. V Roth, *J. Phys. Chem. C* **2015**, *119*, 4406.

4   High-Performance Transparent Copper Grid Electrode Fabricated by Microcontact Lithography for Flexible Organic Photovoltaics

The majority of the work presented in this chapter is to be published in the following article:

4.1   Chapter Summary

This chapter describes the fabrication of high-performance transparent copper grid electrodes on glass and plastic substrates, matched to the needs of solution processed organic photovoltaic devices. The electrodes are fabricated by micro-contact printing a patterned molecular monolayer resist less than 2 nm in thickness onto an evaporated copper film, followed by fast etching with the low-cost, low-toxicity etchant ammonium persulfate. Both processes can be performed in ambient air. The grid linewidth achieved using this approach is > 20 times narrower than is possible using conventional metal printing methods, which enables a line spacing of < 30 µm and so an extremely thin (10 nm) PEDOT:PSS layer is sufficient to span the gaps between grid lines. This approach to electrode fabrication is much faster than conventional lithography, taking < 2 seconds to print the resist layer and tens of seconds to etch the copper film. A range of designs are explored, including demonstrating electrodes with a sheet resistance of 9.2 Ω sq^{-1} and 92.1% average far-field transparency without complex metal mesh transfer, photolithographic or electrochemical deposition steps. Additionally, it is shown that there is no need to embed the grid into the supporting substrate which simplifies the electrode fabrication process.

4.2 Introduction

The power conversion efficiency of organic photovoltaics (OPVs) has now exceeded 15% in the laboratory and there is good reason to expect that the long term stability needed for practical applications is within reach.[1,2] However, there is currently no transparent substrate electrode available that will enable OPVs to realize their full cost-advantage and functional-advantages (e.g. flexibility, light weight, color tuneability) over other types of thin-film photovoltaics, and translate these to module or commercial scale.[3] For practical application in photovoltaic modules, in addition to the basic requirement for a transparency $\geq 80\%$ over the wavelength range 400-900 nm, the electrode sheet resistance should be well below 10 Ω sq^{-1} to minimize ohmic and recombination loses and enable cell dimensions greater than 1 cm.[4,5] Additionally, the electrode must be robust and flexible to enable compatibility with high throughput roll-to-roll processing and be made using low cost and sustainable materials and processes.[6] Conventional transparent conductive oxides such as indium tin oxide (ITO) are unsuitable because, as well as the high cost of indium, they are inherently brittle and require post-deposition annealing at > 300°C to achieve optimal performance, which makes them incompatible with flexible plastic substrates.[7,8] Electrodes based on spray coated silver nanowires are costly because of the high cost of silver and the relatively high cost of nanowire synthesis, and also suffer from poor contact stability at the junctions between nanowires.[9] The high surface roughness of metal nanowire electrodes is also a serious problem for OPVs because the low photoactive layer thickness means that high surface roughness can easily compromise the integrity of the diode, degrading device fill factor.[10] Whilst optically-thin metal films sandwiched between two impedance matching amorphous oxide layers are compatible with flexible substrates, a very high degree of control over the thickness of each layer is needed to achieve high performance which can only be achieved using a slow metal and oxide deposition process.[3,11,12]

To date transparent electrodes based on metal grids with the gaps between grid lines spanned by a conducting polymer offer the highest performance.[13] However, metal grid electrodes are ordinarily fabricated using photolithography which is an inherently high-cost fabrication method because of the time taken to fabricate the mask on top of the metal and remove the mask after metal etching.[14–16] The photoresist layer also has a typical thickness of 0.5-5 µm and so its deposition and removal would require large

volumes of organic solvent if the electrode is to be scaled to the large electrode areas needed for OPVs.

Twenty years ago the group of George Whitesides reported that a alkanethiol layer only one molecule in thickness (1-2 nm) printed using the soft lithographic process of microcontact printing (μ-CP) could be used as an etch mask for patterning films of gold (Au), silver (Ag) and copper (Cu) when used in conjunction with using a thiosulfate/ferricyanide etchant.[17] μ-CP is compatible with roll-to-roll processing and so this pioneering work opened the door to the possibility of patterning these highly conductive metals with sub-micron resolution over large area using tiny amounts of resist.[18] Surprisingly however in the following two decades there has been little interest in the application of this approach to patterning films of these metals to fabricate transparent electrodes, possibly because of the perceived unfeasibility of using such a thin resist layer, or because of the perception that the approach is only really useful for costly metals such as Au and Ag, because Cu readily forms a surface oxide which interferes with the formation of an ideal, compact monolayer.[19] To the author's knowledge, to date there has been only one literature report relating to the use of μ-CP to fabricate transparent electrodes based on a metal grid: Zou *et al.* have shown that silver grids with a line width of ≥ 7 μm and line-spacing of 50 μm on glass can be fabricated using μ-CP printed resist layers of 11-mercaptoundecanoic acid and a thiourea/ferric nitrate silver etchant.[20] However, in addition to the high cost of silver, the performance of these electrodes were limited by the large gaps between the grid lines which compromised fill-factor in OPV devices.[20]

This chapter describes the development of high-performance Cu grid electrodes (Figure 1) on glass and plastic substrates by μ-CP using a hexadecanethiol (HDT) monolayer resist together with the low-cost, low-toxicity and single-component etchant ammonium persulfate (APS). APS is commonly used to etch printed circuit boards and it is known that the Cu etched with APS can be economically recovered,[21,22] although its compatibility with monolayer resists has not been reported before. Cu is the metal of choice because it is ~100 times lower cost than Ag with comparable electrical conductivity. It is shown that this new resist-etchant combination enables excellent selectivity, and that high edge resolution can be achieved without the need for additional additives commonly utilized,[19] enabling the fabrication of highly conductive Cu grids

with lines < 2 μm in width. Furthermore, both printing and etching processes can be performed in ambient air.
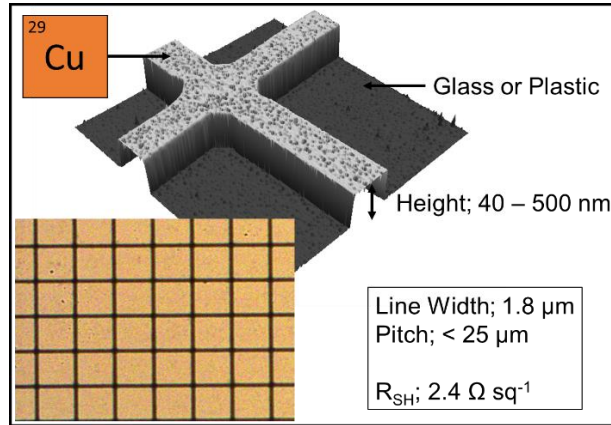
Figure 1: Figure summarizing the grid electrode design based on an AFM image and light microscope image (bottom left) of an optimised electrode with Cu grid lines < 2 μm wide.

Metal grid electrodes in the literature are almost universally utilised in conjunction with the conductive polymer PEDOT:PSS. Although metal grid electrodes have been demonstrated with a sheet resistance of < 1 Ω sq^{-1}, including here, in OPVs charges generated in the regions between grid lines must travel laterally through a much less conductive layer to reach the metallic grid lines with adverse effect on the device fill factor by the increasing series resistance as compared to a planar metal electrode. It is not uncommon for grid electrodes to be used in conjunction with > 100 nm thick PEDOT:PSS overlayers to span the gaps between grid lines, leading to significant parasitic absorption by the relatively thick PEDOT:PSS layer.[23–25] This also adds additional processing steps, because the highly conductive PEDOT:PSS PH1000 formulation does not selectively extract holes. Additionally PEDOT:PSS is highly acidic, relatively expensive and hydroscopic: all of which undermine the device usefulness and long term stability, especially when used with Cu metal.[26]

The vast majority of current collecting grids for use in OPVs in the literature have a pitch (repeating distance) of 150 – 1000 μm, which requires a highly conductive PEDOT:PSS layer.[13] A key advantage of the grids described here is the narrow pitch

afforded by microcontact printing which raises the possibility of PEDOT:PSS-free metal grid electrodes.

Using this molecular resist-etchant pair, line-widths less than one third that previously demonstrated on Ag are achieved, which is > 20 times narrower than is possible using conventional metal printing methods such as industrial screen printing, inkjet printing or electrohydrodynamic jet printing.[5,13] Cu grid electrodes with a sheet resistance of 2.4 Ω sq^{-1} and 80.3% average far-field transparency and > 6 times smaller line spacing than the narrowest reported to date for a grid electrode used in an OPV device have been realized directly on the supporting substrate, without complex metal mesh transfer, photolithographic or electrochemical deposition steps.[13]

4.3   Results and Discussion

4.3.1   *Electrode fabrication and characterisation*

Cu films with a thickness of 40-500 nm (depending on the desired sheet resistance) were deposited onto glass and polyethylene terephthalate (PET) substrates by vacuum evaporation. A polydimethylsiloxane (PDMS) stamp patterned with relief structures and dosed with HDT was bought into intimate contact with the Cu coated substrates for ~ 2 seconds to deposit the HDT mask (Figure 2).
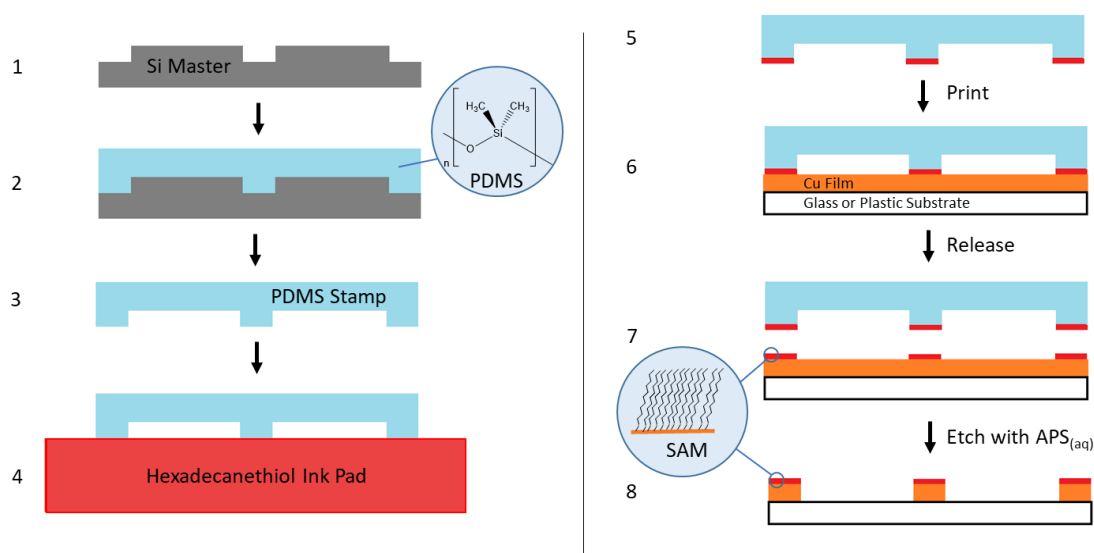
Figure 2: Schematic of the μ-CP/wet-etch system used here. Steps 1 - 4 describe the fabrication of the PDMS elastomer stamp from the patterned silicon master, and subsequent inking with HDT from a dilute solution. The master can be reused > 20 times.[27] Steps 5-8 describe the fabrication of a patterned Cu film from the PDMS stamp infused with HDT. The high purity of the HDT ink allows reuse of each PDMS stamp > 100 times without notable deterioration of the replicated pattern in this work.

Notably using a 11-mercaptoundecanoic acid (MUA) resist, as reported by Zou *et al.* for patterning Ag films,[20] required a 30 - 90 s contact time in order to form a sufficiently dense monolayer to block etching by APS (Appendix, Figure A1); more than an order of magnitude longer than with HDT. The film with patterned HDT monolayer was then submerged in an aqueous solution of APS to etch those areas not functionalized with the HDT monolayer. The time taken to etch the metal depends on the APS concentration (with concentrations in the range 4-50 mM being used in this work) and metal thickness and is of the order of tens of seconds. This process yielded high quality square Cu grids with line widths of 1.8 – 3.0 μm, a pitch of 27.3 μm and thickness of 40-500 nm, an example of which is shown in Figure 3.
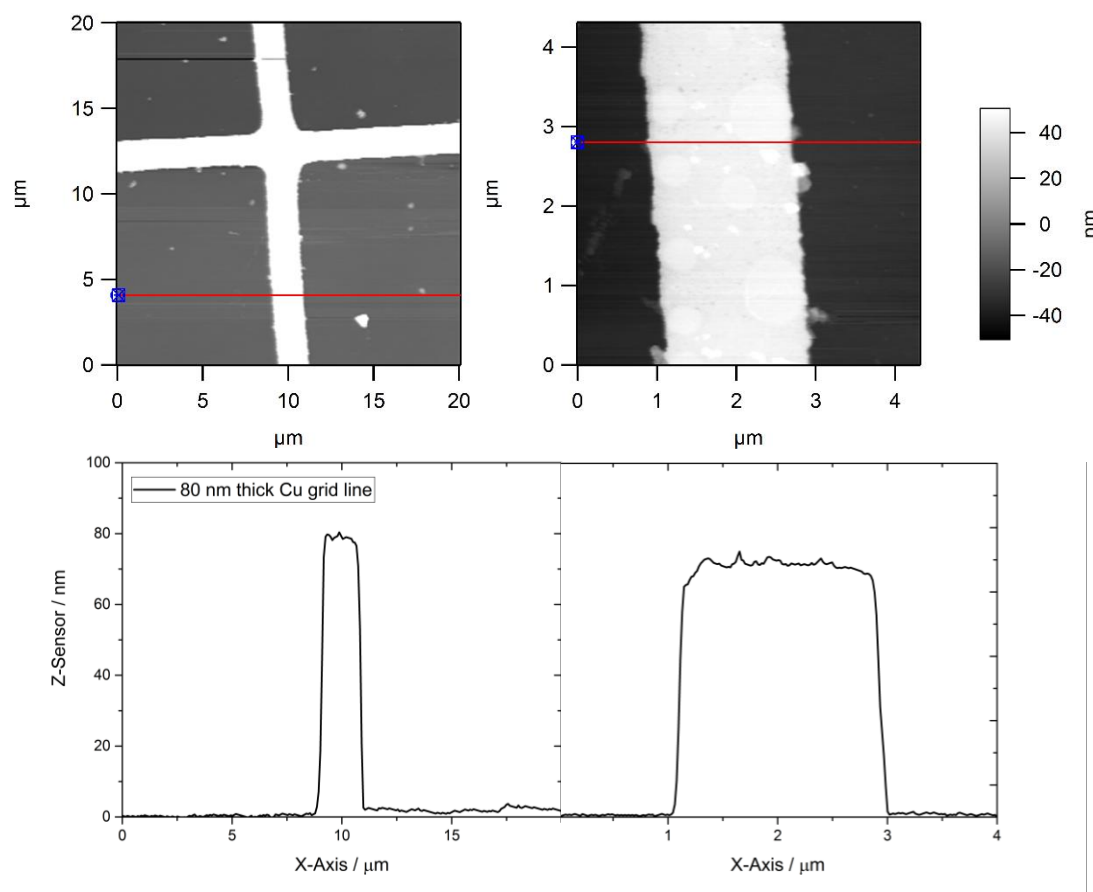
Figure 3: (Upper) Topographical atomic force microscopy (AFM) images of a representative area on 80 nm thick Cu grid lines at different magnification. (Lower) Corresponding cross-sections indicated on upper figures by red lines.

The quality of the grid electrodes was found to be independent of whether the HDT monolayer was stamped in a nitrogen atmosphere or ambient air. This process yielded Cu grid electrodes with a far-field average transparency of 83.3%, 80.3% and 77.2% for 40, 120 and 500 nm grid thickness respectively: Figure 4. The small decrease in transparency when increasing the grid line thickness from 40 to 120 nm can be understood in terms of the loss in transparency of the Cu gridlines themselves, since at a thickness of 40 nm Cu films are semi-transparent. The reason for the further reduction in transparency when going from 120 nm to 500 nm is attributed to the more ragged edges of the grid lines, as highlighted by appendix, Figure A2, where 'steps' at the base of the grid lines were difficult to etch cleanly away without undermining the metal lines.
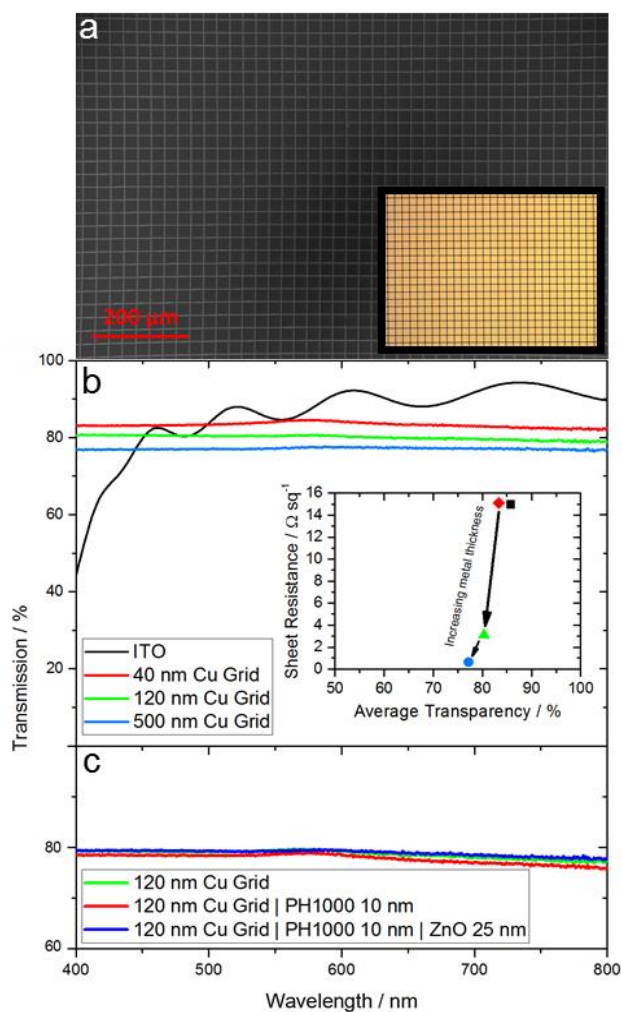
Figure 4: (a) A scanning electron microscope image of a Cu grid on a glass substrate. Inset is an optical microscope image of the same electrode illuminated from the rear; (b) Electronic absorption spectra with the air-substrate interface subtracted for Cu grids with different line thicknesses. Separate total transmission, diffuse transmission and reflection spectra for 120 nm and 500 nm thick Cu grids are given in Figure 5. Inset shows the relationship between metal thickness and the average transparency/sheet resistance. (c) Electronic absorption spectrum of a Cu grid with 120 nm line thickness, with no overlayers (Green), 10 nm PEDOT:PSS (Red) and PEDOT:PSS | 25 nm ZnO (Blue).

Figure 5 shows the optical parameters total transmittance, diffuse transmittance and reflection; measured separately using an UV-vis spectrometer with integrating sphere. This enables discrete analysis of the total transmission (similar to that in Figure 4), diffuse transmission and reflectance. Nearly all losses in the electrode are accounted for as

reflection from the metal-substrate surface (Figure 5, dashed lines) with the remaining losses attributed to absorption by Cu. The diffuse transmission of ~10% (Figure 5, dotted lines) is a component of the total transmission largely attributable to a diffraction grating effect as a result of the repeating array of features on the micron scale. This is a similar process to the famous double-slit experiment where destructive and constructive interference of light after passing through the grating lead to a unique patterning of intensity. This effect is visible by eye when light is incident at a specific angle and is experientially a good indication of the uniformity of the grid lines, since it is reliant on repeating lines of equal width. Importantly, this scattering of light by the diffraction grating effect can improve the device performance of OPVs since the light-harvesting layer is invariably thinner than what is needed to absorb all of the incident light, and so low-angle photons have a far greater path length through the light-harvesting layer.[28]
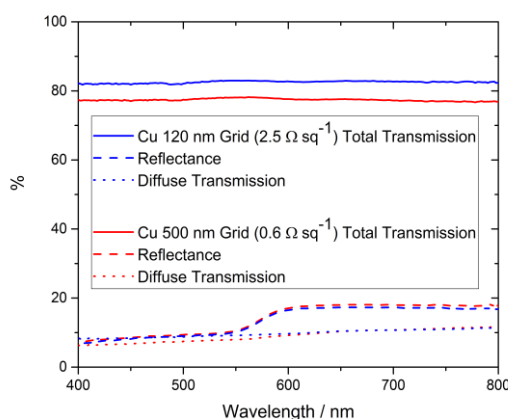
Figure 5: Electronic absorption spectra with the air-substrate interface subtracted for Cu grids with line thicknesses 120 nm (Blue) and 500 nm (Red). Separate total transmission (Solid line), diffuse transmission (Dotted line) and reflection (Dashed line) spectra are given.

The advantage of using very small grid line-widths is that the gaps between lines can be smaller for the same metal coverage of the transparent supporting substrate. This is important for OPV applications because, due to the low conductivity of organic semiconductors the gaps between gridlines must be spanned with a conducting layer such

as poly(3,4-ethylenedioxythiophene):polystyrene sulfonate (PEDOT:PSS) to ensure efficient charge extraction (Figure 6). The larger the spacing between the grid lines the more conductive this layer must be to avoid excessive recombination/ohmic losses which degrade PV device fill-factor.[5] However, increasing the conductivity of the layer spanning the gaps between grid lines inevitably results in more parasitic light absorption by the layer.[24,29] Due to the very small line separation used herein, a PEDOT:PSS layer with a thickness of only 10 nm is needed to achieve the optimal fill factor comparable with a planar reference electrode, which absorbs an insignificant portion of the incident light: Figure 4 (c). Typically grid electrodes reported in the literature use a PEDOT:PSS thickness of 100-300 nm, which reduces the transparency by 5-10%.[24,29]
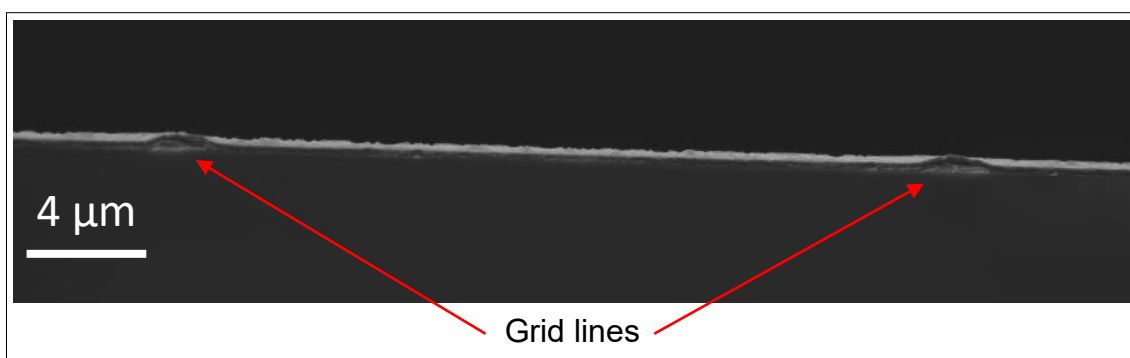
Figure 6: Cross-sectional scanning electron microscopy (SEM) image of an example OPV device based upon the grid electrode developed in this work. Two grid lines can be seen at the left and right of the thin film OPV, with the glass substrate beneath. The intervening distance must be spanned by a layer with sufficient conductivity to be able to conduct charges to the metallic Cu grid lines.

4.3.2   *Chemical and mechanical stability of copper grid electrodes*

The Haacke figure-of-merit (transmittance[10] / sheet resistance)[13] reported for the complete electrode with 120 nm grid thickness is initially 0.035, however it increases to 0.046 with storage at ambient temperature due to a reduction of sheet resistance from 3.2 to 2.4 Ω sq^{-1} (T_{AVG} = 80.3%). An example of this process is shown in Figure 7 (a). This improvement occurs even if the electrode is stored in air despite the parallel competing

process of Cu oxidation, which highlights the very slow rate of Cu oxidation in ambient air. After ~ 400 hours the sheet resistance of this electrode was largely stable in air.[30–33]
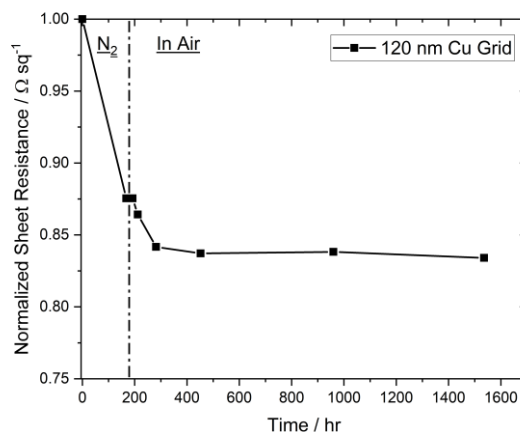
Figure 7: The sheet resistance of a representative 120 nm thick Cu grid electrode stored under N_2 for the first 192 hours then in air for a further 1480 hours (> 2 months).

This unexpected, and surprisingly large, reduction in electrode sheet resistance with storage at room temperature (Figure 7) can be accelerated by low temperature (120°C) thermal annealing under N_2, or ambient air as shown in Figure 8. The ~28% reduction in sheet resistance at 120°C for 15 minutes did not change for longer annealing time (45 minutes) or temperatures up to 180°C. At 300°C a greater improvement of ~40% was seen, however this was not explored further due to the high temperatures involved, which are incompatible with common plastic substrates. It is proposed this could be related to the melting/reforming of thin metal films at temperatures ≥ 200 °C such as reported previously by Stec *et al.*[34] As expected, due to the nature of the grids where metal lines are opaque, the transparency did not significantly change during this process ($T_{AVG} = 80.3$ *vs* 80.25 % when starting resistances were 3.1 - 3.3 Ω sq^{-1}). It is necessary to confine the sheet resistance as marginally under-etched films experientially show lower transparencies but also lower sheet resistances due to the contribution of the excess metal, and fine variation is seen within sets ($\pm$ 5%).
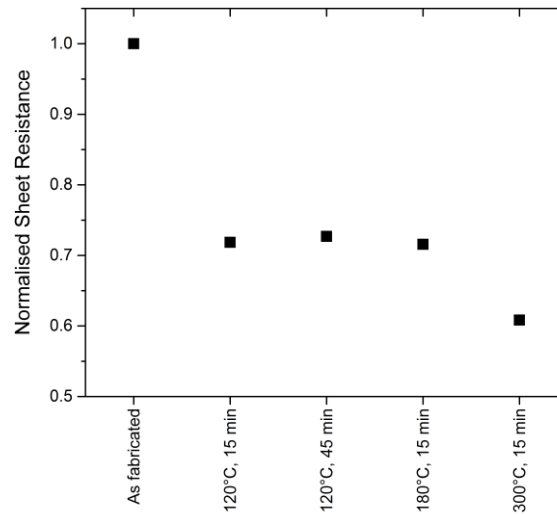
Figure 8: The average normalised sheet resistance of 120 nm Cu grids annealed at 120°C, 180°C and 300°C for different times. Each point represents a set of 3 samples. The transparency did not significantly change during this process (T_{AVG} = 80.3 *vs* 80.25 % when starting resistances was 3.1 - 3.3 Ω sq^{-1}).

To understand the physical reason for the beneficial ageing process a freshly deposited 120 nm thick Cu film deposited directly onto glass was probed before and after low temperature annealing using grazing-angle X-Ray Diffraction (XRD): Figure 9. The most obvious change in the XRD pattern upon annealing is an increase in the measured intensity ratio of the (220) and (111) reflections. This is attributed to the angle dependence of diffracting planes with respect the substrate upon 2θ in grazing-angle XRD however, and not a shift in preferred orientation from (111) which is common to face-centred cubic metals. A more subtle change in the full width at half maximum (FWHM) of the (111), (200) and (220) reflections is associated with the release of strain.[35] This narrowing of the peaks can also be associated with an increase in the particle size, although the root-mean-square (RMS) roughness measured using an AFM is not significantly changed, which might be expected if the crystallite size substantially changes: RMS roughness 1.17 ± 0.05 nm before, 1.12 ± 0.06 nm after. It is known that during the thermal evaporation of reactive metals (including Cu) at vacuum pressures of 10^{-6} – 10^{-8} mbar, residual gases are incorporated into the condensed metal film which effect the crystallinity and optoelectronic properties of the film. It is therefore tentatively suggested that upon

annealing of the film lattice defects and contaminants from residual gases in the vacuum system are pushed to the surface of the film and order increases.
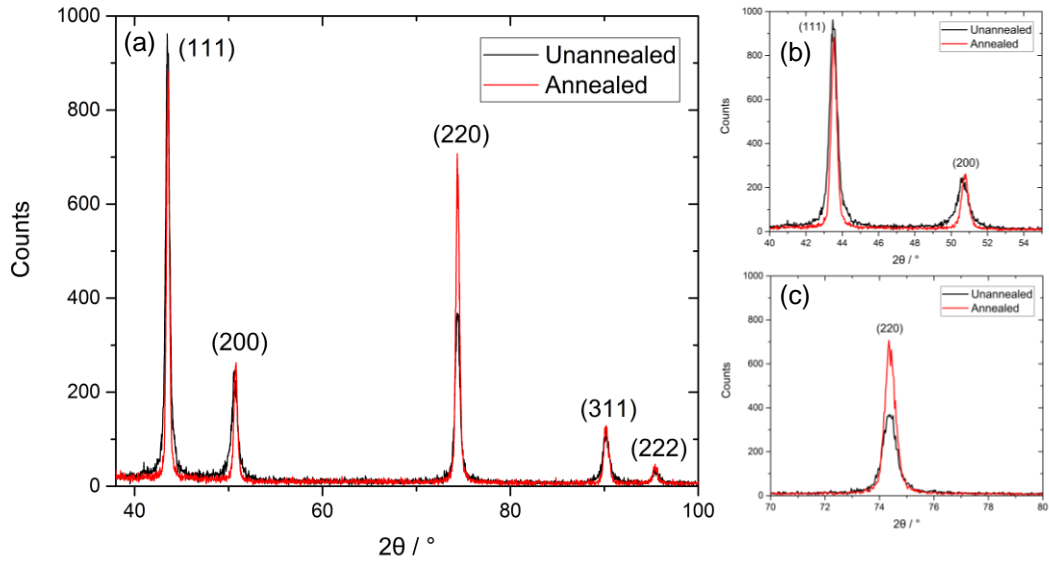
Figure 9: Grazing-angle XRD pattern for the same 120 nm Cu film, deposited directly to glass at 1 Å s^{-1}, before and after the aging process accelerated by 120°C annealing under N$_2$. (a) Sampled region, (b) expanded (111) and (200) peaks, (c) expanded (220) peak.

Figure 10 captures a key point of this discussion, which is discussed in more detail in later chapters: The electrode in Figure 7 exhibits only beneficial changes in sheet resistance over the time frame investigated, attributed to a reduction of strain in the metal film, which hides the detrimental effect of surface oxidation that inevitably occurs over the same time frame when the electrode is in air.

The higher reactivity of Cu, as opposed to the noble metals Ag or Au, results in the formation of a non-limiting native oxide layer composed largely of Cu$_2$O and CuO at the surface of the metal when exposed to ambient air.[36–38] When the electrode has been pre-annealed to accelerate the beneficial ageing process discussed above any increase in sheet resistance can be used to monitor the rate of surface oxide formation, since the mixed oxide has a conductivity many orders of magnitude below that of the metal. After 1408 hours in air the sheet resistance has increased by ≤ 5% above the minimum value

which corresponds to the loss of ~6 nm of metal to the formation of oxide. Assuming literature values for the densities of Cu and Cu_2O (the major oxide component) respectively (8.96 g cm^{-3}, 6.00 g cm^{-3}) the mixed oxide layer is estimated to be ~10 nm in thickness, too great for significant quantum mechanical tunneling of charge carries across.[39–41] Since both CuO and Cu_2O are direct band gap (1.6 and 2.3 eV respectively) *p*-type semiconductors however, it cannot be assumed that their presence at the surface of the Cu electrode will be detrimental to device performance.
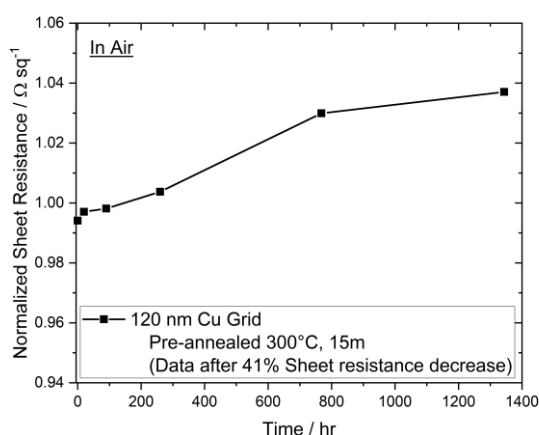
Figure 10: The evolution of the sheet resistance of a representative 120 nm thick Cu grid electrode pre-annealed (300°C, 15 minutes) under N_2 atmosphere before exposure to ambient air.

It is widely understood that roll-to-roll processing is necessary to achieve the potential of OPVs for widespread commercialisation,[6,7] and that this necessitates a highly flexible (typically plastic) substrate such as PET or PEN. Figure 11 shows that, when bent through a tight 4 mm radius of curvature, the sheet resistance of ITO films on PEN increases sharply due to cracking of the inherently brittle nature oxide layer. Conversely the resistance of a Cu grid supported on a PET film, fabricated using the same method as used for glass, does not change over the 100 bending cycle testing.
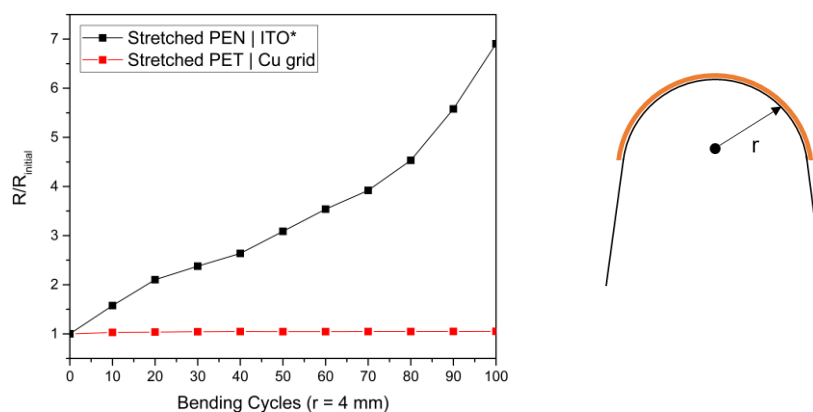
Figure 11: Normalised sheet resistance for ITO on PEN and a 40 nm Cu grid on PET as a function of the number of bends through a radius of curvature (r) of 4 mm.

One additional factor that is important for practical application is the strength of adhesion between the substrate and Cu grid. It is possible to improve the strength of adhesion so that the grid is resistant to ultra-sonic agitation in common solvents by functionalizing the glass or plastic substrate with a mixed molecular monolayer of (3-aminopropyl)trimethoxysilane (APTMS) and (3-mercaptopropyl)trimethoxysilane (MPTMS), immediately prior to metal deposition (Figure 12), although this was not necessary for OPV devices or flexibility testing.[34] These small molecule silanes bind strongly to incoming Cu atoms and the supporting substrate and enable the formation of robust, slab-like Cu films of low thickness.[34]
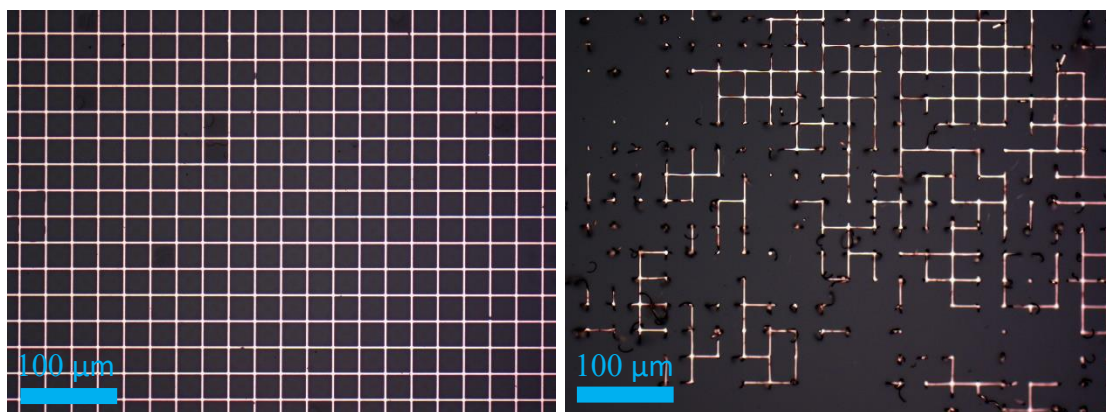
Figure 12: 120 nm Cu grid electrodes after 30 minutes ultra-sonication in deionised water on glass substrates with (left) and without (right) pre-treatment with an MPTMS & APTMS mixed molecular adhesive.

4.3.3 OPV device fabrication

To the author's knowledge a Haacke figure-of-merit of 0.046 (120 nm thick) and 0.119 (500 nm thick) are the highest reported for a metal-oxide free, non-embedded metal grid suitable for OPVs.[13] The very low sheet resistance, which is a factor of 4-5 times lower than ITO at 120 nm thickness, is particularly enabling for OPV module design because it allows for the width of individual cells to be increased beyond 1 cm, reducing scribe area without significant ohmic losses.[4]

To elucidate the effect of the HDT monolayer at the Cu surface on OPV device performance model OPVs were fabricated using a semi-transparent 9 nm Cu electrode patterned with an array of 2 µm circular apertures instead of a Cu grid: Figure 13. Narrow apertures were used as this eliminates the necessary complexity of the PEDOT:PSS layer; in this context the ZnO overlayer is of sufficient conductivity to collect charges from metal-free areas within the 2 µm diameter apertures. The thickness of the HDT monolayer is greater than the distance over which charge carriers can efficiently tunnel and so this insulating layer presents a barrier to charge extraction as can be seen in the current-voltage characteristic in Figure 13 by the 's'-shaped blue curve, which is associated with the accumulation of charges at one of the electrode interfaces in the device.[42,43]. However, with the HDT monolayer still in place, annealing the ZnO layer at 180°C instead of 120°C removes the barrier and increases the fill factor.

For OPV devices where a PEDOT:PSS interlayer was used, the Cu grids were briefly UV/O$_3$ treated to oxidize the HDT monolayer and then rinsed with acetic acid to remove oxidized Cu. This process was not essential in later PEDOT:PSS-free configurations but served to improve wetting between the substrate/grid and the PEDOT:PSS layer. It is possible the wetting of PEDOT:PSS could be improved by surfactant additives, and subsequently annealed at 180°C instead of 120°C, to avoid the UV/O$_3$ and acetic acid treatment however this was not investigated.
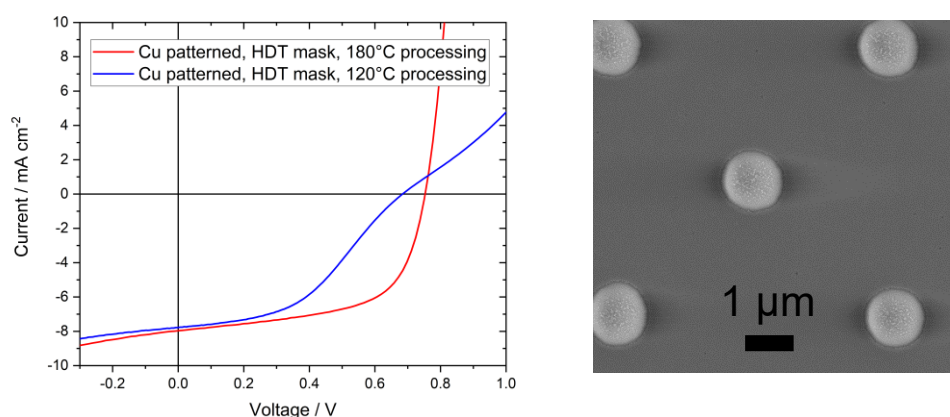
Figure 13: (Left) Representative device characteristics for two electrodes in model OPV devices based around a 9 nm Cu | ZnO electrode: Patterned with HDT mask still in place, 120°C ZnO anneal (Blue) and patterned with HDT mask still in place, 180°C ZnO anneal (Red). (Right) An example area imaged by SEM of the patterned 9 nm Cu film electrodes.

Given the insulating nature of the HDT layer the reduction in device series resistance is most likely explained by the disassociation of the thiol-Cu bond at 180°C and thermally induced disorder in the dense monolayer allowing the ZnO to get closer to the underlying Cu. This hypothesis is supported by the results of high resolution XPS analysis of a pristine Cu film with a μ-CP monolayer of HDT before and after heating at 180°C. The S2p region (Figure 14) features a doublet with peaks at 162.1 eV and 163.3 eV typical of a thiol bound to the metal surface: S 2p$_{3/2}$ and S 2p$_{1/2}$ with a 2:1 area ratio respectively and 1.2 eV splitting due to spin-orbit coupling.[44] After 15 minutes at 180°C in an inert atmosphere (to simulate the annealing process) the intensity of these peaks is reduced by

~75%, which shows that 180ºC is sufficient for the thiolate linkage to the metal to be broken.
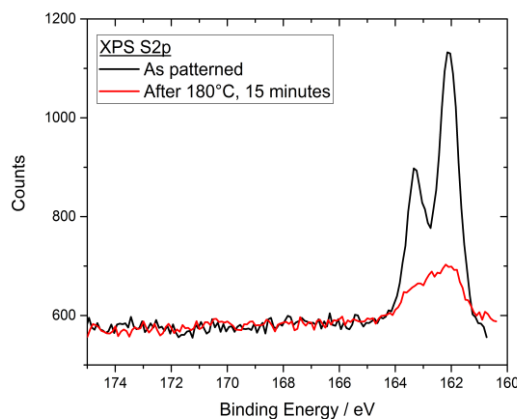
Figure 14: Overlaid XPS S2p spectra (charge referenced to adventitious C1s at 284.8 eV) of a pristine Cu metal surface after a patterned SAM was applied by intimate contact with an inked PDMS stamp (Black), and subsequently heated at 180°C for 15 minutes under an inert N_2 atmosphere (Red).

The absence of any peaks above 163.5 eV in Figure 14 evidences the absence of unbound thiol, such as a second bilayer SAM, or oxidized sulphur species present on the unheated film. There is also no evidence for the latter after heating which indicates that once the thiolate linkage with the surface is broken and the molecule leaves the surface, possibly as fragments. It is of further importance that the SAM is entirely bound to the surface by strong covalent Cu-S bonds as unbound thiols will likely be washed away by the etchant.

By comparison, Choi *et al.* found that for printed monolayers of 11-mercaptoundecanoic acid the minimum feature resolution was 5 μm, due to the lower quality packing of the printed monolayer on Cu.[45] Herein it has been demonstrated that ~1 μm resolution is achievable using HDT, with short contact times and dilute thiol ink solutions which demonstrates the benefits of using the simpler saturated hydrocarbon chain without end group functionalisation: This maximises order in the monolayer and increases the driving force for assembly due to the close packing and cohesive van der Waals interactions between parallel, adjacent, and saturated hydrocarbon chains. Having

reactive functionality on the end of the tail group can however a useful tool for improving the wetting characteristics of subsequent layers deposited from solution.[20]

The utility of these electrodes in OPV devices is demonstrated using the device architecture: Electrode | zinc oxide nanoparticles (ZnO) | PBDB-T/ITIC | MoO_3 | Al. In the first instance a small OPV device area typical of that reported in the literature was used; 6 mm^2. A Cu grid thickness of 40 nm was chosen because it has a sheet resistance of 15 Ω sq^{-1} which is comparable to that of the commercial ITO coated glass reference electrodes used in this study (Thin Film Devices Inc): Figure 15 (a), Table 1. Within error the open-circuit (V_{oc}) and fill-factor (FF) of OPV devices is comparable for devices using ITO and Cu grid electrodes, but the short-circuit current density (J_{sc}) is ~ 13% lower in the latter consistent with its lower far-field transparency: Figure 4 (b). However, an electrode with a sheet resistance of 15 Ω sq^{-1} is too high for practical application in OPVs as is evident when the cell area is increased to 60 mm^2 (Figure 15 (b), Table 1). Even for this modest increase in cell area the average fill-factor is reduced by 23%. A key advantage of transparent electrodes based on an opaque metal grid is that it is possible to reduce the sheet resistance without reducing the transparency simply by increasing the thickness (height) of the metal grid lines. Increasing the Cu grid thickness by a factor of 3 reduces the sheet resistance from 15 to 3.2 Ω sq^{-1}, whilst reducing the transparency by only 3%. When the area of OPV devices using the 120 nm thick Cu grid electrode is increased from 6 to 60 mm^2 there is no significant change in the device performance parameters: Table 1.
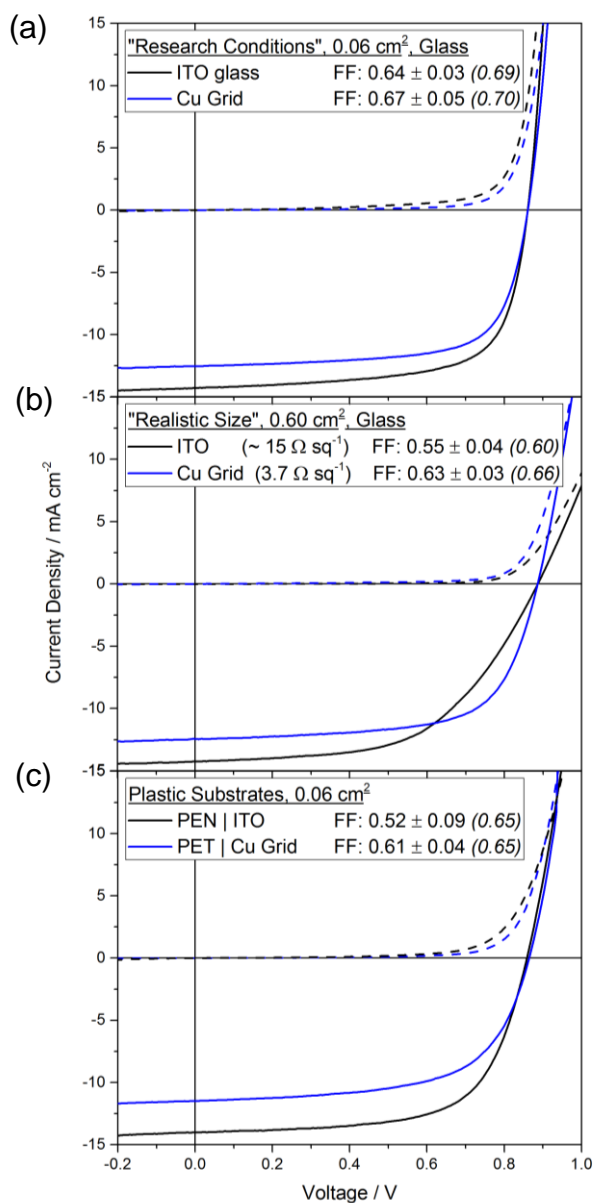
Figure 15: Champion device characteristics for ITO and Cu grid devices in the structure: Electrode (ITO or Cu Grid & PEDOT:PSS) | ZnO | PBDB-T/ITIC | MoO_3 | Al. The active areas are (a) 0.06 cm^2, (b) 0.60 cm^2 and (c) 0.06 cm^2 (on plastic)

Table 1: A series of devices with the structure Electrode | Al-doped ZnO 25 nm | PBDB-T / ITIC | MoO_3 6 nm | Al where both electrode design and active area are varied. Data is presented as the mean of 6 - 18 devices ± Standard Deviation (Champion).

Device Area	Electrode	J_{sc} / mA cm^{-2}	V_{oc} / V	FF	PCE / %
Small (0.06 cm^2)	ITO glass (15 Ω sq^{-1})	14.10 ± 0.68 (*14.27*)	0.84 ± 0.00 (*0.86*)	0.64 ± 0.03 (*0.69*)	7.54 ± 0.37 (*8.48*)
Large (0.60 cm^2)	ITO glass (15 Ω sq^{-1})	14.53 ± 0.24 (14.67)	0.88 ± 0.01 (0.89)	0.55 ± 0.04 (0.60)	7.12 ± 0.64 (7.86)
Small (0.06 cm^2)	40 nm Cu Grid (15.1 Ω sq^{-1})	PEDOT:PSS	12.32 ± 0.43 (*12.53*)	0.86 ± 0.01 (*0.86*)	0.67 ± 0.04 (*0.70*)	7.03 ± 0.61 (*7.55*)
Large (0.60 cm^2)	40 nm Cu Grid (15.1 Ω sq^{-1})	PEDOT:PSS	10.90 ± 2.01 (*11.91*)	0.87 ± 0.01 (*0.87*)	0.51 ± 0.06 (*0.59*)	4.82 ± 1.08 (*6.14*)
Small (0.06 cm^2)	120 nm Cu Grid (3.2 Ω sq^{-1})	PEDOT:PSS	11.31 ± 0.56 (*11.80*)	0.84 ± 0.02 (*0.86*)	0.63 ± 0.07 (*0.70*)	6.03 ± 0.79 (*7.08*)
Large (0.60 cm^2)	120 nm Cu Grid (3.2 Ω sq^{-1})	PEDOT:PSS	11.63 ± 0.45 (*12.48*)	0.88 ± 0.01 (*0.90*)	0.63 ± 0.03 (*0.66*)	6.49 ± 0.49 (*7.26*)
Small (0.06 cm^2)	Highly Flexible 120 nm Cu Grid (PET substrate)	PEDOT:PSS	11.29 ± 0.30 (*11.67*)	0.85 ± 0.03 (*0.87*)	0.61 ± 0.04 (*0.65*)	5.83 ± 0.55 (*6.61*)
Small (0.06 cm^2)	10 nm PEDOT:PSS	0.07 ± 0.03 (*0.10*)	0.69 ± 0.20 (*0.87*)	0.25 ± 0.00 (*0.25*)	0.01 ± 0.01 (*0.02*)

Small (0.06 cm^2)	120 nm Cu Grid (3.2 Ω sq^{-1}) **without** PEDOT:PSS interlayer	10.91 ± 0.86 (*11.71*)	0.86 ± 0.01 (*0.86*)	0.54 ± 0.03 (*0.57*)	5.03 ± 0.55 (*5.74*)
Small (0.06 cm^2)	Flexible ITO (PEN substrate)	13.63 ± 0.53 (*14.01*)	0.77 ± 0.12 (*0.86*)	0.52 ± 0.09 (*0.65*)	5.61 ± 1.82 (*7.84*)

Importantly, translating the Cu grid electrode to flexible PET substrates has no adverse effect on electrode or OPV device performance: (6.03 ± 0.79 % [7.08% champion, 120 nm grid, glass], 5.83 ± 0.55 % [6.61% champion, 120 nm grid, PET]), and unlike ITO films on plastic substrates, these Cu grid structures do not deteriorate when repeatedly bent through a small radius of curvature: Figure 11.

Since the design of grid electrodes is based on opaque metal lines, in principle the metal thickness can be increased from 40 nm, to 120 or 500 nm to reduce the resistance without reducing the transparency: Figure 4 (b). The small drop in corresponding transparencies (83, 80, 77%) is attributed to slight widening of the lines and roughening at the edges of the 500 nm grid lines. The sheet resistance is reduced contrastingly from 15.1 Ω sq^{-1} (similar to ITO on glass) to 3.4 and 0.6 Ω sq^{-1} for 40, 120 and 500 nm respectively. This sheet resistance of < 1 Ω sq^{-1} performs even at the larger area scale devices used here (0.60 cm^2) similarly to the 120 nm Cu grid (Figure 16, Champion PCE: 7.26% at 120 nm, 6.58% at 500 nm), the most significant difference being the short circuit current which is attributable to the lower transparency of the 500 nm grid electrode (77 *vs* 80%). This reduction in sheet resistance is of commercial importance as a sheet resistance of < 1 Ω sq^{-1} (which is greater than a factor of ten lower than that of ITO) enables cell dimensions >> 1 cm to be used. Rowell *et al.* demonstrate that for a model laboratory cell a sheet resistance reduction of an order of magnitude compared to ITO will produce 60% more power in an OPV module with a cell width of 2 cm than can be achieved with a conventional ITO transparent electrode.[4] This allows for transformative new solar cell designs, particularly for low-power applications, where bus-bar free designs become efficient and the unit could be powered by a single cell.
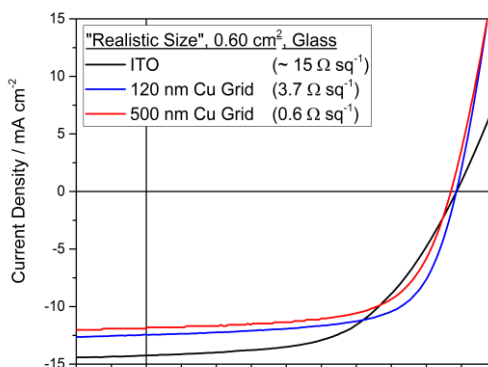
Figure 16: Champion device characteristics for large area (0.60 cm^2) devices of the structure: Electrode (ITO or Cu Grid & PEDOT:PSS) | ZnO | PBDB-T/ITIC | MoO$_3$ | Al. Where the Cu grid is 120 nm (Blue) or 500 nm thick metal (Red).

One factor that has been reported to be problematic for electrodes based on an etched metal film for applications in OPVs is the height of the step at the edge of metallized regions, which results in non-uniform thickness of the organic semiconductor overlayers and current leakage across the device: For example, Lee *et al.* have shown that for a random-metal wire electrode based on an etched metal film, OPV device performance and yield dramatically deteriorates when the metal thickness is increased much beyond 15 nm.[10] Remarkably, using the approach reported herein Cu grids with a grid height of 120 nm achieve comparable performance and yield to that of OPV devices fabricated on planar ITO reference electrodes, even when the organic photoactive layer thickness is comparable to the grid height: 100 nm *vs* 120 nm (Table 2), which indicates that the PEDOT:PSS and ZnO layers planarize the electrode, or that all of the overlayers conformally coat the Cu grid so there is no significant variation in the thickness of the organic semiconductor layers.

Table 2: A series of devices comparing ITO glass against a thick (110 nm) Cu grid electrode for a variety of bulk hetrojunction thicknesses (100, 300 and 400 nm). Data is presented as the mean of 6 - 18 devices ± Standard Deviation (Champion). Glass | 110 nm Cu Grid electrode | PEDOT:PSS 10 nm | ZnO 25 nm | PCE-10 / $PC_{70}BM$ | MoO_3 6 nm | Al 150 nm.

Heterojunction Thickness	Electrode	J_{sc} / mA cm^{-2}	V_{oc} / V	FF	PCE / %
100 nm	110 nm Cu Grid | PEDOT:PSS	12.62 ± 0.49 (*12.74*)	0.70 ± 0.04 (*0.73*)	0.60 ± 0.07 (*0.67*)	5.27 ± 0.81 (*6.17*)
	ITO Glass	15.37 ± 0.85 (*16.11*)	0.71 ± 0.04 (*0.73*)	0.57 ± 0.08 (*0.61*)	6.22 ± 1.19 (*7.22*)
300 nm	110 nm Cu Grid | PEDOT:PSS	13.37 ± 1.11 (*15.38*)	0.71 ± 0.01 (*0.71*)	0.49 ± 0.02 (*0.50*)	4.68 ± 0.40 (*5.41*)
	ITO Glass	16.30 ± 1.88 (*17.84*)	0.66 ± 0.13 (*0.72*)	0.46 ± 0.05 (*0.50*)	5.13 ± 1.57 (*6.36*)
400 nm	110 nm Cu Grid | PEDOT:PSS	8.81 ± 3.11 (*11.42*)	0.67 ± 0.06 (*0.70*)	0.37 ± 0.03 (*0.38*)	2.26 ± 0.97 (*3.02*)
	ITO Glass	12.03 ± 0.86 (*13.08*)	0.71 ± 0.01 (*0.70*)	0.40 ± 0.01 (*0.39*)	3.36 ± 0.21 (*3.58*)

The extent to which the PEDOT:PSS and ZnO layers smooth the grid line edges was elucidated using atomic force microscopy (AFM, Figure 17) from which it is evident that the roughness is reduced by < 20% with each layer relatively conformally coating the underlying grid.
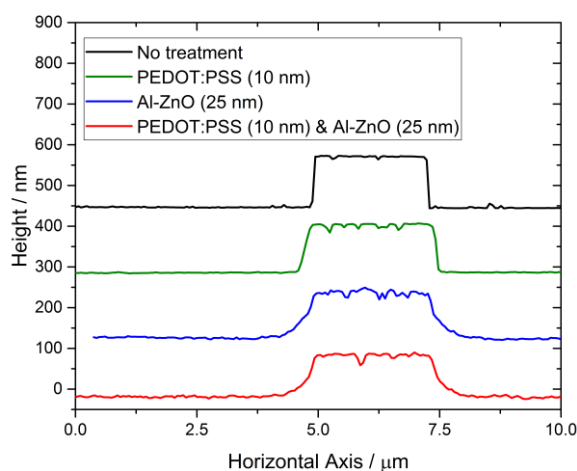
Figure 17: Profiles of an example Cu grid line by AFM without overlayers (black), with PEDOT:PSS (green), Al-doped ZnO 25 nm (blue) and PEDOT:PSS/ZnO (red).

In both Figure 17 (red) and the cross-sectional SEM of a complete OPV device shown in Figure 18 there is evidence of an accumulation, or build-up, of the interfacial PEDOT:PSS and ZnO layers which smooth the abrupt Cu grid edges. This explains why a 500 nm thick Cu grid electrode fabricated by μCP can be used in an OPV device without undermining the diode integrity. Notably it is evident from Figure 17 that this smoothing of the Cu grid is most pronounced for structures utilizing ZnO overlayers (without or without PEDOT:PSS), while PEDOT:PSS has a lesser effect.
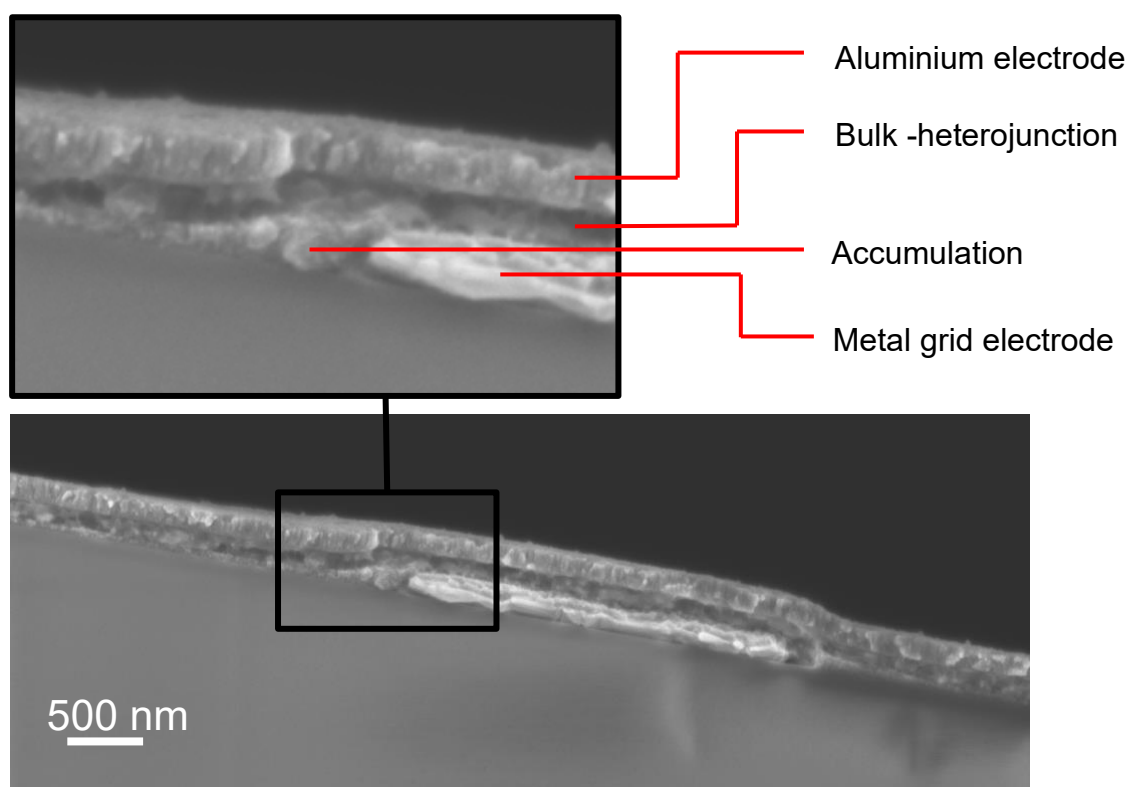
Figure 18: Cross-sectional SEM image showing a metal grid line and expanded section at the ridge between substrate (lower) and metal grid line (bright, centre). The labelled accumulation of interlayers as described in-text smooths the sharp step at the grid edges. Further examples are given in Appendix, Figure A3.

It is evident from the AFM images of the top of an OPV device shown in Figure 19 that the active layer also coats the Cu grid/PEDOT:PSS/ZnO with a uniform thickness, since the morphology of the top of the OPV device is the same as that of the Cu grid/PEDOT:PSS/ZnO and it is reasonable to expect that the evaporated Al electrode is of uniform thickness. This result shows that whether or not the grid line thickness can be tolerated in an OPV device depends on not only the metal thickness, but on a more complex morphological factor including edge gradient and wettability. This finding is important because it shows that it is not necessary to embed the Cu grid into the underlying substrate or to use using a very thick charge transfer layer for utility in OPVs.
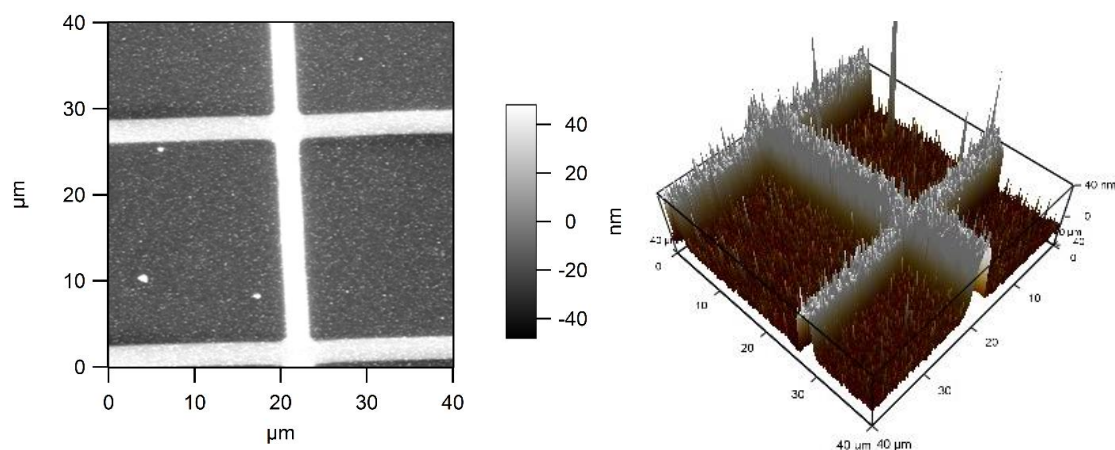
Figure 19: (Left) AFM topographic image of the surface of an OPV device with the structure glass | 110 nm Cu Grid electrode | PEDOT:PSS 10 nm | ZnO 25 nm | PCE-10 / PC$_{70}$BM | MoO$_3$ 6 nm | Al 150 nm. (Right) 3D depiction of the same image.

In order to understand the impact of a mixed Cu-oxide layer formed at the interface between the Cu grid and PEDOT:PSS interlayer during long-term operation of an OPV device, an experiment to accelerate the aging of grid electrodes prior to integration into devices was performed. Firstly the stability of the Cu/PEDOT:PSS grid in ambient air was measured together with that of a bare Cu grid: Figure 20. An extremely thin PEDOT:PSS layer of ~10 nm was applied to the Cu grid, equal to that in devices, and the samples held at 120°C in air for 1400 minutes with the resistance across the electrode measured periodically. It is clear from Figure 20 the PEDOT:PSS overlayer neither protects the Cu from degradation or accelerates the rate of oxide formation on the metal, since there is an insignificant difference between the evolution of the sheet resistances with and without a PEDOT:PSS layer. This result is consistent with the finding of Georgiou *et al.* who reported that the conductivity changes on printed Cu-nanoparticle metal grids coated with PEDOT:PSS and heated in air were similar to when bare Cu was heated in air.[23] The rate of conductivity decrease in that work was far more extreme, likely due to the nano-particulate nature of the Cu. Based on the change in resistance the oxide thicknesses in Figure 20 are estimated to be 16 nm after 240 minutes and 42 nm after 1400 minutes. For comparison, under ambient conditions Figure 10 estimates the formation of only a ~10 nm overlayer after 2 months of exposure to ambient air.

131
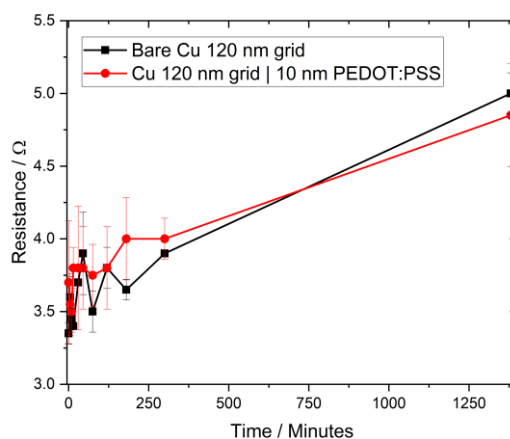
Figure 20: The resistance over time across a 8×8 mm area of 4 bare Cu 120 nm grids and 4 Cu 120 nm grids coated with PEDOT:PSS (PH1000 formulation) whilst heated to 120°C in air. Error bars indicate the standard deviation.

In OPV devices, the oxide layer cannot be removed, and so charges must be transported across the oxide layer to reach the underlying metal. 120 nm Cu grid electrodes were therefore in Figure 21 (Table 3) processed identically by annealing the PEDOT:PSS interlayer in air for 15 minutes (Reference), 240 minutes and 1400 minutes at 120°C before device fabrication to assess the tolerance of device performance to the growth of a Cu oxide layer at the Cu/PEDOT:PSS interface. Notably even in the reference device structure a significant oxide layer exists at the Cu/PEDOT:PSS interface, since initial oxidation of pristine metal is extremely rapid and reference devices are annealed at 120°C for 15 minutes in air during necessary processing of the PEDOT:PSS.
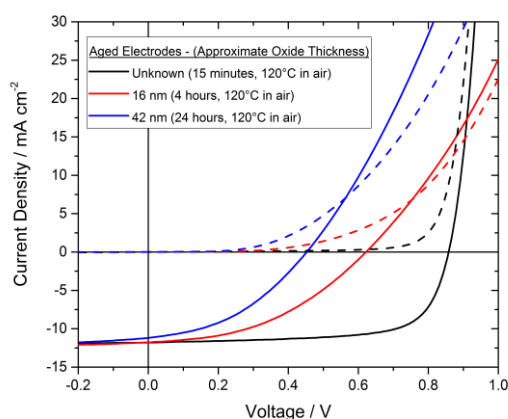
Figure 21: Champion device characteristics of the structure: Oxidised Grid | PEDOT:PSS | ZnO | PBDB-T/ITIC | MoO$_3$ | Al. The 120 nm Cu grids pre-coated with PEDOT:PSS have been annealed in air for 15 minutes (Reference), 4 hours (estimated 16 nm oxide) and 24 hours (42 nm). Solid lines show the IV characteristics under 1 sun illumination while dashed lines show the respective dark current.

Table 3: Tabulated device characteristics of the structure: Oxidised Grid | PEDOT:PSS | ZnO | PBDB-T/ITIC | MoO$_3$ | Al. The 120 nm Cu grids pre-coated with PEDOT:PSS have been annealed in air for 15 minutes (Reference), 4 hours (estimated 16 nm oxide) and 24 hours (42 nm). Data is presented as the mean of 6 - 18 devices ± Standard Deviation (Champion).

Approximate oxide thickness / nm	J_{sc} / mA cm^{-2}	V_{oc} / V	FF	PCE / %
< 10 nm	11.31 ± 0.56 (11.80)	0.84 ± 0.01 (0.86)	0.63 ± 0.07 (0.70)	6.03 ± 0.79 (7.08)
16	10.47 ± 0.88 (11.77)	0.52 ± 0.08 (0.62)	0.42 ± 0.05 (0.43)	2.37 ± 0.59 (3.14)
42	9.57 ± 1.11 (11.19)	0.37 ± 0.04 (0.45)	0.39 ± 0.01 (0.41)	1.38 ± 0.32 (2.06)

It is evident from the data in Figure 21 and Table 3 that in the context of the model devices, Oxidized Grid | PEDOT:PSS | ZnO | PBDB-T/ITIC | MoO$_3$ | Al, J$_{sc}$ remains relatively stable with increasing oxide thickness, but the device series resistance increases degrading the fill factor. This increase in series resistance can be attributed to the low mobility of electrons in CuO and Cu$_2$O and/or an energetic barrier at either oxide interface caused by misalignment of the electronic bands. It is also possible that the series resistance has increased due to degradation of the PEDOT:PSS after heating in air for the extended period needed, although the complete degradation of the PEDOT:PSS would be expected to degrade the short circuit current in Figure 21 which has not occurred.[46,47] Notably, because the reference structure is annealed in air for 15 minutes to dry the PEDOT:PSS overlayer, it is expected to also have a thin oxide layer however the fill factor (0.63 ± 0.07 (0.70 champion)) is similar to that on planar ITO electrodes (0.64 ± 0.03 (0.69 champion)) and as such it is likely that either the low thickness (< 5 nm) enables direct tunnelling across this layer or filaments of Cu along the CuO$_x$ grain boundaries connect PEDOT:PSS to the Cu film.[40,41]

It is clear from the device data in Figure 21 that the thicker mixed copper oxide layers do not completely block the flow of charges across the device, but forms a resistive layer, degrading the fill factor. This can be understood in terms of the energy level diagram, shown in Figure 22. The two dominant oxide products of Cu are CuO and Cu$_2$O and are p-type semiconductors,[36,38,40,41,48] although it is reasonable to ignore the CuO layer because it has been shown to form a distinct phase < 1 nm thick upon air oxidation.[36] This low thickness enables the quantum mechanical tunnelling of charge carriers directly across the CuO layer.[39,41] In this context PEDOT:PSS (PH1000 formula) is categorized as a synthetic metal, and behaves as a metal: The high density of acceptor (p-type) dopant orbitals at the edge of the valence band allow efficient transport of holes. The Fermi level of air-oxidized Cu$_2$O is assumed to lie close to the valence band (< 0.1 eV) due to the heavy p-type doping by vacancies and defects in the air-oxidized semiconductor. The heavy doping of the Cu$_2$O layer narrows the interfacial depletion regions (w_1 and w_2, Figure 22) such that charges can tunnel across.
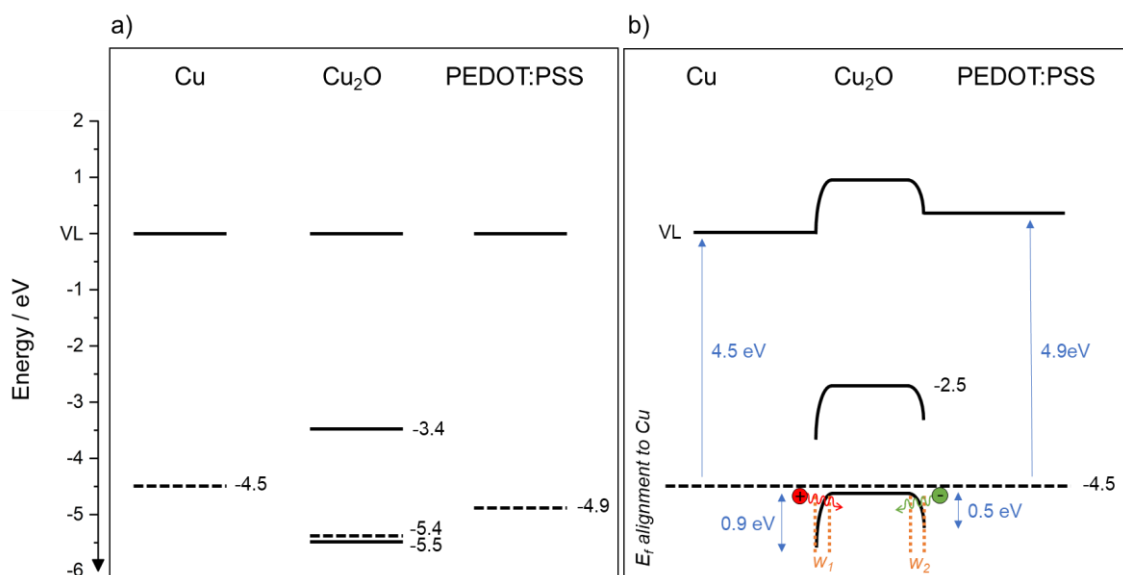
Figure 22: (a) Depiction of the Fermi levels (E_f) of isolated Cu, Cu_2O and PEDOT:PSS (PH1000) and band edges (VB and CB) of Cu_2O.[49] (b) The resultant band structure once the three materials are interfaced.

4.3.4   Exploration of grid design

Until this point in this chapter, a grid design with a pitch of 27.3 µm and line-width 1.4 µm was used to demonstrate the potential of microcontact printed grids with line widths an order of magnitude below that of typical grid electrodes reported in the literature. In this section the grid design is modified to increase the transparency at the expense of sheet resistance because device performance is limited by the J_{sc}. To investigate the implications for OPV devices of increasing the transparency of the electrode in this manner, grid electrodes were produced with a range of different grid-pitches, as shown in Figure 23.

All images, w = 1.4 µm

Pitch = 27.3 µm   Pitch = 40 µm   Pitch = 50 µm

200 µm   200 µm   200 µm

Pitch = 75 µm   Pitch = 150 µm   Pitch (x) = 40 µm
Pitch (y) = 500 µm

200 µm   200 µm   200 µm
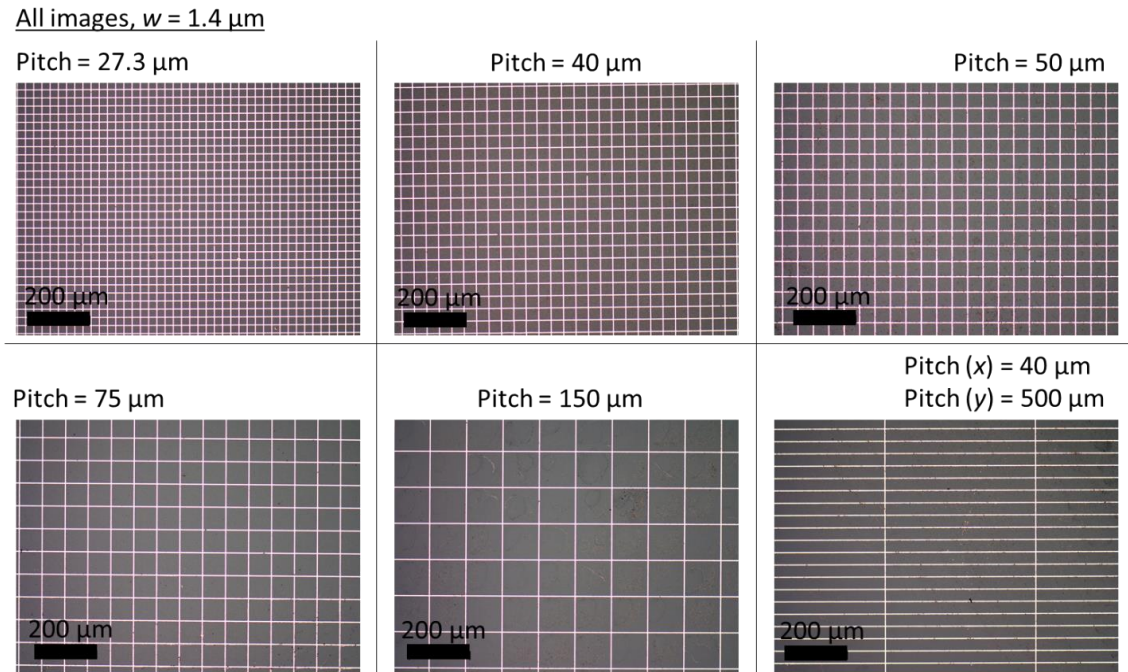
Figure 23: The range of different pitches investigated in this section, with a fixed line width of 1.4 µm with respect to the original master. The grid design with pitch 27.3 µm (Top-Left) depicts the most common design used thus far in this chapter.

Increasing the pitch of the grid from 27.3 µm to 150 µm increases transparency from 74.3% (in this set) to 92.1% at the cost of a 7 Ω sq^{-1} rise in sheet resistance, consistent with the reduction in metal coverage (Figure 24, Table 4); although the sheet resistance is still below 10 Ω sq^{-1}. Additionally, since µ-CP can print designs of any shape and pattern, it was postulated that for applications in OPVs the removal of superfluous lines perpendicular to the current flow will improve transparency without affecting the series resistance of an OPV device. To compare to the grid design with a pitch of 40 µm, a non-symmetrical Cu-grid was produced with a pitch of 40 µm in the x-direction and 500 µm in the y-direction (Figure 23); this resulted in an increase in transparency from 77.9% to 87.1%.
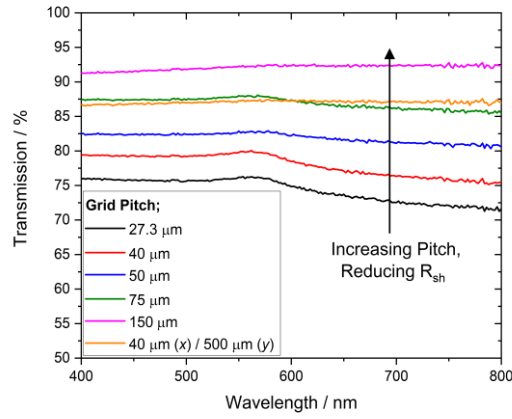
Figure 24: Transmission spectra with the air-substrate interface subtracted for Cu grids with different pitches/designs produced using the same conditions.

Table 4: Tabulated parameters for Cu grids with varying pitch, where the metal thickness is 120 nm.

Line Width / µm	Pitch / µm	Sheet Resistance / Ω sq^{-1}	Average Transparency / %
1.4	27.3	2.4 ± 0.1	74.3
1.4	40	3.7 ± 0.3	77.9
1.4	50	3.9 ± 0.1	81.9
1.4	75	5.8 ± 1.4	86.9
1.4	150	9.6 ± 1.3	92.1
1.4	40 (*x*-direction) / 500 (*y*)	N/A*	87.1

*Sheet resistance is not reflective of the true conductivity of an un-symmetrical film.

The FoM (high transparency and conductivity) for grid electrodes, as elucidated earlier in this thesis, does not translate directly into more efficient OPV devices: The contribution of the current collecting interlayer (typically PEDOT:PSS) to the series resistance rises exponentially with the pitch, which is often overlooked in the literature.[5] To elucidate this relationship in this model system, a series of OPV devices were fabricated on Cu-grids with varying pitch; Figure 25, Table 5. The thickness of the PEDOT:PSS interlayer was kept constant at ~ 10 nm to avoid parasitic absorption: As the macro-scale sheet resistances of the Cu-grids ($2.4 – 9.6$ Ω sq^{-1}) are all below that of the ITO glass reference, the fill-factor is expected to be representative of the contribution of the current-collecting PEDOT:PSS interlayer to the series resistance. The device fill-factor should be compared to the reference ITO device (0.59 ± 0.09 (*0.63*)).
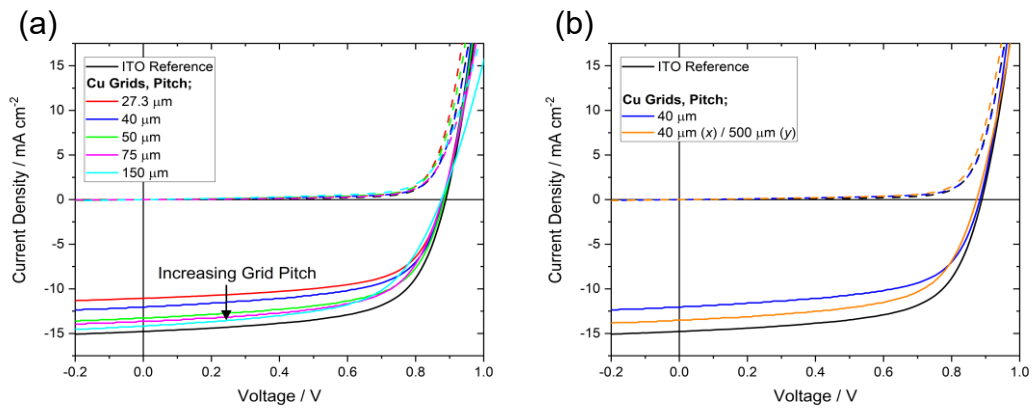
Figure 25: Representative OPV device data for a range of Cu grid electrodes with the structure: Grid | PEDOT:PSS | ZnO | PBDB-T/ITIC | MoO$_3$ | Al. (a) Varying symmetrical pitch. (b) Varying pitch along the perpendicular axis.

Table 5: Tabulated OPV device data for a range of Cu grid electrodes with varying pitch and a fixed line width of 1.4 µm with respect to the original master. Grid | PEDOT:PSS | ZnO | PBDB-T/ITIC | MoO_3 | Al. Data is presented as the mean of 6 - 18 devices ± Standard Deviation (Champion).

Grid Pitch / µm	Current Density / mA cm^{-2}	Voltage / V	Fill Factor (FF)	Efficiency (η) / %
ITO	13.5 ± 2.1 (14.8)	0.83 ± 0.13 (0.88)	0.59 ± 0.09 (0.63)	6.7 ± 2.1 (8.3)
27.3	9.4 ± 1.2 (11.1)	0.85 ± 0.06 (0.89)	0.58 ± 0.06 (0.63)	4.6 ± 1.0 (6.2)
40	10.3 ± 1.4 (12.0)	0.87 ± 0.02 (0.88)	0.58 ± 0.04 (0.62)	5.2 ± 1.0 (6.5)
50	10.4 ± 2.1 (13.3)	0.83 ± 0.11 (0.87)	0.56 ± 0.09 (0.62)	4.9 ± 1.7 (7.2)
75	12.2 ± 1.5 (13.7)	0.86 ± 0.02 (0.87)	0.56 ± 0.05 (0.62)	5.9 ± 0.9 (7.3)
150	12.3 ± 2.3 (14.2)	0.87 ± 0.02 (0.89)	0.57 ± 0.02 (0.60)	6.1 ± 1.3 (7.5)
40 (x) / 500 (y)	11.6 ± 1.1 (13.5)	0.87 ± 0.01 (0.89)	0.62 ± 0.03 (0.61)	6.3 ± 0.8 (7.4)

Although the 10 nm PEDOT:PSS interlayer is of constant resistivity the device fill-factor fluctuates within the associated error with increasing pitch from 27.3 to 75 µm, and closely matches that of the ITO device. For the device with 150 µm pitch however the fill factor is slightly reduced which is supported by the visible increase in series resistance in Figure 25 (a). Within the current system therefore, the pitch can be increased from 27.3 to 75 µm without consequence; this should be optimized for each structure. As anticipated the device photocurrent is directly proportional to the pitch of the grid electrode; the peak value increases incrementally to reach 96% of that of ITO with a 150 µm pitch Cu-grid electrode. The subsequent increase in efficiency from 4.6 ± 1.0 to 6.1 ± 1.3 % is an

important result to highlight the potential application of Cu-grids produced by µ-CP to high-performance OPVs, while maintaining the advantages of low-cost materials and flexibility.

Figure 25 (b) shows a comparison of the champion device performance for model OPV devices based upon an ITO electrode (Black), a symmetrical Cu-grid with pitch 40 µm (Blue) and an unsymmetrical Cu-grid with pitches 40 (x) and 500 (y) µm (Yellow, Figure 23). The reduction in metal coverage with the removal of superfluous grids lines perpendicular to the current flow (y) results in a 12.8% absolute increase in transparency and is reflected in the increase in device photocurrent from 10.3 ± 1.4 to 11.6 ± 1.1 mA cm^{-2}. It is of key importance that as the effective conductivity remains equal, the series resistance of the Cu-based devices in Figure 25 (b) are equivalent. This process is unique to grid electrodes and cannot be replicated with planar or random nanowire electrodes, and results in the highest efficiency Cu-grid device of this comparison: 6.3 ± 0.8 %.

4.4   Conclusion

In summary the development of a high-performance transparent copper grid electrode on glass and plastic substrates has been described and its application demonstrated in solution processed OPVs. Unlike other methods for the fabrication of grid electrodes reported in the literature the process does not involve complex metal mesh transfer, the need for embedding the grid within the supporting substrate, photolithographic or electrochemical deposition steps. Copper is the metal of choice because it is 1% of the cost of silver with comparable electrical conductivity. This approach to electrode fabrication is potentially highly sustainable because: (i) it can be performed in ambient air; (ii) it uses tiny quantities of resist; (ii) ammonium persulfate is a low toxicity etchant which can be recycled. This approach to electrode fabrication is much faster than conventional lithography, taking < 2 seconds to print the resist layer and tens of seconds to etch the film. A key advantage of this fabrication approach over printed metal grid electrodes is that the line width is > 20 times narrower than can be achieved which consequently means that a smaller spacing between grid lines is possible; important for efficient charge collection in OPVs. Given that roll-to-roll printing of the thiol monolayer is known to be possible, this study shows that this approach is viable for the fabrication of transparent electrodes for OPVs.

4.5 Future Work

4.5.1 Constant illumination stability testing

It is commonly believed that PEDOT:PSS negatively impacts the stability of OPV devices: For example, Norrman *et al.* report that the major cause of OPV degradation was the interface between a PEDOT:PSS hole transport layer and the organic active layer.[50] To understand the influence of the highly-conductive PEDOT:PSS (PH1000) interface with Cu, and compare to the established ITO glass electrode, three electrode structures were evaluated under constant 1 sun illumination in OPV devices with the following structure: Electrode | ZnO | PBDB-T/ITIC | MoO$_3$ | Al (Figure 26). In all three structures J_{sc} shows a steady decline to an extrapolated T_{80} (80% of initial value) of ~1400 minutes (23 hours). This trend is typical of degradation of the thin polymeric light harvesting donor:acceptor blend in OPVs under constant illumination, which can also affect FF and V_{oc}. The photostability of the bulk heterojunction is not only sensitive to the donor and acceptor materials,[51,52] but also the presence of DIO additive,[53] UV-irradiance,[54] and other factors. Degradation processes associated with the electrodes and the interfaces with the photoactive layers cannot be separated from this degradation and as such comparisons must be drawn with this in mind. The preliminary data in Figure 26 shows that the Cu grid electrode devices without PEDOT:PSS interlayer (Red), although of lower initial efficiency (5.03 ± 0.55% (Champion 5.74%)), were of far higher stability than both the Cu/PEDOT:PSS and ITO electrode structures. This sets the stage for the future development of highly efficient PEDOT:PSS-free Cu grid OPV devices.
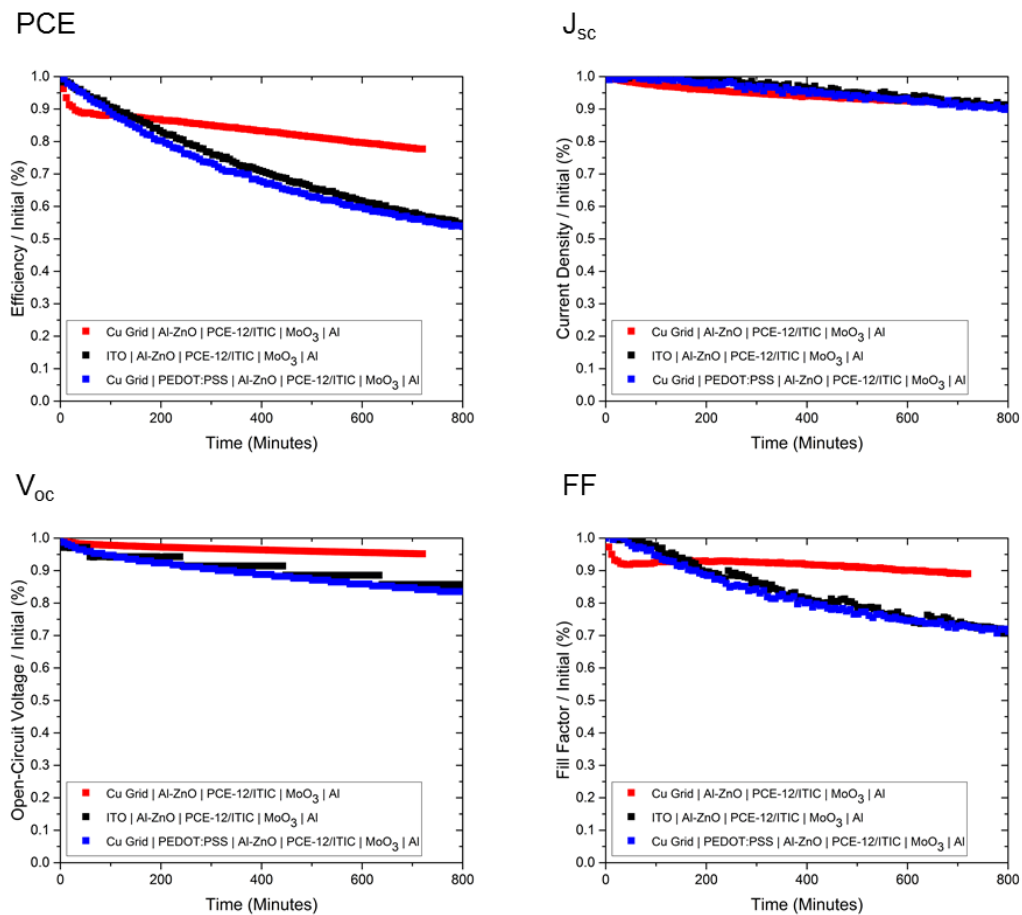
Figure 26: Normalised PCE, J_{sc}, V_{oc} & FF constant illumination study at 1 sun intensity for three device structures: Electrode (120 nm Cu grid or ITO) | Optional PEDOT:PSS | ZnO | PBDB-T/ITIC | MoO_3 | Al. Additionally, an 8 nm planar Cu electrode is compared in Appendix, Figure A4.

4.5.2   PEDOT:PSS-free metal grid OPVs

Typically, grid-based electrodes are reported in the literature in combination with a high-conductivity formation PEDOT:PSS interlayer of 50-250 nm thickness. As discussed, due to the low conductivity of organic semiconductors the gaps between gridlines as shown in Figure 6 must be spanned with a conducting layer such as PEDOT:PSS (PH1000) to ensure efficient charge extraction to the metallic grid lines for OPVs. Using the microcontact fabrication route line-widths less than one third that previously demonstrated on Ag are achieved, which is > 20 times narrower than is possible using conventional metal printing methods.[5,20] The main advantage of such thin metal lines is that, for the same metal surface coverage (and so transparency of the electrode) the grid

lines can be much closer together. The design used throughout the experiments in this chapter to this point are produced from a chromium photolithographic mask with 1.4 µm lines and a pitch (repeating distance) of 27.3 µm.

To understand the limits of such a system, and progress to PEDOT:PSS-free metal grids, this design utilized to date was repeated in small area cells (6 mm^2) to compare the nominal efficiency with and without PEDOT:PSS (Figure 27 (a)). The PCE of these PEDOT:PSS-free devices, 3.21 ± 0.50% (Champion 3.78%) is ~50% of that with the PEDOT:PSS interlayer, 6.47 ± 1.20% (Champion 7.56%). This reliance on the interlayer is attributed to the significant series resistance added when charges must travel from the metal-free regions laterally along the commercial ZnO nanoparticle layer ('ZnO-nps', Sigma Aldrich, Aluminum-doped zinc oxide ink for spin coating/slot-die coating), supported by the gradient after the 'knee' in Figure 27 (a): Blue.
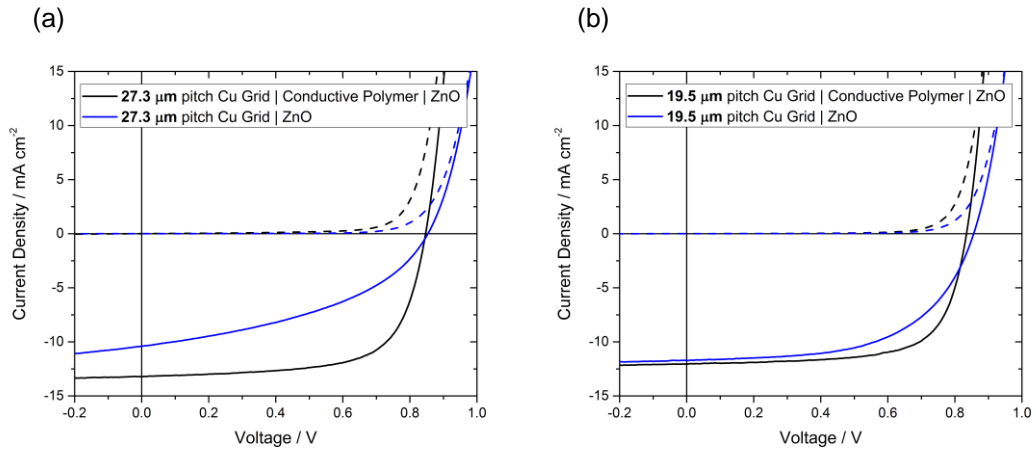
Figure 27: Champion device performance for the structure Cu Grid (10% metal coverage with respect to the original pattern) | Optional PEDOT:PSS | Commercial ZnO-nanoparticles | PBDB-T/ITIC | MoO$_3$ | Al. Where the Cu grid features (a) 1.4 µm lines, 27.3 µm pitch. (b) 1 µm lines, 19.5 µm pitch. (Blue lines) with PEDOT:PSS. (Black lines) PEDOT:PSS-free.

Table 6: Tabulated OPV device performance for the structure Cu Grid (10% metal coverage with respect to the original pattern) | Optional PEDOT:PSS | Commercial ZnO-nanoparticles | PBDB-T/ITIC | MoO_3 | Al. Where the Cu grid features 1.4 μm lines, 27.3 μm pitch or 1 μm lines, 19.5 μm pitch. Data is presented as the mean of 6 - 18 devices ± Standard Deviation (Champion).

Cu Grid Pitch	Interlayers	J_{sc} / mA cm^{-2}	V_{oc} / V	FF	PCE / %
27.3 μm	PEDOT:PSS | ZnO-nps	12.61 ± 0.87 (13.21)	0.84 ± 0.02 (0.85)	0.61 ± 0.09 (0.68)	6.47 ± 1.20 (7.56)
27.3 μm	ZnO-nps	8.99 ± 1.36 (10.41)	0.85 ± 0.01 (0.85)	0.42 ± 0.01 (0.43)	3.21 ± 0.50 (3.78)
19.5 μm	PEDOT:PSS | ZnO-nps	10.79 ± 1.40 (12.06)	0.84 ± 0.01 (0.83)	0.67 ± 0.02 (0.69)	6.03 ± 0.79 (6.96)
19.5 μm	ZnO-nps	10.91 ± 0.86 (11.71)	0.86 ± 0.01 (0.86)	0.54 ± 0.03 (0.57)	5.03 ± 0.55 (5.74)

Since microcontact printing can reliably reproduce features below 50 nm in size,[55] this does not approach the theoretical limit of grids which can be produced using microcontact printing. As such an identical set of devices was produced where the grid lines (Cu) were of the same thickness, but 1 μm wide instead of 1.4 μm with respect to the original design. It follows that the pitch of these devices can be 19.5 μm instead of 27.3 μm for a similar metal coverage and transparency. This is confirmed by the similar performance of the devices on the lower-pitch electrode to the previous design with PEDOT:PSS interlayer in place: 6.03 ± 0.79% (champion 6.96%) *vs* 6.47 ± 1.20% (champion 7.56%). The lower PCE is entirely caused by the lower J_{sc} and attributed to a widening of the lines as compared to the original master which can be compensated for during the design of the master.

Compared to the devices with a grid pitch of 27.3 μm, the devices on a grid with pitch 19.5 μm have a significantly lower requirement for the minimum conductivity requirement of the interlayer, as described by Jacobs *et al.*[5] It is evident from Figure 27 (b) that the fixed conductivity of the ZnO-nps layer is close to the requirements of the structure, as the series resistance is only marginally degraded when compared to the PEDOT:PSS reference device. This is reflected in the champion fill factor of the PEDOT:PSS-free devices: (27.3 μm pitch) 0.43 *vs* (19.5 μm pitch) 0.57. Although the PCE of the PEDOT:PSS-free device is lower than the corresponding PEDOT:PSS reference, caused by the still imperfect fill factor, it is clear that this outlines a promising route to the fabrication of PEDOT:PSS-free grid electrodes (Table 6).

A second approach to improving charge extraction from the spaces between grid lines is to eliminate PEDOT:PSS but increase the conductivity of the ZnO interlayer to compensate for the loss. Experientially, increasing the thickness of the ZnO layer did not significantly improve the device fill-factor; it is believed that this is caused by the conductivity of the layer being limited by the contact resistance between nanoparticles. In principle doping of ZnO can increase the lateral conductivity by orders of magnitude.[56,57] This is easily achieved when using a sol-gel ZnO approach by substituting Zinc Acetate Dihydrate in the precursor solution and yields high quality, transparent ZnO thin films with an order of magnitude lower resistivity than undoped ZnO.[58] Notably although the commercial ZnO nanoparticle formulation used here is doped by Al, the dopant is at extremely low concentration and acts to reduce the UV-light sensitivity of ZnO with little affect upon the conductivity.

To demonstrate this principle, model OPV devices were produced on Cu grid electrodes without PEDOT:PSS but using a ZnO thin film formed by a sol-gel process, the champion device characteristics of which are given in Figure 28. A solution comprised of zinc acetate dihydrate, ethanolamine and 2-methoxyethanol was stirred overnight before s-pin coating at 5000 rpm and annealing at 180°C in air. Unlike the commercial ZnO-nanoparticle solution, heating in air is necessary to drive the chemical oxidation of the component materials *in-situ*.
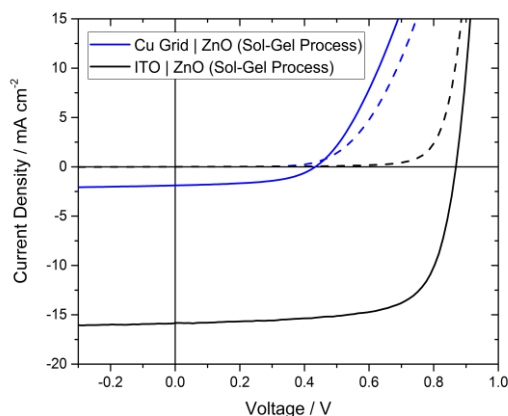
Figure 28: Champion device characteristics for the two electrode structures: Blue Line – Cu Grid | ZnO (Sol-Gel) & Black Line – ITO | ZnO (Sol-Gel). The complete structure is: Electrode as described | PBDB-T / ITIC | MoO_3 | Al.

The representative device characteristics in Figure 28 exhibit extremely low current and higher series resistance as compared to the ITO electrode with an equivalent Sol-Gel ZnO layer; this is attributed to a barrier at a device interface. The problem with depositing the Sol-Gel ZnO on Cu grids is likely twofold; the temperature of processing in air and the wetting. The sheet resistance of a 40 nm Cu grid (17.7 Ω sq^{-1} here) falls to 17.2 Ω sq^{-1} when a ZnO-nanoparticle film is added from commercial nanoparticle solution (and annealed at 120°C under inert N_2 atmosphere). In contrast, the sheet resistance of a Cu grid when ZnO is formed through the sol-gel route described (annealed at 180°C in air) rises to 22.6 Ω sq^{-1} which is symptomatic of Cu oxidation. Cu-oxides can present a barrier to charge extraction, isolating the metallic electrode from the heterojunction. A topographical AFM image of the Cu grid electrode with ZnO (sol-gel) reveals also the non-conformal structure (Figure 29) where the grid lines are isolated from the majority of the ZnO film, or connected only by a thin ZnO bridge. Wetting of ZnO sol-gel solutions have been improved by including a surfactant in the component solution in the literature and likely could be overcome here also.[10]
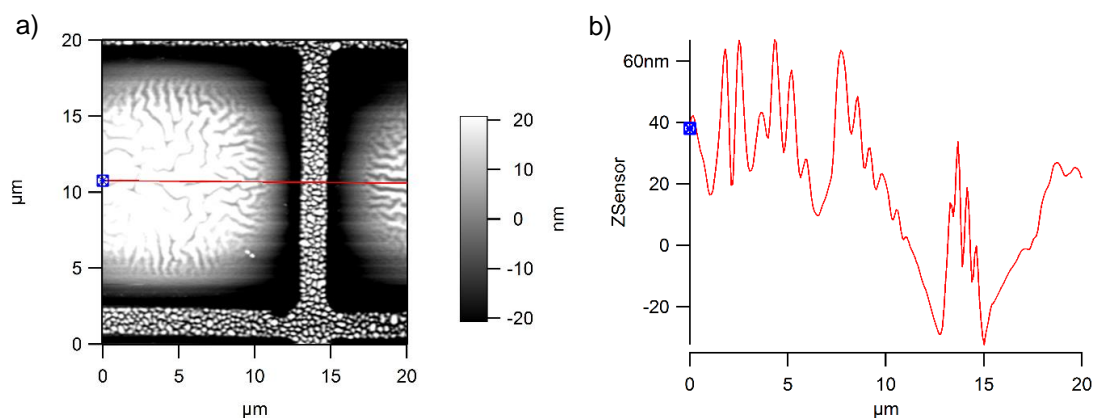
Figure 29: (a) Topographical AFM image of a ZnO thin film formed through a sol-gel process ontop of a Cu Grid electrode. (b) Cross sectional height profile of the film.

In later chapters we show that damage to the Cu metal when annealing at 180°C in air can be protected against by applying a 3 nm Zn metal overlayer, and that Cu | Zn 3 nm | Cu 2 nm films can successfully be patterned in a grid structure. It is hoped that the combination of these approaches could lead to PEDOT:PSS-free metallic grid electrodes with excellent properties.

4.6   Experimental Section

Production of the master/stamps

Onto a 3" polished Si wafer a photoresist bi-layer consisting of MicroChem polydimethylglutarimide (PMGI) SF11 and MICROPOSIT S1818 was layered and exposed to 130 mJ cm^{-2} UV light through a chromium mask patterned with the grid lines and developed for 30s in MF-319 developer. 500 nm Al_2O_3 (99.99%, Kurt J. Lesker) was then evaporated across the wafer before a lift off with acetone, propanol, MF-319 developer and a final rinse with DI water. Through the remaining Al_2O_3 mask the grid lines were etched using an inductively coupled plasma (ICP) etcher to a depth of 5.2 μm into the Si wafer (Figure 30). This extreme depth was used to avoid 'sagging' of the void during printing. The resultant master was used with the Al_2O_3 left in place, after salinization for 1 hr in trichloro(1H,1H,2H,2H-perfluorooctyl)silane vapor. All electrodes unless stated otherwise were produced using the same polymeric PDMS stamp formed upon this master (reused) with 1.4 μm wide lines and 10% coverage defined with respect

to the original master. Differences in current, for example between grids on plastic and glass or 40 and 120 nm high grids are attributed to widening of these lines during printing and can be compensated for by stamp design.
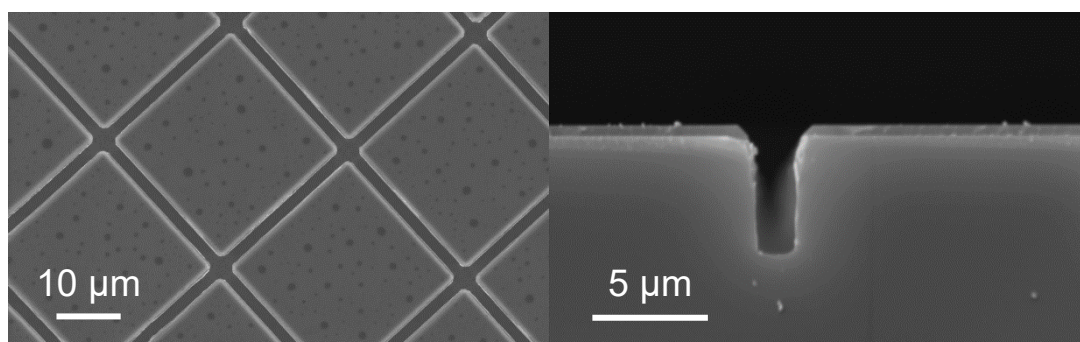
Figure 30: (Left) SEM image of the raised features in the silicon master produced here. (Right) Cross-sectional SEM image of the trench depth etched into the wafer, with the Al_2O_3 mask (which was left in place during use) visible at the interface.

Forming of grid electrodes

40 – 120 nm Cu (99.999%, Kurt J. Lesker) was evaporated at 1 Å s^{-1} to freshly cleaned and UV/O$_3$ treated plastic (polyethylene terephthalate, PET) or glass at $< 10^{-6}$ base pressure. These were then immediately taken into air and gentle contact was made with a patterned PDMS stamp inked with 2 mM hexadecanethiol (HDT, 97% dry wt., Alfa Aesar) and dried for 1 minute. Contact was held for < 2s to minimize widening of the fine grid lines. These electrodes were then dipped in an aqueous 4 mM ammonium persulfate solution (APS) at room temperature for 30 – 90s dependent on metal thickness to form the grid lines. The HDT mask was not removed and these electrodes were washed in acetic acid for 10s before use directly in the devices described.

Sheet resistance measurement

18 x 18 mm patterned Cu grid electrodes were produced as above onto which silver contacts were painted to connect a Keithley 2400 source meter. Resistances were calculated using the Van der Pauw method at an applied voltage of 5 mV. For the sheet

resistance evolution electrodes were stored in ambient laboratory air and remeasured periodically. The temperature fluctuated between 18-30°C and the humidity between 15-50%.

Model optoelectronic devices

To the prepared grid electrodes (on glass or PET) where specified a 10 nm PEDOT:PSS film (Figure 31, PH1000, Ossila) was spin-cast at 5000 rpm from a filtered solution diluted with 2 parts deionized water and annealed at 120°C in air for 15 minutes.
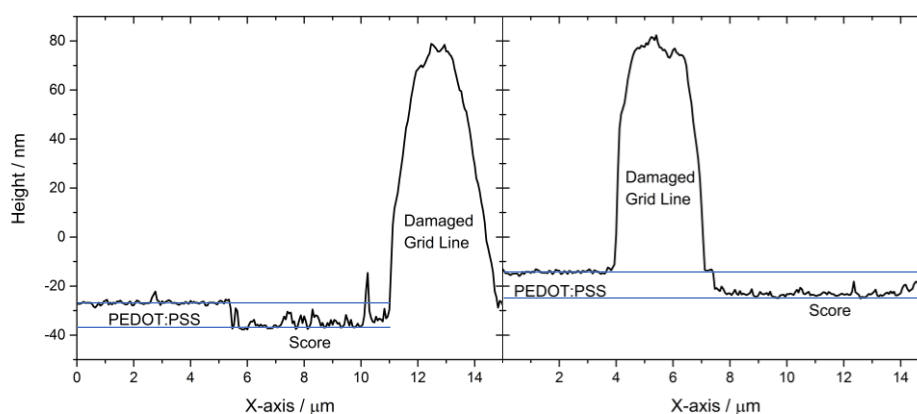
Figure 31: AFM profiles of a scored Cu grid coated with PEDOT:PSS, from which the PEDOT:PSS film thickness is determined to be ~ 10 nm. Blue lines are to guide the eye only. The Cu grid cross-section has rounded, rather than square, edges which is caused by the sharp scoring implement passing over the grid line.

Together with ITO reference electrodes (Washed and UV/O$_3$ treated. Glass, Thin Film Devices. PEN, Diamond Coatings) transferred into a N$_2$ filled glovebox with < 2 ppm O$_2$ and H$_2$O, 25 nm of ZnO was deposited by spin coating (Aluminum-doped zinc oxide ink for spin coating/slot-die coating, Sigma Aldrich, 5000 rpm, filtered) followed by the bulk heterojunction. For the PBDB-T/ITIC (Ossila) devices solutions were prepared in anhydrous chlorobenzene and 0.5% 1,8-Diiodooctane (DIO) at a 1:1 wt% (20 mg per

mL), spin cast at 2500 rpm and annealed at 120°C for 15 minutes. For the PCE-10/PC$_{70}$-BM (Ossila) devices with varying heterojunction thickness solutions were prepared at a 2:3 wt% ratio in anhydrous dichlorobenzene and 3% DIO at 35 and 50 mg per mL. For 100 nm heterojunction thickness 35 mg/mL solution was spin cast at 3000 rpm. For 300 and 400 nm heterojunction thickness 50 mg/mL solution was spin case at 2500 and 1500 rpm respectively. All devices were loaded to the thermal evaporator and held under vacuum overnight. 6 nm MoO$_3$ was then evaporated at 0.2 Å s^{-1} before the devices were transferred under vacuum to the pixel mask and 150 nm Al was evaporated at 1 Å s^{-1}. These devices were tested unencapsulated under 1 sun illumination in an N$_2$ atmosphere (< 2 ppm O$_2$, H$_2$O) through a calibrated shadow mask for the small area devices.

Grazing-Angle X-ray Diffraction

*M*easurements were made using a Malvern Panalytical Empyrean 3 with multicore optics (iCore/dCore), giving Cu Ka radiation. The incident beam was narrowed using a 1/16° slit to minimize beam spread at low angle. A parallel plate collimator with a solid state Pixcel 3D detector operating as a point detector (0D) mode was used with a step size of 0.03° 2q. Prior to measurement, the sample surface was adjusted to be flat and cut the direct X-ray beam in half, assuring that the sample was in the center of rotation of the goniometer. An incident angle of 0.5° was used.

4.7 References

[1]   Q. Burlingame, X. Huang, X. Liu, C. Jeong, C. Coburn, S. R. Forrest, *Nature* **2019**, *573*, 394.

[2]   J. Yuan, Y. Zhang, L. Zhou, G. Zhang, H. L. Yip, T. K. Lau, X. Lu, C. Zhu, H. Peng, P. A. Johnson, M. Leclerc, Y. Cao, J. Ulanski, Y. Li, Y. Zou, *Joule* **2019**, *3*, 1140.

[3]   H. Lu, X. Ren, D. Ouyang, W. C. H. Choy, *Small* **2018**, *14*, 1703140.

[4]   M. W. Rowell, M. D. McGehee, *Energy Environ. Sci.* **2011**, *4*, 131.

[5]   D. A. Jacobs, K. R. Catchpole, F. J. Beck, T. P. White, *J. Mater. Chem. A* **2016**, *4*, 4490.

[6]   F. Machui, M. Hösel, N. Li, G. D. Spyropoulos, T. Ameri, R. R. Søndergaard, M. Jørgensen, A. Scheel, D. Gaiser, K. Kreul, D. Lenssen, M. Legros, N. Lemaitre, M. Vilkman, M. Välimäki, S. Nordman, C. J. Brabec, F. C. Krebs, *Energy Environ. Sci.* **2014**, *7*, 2792.

[7]   M. J. Griffith, N. A. Cooling, B. Vaughan, D. C. Elkington, A. S. Hart, A. G. Lyons, S. Quereshi, W. J. Belcher, P. C. Dastoor, *IEEE J. Sel. Top. Quantum Electron.* **2016**, *22*, 4100714.

[8]   A. Gambhir, P. Sandwell, J. Nelson, *Sol. Energy Mater. Sol. Cells* **2016**, *156*, 49.

[9]   R. Zhang, M. Engholm, *Nanomaterials* **2018**, *8*, 1.

[10]   K. W. Seo, J.-Y. J. J. Y. J. Lee, J. Jo, C. Cho, J.-Y. J. J. Y. J. Lee, *Adv. Mater.* **2019**, *31*, 1902447.

[11]   H. Kang, S. Jung, S. Jeong, G. Kim, K. Lee, *Nat. Commun.* **2015**, *6*, 6503.

[12]   D. R. Sahu, J. L. Huang, *Appl. Surf. Sci.* **2006**, *253*, 915.

[13]   H. B. Lee, W. Y. Jin, M. M. Ovhal, N. Kumar, J. W. Kang, *J. Mater. Chem. C* **2019**, *7*, 1087.

[14]   S. Choi, S.-J. Kim, C. Fuentes-Hernandez, B. Kippelen, *Opt. Express* **2011**, *19*, A793.

[15] F. L. M. Sam, M. A. Razali, K. D. G. D. G. I. Jayawardena, C. A. Mills, L. J. Rozanski, M. J. Beliatis, S. R. P. Silva, *Org. Electron.* **2014**, *15*, 3492.

[16] F. L. M. Sam, C. A. Mills, L. J. Rozanski, S. R. P. Silva, *Laser Photonics Rev.* **2014**, *8*, 172.

[17] Y. Xia, X. M. Zhao, E. Kim, G. M. Whitesides, *Chem. Mater.* **1995**, *7*, 2332.

[18] C. Merian, X. Du, D. Hardt, H. AlQahtani, In *ASME International Mechanical Engineering Congress and Exposition, Proceedings (IMECE)*; American Society of Mechanical Engineers, 2015; Vol. 14–2015.

[19] M. Geissler, H. Schmid, A. Bietsch, B. Michel, E. Delamarche, *Langmuir* **2002**, *18*, 2374.

[20] J. Zou, H. L. Yip, S. K. Hau, A. K. Y. K.-Y. Jen, *Appl. Phys. Lett.* **2010**, *96*, 203301.

[21] T. Oishi, K. Koyama, S. Alam, M. Tanaka, J. C. Lee, *Hydrometallurgy* **2007**, *89*, 82.

[22] A. Alzate, M. E. López, C. Serna, *Waste Manag.* **2016**, *57*, 113.

[23] E. Georgiou, S. A. Choulis, F. Hermerschmidt, S. M. Pozov, I. Burgués-Ceballos, C. Christodoulou, G. Schider, S. Kreissl, R. Ward, E. J. W. List-Kratochvil, C. Boeffel, *Sol. RRL* **2018**, *2*, 1700192.

[24] L. Mao, Q. Chen, Y. Li, Y. Li, J. Cai, W. Su, S. Bai, Y. Jin, C. Q. Ma, Z. Cui, L. Chen, *Nano Energy* **2014**, *10*, 259.

[25] Y. Li, L. Mao, Y. Gao, P. Zhang, C. Li, C. Ma, Y. Tu, Z. Cui, L. Chen, *Sol. Energy Mater. Sol. Cells* **2013**, *113*, 85.

[26] X. Fan, W. Nie, H. Tsai, N. Wang, H. Huang, Y. Cheng, R. Wen, L. Ma, F. Yan, Y. Xia, *Adv. Sci.* **2019**, *6*.

[27] D. Qin, Y. Xia, G. M. Whitesides, *Nat. Protoc.* **2010**, *5*, 491.

[28] L. Wang, Y. Yao, X. Ma, C. Huang, Z. Liu, H. Yu, M. Wang, Q. Zhang, X. Li, S. Chen, W. Huang, *Org. Electron.* **2018**, *61*, 96.

[29]   Y. Li, L. Meng, Y. Yang, G. Xu, Z. Hong, Q. Chen, J. You, G. Li, Y. Yang, Y. Li, *Nat. Commun.* **2016**, *7*, 10214.

[30]   P. Bellchambers, M. Walker, S. Huband, A. Dirvanauskas, R. A. Hatton, *ChemNanoMat* **2019**, *5*, 619.

[31]   P. Bellchambers, J. Lee, S. Varagnolo, H. Amari, M. Walker, R. A. Hatton, *Front. Mater.* **2018**, *5*, 71.

[32]   C. Zhong, Y. M. Jiang, D. M. Sun, J. Gong, B. Deng, S. Cao, J. Li, *Chinese J. Phys.* **2009**, *47*, 253.

[33]   P. Keil, D. Lützenkirchen-Hecht, R. Frahm, In *AIP Conference Proceedings*; 2007; Vol. 882, pp. 490–492.

[34]   H. M. Stec, R. A. Hatton, *ACS Appl. Mater. Interfaces* **2012**, *4*, 6013.

[35]   L. Lu, N. R. Tao, L. B. Wang, B. Z. Ding, K. Lu, *J. Appl. Phys.* **2001**, *89*, 6408.

[36]   I. Platzman, R. Brener, H. Haick, R. Tannenbaum, *J. Phys. Chem. C* **2008**, *112*, 1101.

[37]   M. C. Biesinger, *Surf. Interface Anal.* **2017**, *49*, 1325.

[38]   J. Iijima, J. W. Lim, S. H. Hong, S. Suzuki, K. Mimura, M. Isshiki, *Appl. Surf. Sci.* **2006**, *253*, 2825.

[39]   J. Shewchun, R. Singh, M. A. Green, *J. Appl. Phys.* **1977**, *48*, 765.

[40]   J. Maserjian, *J. Vac. Sci. Technol.* **1974**, *11*, 996.

[41]   M. Depas, B. Vermeire, P. W. Mertens, R. L. Van Meirhaeghe, M. M. Heyns, *Solid State Electron.* **1995**, *38*, 1465.

[42]   A. Sundqvist, O. J. Sandberg, M. Nyman, J. H. Smått, R. Österbacka, *Adv. Energy Mater.* **2016**, *6*, 1.

[43]   L. Zuo, J. Yao, H. Li, H. Chen, *Sol. Energy Mater. Sol. Cells* **2014**, *122*, 88.

[44]   D. G. Castner, K. Hinds, D. W. Grainger, *Langmuir* **1996**, *12*, 5083.

[45]   H. S. Choi, Y. Kang, H. Lee, C. Lee, *Curr. Appl. Phys.* **2007**, *7*, 522.

[46]   S. Chen, L. Song, Z. Tao, X. Shao, Y. Huang, Q. Cui, X. Guo, *Org. Electron. physics, Mater. Appl.* **2014**, *15*, 3654.

[47]   E. Vitoratos, *Open J. Org. Polym. Mater.* **2012**, *02*, 7.

[48]   G. D. M. R. Dabera, M. Walker, A. M. Sanchez, H. J. Pereira, R. Beanland, R. A. Hatton, *Nat. Commun.* **2017**, *8*, 1894.

[49]   M. Janczarek, E. Kowalska, *Catalysts* **2017**, *7*.

[50]   K. Norrman, M. V Madsen, S. A. Gevorgyan, F. C. Krebs, *J. Am. Chem. Soc.* **2010**, *132*, 16883.

[51]   S. Holliday, R. S. Ashraf, A. Wadsworth, D. Baran, S. A. Yousaf, C. B. Nielsen, C. H. Tan, S. D. Dimitrov, Z. Shang, N. Gasparini, M. Alamoudi, F. Laquai, C. J. Brabec, A. Salleo, J. R. Durrant, I. McCulloch, *Nat. Commun.* **2016**, *7*, 1.

[52]   D. Baran, R. S. Ashraf, D. A. Hanifi, M. Abdelsamie, N. Gasparini, J. A. Röhr, S. Holliday, A. Wadsworth, S. Lockett, M. Neophytou, C. J. M. Emmott, J. Nelson, C. J. Brabec, A. Amassian, A. Salleo, T. Kirchartz, J. R. Durrant, I. McCulloch, *Nat. Mater.* **2017**, *16*, 363.

[53]   B. J. Tremolet de Villers, K. A. O'Hara, D. P. Ostrowski, P. H. Biddle, S. E. Shaheen, M. L. Chabinyc, D. C. Olson, N. Kopidakis, *Chem. Mater.* **2016**, *28*, 876.

[54]   N. Y. Doumon, M. V. Dryzhov, F. V. Houard, V. M. Le Corre, A. Rahimi Chatri, P. Christodoulis, L. J. A. Koster, *ACS Appl. Mater. Interfaces* **2019**, *11*, 8310.

[55]   Y. Xia, G. M. Whitesides, *Annu. Rev. Mater. Sci.* **1998**, *28*, 153.

[56]   H. Hagendorfer, K. Lienau, S. Nishiwaki, C. M. Fella, L. Kranz, A. R. Uhl, D. Jaeger, L. Luo, C. Gretener, S. Buecheler, Y. E. Romanyuk, A. N. Tiwari, *Adv. Mater.* **2014**, *26*, 632.

[57]   Y. H. Lin, S. R. Thomas, H. Faber, R. Li, M. A. McLachlan, P. A. Patsalas, T. D. Anthopoulos, *Adv. Electron. Mater.* **2016**, *2*, 1.

[58]   J. H. Lee, B. O. Park, *Mater. Sci. Eng. B Solid-State Mater. Adv. Technol.* **2004**,

106, 242.

[59] K. Ellmer, Past achievements and future challenges in the development of optically transparent electrodes. *Nat. Photonics* **2012**, *6*, 809–817.

[60] S. Jeong, S. Jung, H. Kang, D. Lee, S. Choi, S. Kim, B. Park, K. Yu, J. Lee, K. Lee, *Adv. Funct. Mater.* **2017**, *27*, 1.

[61] T. Gao, B. Wang, B. Ding, J. K. Lee, P. W. Leu, *Nano Lett.* **2014**, *14*, 2105.

[62] J. Yun, *Adv. Funct. Mater.* **2017**, *27*, 1606641.

[63] K. Sivaramakrishnan, T. L. Alford, *Appl. Phys. Lett.* **2009**, *94*, 2104.

[64] D. S. Ghosh, Q. Liu, P. Mantilla-Perez, T. L. Chen, V. Mkhitaryan, M. Huang, S. Garner, J. Martorell, V. Pruneri, *Adv. Funct. Mater.* **2015**, *25*, 7309.

[65] F. C. Krebs, N. Espinosa, M. Hösel, R. R. Søndergaard, M. Jørgensen, *Adv. Mater.* **2014**, *26*, 29.

[66] J. R. Davis, *Copper and Copper Alloys*; ASM International: Ohio, 2001.

[67] Nasdaq, Nasdaq: Commodity Prices.

[68] HKEX, London Metal Exchange.

[69] G. Zhao, S. M. Kim, S. G. Lee, T. S. Bae, C. W. Mun, S. Lee, H. Yu, G. H. Lee, H. S. Lee, M. Song, J. Yun, *Adv. Funct. Mater.* **2016**, *26*, 4180.

[70] O. S. Hutter, R. A. Hatton, *Adv. Mater.* **2015**, *27*, 326.

[71] H. J. Pereira, J. Reed, J. Lee, S. Varagnolo, G. D. M. R. Dabera, R. A. Hatton, *Adv. Funct. Mater.* **2018**, *28*, 1802893.

[72] J. H. Im, K. T. Kang, S. H. Lee, J. Y. Hwang, H. Kang, K. H. Cho, *Org. Electron.* **2016**, *33*, 116.

[73] L. Leandro, R. Malureanu, N. Rozlosnik, A. Lavrinenko, *ACS Appl. Mater. Interfaces* **2015**, *7*, 5797.

[74] I. P. Lopéz, L. Cattin, D.-T. Nguyen, M. Morsli, J. C. Bernède, *Thin Solid Films*

2012, *520*, 6419.

[75]   N. Formica, D. S. Ghosh, A. Carrilero, T. L. Chen, R. E. Simpson, V. Pruneri, *ACS Appl. Mater. Interfaces* **2013**, *5*, 3048.

[76]   J. Meiss, M. K. Riede, K. Leo, *J. Appl. Phys.* **2009**, *105*, 1.

[77]   O. S. Hutter, H. M. Stec, R. A. Hatton, *Adv. Mater.* **2013**, *25*, 284.

[78]   D. Yu, Y. Q. Yang, Z. Chen, Y. Tao, Y. F. Liu, *Opt. Commun.* **2016**, *362*, 43.

[79]   A. Behrendt, C. Friedenberger, T. Gahlmann, S. Trost, T. Becker, K. Zilberberg, A. Polywka, P. Görrn, T. Riedl, *Adv. Mater.* **2015**, *27*, 5961.

[80]   J. B. Kim, C. S. Kim, Y. S. Kim, Y.-L. Loo, *Appl. Phys. Lett.* **2009**, *95*, 183301.

[81]   C. Zuo, L. Ding, *Small* **2015**, *11*, 5528.

[82]   G. Zhou, L. Wang, J. C. Yang, *J. Appl. Phys.* **2005**, *97*, 063509.

[83]   C. Gattinoni, A. Michaelides, *Surf. Sci. Rep.* **2015**, *70*, 424.

[84]   Y.-R. Luo, *Comprehensive Handbook of Chemical Bond Energies*; CRC Press: Boca Raton, FL, 2007.

[85]   W. Gao, H. Gong, J. He, A. Thomas, L. Chan, S. Li, *Mater. Lett.* **2001**, *51*, 78.

[86]   M. O'Reilly, X. Jiang, J. T. Beechinor, S. Lynch, C. NíDheasuna, J. C. Patterson, G. M. Crean, *Appl. Surf. Sci.* **1995**, *91*, 152.

[87]   J. Li, J. W. Mayer, E. G. Colgan, *J. Appl. Phys.* **1991**, *70*, 2820.

[88]   M. C. Biesinger, L. W. M. Lau, A. R. Gerson, R. S. C. Smart, *Appl. Surf. Sci.* **2010**, *257*, 887.

[89]   D. S. Ghosh, R. Betancur, T. L. Chen, V. Pruneri, J. Martorell, *Sol. Energy Mater. Sol. Cells* **2011**, *95*, 1228.

[90]   W. A. Lanford, P. J. Ding, W. Wang, S. Hymes, S. P. Muraka, *Thin Solid Films* **1995**, *262*, 234.

[91]   R. Liu, F. Zhang, C. Con, B. Cui, B. Sun, *Nanoscale Res. Lett.* **2013**, *8*, 155.

[92]   B. Lesiak, A. Jablonski, J. Zemek, P. Jiricek, *Surf. Interface Anal.* **1998**, *26*, 400.

[93]   M. A. Marcus, J. E. Bower, *J. Appl. Phys.* **1997**, *82*, 3821.

[94]   S. Yu, G. Santoro, Y. Yao, D. Babonneau, M. Schwartzkopf, P. Zhang, S. K. Vayalil, P. Wessels, R. Döhrmann, M. Drescher, P. Müller-Buschbaum, S. V Roth, *J. Phys. Chem. C* **2015**, *119*, 4406.

[95]   G. Kaune, M. A. Ruderer, E. Metwalli, W. Wang, S. Couet, K. Schlage, R. Röhlsberger, S. V Roth, P. Müller-Buschbaum, *ACS Appl. Mater. Interfaces* **2009**, *1*, 353.

[96]   J. R. Levine, J. B. Cohen, Y. W. Chung, P. Georgopoulos, *J. Appl. Crystallogr.* **1989**, *22*, 528.

[97]   T. L. Barr, *Surf. Interface Anal.* **1982**, *4*, 185.

[98]   B. R. Strohmeier, *Surf. Interface Anal.* **1990**, *15*, 51.

[99]   B. R. Strohmeier, D. M. Hercules, *J. Catal.* **1984**, *86*, 266.

[100] B. P. Payne, M. C. Biesinger, N. S. McIntyre, *J. Electron Spectros. Relat. Phenomena* **2009**, *175*, 55.

[101] B. P. Payne, A. P. Grosvenor, M. C. Biesinger, B. A. Kobe, N. S. McIntyre, *Surf. Interface Anal.* **2007**, *39*, 582.

[102] Y. Cudennec, A. Lecerf, *Solid State Sci.* **2003**, *5*, 1471.

[103] K. L. Chavez, D. W. Hess, *J. Electrochem. Soc.* **2001**, *148*, G640.

[104] H. J. Pereira, O. S. Hutter, G. D. M. R. Dabera, L. A. Rochford, R. A. Hatton, F. Flory, J. C. Bernéde, Y. Li, J. Hou, J. You, Y. Yang, F. von Wrochem, W. Wenzel, *Sustain. Energy Fuels* **2017**, *112*, 63505.

[105] J. Hun Park, W.-K. Kim, J. Seong Bae, D. Hee Lee, I. Hee Park, T. Woo Lee, Y. Chan Cho, J.-Y. Kim, S. Lee, C. Ryong Cho, S.-Y. Jeong, *Sci. Rep.* **2015**, *5*, 305.

[106] S. Lim, D. Han, H. Kim, S. Lee, S. Yoo, *Sol. Energy Mater. Sol. Cells* **2012**, *101*, 170.

[107] H. J. Pereira, R. A. Hatton, *Front. Mater.* **2019**, *6*, 228.

[108] F. Wiame, V. Maurice, P. Marcus, *Surf. Sci.* **2007**, *601*, 1193.

[109] T. K. S. Wong, S. Zhuk, S. Masudy-Panah, G. K. Dalapati, *Materials (Basel).* **2016**, *9*, 1.

[110] C. Zhang, D. Zhao, D. Gu, H. Kim, T. Ling, Y. K. R. Wu, L. J. Guo, *Adv. Mater.* **2014**, *26*, 5696.

[111] C. Y. Ho, M. W. Ackerman, K. Y. Wu, T. N. Havill, R. H. Bogaard, R. A. Matula, S. G. Oh, H. M. James, Electrical Resistivity of Ten Selected Binary Alloy Systems. *J. Phys. Chem. Ref. Data* **1983**, *12*, 183–322.

[112] J. Ilavsky, P. R. Jemian, *J. Appl. Crystallogr.* **2009**, *42*, 347.

[113] M. S. Wertheim, *Phys. Rev. Lett.* **1963**, *10*, 321.

[114] J. K. Percus, G. J. Yevick, *Phys. Rev.* **1958**, *110*, 1.

[115] E. Thiele, *J. Chem. Phys.* **1963**, *39*, 474.

4.8   Appendix
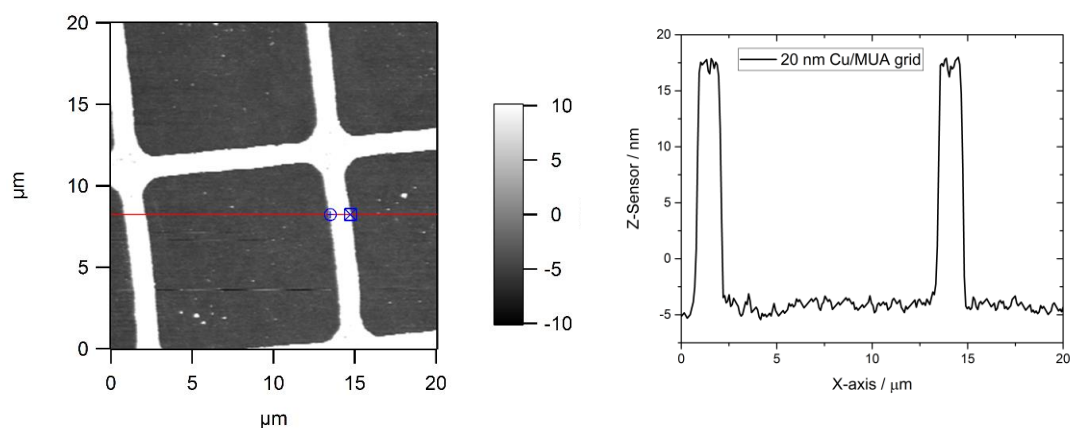
Figure A1: Topographical AFM image of an example 20 nm thick Cu grid line using the molecule 11-mercaptoundecanoic acid (MUA) with microcontact printing and 60 s contact time, ~60× what is necessary for HDT.
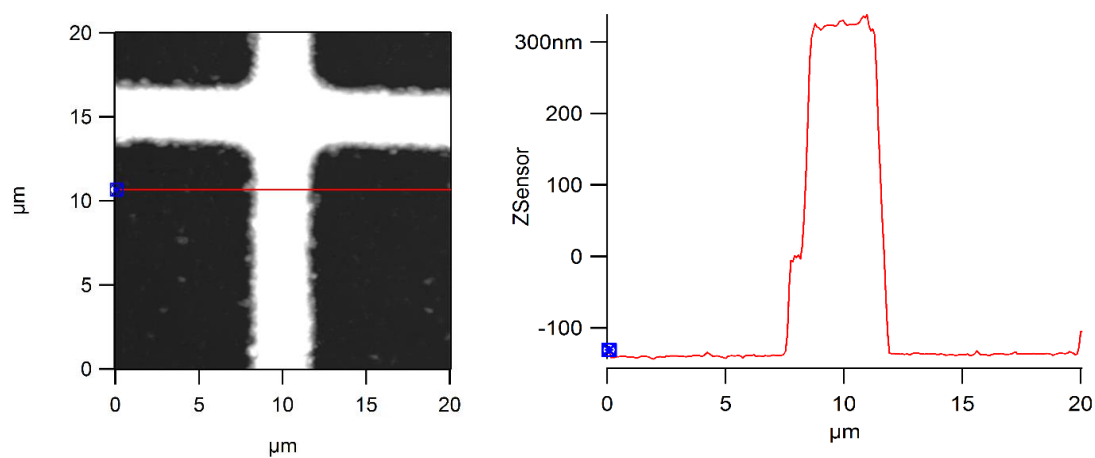
Figure A2: Topographical AFM image of a ~500 nm thick Cu grid line where the 'ragged' substrate-grid edge is caused by metallic 'steps'.
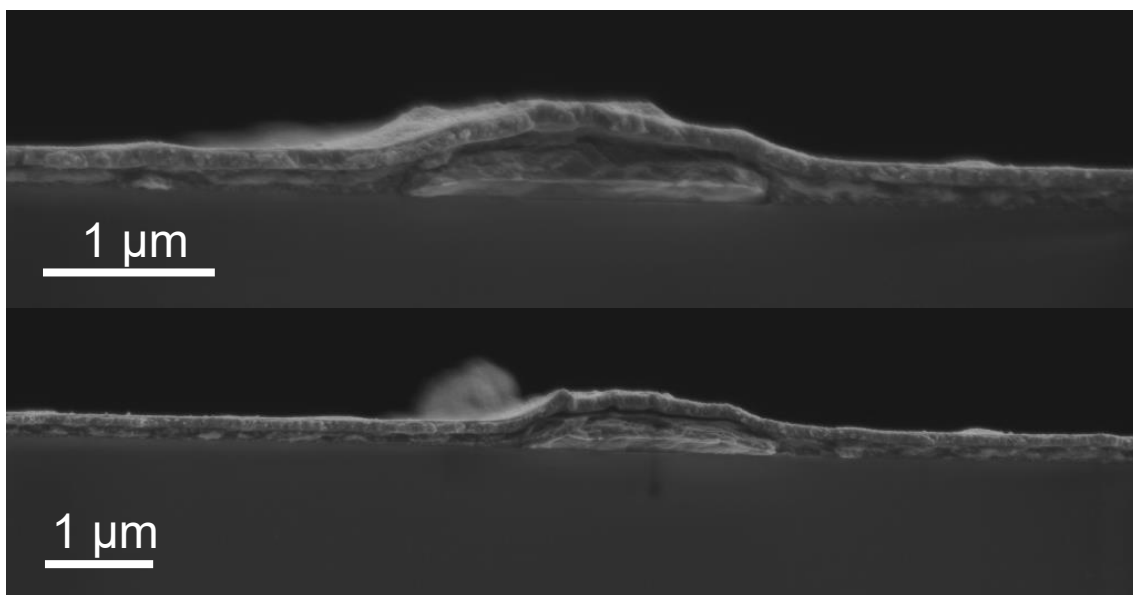
Figure A3: Two further cross-sectional SEM images of thick Cu grid lines at which the build-up of PEDOT:PSS/ZnO can be seen at the step between metal grid line and substrate which it is postulated smooths the interface.
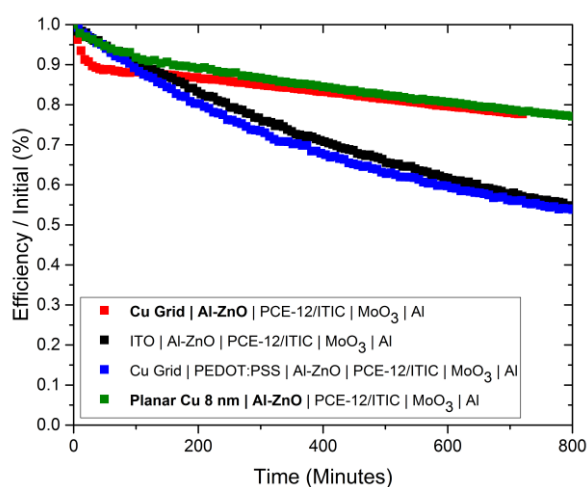
Figure A4: Normalized constant illumination study at 1 sun intensity for four device structures: Electrode (120 nm Cu grid, 8 nm planar Cu film or ITO) | Optional PEDOT:PSS | *ZnO* | PBDB-T/ITIC | MoO_3 | Al.

5   Elucidating the exceptional passivation effect of 0.8 nm evaporated aluminium on transparent copper films

The majority of the work presented in this chapter has been published in the following article:

P. Bellchambers, J. Lee, S. Varagnolo, H. Amari, M. Walker and R. A. Hatton, *Front. Mater.* **2018**, *5,* 71

5.1   Chapter Summary

Slab-like copper films with a thickness of 9 nm (~70 atoms) and sheet resistance of ≤ 9 Ω sq^{-1} are shown to exhibit remarkable long-term stability towards oxidation in ambient air when passivated with an 0.8 nm aluminium layer deposited by simple thermal evaporation. The sheet resistance of 9 nm Cu films passivated in this way, and lithographically patterned with a dense array of ~6 million apertures per cm^2, increases by less than 1% after 2 years exposure to ambient air. Using a combination of annular-dark field scanning transmission electron microscopy, nanoscale spatially resolved elemental analysis and atomic force microscopy, the surprising effectiveness of this layer is found to result from spontaneous segregation of the aluminium to grain boundaries in the copper film where it forms a ternary oxide plug at those sites in the metal film most vulnerable to oxidation. Crucially, the heterogeneous distribution of this passivating oxide layer combined with its very low thickness ensures that the underlying metal is not electrically isolated, and so this simple passivation step renders Cu films stable enough to compete with Ag as the base metal for transparent electrode applications in emerging optoelectronic devices.

5.2 Introduction

It is now widely recognised that alternatives to conventional conducting oxide window electrode materials, such as tin doped indium oxide and fluorine doped tin oxide, are required to enable optoelectronic devices compatible with flexible substrates and low cost roll-to-roll manufacturing.[1,2] Unpatterned optically thin metal film electrodes are now emerging as a viable challenger because they are compatible with flexible substrates and roll-to-roll processing, whilst also offering the important advantages over metal nanowire electrodes of much lower surface roughness and superior stability towards electromigration.[3–6] On plastic substrates lithographic patterning of thin metal film electrodes and/or the use of wide band gap anti-reflecting interlayers enables performance competitive with high performance conducting oxide electrodes.[2,7–12] Vacuum evaporation is also well established as a low cost production method for thin metal films over large areas, most notably for the packaging industry, and so is particularly attractive as a low cost path to large scale deposition of optically thin metal films.[4,13]

Due to the high electrical conductivity and low optical loses, Ag has historically been the metal of choice for metal window electrode applications,[4] although it is recognised that its high cost may necessitate recycling if it is to be used in low cost applications such as organic photovoltaics (OPVs).[14] Ag films are also sensitive to oxidation in ambient air, a process which is detrimental to their performance as electrodes in devices.[15–17] Zhang *et al.* have shown that alloying Ag with ~10% aluminium by co-sputtering is a very effective approach for stabilizing optically thin Ag films without compromising the optical properties, although the sheet resistance of Al doped Ag electrodes is not as low as can be achieved with pure Ag.[18] In general, literature reports pertaining to the long-term stability of optically thin Ag films towards oxidation in air are sparse,[2,5,17,19] which is surprising given the potential technological importance. The substrate electrode is very often manipulated in air prior to integration into a device, and it is well understood that the gradual ingress of air into flexible electronic devices is inevitable due to the limited barrier properties of transparent encapsulants compatible with flexible substrates,[20,21] so the long term stability of metal electrodes towards air-oxidation is an important consideration for many applications.

Copper (Cu) is an attractive alternative to Ag for use as a window electrode for cost sensitive applications such as OPVs because it has a conductivity comparable to Ag at ~1% of the cost.[22,23] The higher optical losses in Cu for wavelengths below 500 nm

can be mitigated by electrode and/or device design, including using a metal oxide overlayer to increase transparency.[24–26] However, the application of Cu window electrodes has so far been limited, due to the higher susceptibility of Cu towards oxidation in air which results in the formation of a mixture of the short-lived hydroxide ($Cu(OH)_2$), Cu_2O and CuO.[27] Notably, some crystal faces of Cu are far more resistant to oxidation than others, although the order of reactivity and mechanism is debated.[28–31] In contrast to the native oxide layer at the surface of aluminium (Al) the process of Cu oxidation in air is not self-limiting,[28,30,32–34] although Cu_2O and CuO do not necessarily electrically isolate the metal since both are *p*-type semiconductors with accessible valance bands for hole conduction.[35] In the context of very thin Cu films suitable for window electrode applications, surface oxidation does however have the detrimental effect of increasing the electrode sheet resistance due to the significant reduction in metal thickness, and so it is important to limit surface oxidation as far as possible.[36–39]

One approach for the passivation of Cu films that has proved remarkably effective is the use of a sub-1 nm Al layer deposited by simple vacuum evaporation.[40–42] Hutter *et al.* have shown there is no increase in the sheet resistance of a 7 nm thick Cu film after 120 hours in ambient air when capped with 0.8 nm Al.[40] In that work it was postulated that a compact ternary oxide layer of aluminium-copper-oxide caps the entire surface of the Cu film, since both Cu and Al oxide fragments were observed using secondary ion mass spectroscopy. It is however remarkable that such a thin oxide layer is so effective given that the native oxide on both Al and Cu exceeds 2 nm in thickness,[28,43,44] and the Al layer is deposited by simple vacuum evaporation rather than the more involved techniques of atomic layer deposition,[38,45] or electrochemical deposition.[37] The extraordinary effectiveness of this easily implemented approach to Cu passivation indicates there is either something very special about the passivating effect of aluminium-copper-oxide, or that the proposed explanation for its effectiveness is lacking. Importantly, for optoelectronic device applications the very low thickness of this passivation layer ensures it is sufficiently thin not to impede the transport of charge across the interface by quantum mechanical tunnelling.[40,46] Given the current surge of interest in transparent metal film electrodes for emerging optoelectronic device applications, this chapter provides a timely insight into the science that underpins the effectiveness of this approach to Cu passivation, together with a quantification of the long-term stability and direct comparison of the stability with pure Ag electrodes of the same thickness fabricated using the best reported practice to date.

5.3   Results and Discussion

In this study slab-like Cu films with a thickness equivalent to ~70 Cu atoms (9 nm ± 3%) were fabricated on glass: Figure 1. To achieve this the substrate was derivatised with a mixed molecular adhesive layer (MM) of 3-mercaptopropyl(trimethoxysilane) (APTMS) and 3-aminopropyl(thrimethoxysilane) (MPTMS), using our previously reported protocol developed by the Hatton group, which has been shown to enable the formation of robust films resistant to ultra-sonic agitation in a variety of solvents including water.[3,47] A thickness of 0.8 nm Al, equivalent to 6 atoms, was deposited onto the Cu electrode immediately after Cu evaporation without breaking vacuum.
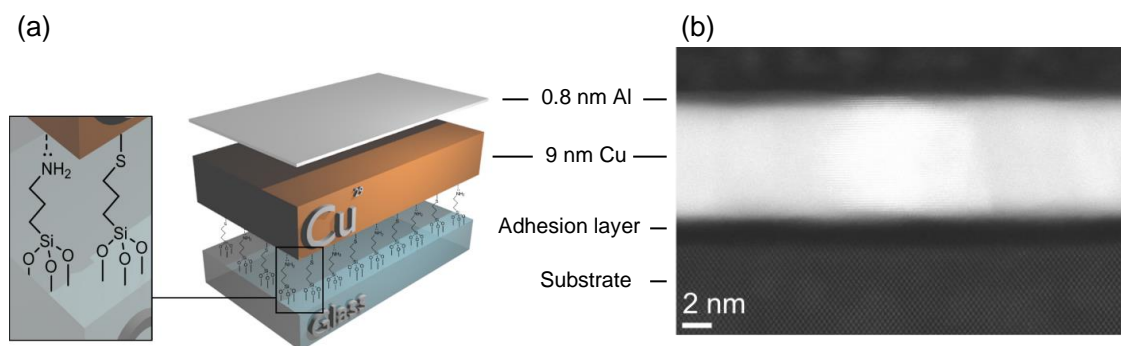
Figure 1: (a) Simplified schematic illustration of the electrode structure. (b) High resolution cross-sectional STEM (HR-STEM) image of a 9 nm Cu film with 0.8 nm Al overlayer, supported on a mixed silane adhesive layer derivatized Si wafer with native oxide. Both the Si atoms and rows of Cu atoms are resolved in the image.

APTMS molecules rapidly bind to glass and UV/O$_3$ treated plastic films because the primary amine can form hydrogen bonds with native hydroxyl groups at the glass surface (Figure 2 (a)). This interaction brings the methoxysilane group close to the surface so that a condensation reaction between the methoxysilane groups on the APTMS molecule and hydroxyl groups at the glass surface can occur, forming strong siloxane linkages. The primary amine also catalyses the formation of further siloxane linkages by deprotonating the surface hydroxyl groups, which also facilitates the binding of MPTMS (Figure 2 (b)).[47–49] Typical plastic substrates used for OPVs; PET and polyethylene naphthalate (PEN), do not have reactive hydroxyl groups at their surface to which methoxysilanes can

bind. A brief exposure to O₃ or oxygen plasma however forms sufficient to reactive oxygen sites (e.g. hydroxyls) onto which silanes can bind.[3]
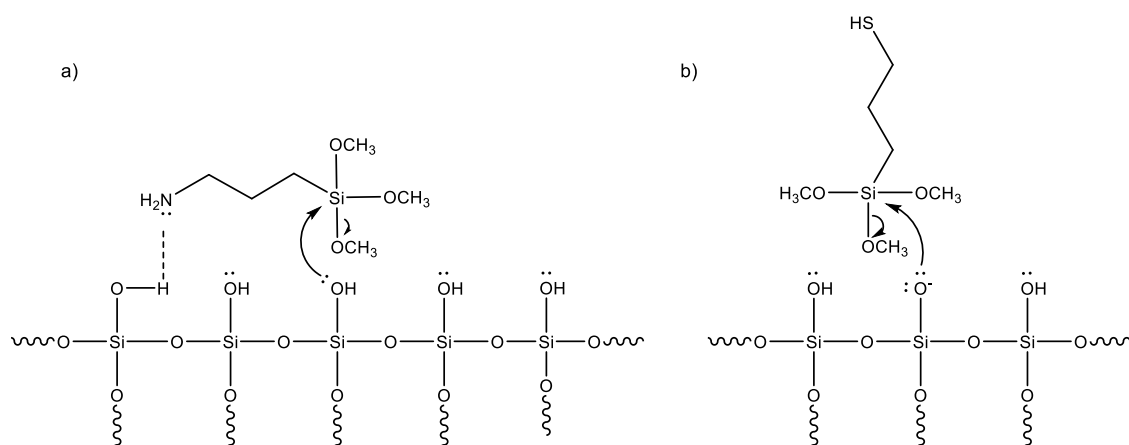
Figure 2: a) The hydrogen-bond facilitated condensation reaction of APTMS to a glass surface. b) The amine-deprotonated hydroxyl moiety reacting with MPTMS.

The amine-Cu bond is weaker than thiol-Cu bond and so a combination of the two is used to benefit both from the catalytic properties of the amine (which speeds up the coupling reaction) and the strength of the Cu-S bond (which improves the mechanical robustness of the film).[3] The resulting mixed monolayer of APTMS and MPTMS has previously been shown to be ~ 1 nm thick with an APTMS: MPTMS ratio of 3.4 ± 0.1 : 1, with a amine and thiol groups orientated towards the vacuum, all of which can serve as potential nucleation sites for the incoming metal atoms.[50]

The alkylsilane molecular adhesive layer presents a very high density of nucleation sites to the incoming metal and so suppresses metal diffusion at the early stages of film growth enabling the formation of compact and extremely smooth films of Cu at sub-10 nm film thickness,[47] as is evident from the scanning transmission electron microscope (STEM) image in Figure 1 (b) for a 9 nm thick Cu film. Low surface roughness, slab-like metal films are ideal for application as the transparent electrode for optoelectronic devices because when the density of packing between crystallites increases the contact area between adjacent crystallites is increased, facilitating easier electron transfer between them and so lower lateral resistivity (Table 1). The predominant

crystallographic orientation of Cu films prepared using this method has been shown previously to be (111).[26]

Table 1: Summary of the sheet resistance of the different electrodes fabricated. The sheet resistance measurements were made in ambient air within 2 minutes of removal from the glovebox.

Abbreviations	Full Structure	Average Sheet Resistance ± Standard Deviation (Ω sq^{-1}) *(Champion)*
MM | Cu	Glass | APTMS:MPTMS | 9 nm Cu	**10.8 ± 0.2** *(10.5)*
MM | Cu | Al	Glass | APTMS:MPTMS | 9 nm Cu | 0.8 nm Al	**8.7 ± 0.2** *(8.6)*
PET | MM | Cu | Al	PET | APTMS:MPTMS | 9 nm Cu | 0.8 nm Al	**9.1 ± 0.3** *(8.8)*
Glass | Cu	9 nm Cu directly on glass	**13.8 ± 0.6** *(13.3)*
Glass | Cu | Al	9 nm Cu | 0.8 nm Al directly on glass	**9.1 ± 0.2** *(9.0)*
PEI | Ag*	Glass | PEI (spin coated) | 9 nm Ag	**9.4 ± 0.3** *(9.0)*

*Matching 9 Ω sq^{-1} reported by Kang *et al.*[6]

In Figure 1 (b) the Cu film is supported on the oxidised surface of a silicon wafer chemically derivatized with the mixed silane adhesion layer rather than silicate glass, to facilitate HR-STEM imaging and avoid image distortion due to charging. The native oxide at the surface of silicon has a very similar native hydroxyl density (onto which the mixed alkylsilane adhesion layer can bind) and chemical composition to that of silicate glass and so serves as a useful conducting substrate for STEM imaging.[51–53] Conventional wisdom is that Cu films deposited by thermal evaporation should be deposited at high vacuum to prevent contamination by residual gases and produce the most uniform films.[7] Water vapour for example, the dominant residual gas in the ultra-

high vacuum regime, will adsorb on metal films during deposition pinning grain boundaries which reduces grain growth and prevents the merging of grains.[54] The reactivity of Cu to residual oxygen also results in the incorporation of oxygen within the Cu lattice which serve as electron scattering centres and decrease electron mobility, increasing the resistance to current flow. Consistent with this we have found that Cu films deposited at a base pressure of $< 5 \times 10^{-8}$ mbar are more conductive and stable (Figure 3) than those produced at higher pressure (5×10^{-6} mbar), and so all films in this study were deposited using $< 5 \times 10^{-8}$ mbar base pressure.
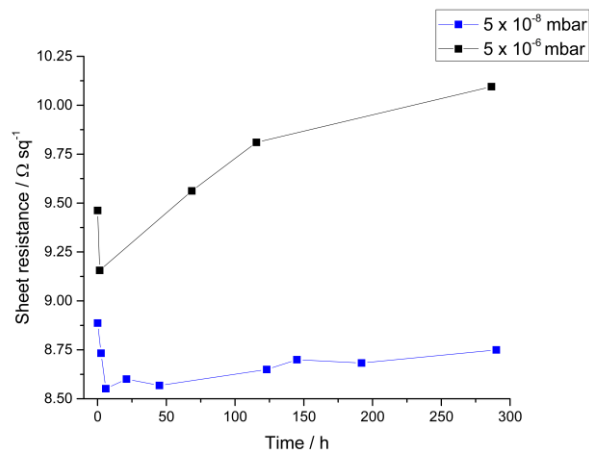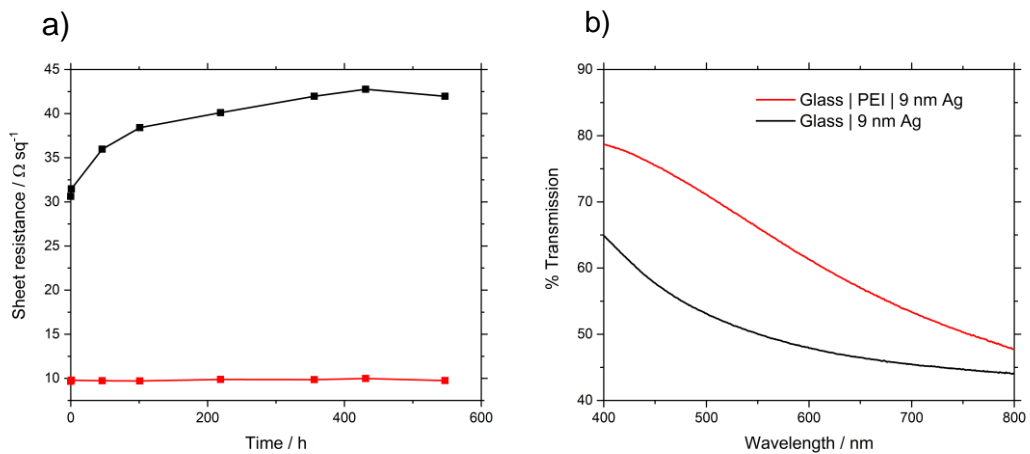

Figure 3: Evolution of the sheet resistance for representative MM | 9 nm Cu | 0.8 nm Al upon exposure to ambient laboratory air, for Cu films evaporated at a base pressure of 5 $\times 10^{-6}$ mbar (black) and 5×10^{-8} mbar (blue). The temperature and humidity fluctuated within the range of 18-30°C and 15-50% respectively.

On glass the surface roughness of a 9 nm thick Cu film measured over an area of 1 μm^2 is reduced by one third when the substrate is derivatised with a monolayer of molecular adhesive from 1.44 ± 0.12 to 1.02 ± 0.05 nm, and the starting sheet resistance measured in air is reduced from 13.8 ± 0.6 to 10.8 ± 0.2 Ω sq^{-1}, consistent with the formation of a more compact, uniform Cu film when using the molecular adhesive layer.[3,40,47] For metal films of such low thickness the sheet resistance is strongly dependent on the thickness and quality of the metal film, and so small reductions in the metal thickness that result from surface oxidation can be monitored in real time via the film sheet resistance, making very thin slab-like metal films (like that in Figure 1) an ideal model to evaluate methods

167

of passivating Cu as well as being of direct relevance as a window electrode for optoelectronics.[2]

To date optically thin Ag supported on PEI (polyethylenimine) modified polyethylene terephthalate (PET) substrates are the best performing metal transparent electrode in terms of the transparency and sheet resistance,[8,55] and so in this chapter this Ag electrode was used as a benchmark against which the stability of Cu electrodes can be evaluated. PEI has been shown to bind incident Ag atoms to a substrate by coordination bonds, and so serves the same function for Ag as the alkylsilane molecular adhesive layer used in the current study for Cu; promoting the formation of morphologically stable slab-like metal films (Figure 4 (a)).[55] In this study we have translated this procedure to glass substrates for ease of substrate handing, achieving comparable sheet resistance and transparency to that reported on PET: $9.4 \pm 0.3 \ \Omega \ sq^{-1}$ (Table 1). The far-field transparency of the Ag films is greatly increased by incorporation of this adhesion layer ((Figure 4 (b))) because the relatively low adhesion of Ag to silica results in the formation of morphologically unstable films of small crystallites which strongly scatter incident light.

Figure 4: A comparison between 9 nm Ag films deposited with (red) and without (black) the polymeric PEI nucleation layer on glass (a) representative sheet resistance evolution in ambient air; (b) film transparency.
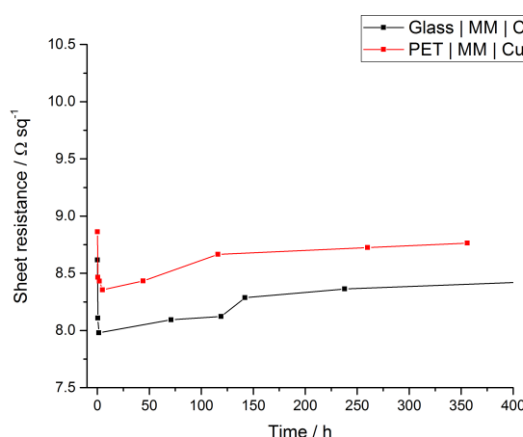
Figure 5 shows the evolution of the sheet resistance of 9 nm thick Cu and Ag films with time exposed to ambient air. The sheet resistance of the Cu film without an 0.8 nm Al overlayer increases rapidly from a starting resistance of 10.8 ± 0.2 Ω sq^{-1}, and then more steadily at 0.0048 Ω sq^{-1} hr^{-1} due to surface oxidation.[56] Also shown is the stability of a 9 nm Ag film supported on a PEI nucleation layer fabricated using the method reported by *Kang et al*. and compared to an alkylsilane monolayer above.[8] The sheet resistance of the 9 nm Ag film increases continually at a rate of 0.0012 Ω sq^{-1} hr^{-1}, which is significantly slower than the comparable (unprotected) Cu electrode.
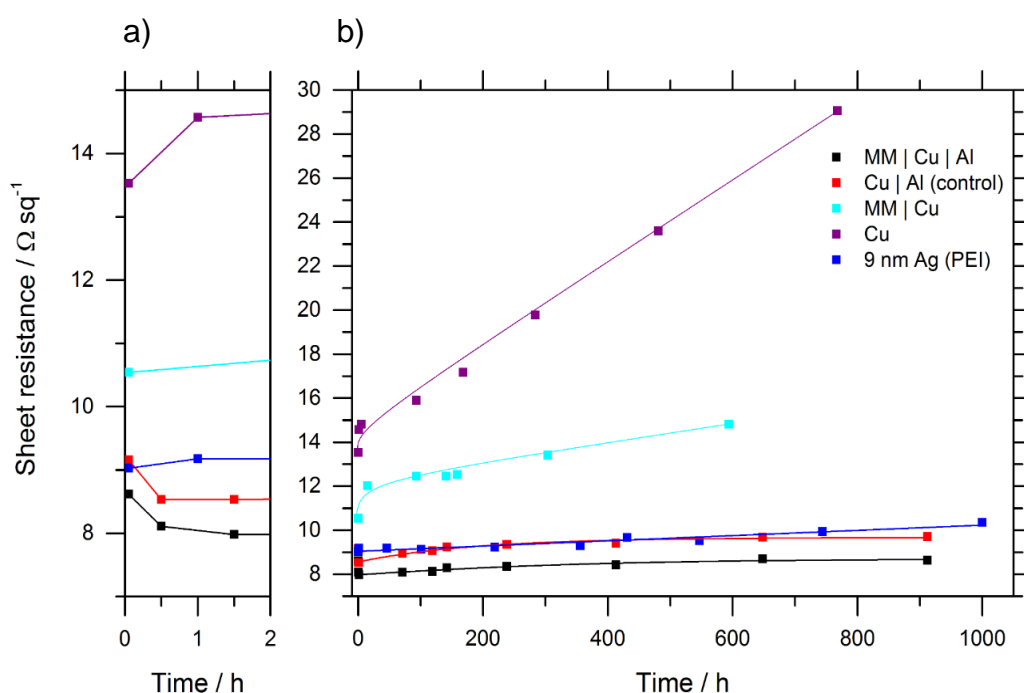
Figure 5: Evolution of the sheet resistance for representative Cu and Ag film electrodes stored in ambient air: (a) First 2 hours expanded. (b) Extended 1000-hour test period. All Cu layers are 9 nm thick. Where Al forms part of the electrode it has a nominal thickness of 0.8 nm. The fitted lines are to guide-the-eye only. Table gives the details of the complete data sets for all electrode structures. The temperature and humidity fluctuated in the range 18-30°C and 15-50% respectively.

The initial sheet resistance of the 9 nm Cu film with an 0.8 nm Al overlayer is comparable to that of the 9 nm Ag film (8.7 ± 0.2, 9.4 ± 0.3 Ω sq^{-1}), and more stable than that of Ag

with a long-term rate of increase in sheet resistance of only 0.0009 Ω sq^{-1} hr^{-1} compared to 0.0012 Ω sq^{-1} hr^{-1} for Ag. The fact that the stability of the Cu electrode with an 0.8 nm Al overlayer is at least as good as that of the Ag electrode is of significant practical importance for emerging applications requiring the use of low-cost transparent electrode materials. A direct comparison between the two complete sets is shown in Appendix, Figure A1. Importantly, this finding is also translatable to flexible PET substrates (Table and Figure 6).

Figure 6: The comparable evolution of the sheet resistance for two representative MM | Cu 9 nm | Al 0.8 nm film electrodes deposited onto flexible PET plastic (red) and glass (black).

The extended 1000-hour stability study in air in Figure 5 also clarifies the relevance of the nucleation layer for the formation of low-resistivity Cu films. For standalone Cu films the stability of the film, as well as the starting sheet resistance is highly dependent on the nucleation layer (Table , Figure 5) as the roughness of the film has an impact upon the lateral conductivity but also its stability to air as the number and depth of exposed grain boundaries changes. It is important that the stability of Cu 9 nm | Al 0.8 nm film is very similar with and without the nucleation layer (Appendix, Figure A2) to oxidation in air. This lower reliance on the structural properties of the Cu film allows for a higher tolerance to variations in industrial procedure on the stability of the resultant film electrode, and in the case of Cu deposited onto glass substrates may eliminate the necessity for the functionalisation of the substrate.

X-ray photoelectron spectroscopy analysis of Ag films aged for 2000 hours in air show that the oxidation products are primarily the sulfide Ag_2SO_4 and carbonate Ag_2CO_3, based on an assignment of the peaks at 168.5 eV and 288.8 eV respectively; Figure 7 and Table 2. This is consistent with the findings of Sanders *et al.* for thick Ag films exposed to air for 720-1440 hours and corroborated by the corresponding oxygen components and concentrations at 531.5 eV and 530.7 eV respectively.[57] Notably, neither AgO or Ag_2O are present in the O1s spectrum (528.6 eV, 529.5 eV), consistent with the hypothesis that silver oxide is only an intermediary for the formation of Ag_2SO_4 and AgCl.[57] It is also likely that morphological instability of the ultra-thin Ag films contributes to the deterioration in sheet resistance.[58,59]
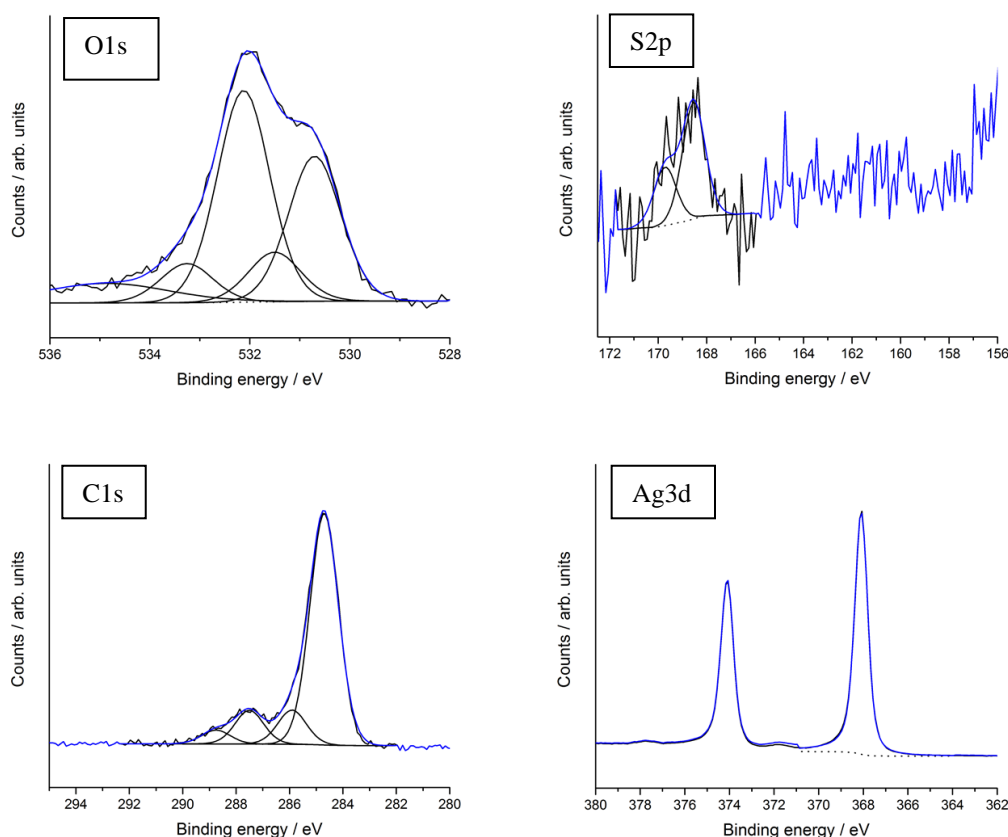
Figure 7: High resolution (HR) XPS spectra for a Glass | PEI | Ag 9 nm electrode aged in air for 2000 hours. The overlap of common products (Ag, Ag_2S, AgCl, Ag_2O, Ag_2SO_4, etc.) in the Ag 3d spectrum prevents fitting (all peaks within 0.4 eV). Tabulated peak positions are given in Table 2.

Table 2: HRXPS peak positions tabulated for the fitted peaks depicted in Figure 7.

Spectra	Peak position / eV	Assignment
O1s	530.7	Ag_2CO_3
	531.5	Ag_2SO_4
	532.1	C-O
	533.3	C-O-H
	534.9	Na KLL
S2p	168.5	Ag_2SO_4 ($2p_{3/2}$)
	169.7	Ag_2SO_4 ($2p_{1/2}$)
Ag3d	368.1	Ag mixture
C1s	284.7	C-C / C-H
	285.9	C-O-C
	287.5	C=O
	288.8	O=C-O / Ag_2CO_3

Notably, the sheet resistance of the Cu | Al electrode dips below its starting value until ~ 600 hours air exposure due to an initial sharp decrease in sheet resistance within the first 30 minutes (Figure 5 (a)). This unusual effect has previously been attributed to partial de-alloying of Al from the underlying Cu driven by Al oxidation: Hutter *et al.* have shown that even if the Al thickness on Cu is increased to 4.2 nm, Cu is still present at the surface of the bilayer film, showing that the Cu and Al mix when Al is evaporated directly onto Cu without breaking vacuum.[40] The high solubility of Al in Cu is well known to depend on temperature, and phase separation can occur when oversaturated, upon cooling or ageing.[60–62] Since doping Cu with just 1% Al doubles the resistivity of Cu,[63] reducing the Al content of the alloyed interfacial layer would be expected to reduce the Cu film sheet resistance. Given that the Cu film is slab-like (as shown in Figure 1) the change in sheet resistance over 910 hours, between the minimum at 1.5 hours and after 912 hours, is equivalent to a decrease in metal thickness of ~0.7 nm. This equates to an oxide thickness of ≤ 1 nm which is thin enough for electrons to efficiently tunnel across the oxide layer, ensuring the underlying metal does not become electrically isolated by the oxide overlayer.[46,64] It is possible this is also a consequence of the redistribution of material to the grain boundaries, as supported below, which may improve the contact resistance between crystallites.

It is reasonable to assume that the vacuum deposited Al is initially distributed uniformly over the Cu surface due to the high cohesive energy between metal atoms, and that it partially alloys with the Cu, since Cu is well known to readily alloy with Al.[30,65] Direct evidence that the Al initially forms a uniform layer is provided by surface roughness analysis of Cu films with and without a 0.8 nm Al layer: Figure 8 and Table 3. In this experiment a molecular adhesive layer was deliberately not used, to ensure the Cu film has a significant surface roughness prior to Al evaporation. Samples were fabricated by deposition of Cu across all the glass substrates, followed by masking one half, without breaking vacuum, and evaporation of 0.8 nm Al.
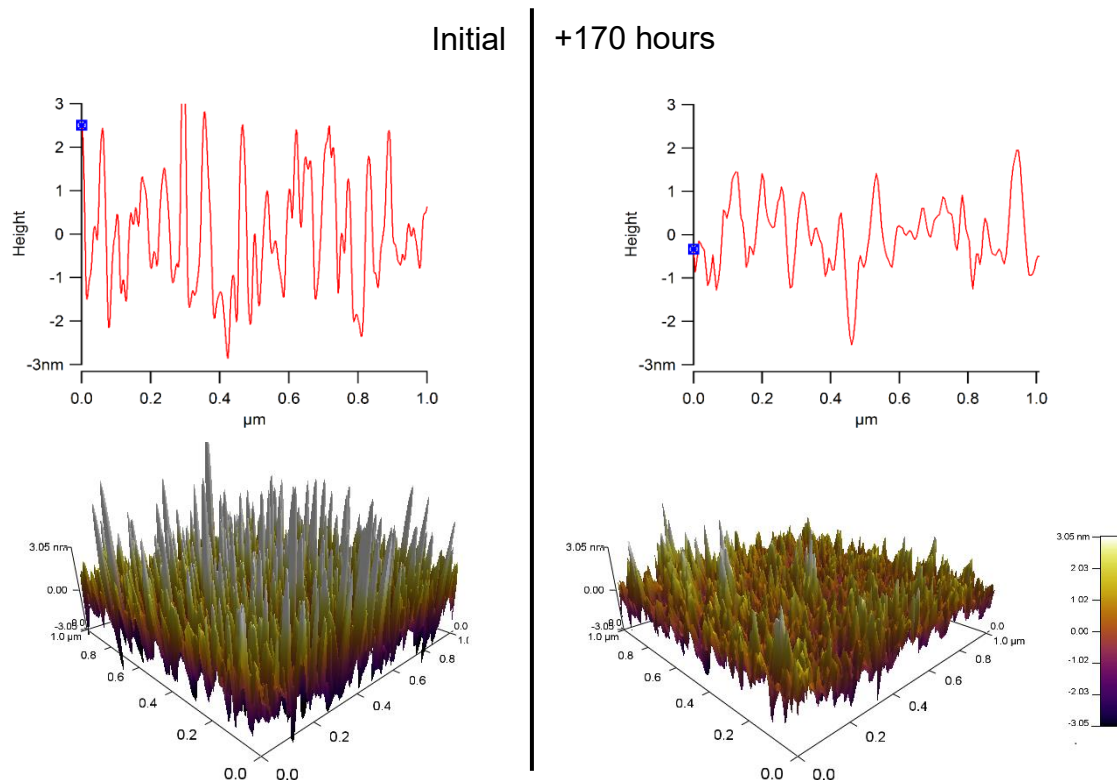
Figure 8: (Upper) A representative cross section showing the change in roughness for a Glass | 9 nm Cu | 0.8 nm Al electrode when exposed to air for 1 week. The accumulation of Al in $Cu_xAl_yO_z$ clusters at grain boundaries smooths the surface of the film. (Lower) 3D representations of a representative 1×1 µm area sampled immediately and after 1 week of air exposure.

Table 3: A comparison of the roughness of electrodes with and without a 0.8 nm Al overlayer. All films were prepared on glass with no alkylsilane monolayer to make measurement of changes in surface roughness more pronounced, since without a molecular adhesive layer the Cu film has a higher initial surface roughness. Cu was deposited across all samples before half were masked and Al evaporated on top (1×1 µm

area sampled by AFM). Measurements were made before and after 170 hours oxidation in air at ambient conditions.

Film structure	Initial root-mean square surface roughness (nm)	Surface roughness after storage for 170 hours in ambient air (nm)
Glass | 9 nm Cu	1.44 ± 0.12	1.24 ± 0.25
Glass | 9 nm Cu | 0.8 nm Al	1.43 ± 0.04	0.81 ± 0.14

The surface roughness of Cu films with and without an Al overlayer is initially equal at 1.43 ± 0.04 and 1.44 ± 0.12 nm respectively, consistent with conformal coverage of the Cu surface by Al; expected due to the metallic bonding interaction between Cu and Al. However Al is known to readily alloy with Cu and diffuse into Cu surfaces even at ambient temperature, so for such low Al thickness it seems likely the Al is not a discrete layer, but an alloy.[40] Evidence that the Al has alloyed with the Cu, rendering it more stable towards oxidation so that it retains its metallic nature, is provided by comparison of the measured and simulated transmission/reflectance spectra: Figure 9. If the Al was a discrete 0.8 nm thick layer on top of the Cu film, it would be expected to oxidize within a fraction of a second immediately after removal from the vacuum to form a ~1 nm Al_2O_3 layer.[66] Transfer matrix optical modelling shows that the transmittance and reflectance of a 9 nm Cu film with and without a 1 nm Al_2O_3 oxide layer are essentially indistinguishable: Figure 9 (b). The measured transmittance/reflectance spectra are consistent however with the Al largely retaining its metallic nature; Figure 9 (a). Although the difference is not as great as the simulated data this could be due to the aforementioned alloying, errors in thickness, partial surface oxidation or differences between the optical properties of Al literature films and those here.

a)   b)
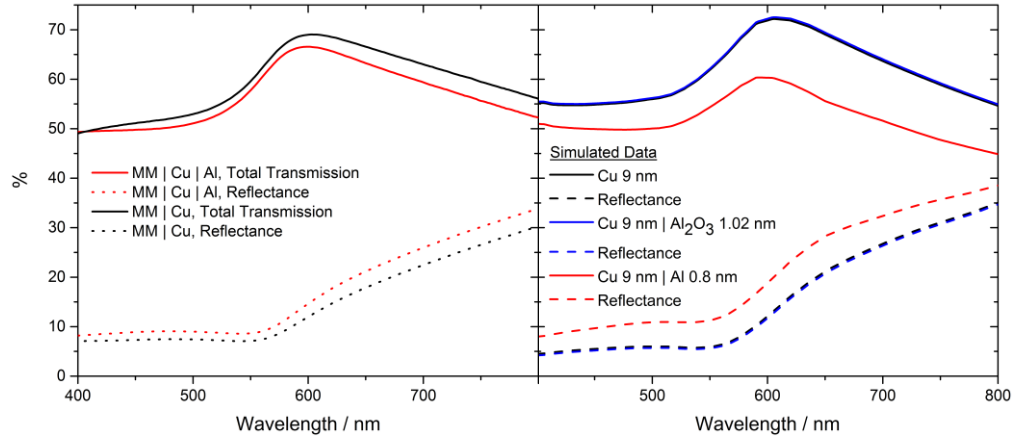
Figure 9: (a) Measured total transmission (Solid lines) and reflection (Dotted lines) for 9 nm Cu films with (Red) and without (Black) a 0.8 nm thick Al overlayer. Samples were measured after ~ 2 hours air exposure. (b) Simulated transmission and reflectance spectra for 9 nm Cu films with no overlayer (Black), a 1.02 nm Al_2O_3 overlayer to account for volume expansion upon oxidation, and a 0.8 nm metallic Al overlayer. N.B. Blue and Black lines overlap.

After 170 hours exposed to ambient air, the electrodes without the passivation layer show a ~14% reduction in average surface roughness from 1.44 ± 0.12 to 1.24 ± 0.25 nm, although the magnitude of this reduction falls within the spread of error (Table 3). This decrease in surface roughness can be attributed to volume expansion associated with a gradual conversion of Cu to Cu oxides, since the density of Cu oxides are ~1/3 lower than the metal (relative densities to [Cu]; [Cu_2O] 0.67 and [CuO] 0.71) and so the gaps between Cu grains that give rise to the nanoscale surface roughness will be reduced to accommodate this extra volume. Conversely the electrodes with the 0.8 nm Al overlayer show a very pronounced ~43% decrease in surface roughness over the same time period, which could only have resulted from a significant redistribution of metal atoms over the film surface, filling the gaps between Cu grains. Given that this large reduction in surface roughness only occurs for the Cu film with an Al over layer, the most plausible explanation is that the Al component has preferentially segregated to the grain boundaries in the Cu film surface. To test this hypothesis cross-sectional STEM images with corresponding nano-scale elemental analysis by energy-dispersive X-ray spectroscopy

(EDXS) of a MM | Cu | Al film exposed to ambient air for 200 hours were collected: Figure 10.
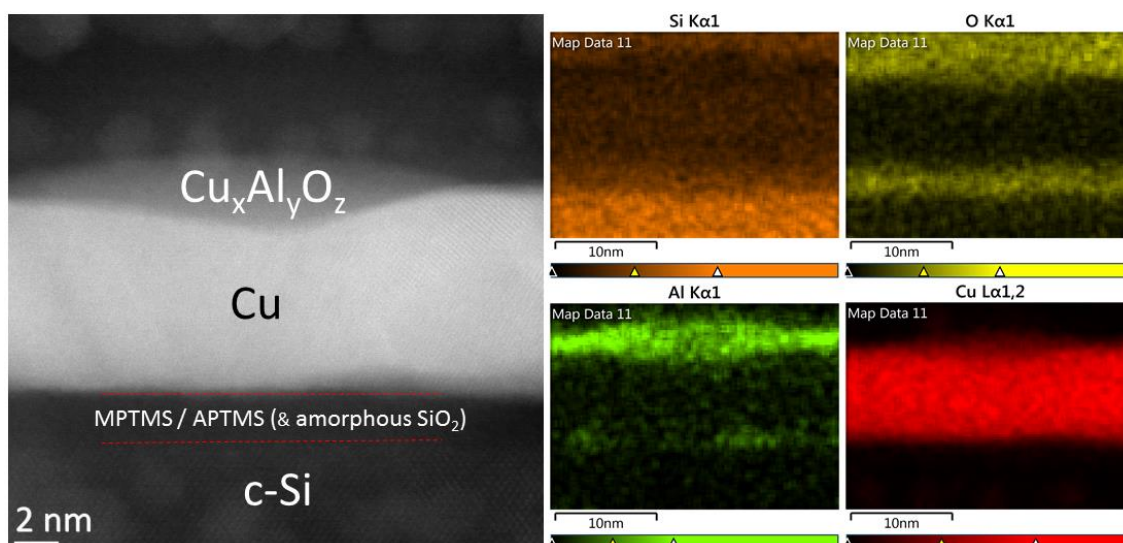
Figure 10: Left - A HR-STEM image of a MM | Cu | Al film, supported on crystalline silicon, exposed to air for > 170 hours. Right (4) – Spatially resolved EDXS mapping of the STEM image for the elements Si, O, Al and Cu.

It is evident from both the contrast image (Left) and elemental EDXS analysis (Right) in Figure 10, that after this extended period of air exposure the Al is not evenly distributed over the Cu surface (also evident Figure 11), but has segregated to Cu grain boundaries where it forms an oxide plug with a maximum thickness comparable to that of the self-limiting thickness of oxide on Al (2-3 nm).[43] Given that grain boundaries will be most susceptible to oxidation, both due to the higher radius of curvature and increased permeability of oxygen along grain boundaries, this accumulation at the grain boundaries explains the remarkable effectiveness of such a thin Al overlayer at passivating the underlying Cu: A copper-doped aluminium-oxide plug would be expected to serve as an effective local barrier to oxygen and moisture. The findings of the cross-sectional TEM imaging are also consistent with the ~43% decrease in surface roughness measured using AFM that occurs after exposure of the electrode to air, since filling the grain boundaries will inevitably reduce the surface roughness.
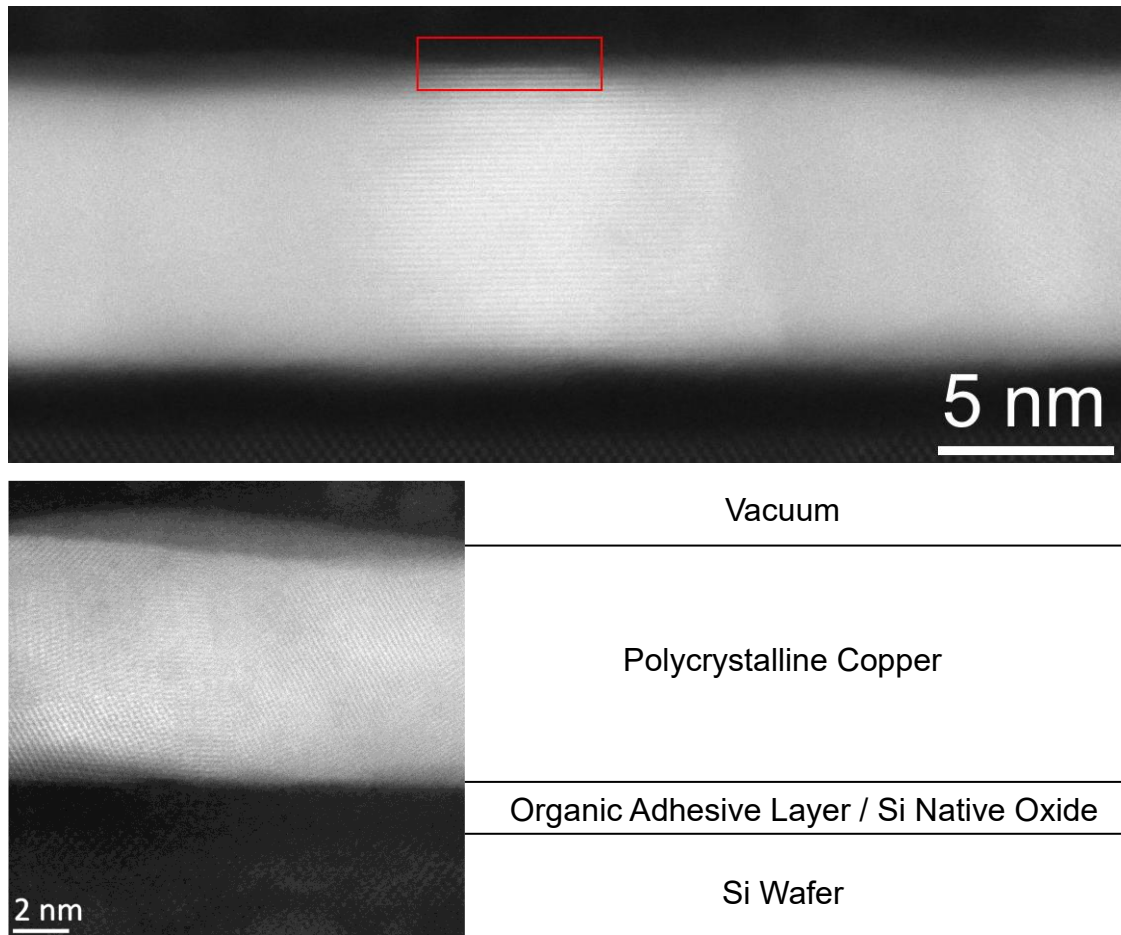
Figure 11: (Upper) Enlarged region from a MM | Cu | Al electrode detailing the surface of the film. The red square highlights the clearest region where a single copper crystallite extends through the entire thickness of the film as deposited. The extension of the lattice fringes to the very surface of the film supports the conclusion that the Al does not remain uniformly distributed but is redistributed across the surface of the film. (Lower) Further high-resolution STEM image of an MM | Cu | Al film, showing the non-uniform distribution of the metal oxide layer over the surface of the film.

5.3.1 Model patterning

For many practical applications it is necessary to pattern metal films, which risks undermining the effectiveness of a surface passivation layer. To investigate this conventional photolithography has been used to fabricate a regular array of 2 μm diameter holes in a 9 nm Cu film with and without a 0.8 nm Al over layer: Figure 12. The aperture density is ~6 million apertures per cm^{-2} which increases the sheet resistance of the bilayer

electrode from 8.7 ± 0.2 to $11.2 \pm 0.4\ \Omega\ \mathrm{sq}^{-1}$. At high resolution in Figure 12 (b), it can be seen that the chosen etchant and parameters does not cleanly remove all material and some debris remains within the aperture.
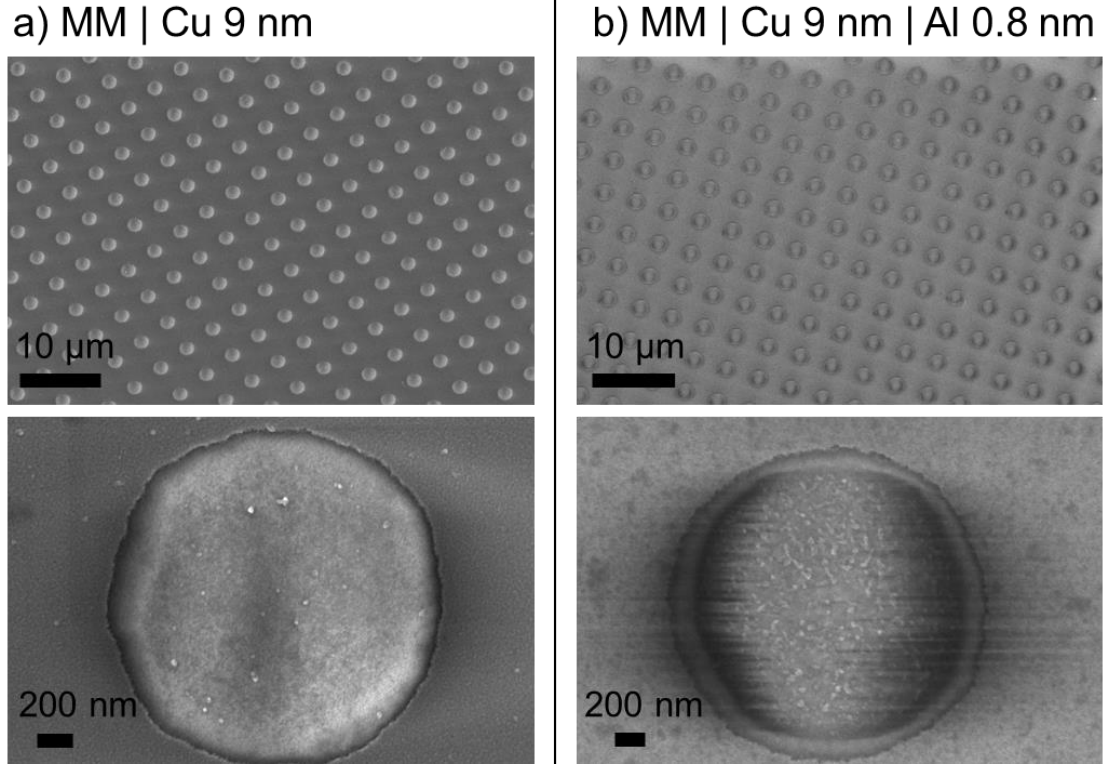
Figure 12: SEM images comparing the size and uniformity of the patterned electrodes produced using a conventional photolithography method and etched using ammonium persulfate solution. The cat's eye effect in the aperture is caused by charging of the underlying glass substrate.

The linear gain in transparency across the spectrum for the MM | Cu film (Figure 13) corroborates the images in Figure 12 where at high magnification the holes appear clean and free of particulate debris. Using this mask, the removal of a theoretical ~ 20% metal coverage (confirmed from the SEM images) would predict an average increase of (% Material removed $\times$ T$_{average}$) ~ 11% transmission which is in excellent agreement with Figure 13. The sheet resistance of the same film rises by 30% increase in the sheet resistance from 10.8 ± 0.2 to $14.1 \pm 0.4\ \Omega\ \mathrm{sq}^{-1}$ with patterning of the apertures: This non-ideal (> 20%) behaviour is attributed to scattering of electrons by the apertures.
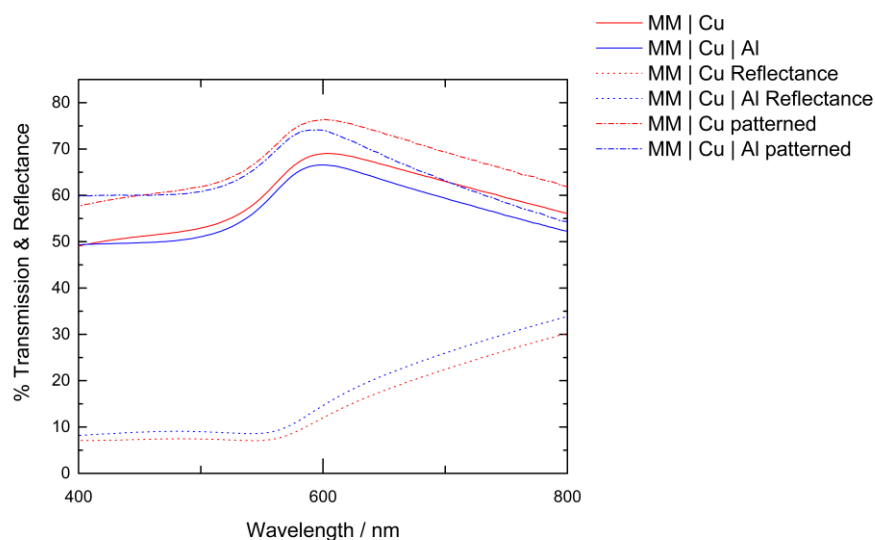
Figure 13: Far-field transparency of the MM | Cu 9 nm | Al 0.8 nm electrode (solid blue line) and MM | Cu 9 nm (solid red line), both with reflectance (dotted). The increase in transparency by patterning with a model structure of 2 μm diameter holes is shown (dotted-dashed lines).

Figure 14 shows the normalised evolution of the sheet resistance of the patterned films upon exposure to ambient air. As expected, the electrode without the 0.8 nm Al passivation layer oxidises more quickly upon incorporation of apertures, with the sheet resistance increasing at a rate of 0.0071 Ω sq^{-1} hr^{-1}, as compared to the unpatterned electrode which is effectively passivated (0 Ω sq^{-1} hr^{-1}). In contrast the stability of the MM | Cu | Al electrode is not adversely affected; Figure 14. After > 2 years exposure to air, the sheet resistance remained within < 1% of the starting value, and only 3.4% higher than its lowest value (which occurs after the initial decrease in sheet resistance). This can be rationalised by considering the small additional surface area of Cu that is created by the inclusion of apertures: a ~ 0.15% increase, which is a consequence of the very low metal thickness.
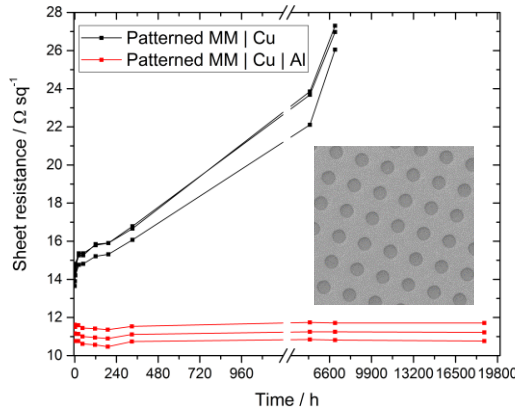
Figure 14: The change in sheet resistance of 9 nm Cu electrodes with an array of 2 µm dimeter apertures (as shown in the inset) upon exposure to ambient air for Cu films with (red) and without (black) an 0.8 nm Al over layer. Full SEM images are given in Figure 12 and the far-field transparency with and without apertures Figure 13.

5.4   Conclusion

It has been shown that over 900 hours in ambient air, unpatterned 9 nm thick Cu films passivated with an 0.8 nm evaporated Al layer are more stable than pure-Ag films of the same thickness fabricated using the best reported practice. Furthermore, after perforating with an array of ~6 million apertures per cm^{-2} the sheet resistance after 5000 hours in air is increased by only 3.4% from its lowest value. Due to the initial decrease in sheet resistance that occurs within the first hour of air exposure, the increase in sheet resistance for the starting value is < 1%. The remarkable effectiveness of this approach is shown to result from segregation of aluminium-copper-oxide at the boundaries between Cu crystallites upon exposure to air, which retards oxidation at those sites in the Cu film most vulnerable to oxidation. Crucially, the very low thickness of this passivation layer ensures that the underlying metal is not electrically isolated, and so this simple passivation step renders Cu films stable enough to compete with Ag as the base metal for transparent electrode applications in emerging optoelectronic devices.

5.5   Experimental

(Customised SPECTROS system integrated with N_2 glovebox, Kurt. J. Lesker)

Electrode preparation

Glass microscope slides (7525 M, J. Melvin Freed Brand) or polyethylene terephthalate (PET) substrates were ultra-sonically agitated for 15 minutes each in diluted surfactant (Hellmanex III, Hellma Analytics), deionised water and propan-2-ol (AnalaR, VWR). These substrates were then UV/O_3 treated for 15 minutes immediately prior to use. Where stated, these slides were transferred to a desiccator for derivatization with a molecular adhesive. Although high quality noble metal films form upon APTMS-derivatised glass substrates, the lower robustness of the Amine-Cu bonds is a vulnerability demonstrated when ultra-sonication in water is able to undermine and break apart the noble metal (Au) film. To compensate for this MPTMS and APTMS were added in equal quantities to a vial for the solvent-less deposition of the adhesive layer, where cleaned substrates were held at low pressure (< 50 mBar) for 4 hours in close proximity to the liquid phase alkylsilanes as the published protocol.[47] All substrates were then transferred to the evaporator for Al, Cu or Ag deposition using a base pressure of $< 5 \times 10^{-8}$ mbar unless stated. Al was evaporated at a rate of 0.1 Å s^{-1}, while Cu and Ag were evaporated at 1 Å s^{-1}. Thicknesses were calibrated using an Asylum Research MFP-3D AFM and monitored using quartz-crystal microbalances. Masks were exchanged where required by a series of transfer arms without breaking the vacuum. During metal deposition, the chamber pressure rose to approximately 5×10^{-7} mbar. For the Ag electrodes, two nucleation layers were compared (Figure). Polyethylenimine (PEI) was spin-cast onto freshly cleaned and UV/O_3 treated substrates (5000 rpm) from a 0.3% wt. aqueous solution and dried in air (110°C, 20 mins). Separate cleaned and UV/O_3 treated substrates were heated at 120°C overnight in a loosely sealed container together with 4 drops of MPTMS. Annealed samples were heated at 150°C for 3 hours unless stated otherwise, in a positive pressure glovebox with < 1 ppm O_2 and H_2O.

Sheet resistance evolution

25×25 mm substrates were used to evaporate an electrode onto which silver contacts were painted to connect a Keithley 2400 source meter. Resistances were calculated using the Van der Pauw method and an applied voltage of 5 mV. Electrodes were stored in ambient laboratory air and re-measured periodically. The temperature fluctuated between 18-30°C and the humidity between 15-50%.

AFM images

An Asylum Research MFP3D instrument was used in tapping mode to map the surface of the electrodes and calculate the surface roughness (RMS) value. For roughness

measurements, a 10 × 10 μm area was mapped and an area free of interference selected for a detailed scan (1 × 1 μm).

STEM and EDXS analyses

Transmission electron microscopy (TEM) specimens were prepared using conventional mechanical polishing followed by cryo-ion milling to electron transparency using Ar^+ at 6 keV. A final low-energy milling step was performed at < 2 keV in order to minimize surface damage. For local microstructure analyses, the samples were analysed using JEOL ARM200F TEM/scanning TEM (STEM) with a Schottky gun operating at 200 kV with probe and image aberration correctors. Images were obtained using a JEOL annular field detector with a probe current of approximately 19 pA, a convergence semi-angle of ~25 mrad, and an inner angle of 50 mrad. An Oxford Instruments X-MaxN 100TLE windowless silicon drift detector was used to perform STEM-EDX analysis.

Electrode patterning using photolithography

Electrodes were prepared as above, but on polished glass substrates (Borofloat BF33 glass wafers, Pi-Kem) and were patterned in air. Cu electrodes as prepared were primed with Microposit Primer and then Microposit S1818 photoresist was spin-cast at 4000 rpm, before baking in air at 115°C for 2 minutes. Samples were masked using Rubylith and exposed to 150 mJ cm^{-2} UV light (Suss Microtec MA/BA8 mask aligner). These were developed in Microposit MF-319 developer for 1 minute to remove the edge beads (2 mm strip removed). The holes were patterned using a 2 μm diameter patterned mask, with separation 2 μm (130 mJ cm^{-2}) and again developed for 2 minutes. The Cu was etched using a 3.65 mM ammonium persulfate solution. All samples were exposed for 20 s for clean holes, although after 10s the edge strip was completely removed. The mask was then removed using acetone. All samples were processed together and checked using SEM that hole size was comparable between sets (Figure 12).

X-ray photoelectron spectroscopy

Surface compositional and chemical state analysis was carried out using x-ray photoelectron spectroscopy (XPS) measurements conducted on a Kratos Axis Ultra DLD spectrometer at the University of Warwick Photoemission Facility. The samples were mounted on to a standard sample bar using electrically conductive carbon tape and loaded into the instrument. XPS measurements were performed in the main analysis chamber, with the sample being illuminated using a monochromated Al Kα x-ray source. The measurements were conducted at room temperature and at a take-off angle of 90° with

respect to the surface parallel. The core level spectra were recorded using a pass energy of 20 eV (resolution approx. 0.4 eV), from an analysis area of 300 microns $\times$ 700 microns. The spectrometer work function and binding energy scale of the spectrometer were calibrated using the Fermi edge and $3d_{5/2}$ peak recorded from a polycrystalline Ag sample prior to the commencement of the experiments. The data were analysed in the CasaXPS package, using Shirley backgrounds and mixed Gaussian-Lorentzian (Voigt) lineshapes. For compositional analysis, the analyser transmission function has been determined using clean metallic foils to determine the detection efficiency across the full binding energy range. Where samples were found to charge slightly under the x-ray beam the samples were flooded with a beam of low energy electrons during the experiment to compensate. This in turn necessitated charge referencing of the binding energy scale, with the C-C/C-H component of the C 1s region at 284.7 eV used as the reference energy.

5.6 References

[1]   D. S. Ghosh, *Ultrathin Metal Transparent Electrodes for the Optoelectronics Industry*; 2013.

[2]   J. Yun, *Adv. Funct. Mater.* **2017**, *27*, 1606641.

[3]   H. M. Stec, R. A. Hatton, *ACS Appl. Mater. Interfaces* **2012**, *4*, 6013.

[4]   M. J. Griffith, N. A. Cooling, B. Vaughan, D. C. Elkington, A. S. Hart, A. G. Lyons, S. Quereshi, W. J. Belcher, P. C. Dastoor, *IEEE J. Sel. Top. Quantum Electron.* **2016**, *22*, 4100714.

[5]   H. Lu, X. Ren, D. Ouyang, W. C. H. Choy, *Small* **2018**, *14*, 1703140.

[6]   T. Sannicolo, M. Lagrange, A. Cabos, C. Celle, J. P. Simonato, D. Bellet, *Small* **2016**, *12*, 6052.

[7]   T. Gao, B. Wang, B. Ding, J. K. Lee, P. W. Leu, *Nano Lett.* **2014**, *14*, 2105.

[8]   H. Kang, S. Jung, S. Jeong, G. Kim, K. Lee, *Nat. Commun.* **2015**, *6*, 6503.

[9]   K. Sivaramakrishnan, T. L. Alford, *Appl. Phys. Lett.* **2009**, *94*, 2104.

[10]   D. R. Sahu, J. L. Huang, *Appl. Surf. Sci.* **2006**, *253*, 915.

[11]   K. Zilberberg, T. Riedl, *J. Mater. Chem. A* **2016**, *4*, 14481.

[12]   H. Kim, J. S. Horwitz, G. P. Kushto, Z. H. Kafafi, D. B. Chrisey, *Appl. Phys. Lett.* **2001**, *79*, 284.

[13]   B. Vaughan, X. Zhou, G. Bryant, M. Wilson, P. C. Dastoor, C. J. Mulligan, W. J. Belcher, *Sol. Energy Mater. Sol. Cells* **2013**, *120*, 9.

[14]   F. C. Krebs, N. Espinosa, M. Hösel, R. R. Søndergaard, M. Jørgensen, *Adv. Mater.* **2014**, *26*, 29.

[15]   M. Watanabe, H. Watanabe, H. Ando, T. Handa, T. Ichino, N. Kuwakiet, *Zairyo-to-Kankyo* **2007**, *56*, 10.

[16]   J. B. Kim, C. S. Kim, Y. S. Kim, Y.-L. Loo, *Appl. Phys. Lett.* **2009**, *95*, 183301.

[17]   A. Behrendt, C. Friedenberger, T. Gahlmann, S. Trost, T. Becker, K. Zilberberg, A. Polywka, P. Görrn, T. Riedl, *Adv. Mater.* **2015**, *27*, 5961.

[18]   C. Zhang, D. Zhao, D. Gu, H. Kim, T. Ling, Y. K. R. Wu, L. J. Guo, *Adv. Mater.* **2014**, *26*, 5696.

[19]   K. Ellmer, Past achievements and future challenges in the development of optically transparent electrodes. *Nat. Photonics* **2012**, *6*, 809–817.

[20]   G. Dennler, C. Lungenschmied, H. Neugebauer, N. S. Sariciftci, M. Latrèche, G. Czeremuszkin, M. R. Wertheimer, *Thin Solid Films* **2006**, *511–512*, 349.

[21]   M. Lu, S. Huang, S. Chen, Q. Ju, M. Xiao, X. Peng, S. Wang, Y. Meng, *Polym. J.* **2018**, *50*, 239.

[22]   R. A. Matula, *J. Phys. Chem.* **1979**, *8*, 1147.

[23]   Nasdaq, Nasdaq: Commodity Prices.

[24]   G. Zhao, S. M. Kim, S. G. Lee, T. S. Bae, C. W. Mun, S. Lee, H. Yu, G. H. Lee, H. S. Lee, M. Song, J. Yun, *Adv. Funct. Mater.* **2016**, *26*, 4180.

[25]   O. S. Hutter, R. A. Hatton, *Adv. Mater.* **2015**, *27*, 326.

[26]   H. J. Pereira, J. Reed, J. Lee, S. Varagnolo, G. D. M. R. Dabera, R. A. Hatton, *Adv. Funct. Mater.* **2018**, *28*, 1802893.

[27]   C. Gattinoni, A. Michaelides, *Surf. Sci. Rep.* **2015**, *70*, 424.

[28]   I. Platzman, R. Brener, H. Haick, R. Tannenbaum, *J. Phys. Chem. C* **2008**, *112*, 1101.

[29]   F. Wiame, V. Maurice, P. Marcus, *Surf. Sci.* **2007**, *601*, 1193.

[30]   J. Li, J. W. Mayer, E. G. Colgan, *J. Appl. Phys.* **1991**, *70*, 2820.

[31]   F. W. Young, J. V Cathcart, a. T. Gwathmey, *Acta Metall.* **1956**, *4*, 145.

[32]   W. Gao, H. Gong, J. He, A. Thomas, L. Chan, S. Li, *Mater. Lett.* **2001**, *51*, 78.

[33]   M. O'Reilly, X. Jiang, J. T. Beechinor, S. Lynch, C. NíDheasuna, J. C. Patterson,

G. M. Crean, *Appl. Surf. Sci.* **1995**, *91*, 152.

[34]   M. C. Biesinger, L. W. M. Lau, A. R. Gerson, R. S. C. Smart, *Appl. Surf. Sci.* **2010**, *257*, 887.

[35]   F. K. Mugwang'a, P. K. Karimi, W. K. Njoroge, O. Omayio, S. M. Waita, *Int. J. Thin Film. Sci. Technol.* **2013**, *2*, 12.

[36]   I. E. Stewart, S. Ye, Z. Chen, P. F. Flowers, B. J. Wiley, *Chem. Mater.* **2015**, *27*, 7788.

[37]   C. Lee, N. R. Kim, J. Koo, Y. J. Lee, H. M. Lee, *Nanotechnology* **2015**, *26*.

[38]   P. C. Hsu, H. Wu, T. J. Carney, M. T. McDowell, Y. Yang, E. C. Garnett, M. Li, L. Hu, Y. Cui, *ACS Nano* **2012**, *6*, 5150.

[39]   Z. Chen, S. Ye, I. E. Stewart, B. J. Wiley, *ACS Nano* **2014**, *8*, 9673.

[40]   O. S. Hutter, H. M. Stec, R. A. Hatton, *Adv. Mater.* **2013**, *25*, 284.

[41]   M. S. Tyler, O. S. Hutter, M. Walker, R. A. Hatton, *ChemPhysChem* **2015**, *16*, 1203.

[42]   L. Gan, R. D. Gomez, A. Castillo, P. J. Chen, C. J. Powell, W. F. Egelhoff, *Thin Solid Films* **2002**, *415*, 219.

[43]   J. Evertsson, F. Bertram, F. Zhang, L. Rullik, L. R. Merte, M. Shipilin, M. Soldemo, S. Ahmadi, N. Vinogradov, F. Carlà, J. Weissenrieder, M. Göthelid, J. Pan, A. Mikkelsen, J. O. Nilsson, E. Lundgren, *Appl. Surf. Sci.* **2015**, *349*, 826.

[44]   S. K. Chawla, B. I. Rickett, N. Sankarraman, J. H. Payer, *Corros. Sci.* **1992**, *33*, 1617.

[45]   A. Khan, V. H. Nguyen, D. Muñoz-Rojas, S. Aghazadehchors, C. Jiménez, N. D. Nguyen, D. Bellet, *ACS Appl. Mater. Interfaces* **2018**, *10*, 19208.

[46]   J. Shewchun, R. Singh, M. A. Green, *J. Appl. Phys.* **1977**, *48*, 765.

[47]   H. M. Stec, R. J. Williams, T. S. Jones, R. A. Hatton, *Adv. Funct. Mater.* **2011**, *21*, 1709.

[48] K. C. Vrancken, K. Possemiers, P. Van Der Voort, E. F. Vansant, *Colloids Surfaces A Physicochem. Eng. Asp.* **1995**, *98*, 235.

[49] K. M. R. Kallury, P. M. Macdonald, M. Thompson, *Langmuir* **1994**, *10*, 492.

[50] H. M. Stec, Metal window electrodes for organic photovoltaics, University of Warwick, 2013.

[51] D. K. Aswal, S. Lenfant, D. Guerin, J. V Yakhmi, D. Vuillaume, *Anal. Chim. Acta* **2006**, *568*, 84.

[52] P. M. Dietrich, C. Streeck, S. Glamsch, C. Ehlert, A. Lippitz, A. Nutsch, N. Kulak, B. Beckhoff, W. E. S. Unger, *Anal. Chem.* **2015**, *87*, 10117.

[53] T. Plach, K. Hingerl, S. Tollabimazraehno, G. Hesser, V. Dragoi, M. Wimplinger, *J. Appl. Phys.* **2013**, *113*, 094905.

[54] K. M. McPeak, S. V. Jayanti, S. J. P. Kress, S. Meyer, S. Iotti, A. Rossinelli, D. J. Norris, *ACS Photonics* **2015**, *2*, 326.

[55] S. Jeong, S. Jung, H. Kang, D. Lee, S. Choi, S. Kim, B. Park, K. Yu, J. Lee, K. Lee, *Adv. Funct. Mater.* **2017**, *27*, 1.

[56] J. Iijima, J. W. Lim, S. H. Hong, S. Suzuki, K. Mimura, M. Isshiki, *Appl. Surf. Sci.* **2006**, *253*, 2825.

[57] C. E. Sanders, D. Verreault, G. S. Frankel, H. C. Allen, *J. Electrochem. Soc.* **2015**, *162*, C630.

[58] C. Zhang, N. Kinsey, L. Chen, C. Ji, M. Xu, M. Ferrera, X. Pan, V. M. Shalaev, A. Boltasseva, L. J. Guo, *Adv. Mater.* **2017**, *29*, 1605177.

[59] R. Liu, F. Zhang, C. Con, B. Cui, B. Sun, *Nanoscale Res. Lett.* **2013**, *8*, 155.

[60] K. Ralls, T. Courtney, J. Wulff, *Introduction to Materials Science and Engineering*; John Wiley & Sons: New York, 1976.

[61] M. A. Marcus, J. E. Bower, *J. Appl. Phys.* **1997**, *82*, 3821.

[62] V. Vaithyanathan, C. Wolverton, L. Q. Chen, *Acta Mater.* **2004**, *52*, 2973.

[63]   W. A. Lanford, P. J. Ding, W. Wang, S. Hymes, S. P. Muraka, *Thin Solid Films* **1995**, *262*, 234.

[64]   G. D. M. R. Dabera, M. Walker, A. M. Sanchez, H. J. Pereira, R. Beanland, R. A. Hatton, *Nat. Commun.* **2017**, *8*, 1894.

[65]   C. Y. Ho, M. W. Ackerman, K. Y. Wu, T. N. Havill, R. H. Bogaard, R. A. Matula, S. G. Oh, H. M. James, Electrical Resistivity of Ten Selected Binary Alloy Systems. *J. Phys. Chem. Ref. Data* **1983**, *12*, 183–322.

5.7 Appendix
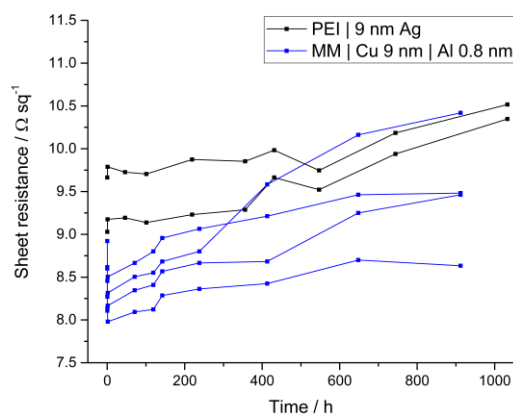
Figure A1: A direct comparison as made in text of all MM | Cu | Al electrodes and the best performing Ag electrode structure (PEI nucleation layer). The temperature and humidity fluctuated in the range 18-30°C and 15-50% respectively.
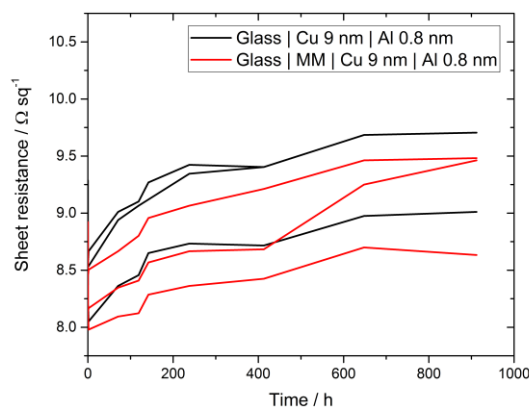
Figure A2: A direct comparison as made in text of equivalent Cu | Al electrodes with and without a molecular adhesive nucleation layer (mixed MPTMS/APTMS). One MM | Cu | Al electrode was excluded due to mechanical damage from testing or a natural defect which has expressed itself as earlier discussed. The temperature and humidity fluctuated in the range 18-30°C and 15-50% respectively.

6 Enhanced Oxidation Stability of Transparent Copper Films Using a Hybrid Organic-Inorganic Nucleation Layer

The majority of the work presented in this chapter has been published in the following article:

6.1 Chapter Summary

This chapter describes a novel seed layer for the formation of slab-like transparent copper films on glass and plastic substrates, based on a mixed molecular monolayer and an ultra-thin (0.8 nm) aluminium layer, both deposited from the vapour phase, which substantially outperforms the best nucleation layer for optically thin copper films reported to date. Using this hybrid layer, the metal percolation threshold is reduced to < 4 nm nominal thickness and the long-term stability of sub-10 nm films towards oxidation in air is comparable to that of silver films of the same thickness fabricated using the best reported seed layer for optically thin silver films reported to date. The underlying reason for the remarkable effectiveness of this hybrid nucleation layer is elucidated using a combination of photoelectron spectroscopy, small angle X-ray studies, atomic force microscopy and transmission electron microscopy.

6.2 Introduction

Despite their current dominance, it is clear that an alternative to the transparent conducting oxides indium tin oxide (ITO), fluorine doped tin oxide and aluminium doped zinc oxide is required as the window electrode for flexible and low cost optoelectronic devices including organic photovoltaics (OPVs).[3,59] Metal films with a thickness of 6-10 nm deposited by vacuum evaporation are a promising contender because they are chemically well-defined and compatible with flexible substrates, whilst also offering high electrical conductivity and very low surface roughness.[3] Additionally, vacuum evaporation is established as a low-cost large-scale production method for the deposition of thin metal films that is compatible with roll-to-roll processing.[60] Lithographic patterning of thin metal films and/or using wide band gap anti-reflecting interlayers enables sufficient far-field transparency for metal film electrodes to be competitive with ITO glass for the same sheet resistance.[11,12,61–63]

Until now, silver (Ag) has been the favoured base metal for this purpose due to its low optical losses and highest electrical conductivity amongst metals.[64] However, Ag is a costly metal and so its use in large area, low cost applications would necessitate recovery and re-use of the metal.[65] In recent years copper (Cu) has received growing attention as a low cost alternative to Ag for window electrode applications because it has an electrical conductivity comparable to Ag at ~1% of the cost.[66–68] It has also been shown that the higher optical losses in Cu, as compared to Ag, can be mitigated by electrode and/or device design, including using a metal oxide overlayer to increase transparency.[69–71]

Due to the high surface energy of Cu and Ag these metals interact only weakly with glass and other technologically important transparent plastic substrates, such as polyethylene terephthalate (PET) and polyethylene naphthalate (PEN), and so the formation of robust and continuous films of these metals with thickness < 10 nm is notoriously difficult to achieve using thermal evaporation.[60,72] Metal atoms condensing on the substrate diffuse over the surface and aggregate into particles which only form a continuous network for nominal thicknesses > 10 nm.[11,73,74] To enable the formation of uniform slab-like Cu and Ag films at sub-10 nm metal thickness a variety of different inorganic and organic nucleation layers have been proposed whose primary function is to suppress metal atom diffusion during early stages of film growth.[62,72,75,76] For evaporated Cu films the most successful seed layers to date are based on the use of molecular

monolayers that chemically bind both to the substrate and Cu, including 3-mercaptopropyl(trimethoxysilane) [MPTMS] and 3-aminopropyl(trimethoxysilane) [APTMS] (Figure 1).[31,34,77] In particular a mixed monolayer (MM) of APTMS and MPTMS is (as described in Chapter 1) balances strong mechanical strength of the resultant Cu films with fast, solvent-free processing and is transferrable directly from glass to plastic substrates for flexible electrodes. For Ag films, PEI is the seed layer of choice because it is proven to facilitate the formation of compact Ag films that are strongly adhered to the substrate.[11]
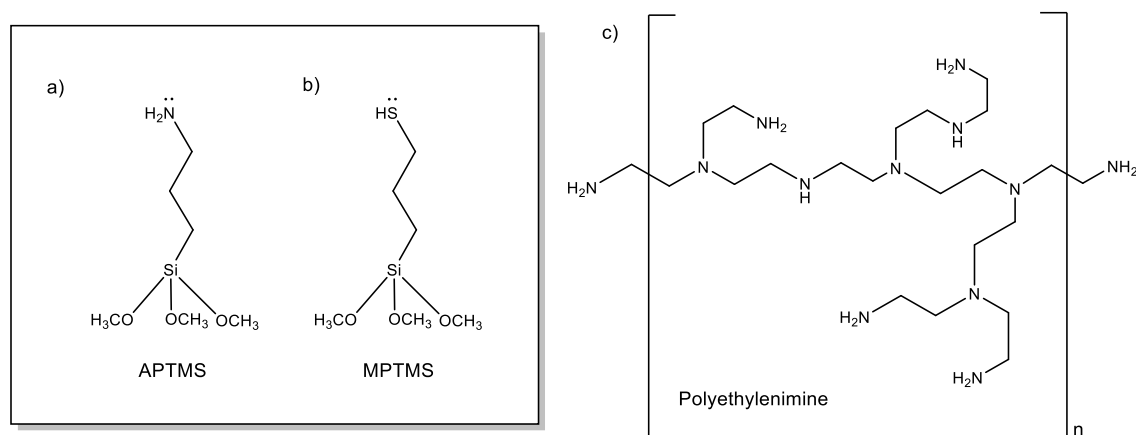

Figure 1: Chemical structures of the three conventional seed layer materials used in this chapter: (a) APTMS and (b) MPTMS which are typically used together for Cu films in this work and (c) Polyethylenimine (PEI) for Ag films.

Surprisingly, despite the high potential of optically thin Ag and Cu films as transparent electrodes for optoelectronic applications, studies of the long-term stability of Ag or Cu window electrodes are sparse.[31,78–80] Stability towards air oxidation is a particularly important consideration because oxidation of the surface of very thin metal films can have a large detrimental effect on the electrode sheet resistance, as well as forming a barrier to charge transport between the electrode and an adjacent semiconducting layer in a device.[79] In practice the substrate electrode is inevitably exposed to air during transportation, or during one or more device fabrication steps, and even with device encapsulation air gradually ingresses into the device over time; a particular challenge for achieving useful lifetimes on plastic substrates.[78]

It is known that for insulating layers below 5 nm that (inelastic) direct quantum tunnelling through the insulating layer becomes significant and so it is possible that, in the context of an OPV, a thin oxide layer at the surface of a Cu electrode could be tolerated.[40,41] In fact for practical application in photovoltaics Shewchun *et al.* demonstrated that the device characteristics are not significantly degraded by inclusion of an insulating layer with thickness below 15 Å.[39] Furthermore, both CuO and Cu_2O are direct band gap semiconductors, with band gaps of 1.6 and 2.3 eV respectively,[81] and C. Zuo *et al.* showed exceptional performance in a perovskite PV device using a < 10 nm thick solution processed CuO/Cu_2O hole transport layer (HTL): The current, voltage and stability exceeded that of the reference devices using a conventional PEDOT:PSS HTL.[81]

In Chapter 5 it was shown that the surface of Cu can be effectively passivated with an extremely thin film of Al (0.8 nm). The remarkable effectiveness of such a thin Al overlayer was shown to be a consequence of the diffusion of Al selectively to the grain boundaries between Cu crystallites where it forms $Cu_xAl_yO_z$ plugs that block oxidation at the grain boundaries which are the most vulnerable points in the Cu film to oxidation, and which nucleate further oxidation.[82,83] In this chapter the possibility that a small quantity of metallic Al buried at the interface between the Cu film and the organic seed layer can spontaneously diffuse vertically along the grain boundaries between crystallites of the Cu film, until it reaches the surface and forms an oxide plug thereby passivating the grain boundaries toward oxidation, was explored (Figure 2).
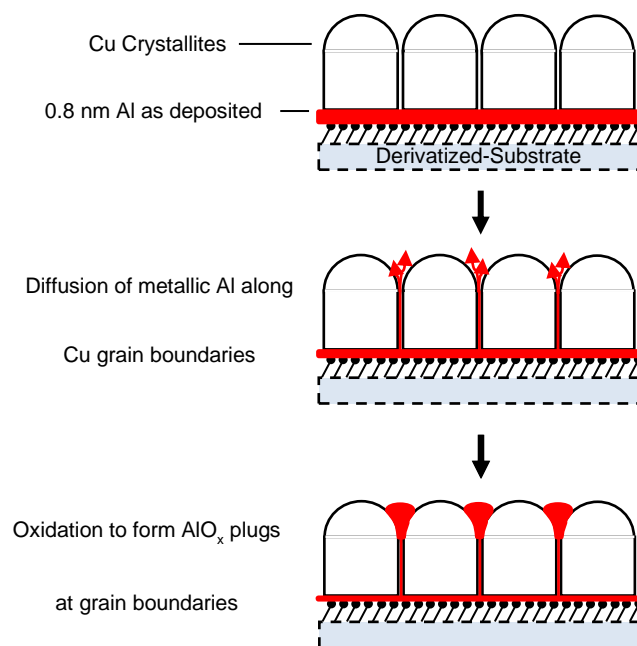
Figure 2: Schematic of the mechanism by which a thin buried Al layer may act as a barrier to the oxidation of Cu films as initially proposed.

Whilst it is shown in this chapter that the addition of an ultra-thin Al layer buried at the organic-Cu interface did dramatically improve the stability of the subsequent Cu film, experimental evidence shows that this was achieved primarily not through diffusion of Al along grain boundaries but by the formation of an exceptionally slab-like Cu film composed of larger crystallites. Thus, in this chapter a novel organic-inorganic bilayer for seeding the formation of Cu films is described which substantially outperforms the molecular monolayer approach alone in terms of the percolation threshold for Cu films and dramatically improves the long-term stability towards oxidation in air. The hybrid layer is based on a mixed molecular monolayer (MM) deposited from the vapour phase followed by an ultra-thin (0.8 nm) aluminium (Al) layer. A combination of photoelectron spectroscopy, small angle X-ray studies (SAXS), atomic force microscopy and transmission electron microscopy are used to elucidate the underlying reasons for the effectiveness of this hybrid layer.

6.3 Results and Discussion

Figure 3 is an expanded schematic of the electrode structure studied. The Al and Cu films were deposited sequentially without breaking vacuum and the metal film is supported on a glass or plastic substrate derivatized with a mixed APTMS and MPTMS monolayer. The thiol-Al bond is equal to, or stronger than, the thiol-Cu bond and as such the mechanical robustness of the electrode should not be compromised by the inclusion of a thin Al layer between the molecular adhesion layer and Cu film.[84]
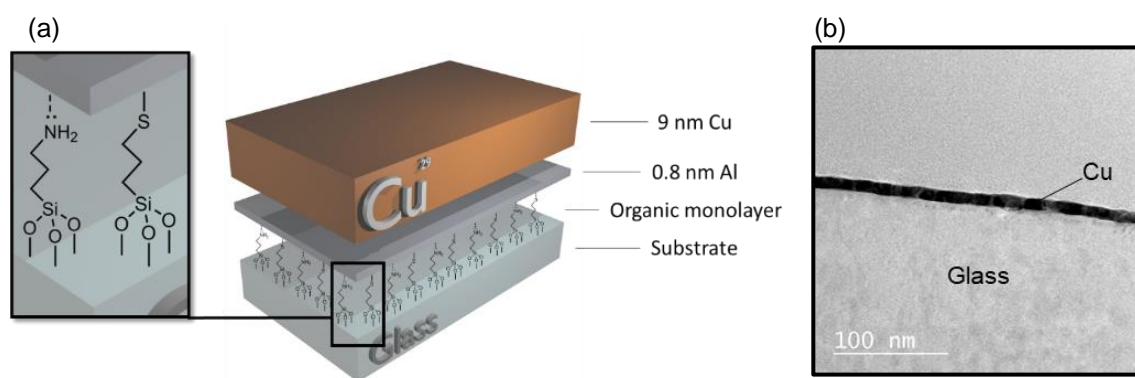

Figure 3: (a) Schematic diagram depicting the structure of the hybrid nucleation layer and Cu electrode. The expansion (left) shows the mixed molecular monolayer bound to the substrate which can be glass (as shown) or plastic. (b) TEM image of the MM | Al | Cu electrode cross-section which the slab-like form of the Cu film.

Stec *et al.* have demonstrated the transferability of Cu films deposited on the organic mixed monolayer from glass to plastic substrates.[34] Figure 4 shows that the choice of transparent substrate does not affect the initial properties of a Cu film upon the organic monolayer with the addition of an intermediary 0.8 nm Al layer, since the transparency and sheet resistance are equivalent on flexible plastic and glass substrates.
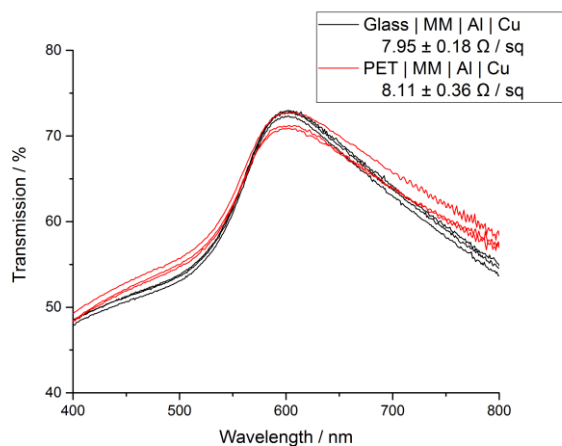
Figure 4: Transmission spectra of evaporated 9 nm Cu films on glass (black) and PET (red) modified with a mixed monolayer (MM) / 0.8 nm Al seed layer. The transparency and initial sheet resistance on both substrates are equivalent.

The oxidation of Cu in air is not a self-limiting process and results in the formation of a mixture of the short-lived hydroxide ($Cu(OH)_2$) and stable oxides (Cu_2O and CuO), all of which have a conductivity at least six orders of magnitude lower than the base metal.[36,85–88] Consequently, due to the very low metal thickness the sheet resistance is a sensitive probe of oxidation of optically thin Cu films in air.[32,70,77] It is evident from Figure 5 that using a mixed APTMS/MPTMS seed layer reduces the rate of oxidation of a 9 nm Cu film on glass by a factor of 4 from 0.0198 to 0.0048 Ω sq^{-1} hr^{-1}. This large improvement in stability can be rationalized in terms of the more compact slab-like structure of the Cu film deposited onto seed layer modified glass, which impedes the diffusion of oxygen along the grain boundaries between crystallites.[31]
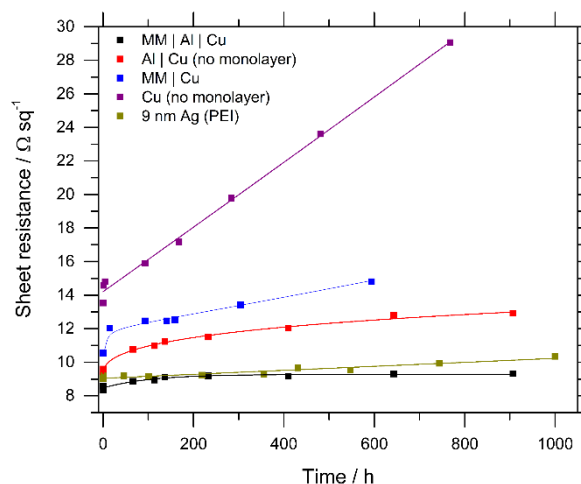
Figure 5: Evolution of the sheet resistance for representative electrodes in air for 6 electrode structures. All Al layers are 0.8 nm thick and all Cu layers 9 nm thick for comparison. The fitted lines are to 'guide the eye' only. The corresponding electrode structures are given in full in Table 1. Appendix Figures A1 and A2 show the complete data sets for all electrode structures. The temperature and humidity fluctuated in the range 18-30°C and 15-50% respectively during testing.

Table 1: The sheet resistance of the different electrode structures investigated. Sheet measurements were made immediately after electrode fabrication.

Abbreviations	Full Structure (Glass Substrates)	Average Sheet Resistance ± Standard Deviation (Ω sq^{-1}) *(Champion)*
MM | Cu	APTMS:MPTMS | 9 nm Cu	10.8 ± 0.2 *(10.5)*
MM | Al | Cu	APTMS:MPTMS | 0.8 nm Al | 9 nm Cu	8.7 ± 0.1 *(8.6)*
Glass | Cu	9 nm Cu directly on glass	13.8 ± 0.6 *(13.3)*
Glass | Al | Cu	0.8 nm Al | 9 nm Cu directly on glass	9.0 ± 0.3 *(8.8)*
PEI | Ag*	PEI (spin coated) | 9 nm Ag	9.4 ± 0.3 *(9.0)*

*Matching 9 Ω sq^{-1} reported by Kang *et al.*[5]

198

The stability of the films towards oxidation in air is dramatically improved by a factor of ~ 8 from 0.0198 to 0.0026 Ω sq^{-1} hr^{-1} over those deposited directly on glass upon inclusion of an 0.8 nm Al seed layer, as compared to a ~4× improvement for the organic seed layer. These beneficial effects are additive and so using the organic monolayer in conjunction with the Al nucleation layer improves the stability in air by > 37× to 0.0005 Ω sq^{-1} hr^{-1}. This stabilizing effect is also achieved on flexible plastic substrates (Appendix, Figure A3). Remarkably the rate of oxidation of the Cu film with a buried Al layer is comparable to that achieved using an Al or Ni deposited to the top surface of the Cu film.[31,89] Also included in Figure 5 is the evolution of the sheet resistance of a 9 nm Ag film fabricated using a polyethylenimine (PEI) adhesion layer, which serves as a benchmark against which the stability of the Cu films can be judged, since optically-thin Ag films supported on PEI modified plastic substrates are the best performing Ag film electrodes to date.[11,60] It is evident from Figure 5 that Cu films supported on the hybrid seed layer are more stable towards increasing sheet resistance than Ag films of the same thickness deposited onto a PEI seed layer.

Stec *et al.* have shown that for sub-10 nm Au films bound strongly to the substrate by a mixed MPTMS/APTMS monolayer (MM) the film crystallinity can be significantly increased by annealing at 200°C for 10 minutes which reduces the film resistivity.[34] To determine the effect of heating in the current case, 9 nm Cu films supported on a mixed molecular monolayer with and without an intermediary Al layer were heated in a nitrogen atmosphere for 10 minutes at increasing temperature, and the sheet resistance measured: Figure 6. Annealing at only 120°C reduced the sheet resistance of both films, although the reduction was largest for the MM | Al 0.8 nm | Cu 9 nm films which reduced from 8.4 ± 0.1 Ω sq^{-1} to a minimum of 6.9 ± 0.3 Ω sq^{-1}. Although in Figure 6 Cu films both with and without a 0.8 nm Al underlayer reduce in sheet resistance as expected, the magnitude of the reduction is higher with the inclusion of the Al layer. It is possible this is caused by an additional effect of the dealloying of Al from Cu, since we have established this occurrence when Al is deposited on top of Cu in Chapter 5 and Cu/Al alloys are well known to have a much higher resistivity than pure Cu.[31,87,90] All thin metal films are susceptible to dewetting at elevated temperature when the metal atoms have sufficient thermal energy to overcome the adhesion to the substrate, although Cu is known to have a higher morphological stability than Ag and Au.[91] Dewetting leads to the formation of isolated or semi-isolated metal nanoparticles at which point the conductivity of the film rapidly deteriorates. It is clear from Figure 6 that the onset of this dewetting occurs at

significantly higher temperature for MM | Al | Cu (> 220°C) than the MM | Cu film (~180°C).
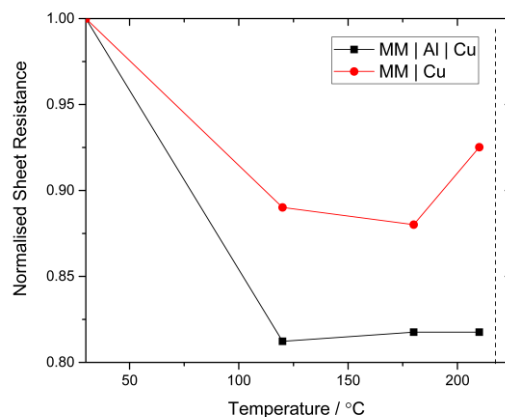
Figure 6: A graph showing normalised sheet resistance while gradually ramping up temperature stepwise under inert N_2 atmosphere for 10 minutes at 120, 160, 210 and 250°C for two classes of electrode; MM | Cu 9 nm and MM | Al 0.8 nm | Cu 9 nm. The dotted line represents that when heated above 220°C the sheet resistance of both films increased by orders of magnitude.

As explained earlier the idea behind the inclusion of a buried 0.8 nm Al layer at the organic/Cu interface was that the metallic Al would diffuse along the Cu grain boundaries to the surface of the film where it would oxidize to form AlO_x 'plugs' passivating the most vulnerable points of the Cu film to oxidation (i.e. the grain boundaries), so that the final result is essentially the same as the 0.8 nm Al overlayer approach to passivation described in Chapter 5.[31] To investigate this possibility X-ray photoelectron spectroscopy was used to probe for Al at the surface of the film before and after 400 hours air-exposure (Figure 7). Based on the inelastic electron mean-free path (λ) of photoelectrons ejected from the Al 2s orbital (binding energy: 119.3 eV, λ = 22 Å for metallic Cu) it is estimated that > 95% of the signal is derived from the top 6 nm of the metal film (3λ).[92] The absence of a significant peak that can be assigned to Al or Al_2O_3 is compelling evidence that the Al remains buried at the substrate interface. Over time exposed to air however a significant peak at 117.9 eV appears, associated with metallic Al. This is evidence that after > 400 hours Al is mobile, either through alloying with Cu

or diffusing along grain boundaries. The low intensity and presence of metallic Al, rather than the oxide Al_2O_3, indicates that Al diffuses through the Cu lattice and forms a graduated alloy of highest concentration at the substrate interface and little at the air interface. If Al were diffusing along grain boundaries it would be expected to oxidize rapidly. This, together with the long timescale of this process (400 to 8700+ hours), indicate that this process is not the origin of the initial improvement in stability towards air oxidation with the buried Al layer.
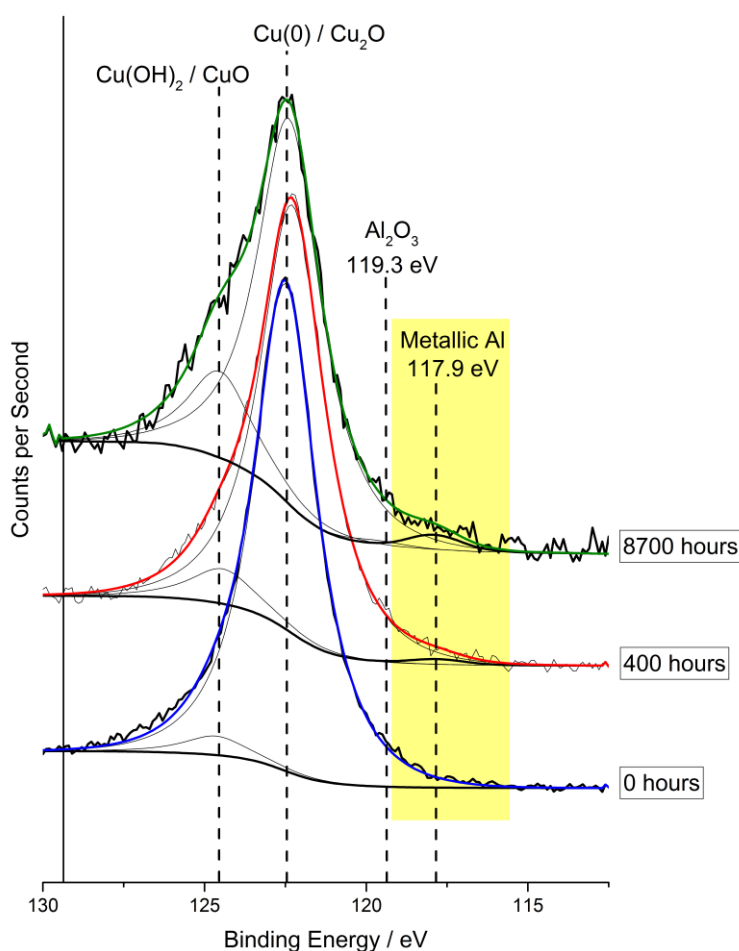
Figure 7: High resolution X-ray photoelectron spectroscopy (XPS) spectra showing the overlapping Cu 3s and Al 2s regions for a MM | Al 0.8 nm | Cu 9 nm electrode at 3 time points; Initial (Blue), after 400 hours in ambient air (Red) and after 1 year in ambient air (green). The highlighted region in yellow shows where metallic Al 2s is predicted to feature. The detector was placed incident normal to the substrate (take-off angle: 90°) and so the sampling depth is approximately 6 nm.

Further evidence that the ultra-thin Al is confined to the buried interface is corroborated by the small but significant reduction in sheet resistance during the first 48 hours after deposition. The 0.3 Ω sq^{-1} average reduction is sheet resistance over this period is consistent with de-alloying of Al as previously observed for the case of the 0.8 nm Al on top of the Cu film (Chapter 5): At the very early stages of Cu deposition onto the Al layer it is reasonable to assume that the Cu forms an over-saturated solid solution of Cu and Al at the interface and, as established in bulk Cu/Al alloys, segregation (precipitation) then occurs spontaneously.[93] As sheet resistance increases in proportion to the Al content in Cu, precipitation from the alloy layer is expected to lower the sheet resistance.

To gain insight into why the hybrid layer is more effective than the molecular nucleation layer alone at seeding Cu film formation, small-angle X-ray scattering (SAXS) was used to determine the size distribution of the Cu crystallites both for a Cu film thickness of 9 nm and 4 nm deposited onto a glass derivatized with a molecular monolayer, with and without an 0.8 nm Al seed layer.[94–96]
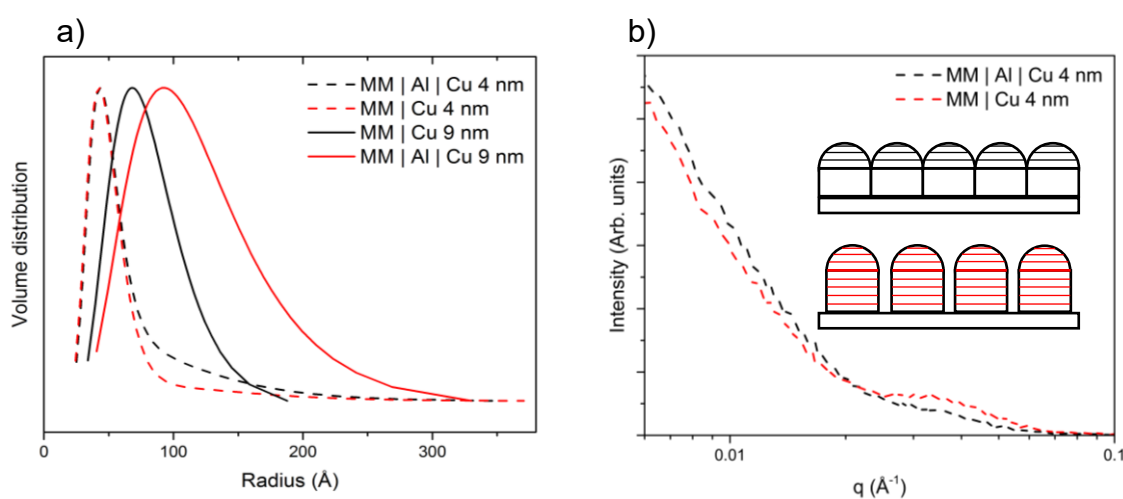
Figure 8: The results of a Small-Angle X-ray Scattering (SAXS) study for 4 and 9 nm thick Cu films deposited onto two seed layers. a) The outputs of a simplified model fitting the SAXS data of the electrodes as prepared, where the polycrystalline structure is modelled as a monolayer of spherical particles. An example of how this data was extracted is shown below in Figure 9. b) The raw SAXS data for the early-stage (4 nm) Cu films. (Inset) A simplified depiction of the difference between the Cu film structure with (black) and without (red) the 0.8 nm Al layer, with the volume sampled by SAXS lined. The slab-like nature of these polycrystalline films is well established on the

molecular monolayer,[31] and confirmed on the hybrid nucleation layer reported here by TEM in Figure 3 (b).
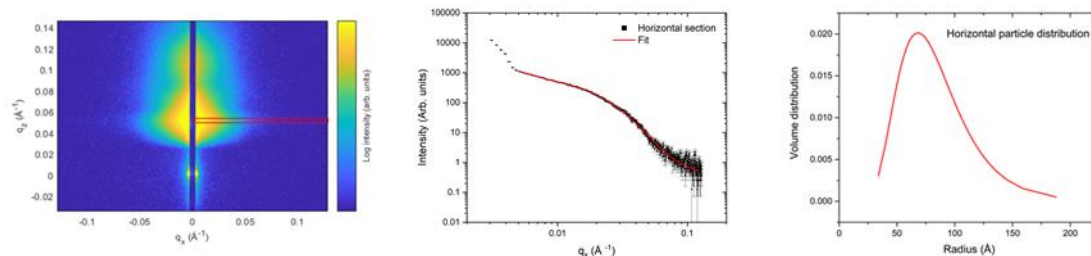
Figure 9: (Left) An example 2D detector image from GISAXS of a MM | Cu (9 nm) film, with the horizonal section used to extract particle radii highlighted in red. (Centre) The results of fitting the horizontal sub-section using a model based upon a monolayer of spherical particles. (Right) The resultant particle size distribution.

It is evident from Figure 8 (a) that for a Cu thickness of 4 nm (i.e. in the early stage of film formation) the mean horizontal crystallite radius is comparable with and without the 0.8 nm Al. However, the much less pronounced hump in intensity in Figure 8 (b) indicates that the surface roughness of the 4 nm Cu film supported on hybrid layer is significantly reduced, consistent with a more compact metal film having a smaller volume that can be sampled by SAXS (illustrated in Figure 8 (b)).
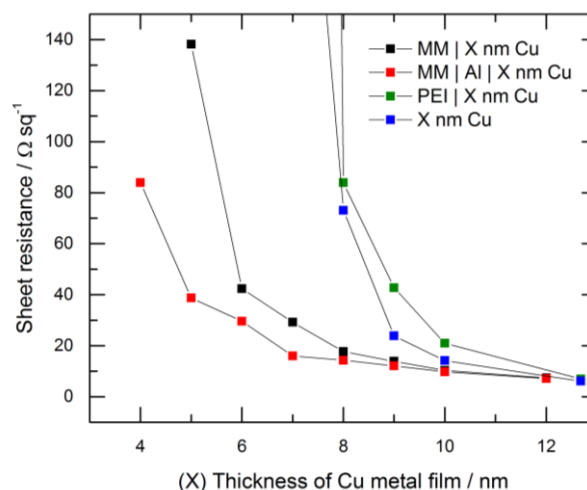
Figure 10: A comparison of the effect that reducing the Cu film thickness has on the sheet resistance for a series of nucleation layers.

When the Cu thickness is increased to 9 nm there is a doubling of the size of the Cu crystallites formed on the hybrid adhesive later, that does not occur to the same extent for films on the molecular seed layer. This increase in crystallite size is largely accommodated by more densely packing the crystallites within the film, reducing the contact resistance between them and so reducing sheet resistance (Figure 7). This is reflected in the lower sheet resistance and percolation thickness, but was difficult to probe using AFM because the radius of the AFM tip was 7 nm and crystallite radii are in the range 5 – 30 nm (Figure 12); although a small reduction in the root mean square roughness (RMS) from 1.02 ± 0.01 nm to 0.93 ± 0.03 nm does support the finding of the SAXS experiment.
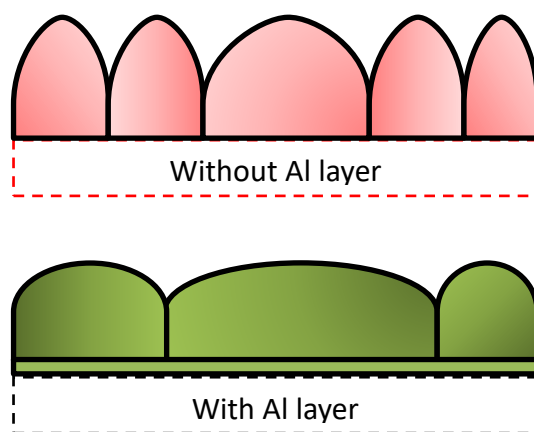
Figure 11: Schematic diagram depicting how the morphology of the Cu film differs with and without an Al interlayer, based on the available evidence.
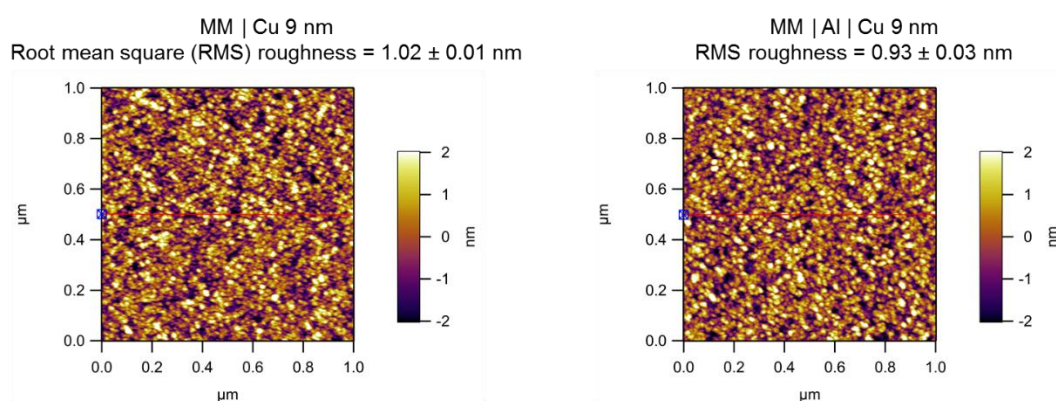
Figure 12: AFM images comparing the surface roughness of two electrode structures; MM | Cu 9 nm and MM | Al 0.8 nm | Cu 9 nm.

The onset of this process of coalescence is expected to occur for lower metal thickness when the isolated particles are more densely packed crystallites. This conclusion is corroborated by the much lower percolation threshold for electrical conductivity for Cu films supported on the hybrid seed layer (Figure 10): It is evident from the correlation between sheet resistance and metal thickness in Figure 10 that the hybrid layer is remarkably effective as a nucleation layer for evaporated Cu films on glass, reducing the percolation threshold substantially below that of either the mixed molecular adhesive layer or Al seed layer. For example, at 5 nm Cu thickness the sheet resistance is 39 Ω sq⁻

[1]. The very low percolation threshold of Cu on the hybrid nucleation layer is also reflected in the degree of optical scattering associated with the formation of islands, seen by a uniform darkening and as a peak shift in the transmission spectra in Figure 13.
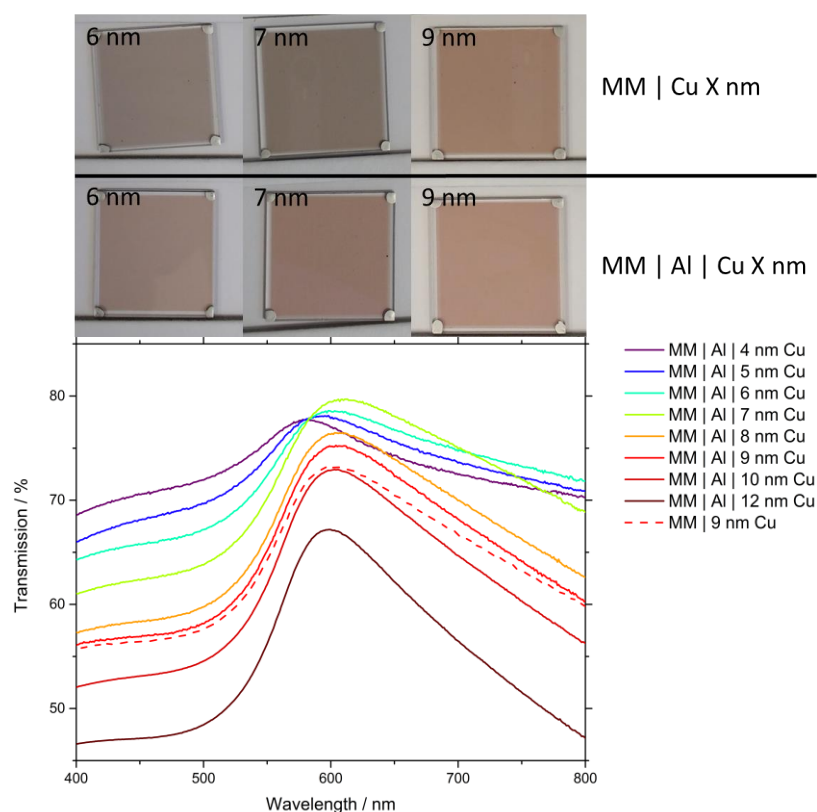
Figure 13: (Upper) Optical images of two series of Cu-based electrodes pictured in air < 5 minutes with and without an Al underlayer at varying Cu thickness. The lower percolation thickness of Cu on the 0.8 nm Al layer is visible here as the onset of the dark colouration, associated with scattering from isolated crystallites, is reduced beneath 6 nm. (Lower) The evolution of the transmission spectrum of thin MM | 0.8 nm Al | X nm Cu electrodes. Measurements referenced to glass substrate to exclude reflection from the glass/air interface.

Although PEI is effective at nucleating low-roughness planar Ag films it is shown in Figure 10 not to nucleate the growth of large, densely packed Cu crystallites during deposition leading to poorly conductive films. These data collectively show that the improvement in stability towards air-oxidation correlates with the larger mean Cu

crystallite size. It is reasonable to expect that oxygen diffuses most easily along grain boundaries between crystallites, rather than directly into the crystallites, and so boundaries between grains will be particularly susceptible to oxidation in air.[31] Increasing the mean crystallite size reduces the density of grain boundaries, and thus the susceptibility of the film to oxidation in air.

Figure 14 shows the effect of the thin Al layer on the transmittance of the Cu-based electrode. The additional reflectance caused by the 0.8 nm Al layer is offset by suppression of the parasitic absorption due to surface plasmonic excitations,[72] and so far-field transparency is not degraded by including the 0.8 nm Al interlayer as might ordinarily be expected when using a metallic seed layer.
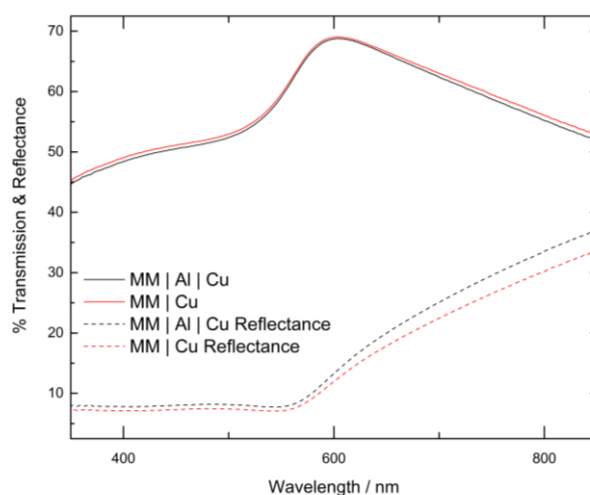
Figure 14: The UV-vis spectra of four comparable electrodes based upon a 9 nm Cu film (0.8 nm Al layer where stated). A glass reference was used to subtract the reflection from the substrate/air boundary to reflect that this is greatly reduced in commercial applications when using anti-reflective coatings.

### 6.3.1 Evaluation of the surface oxide layer

Figure 15 shows the Cu $2p_{3/2}$ and Cu LMM regions from a high-resolution XPS spectrum of the surface of a Cu electrode supported on a hybrid seed layer, before (left) and after (right) 400 hours oxidation in ambient air. For the initial scan the sample was transferred to the spectrometer in an inert atmosphere to minimise surface oxidation.[97] After 400

hours air exposure the thickness of the upper CuO overlayer was estimated to be 0.34 nm from the ratio of the Cu $2p_{3/2}$ peak intensities using the Strohmeir equation:[98]

Equation 10:

$$Oxide\ thickness\ =\ \lambda_0 \sin\theta\ ln\left(\frac{N_m\lambda_m I_o}{N_o\lambda_o I_m} + 1\right)$$

where λ: inelastic mean free path, θ: take-off angle (XPS), N: volume density of metal atoms in the oxide, I: peak area (XPS) and the subscripts o and m denote the oxide and metal parameters respectively. The Strohmeir equation uses the attenuation of the underlying metal peak as compared to the oxide and assumes an idealized oxide overlayer of uniform thickness to estimate the thickness of the overlayer.[36,98,99] This equation has widely been shown to give a good estimate of the oxide thickness in agreement with other techniques, provided the metal oxide thickness is less than the sampling depth of XPS (< 10 nm).[100,101] There is likely more significant error when used to estimate Cu oxide thicknesses, because the Cu_2O, CuO and $Cu(OH)_2$ co-exist as a multi-layer system and this requires additional assumptions: For example no consideration is made for attenuation of the metal peak by the other oxides when each is considered in isolation, or any adsorbed surface contaminants that accrue during oxidation in ambient air. To reduce the surface sensitivity and accurately determine the intensity of the metal peak a 90° take-off angle was used for all XPS scans. It was assumed that the attenuation by the thin adsorbed surface contaminant layer is negligible in line with the literature.[98]
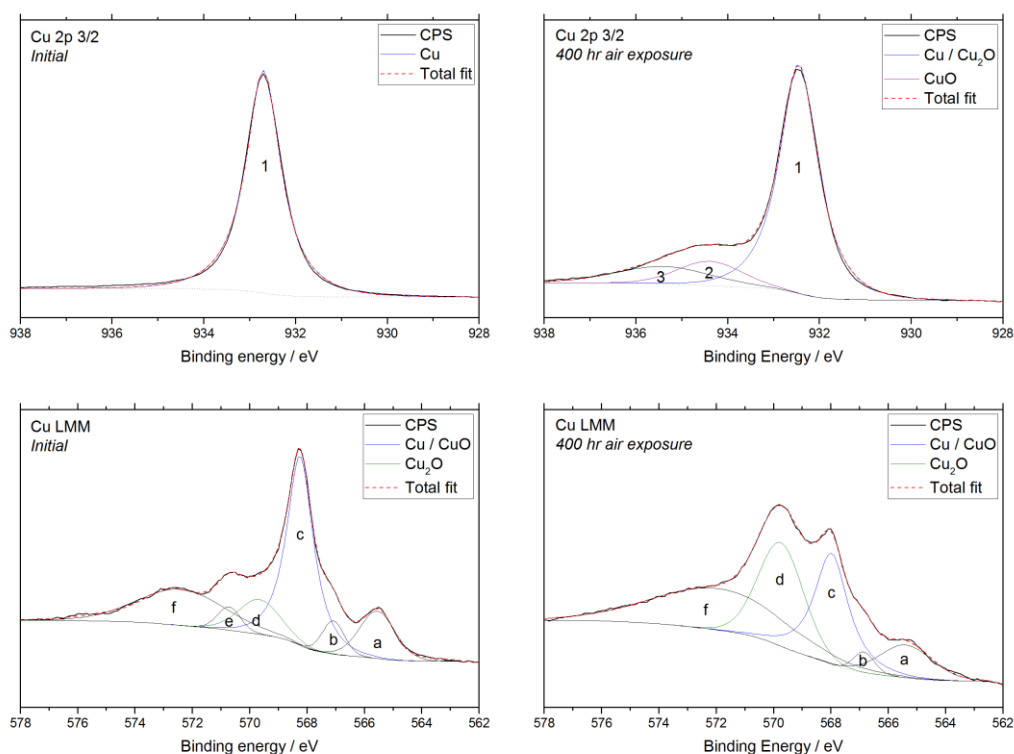
Figure 15: Cu 2p$_{3/2}$ and Cu LMM high resolution regions of XPS scan before (left) and after (right) 400 hours oxidation in laboratory air of a MM | Al | Cu electrode used to estimate the thickness of the oxide layer using the strohmeir equation.[36,98] The Y-scale, intensity, was normalised for clarity. A summary of the peak positions and areas is given in Appendix, Table A1.

Consistent with the simplified oxidation model used by Platzman *et al.* the influence of the thin Cu(OH)$_2$ uppermost layer was not taken into account, which is justified by its constant thickness after the initial stages: Cu(OH)$_2$ is a metastable intermediary and its formation by a reaction with H$_2$O is in equilibrium with its spontaneous conversion to CuO.[102] Due to the overlap between the peak positions of Cu^0 and Cu^{1+} in the Cu 2p$_{3/2}$ region of the XPS spectrum, the thickness of Cu$_2$O was estimated to be 3.08 nm from the ratio of Cu$_2$O to Cu^0 Auger peaks in the Cu LMM region. The Cu and CuO peaks overlap in the Cu LMM region and so an estimation of the CuO contribution to the Cu^0 peak was first subtracted by applying a correction factor (the Cu metal intensity ratio of the unoxidized (0 hours) Cu 2p$_{3/2}$ and Cu LMM Cu^0 peaks) to the CuO intensity in the Cu 2p$_{3/2}$ spectrum using the procedure previously reported by Platzman *et al.*[36] This correction factor accounts for the difference in emission probability of an Auger electron

209

as compared to conventional XPS and in the transmission of ejected electrons through the bulk at different energies (regions).[36]

The total oxide thickness (CuO + Cu$_2$O) measured by XPS (3.4 nm) was also compared to a direct measurement determined using AFM. The electrode was scratched and the thickness recorded at multiple points for consistency before and after 400 hours exposure to ambient air (Figure 3). Before the second measurement the electrode was rinsed for 30 s with glacial acetic acid which is known to selectively etch copper oxide.[103] After 400 hours air exposure and subsequent glacial acetic acid rinsing the film was 2.2 ± 0.6 nm thinner. Assuming literature values for the densities of Cu and Cu$_2$O (the major oxide component) respectively (8.96 g cm^{-3}, 6.00 g cm^{-3}) this equates to the loss of an estimated 1.3 ± 0.6 nm of metal. This value is likely to be an overestimation of the loss in metal thickness since the glacial acetic acid etch of the thin Cu films was performed under ambient conditions and so some oxidation of pristine Cu during the oxide removal step is likely. Unlike with XPS, AFM measurements are not affected by an adsorbed contaminant overlayer because the AFM tip penetrates this physisorbed layer in tapping mode.
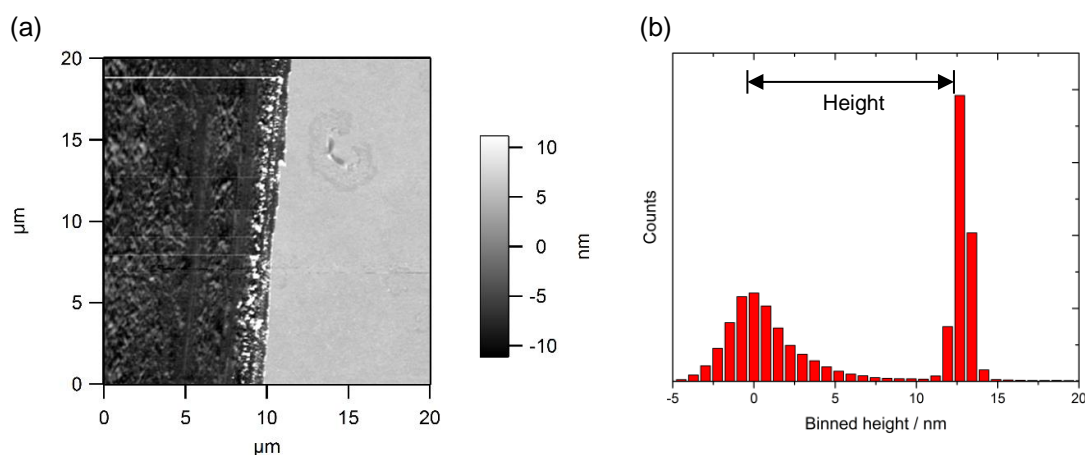
Figure 16: (a) A representative AFM image of a scratch through the MM | Al | Cu electrode from which the height difference was calculated by histogram in (b).

Both the estimated oxide thickness after 400 hours air exposure of a MM | Al | Cu 9 nm film by XPS (3.4 nm) and AFM (2.2 ± 0.6 nm) model the metal and oxide as uniform and ideally slab-like surfaces. Another estimate of oxide thickness can be made from the

change in sheet resistance over time, provided the film is slab-like and assuming the oxide layer to be of uniform thickness. Over 400 hours exposure in ambient air, the sheet resistance in Figure 5 of an MM | Al | Cu 9 nm electrode has risen by 10.9%, which represents ~1 nm of metal lost (1.7 nm of oxide). This value is in close agreement with the direct measurement of oxide thickness using the AFM (2.2 ± 0.6 nm). The estimated thickness of oxide estimated using XPS data, 3.4 nm, falls outside this range. This method involved a number of assumptions, and the combined attenuation of the Cu^0 signal by an adsorbed hydrocarbon layer (assumed in the model to be negligible) and the other components of the oxide layer when each of CuO and Cu_2O is considered in isolation are collectively the likely source of the disparity between these values.

6.3.2   *Model OPV devices*

Cu films with a thickness of 7-15 nm are effective transparent electrodes in OPVs due to their inherent flexibility and the low cost of Cu as compared to the alternatives (Ag, ITO).[34,70,89,104–106] To demonstrate this Figure 17 shows the champion device characteristics for model OPVs based upon the ternary PCE-10 / COi8DFIC / $PC_{70}BM$ bulk-heterojunction: ITO (Black) and the Cu electrode on a hybrid adhesion layer, MM | Al 0.8 nm | Cu 9 nm (Red). Devices using a Cu electrode have a similar fill-factor and open-circuit voltage to the ITO reference, as well as similar shunt and series resistances (evident from the gradient at < 0.0 V and > 0.75 V respectively). The lower photocurrent density is a result of the lower far-field transparency of the copper electrode as compared to ITO glass, but this can be improved with optimisation of the device optics through the addition of wide band gap interlayers or by patterning the Cu metal to improve its transparency.[71]
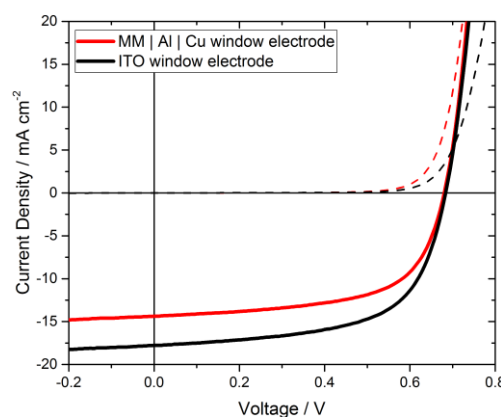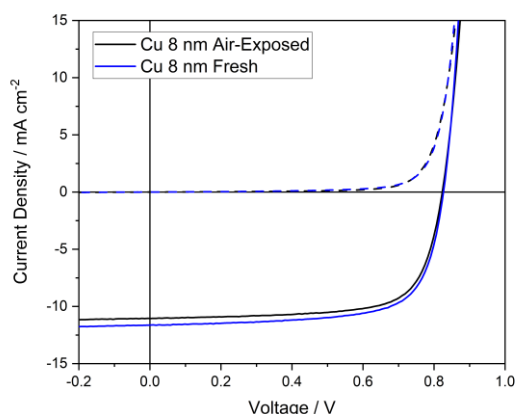
Figure 17: Champion device characteristics for two different electrodes in the structure; *Electrode | ZnO | PCE-10 / COi8DFIC /* PC$_{70}$BM *| MoO$_3$ 8 nm | Ag 100 nm*. Light characteristics: Solid lines. Dark characteristics: Dashed lines.

To understand the effect of oxidation of the Cu electrode surface which will occur *in-situ* due to the inevitable ingress of air into the device over extended periods, OPV devices were fabricated using MM | Cu 9 nm electrodes that had been exposed to ambient laboratory air for 2 weeks (336 hours, Figure 18). After 2 weeks in ambient air the sheet resistance of a MM | Cu 9 nm film had risen by ~36% from 10.8 to 14.7 Ω sq^{-1} (Figure 5), which corresponds to the conversion of ~2.5 nm of the Cu metal thickness into ~3.2 nm of Cu oxides. This oxide thickness is far greater than the oxide thickness formed over the same period on the MM | Al | Cu 9 nm electrodes developed in this chapter, but is deliberately used to determine the extent to which Cu oxide formation is a problem when it forms *in-situ* in at the Cu/ZnO interface in an OPV device with the structure: Cu electrode | ZnO | PBDB-T/ITIC | MoO$_3$ | Al. Notably the air-exposed Cu electrode was briefly heated to 120°C under inert atmosphere to drive off adsorbed water and hydrocarbons immediately prior to device fabrication. Additionally, both oxides of Cu; Cu$_2$O and CuO, are insoluble in ethanol which is the solvent used to deposit the ZnO nanoparticle film, so it is reasonable to assume it remains in place during device fabrication.

Table 2: Tabulated device data for the device structure: Electrode | ZnO | PBDB-T/ITIC | MoO$_3$ | Al. Data is presented as the mean of 6 - 18 devices ± Standard Deviation (Champion). Half of the Cu electrodes (MM | Cu 8 nm) were aged in ambient laboratory air for 2 weeks before building the device.

Electrode	Aged / Fresh	Annealed	J$_{sc}$ / mA cm^{-2}	V$_{oc}$ / V	FF	PCE / %
MM	Cu 8 nm	Aged	No	10.16 ± 1.00 (11.05)	0.81 ± 0.03 (0.82)	0.64 ± 0.13 (0.72)	5.29 ± 1.33 (6.51)
MM	Cu 8 nm	Fresh	No	11.46 ± 0.21 (11.63)	0.83 ± 0.00 (0.83)	0.69 ± 0.01 (0.71)	6.54 ± 0.16 (6.78)

Figure 18: Champion device characteristics for two MM | Cu 8 nm electrodes, aged for 336 hours in ambient air (Black) and fresh (Blue), in the structure; Electrode | ZnO | PBDB-T/ITIC | MoO$_3$ 8 nm | Ag 100 nm.

It is evident from the data in Table 2 and Figure 18 that although the relatively thick Cu oxide layer at the Cu/ZnO interface does increase the spread of all three device parameters (J$_{sc}$, V$_{oc}$ and FF) there is no statistically significant difference in device performance, and the champion PCE is comparable at 6.51% *vs* 6.78% for a pristine Cu electrode. This is

surprising since the oxide of Cu formed is primarily Cu_2O, which has valence and conduction band edges poorly aligned with those of ZnO for conduction (Figure 19 (a)) and is too thick for charges to efficiently quantum mechanically tunnel through. Three possible mechanisms are proposed to explain this finding: (i) Cu is well known to spontaneously diffuse into metal oxides at room temperature and may form dendrites along the Cu oxide grain boundaries which connect the Cu metal film to the ZnO.[71,107]; (ii) The rate of oxidation for different crystal faces of polycrystalline Cu can be very different,[108] and so it is plausible that the Cu oxide thickness is not uniform and in some places is sufficiently thin for electrons to efficiently quantum mechanically tunnel across. (iii) The high density of intrinsic dopant states and subsequent narrow depletion regions of both Cu_2O and ZnO may enable charges to tunnel between across the junction, highlighted in blue in Figure 19 (b). As in Figure 19 (b), this transfer may be facilitated by interfacial defect states as depicted: These interfacial defect states are well accepted, but their origin not yet understood, in the literature and are the leading culprit for the low efficiency of Cu_2O/ZnO p-n heterojunction solar cells as compared to their theoretical efficiency.[109]
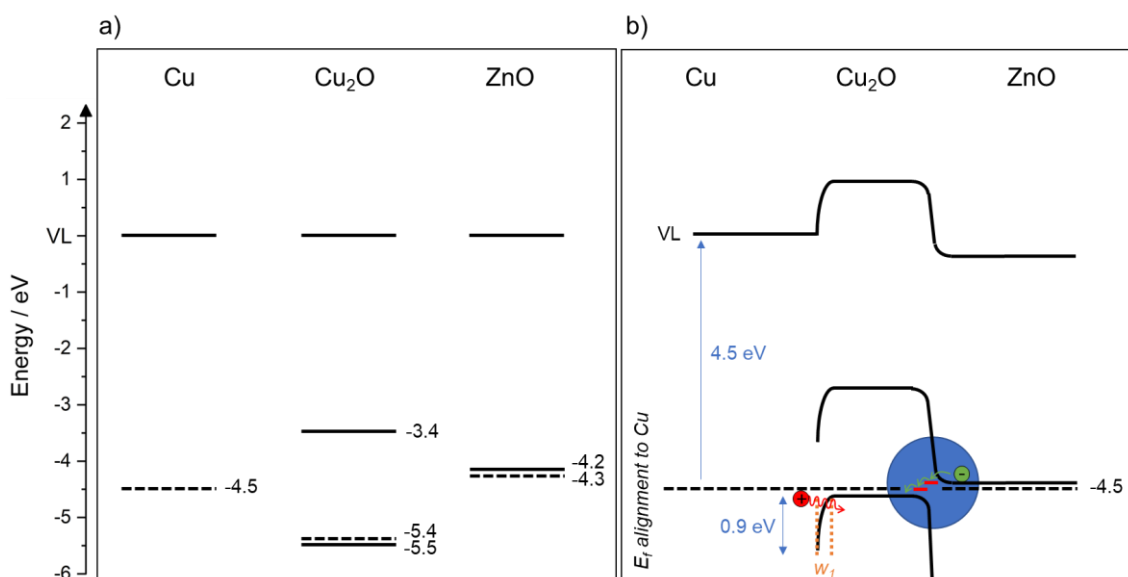

Figure 19: (a) Depiction of the simplified electronic structure of Cu, Cu_2O and ZnO showing the band edges (VB and CB) and (b) aligned Fermi levels once the three materials are interfaced. Circled in blue is one proposed mechanism for charge transfer between Cu_2O and ZnO through defect interfacial states. The deep-lying valence band of ZnO is omitted for visual clarity.

This important result shows that the surface of a Cu electrode could be substantially oxidized without detriment to the efficiency of charge transfer across the contact. Since the formation of more than 3 nm of Cu oxide *in-situ* by air ingress is anticipated to occur only very slowly with encapsulation of the OPV device, it is unlikely that this factor will limit the lifetime of OPV devices.

6.3.3   Aluminium | Copper | Aluminium electrodes

A natural extension of the work presented in this and the preceding chapters of this thesis is to combine both the exceptional passivation effect of an 0.8 nm Al layer on top of Cu and the enhanced morphology and stability imparted by an ultra-thin Al layer beneath the Cu. To investigate the effectiveness of this approach the Cu film thickness was reduced to 4 nm which dramatically increases the sensitivity to changes in sheet resistance as a result of surface oxidation. A slab-like Cu electrode of this thickness is not possible using the MPTMS/APTMS seed layer alone as described earlier.

Grown on the hybrid seed layer but without a capping Al overlayer, 4 nm Cu films exhibit a sheet resistance of $\sim$ 85 Ω sq^{-1}, measured in ambient air (Figure 10). However, when 0.8 nm of Al is deposited onto the 4 nm Cu film without breaking vacuum creating an Al | Cu | Al sandwich structure, the sheet resistance is reduced to < 40 Ω sq^{-1}. This 50% reduction in sheet resistance is associated with the passivating effect of the top Al layer, since such a thin Cu layer is expected to be extremely sensitive to rapid initial oxidation during measurement in air. Figure 20 shows the evolution in sheet resistance of a set of four identical electrodes over a period of > 2500 hours exposed to ambient air from which it is evident that these ultra-thin metal films are remarkably stable to oxidation. These electrodes also exhibit the previously described initial reduction in sheet resistance associated with the dealloying of Al from the Cu.
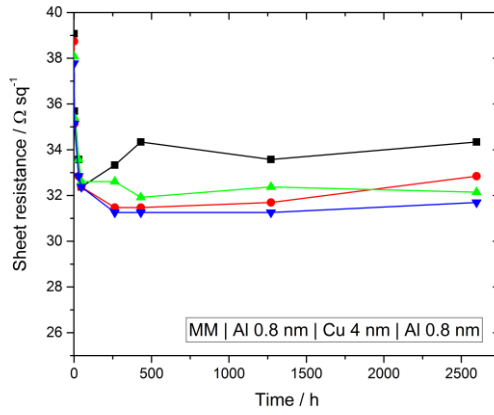
Figure 20: Evolution of the sheet resistance for MM | Al 0.8 nm | Cu 4 nm | Al 0.8 nm electrodes in air. The temperature and humidity fluctuated in the range 18-30°C and 15-50% respectively during testing.

6.3.4   Aluminium / Copper alloy electrodes

A second logical continuation of the work reported in this chapter is to investigate the stability of a Cu/Al alloy instead of the discrete layer Al/Cu/Al structure. This approach is similar to that of reported by Zhang *et al.* for Ag electrodes where 10% Al (at. %) doped Ag films exhibited improved wetting and surface roughness to pure-Ag films.[110] In that work however, the stability of the Al/Ag alloy electrode in the ambient environment was not evaluated.
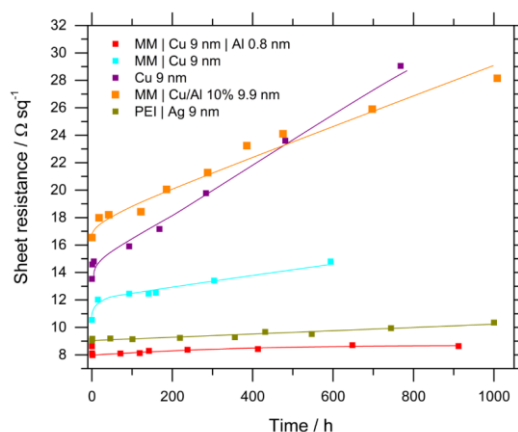
Figure 21: Evolution of the sheet resistance for representative electrodes in air for 5 electrode structures to demonstrate the relative stability of the Cu/Al alloy electrode (Orange). The fitted lines are to 'guide the eye' only. The temperature and humidity fluctuated in the range 18-30°C and 15-50% respectively during testing.

To evaluate whether a co-evaporated Cu/Al alloy layer offers high stability towards oxidation in air, an equivalent thickness of 9 nm Cu was co-evaporated with 0.9 nm Al (at rates of 1 and 0.1 Ås^{-1} respectively) onto a mixed organic monolayer (MM) of APTMS/MPTMS. Despite having the same total metal thickness and elemental composition to a 9 nm Cu film with 0.8 nm Al underneath, or on top of the Cu, the electrode had the highest starting sheet resistance of 16.7 ± 0.3 (16.5 champion) of any combination produced, even when compared to 9 nm Cu directly deposited on glass. This is in line with the resistivity of bulk Cu/Al alloys which increase sharply with increasing Al content.[90,111] Co-deposited Al/Cu also exhibits reduced average transparency in the visible region (Figure 22).
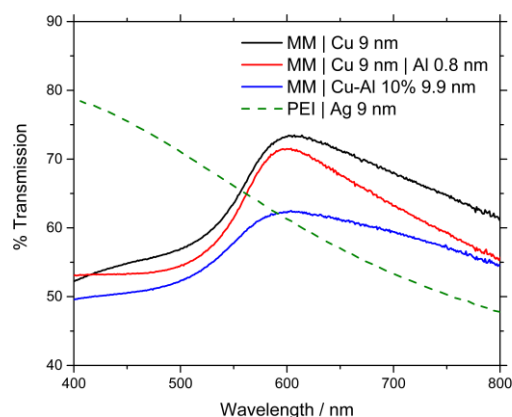
Figure 22: A comparison of the transparency in the visible region of four electrode structures, all referenced to the glass substrates, including the model MM | Cu-Al 10% alloy electrode described (Blue).

Furthermore, co-depositing Cu with Al does not increase the stability of the metal film electrode towards oxidation in air (Figure 21). The MM | 9.9 nm Cu/Al 10% electrode exhibited significantly worse stability than the MM | 9 nm Cu electrode reference which was unexpected as in bulk Cu, Al-doping has been shown to improve the stability toward oxidation.[90] The reasons for this were not investigated.

6.4   Conclusion

In summary, a monolayer of 3-mercaptopropyl(trimethoxysilane) and 3-aminopropyl(trimethoxysilane) together with an 0.8 nm Al layer is shown to be a remarkably effective seed layer for the formation of slab-like evaporated copper films on glass and plastic substrates. The ultra-thin Al layer is deposited immediately prior to copper evaporation in the same vacuum. This hybrid seed layer outperforms the best nucleation layer for copper films reported to date in two key respects: (1) by reducing the metal percolation threshold to < 4 nm nominal thickness without incurring additional optical loses; (2) by dramatically improving the long term stability of sub-10 nm copper films towards oxidation in air, such that the stability is comparable to that of silver films of the same thickness fabricated using the best reported seed layer for optically thin silver films to date. The remarkable effectiveness of this hybrid nucleation layer is attributed to an increase in the Cu mean crystallite size when using this hybrid seed layer, which

reduces the density of Cu grain boundaries – that part of the film most susceptible to oxidation.

6.5   Experimental

Electrode preparation

Glass microscope slides (7525 M, J. Melvin Freed Brand) or PET substrates were ultra-sonically agitated for 15 minutes each in diluted surfactant (Hellmanex III, Hellma Analytics), deionised water and propan-2-ol (AnalaR, VWR). These substrates were then UV/O$_3$ treated for 15 minutes immediately prior to use. Where stated, these slides were transferred to a dessicator and held at approx. 50 mBar for 4 hours with an open vial of mixed APTMS/MPTMS. All substrates were then transferred to the evaporator for Al, Cu or Ag deposition using a base pressure of $< 5 \times 10^{-8}$ mbar unless stated. Al was evaporated at a rate of 0.1 Ås^{-1}, while Cu and Ag were evaporated at 1 Ås^{-1}. Thicknesses were calibrated using an Asylum Research MFP-3D AFM and monitored using quartz-crystal microbalances. Masks were exchanged where required by a series of transfer arms without breaking the vacuum. During metal deposition, the chamber pressure rose to approximately 5×10^{-7} mbar. For the Ag electrodes, two nucleation layers were compared (Figure A1). Polyethylenimine (PEI) was spin-cast onto freshly cleaned and UV/O$_3$ treated substrates (5000 rpm) from a 0.3% wt. aqueous solution and dried in air (110°C, 20 mins). Separate cleaned and UV/O$_3$ treated substrates were heated at 120°C overnight in a loosely sealed container together with 4 drops of MPTMS.

Sheet resistance evolution

25 × 25 mm substrates were used to evaporate an electrode onto which silver contacts were painted to connect a Keithley 2400 source meter. Resistances were calculated using the Van der Pauw method and an applied voltage of 5 mV. Electrodes were stored in ambient laboratory air and re-measured periodically. The temperature fluctuated between 18-30°C and the humidity between 15-50%.

UV-vis spectroscopy

A PerkinElmer Lambda 1050 UV/Vis spectrophotometer was used with reflectivity measured using an Integrating sphere where given.

AFM images

An Asylum Research MFP3D instrument was used in tapping mode to map the surface of the electrodes and calculate the root mean square (RMS) roughness. For roughness measurements, a 10 × 10 μm area was mapped and an area free of interference selected for a detailed scan.

X-ray photoelectron spectroscopy (XPS)

Surface compositional and chemical state analysis was carried out using X-ray photoelectron spectroscopy (XPS) measurements conducted on a Kratos Axis Ultra DLD spectrometer at the University of Warwick Photoemission Facility. The air-exposed samples were mounted on to a standard sample bar using electrically conductive carbon tape and loaded into the instrument. Samples kept under an inert atmosphere were mounted on to Cu stubs using conductive carbon tape inside a nitrogen glovebox. The stubs were then loaded into a vacuum transfer unit filled with nitrogen and transported to the XPS laboratory and loaded in such a manner that samples were under a nitrogen atmosphere throughout. XPS measurements were performed in the main analysis chamber, with the sample being illuminated using a monochromated Al Kα X-ray source. The measurements were conducted at room temperature and at a take-off angle of 90° with respect to the surface parallel. The core level spectra were recorded using a pass energy of 20 eV (resolution approx. 0.4 eV), from an analysis area of 300 mm x 700 mm. The spectrometer work function and binding energy scale of the spectrometer were calibrated using the Fermi edge and $3d_{5/2}$ peak recorded from a polycrystalline Ag sample prior to the commencement of the experiments. The data were analysed in the CasaXPS package, using Shirley backgrounds and mixed Gaussian-Lorentzian (Voigt) lineshapes, with asymmetry parameters employed where appropriate. For compositional analysis, the analyser transmission function has been determined using clean metallic foils to determine the detection efficiency across the full binding energy range.

TEM images

Images in Figure 3 (b) were collected on a Jeol 2100 LaB6 instrument. A focused ion beam (FIB) was used to prepare a thin section.

XRD SAXS

Grazing incidence small-angle X-ray scattering (GISAXS) measurements were made using a Xenocs Xeuss 2.0 equipped with a micro-focus Cu Kα source collimated with Scatterless slits. The scattering was measured using a Pilatus 300k detector with a pixel

size of 0.172 mm x 0.172 mm. The detector was translated horizontally, and multiple data collections were combined creating a larger virtual detector. The distance between the detector and the sample was calibrated using silver behenate ($AgC_{22}H_{43}O_2$), giving a value of 2.487(5) m. The magnitude of the scattering vector (q) is given by $q = 4\pi \sin\theta / \lambda$, where 2θ is the angle between the incident and scattered X-rays and λ is the wavelength of the incident X-rays. This gave a q range for the detector of 0.003 Å^{-1} and 0.13 Å^{-1} in the horizontal plane. This q range allows crystallite sizes between 1 and 200 nm to be determined.

Samples were aligned such that the surface was parallel to the beam and in the center of the beam. To maximize the scattering signal from the Cu layer the sample was positioned at an incidence angle (α_i) of 0.35° which is just below the critical angle of 0.4° for Cu and Cu Kα radiation. The 2d virtual detector image for the MM | Cu structure is shown in Figure 9 (left). Scattering in the q_z direction (out-of-plane) is related to vertical morphology of the sample and the q_y direction (in-plane) to the horizontal morphology.

The in-plane scattering from the Cu crystallites highlighted in Figure 9 (center) was integrated as a function of q producing a 1d intensity versus q data set as shown in Figure 9 (center). Selecting only in-plane scattering allows the horizontal radius of the crystallites to be determined. SAXS fitting was performed in the Irena analysis package.[112] The scattering was fitted using spheres with a lognormal distribution of the radius. The fit to the measured data for the MM | Cu structure is given by the red line in Figure 9 (center). When the interaction between crystallites affected the scattering a hard-sphere structure factor was included.[94,113–115]

Model inverted OPV devices
To either UV/O_3 plasma treated ITO glass or the pre-deposited Cu-based electrode, ZnO NPs were spin cast from commercial ink (InfinityPV, ZnO in IPA, 0.7% wt.) at 1000 rpm. PCE-10 (Ossila) / CO$_i$8DFIC (1Material) / PC$_{70}$BM (Ossila) 22 mg / mL (1:1.05:0.45 weight ratio) in chlorobenzene / 1% 1,8-diiodooctane solution was then spin cast at 3200 rpm. The active layer was held under vacuum overnight to remove the DIO additive before evaporation of 8 nm MoO_3 at 0.3 Ås^{-1} and subsequent Ag 100 nm at 1 Ås^{-1}.

All devices were tested under an inert N_2 atmosphere (< 5 ppm O_2, H_2O) under 1 sun illumination and then dark conditions. For the ternary BHJ devices here, the 100 mW cm⁻

^{2} (1 sun) was calibrated across a wider spectrum between 400-1100 nm due to the extended absorption bands.

6.6 References

[1]   Q. Burlingame, X. Huang, X. Liu, C. Jeong, C. Coburn, S. R. Forrest, *Nature* **2019**, *573*, 394.

[2]   J. Yuan, Y. Zhang, L. Zhou, G. Zhang, H. L. Yip, T. K. Lau, X. Lu, C. Zhu, H. Peng, P. A. Johnson, M. Leclerc, Y. Cao, J. Ulanski, Y. Li, Y. Zou, *Joule* **2019**, *3*, 1140.

[3]   H. Lu, X. Ren, D. Ouyang, W. C. H. Choy, *Small* **2018**, *14*, 1703140.

[4]   M. W. Rowell, M. D. McGehee, *Energy Environ. Sci.* **2011**, *4*, 131.

[5]   D. A. Jacobs, K. R. Catchpole, F. J. Beck, T. P. White, *J. Mater. Chem. A* **2016**, *4*, 4490.

[6]   F. Machui, M. Hösel, N. Li, G. D. Spyropoulos, T. Ameri, R. R. Søndergaard, M. Jørgensen, A. Scheel, D. Gaiser, K. Kreul, D. Lenssen, M. Legros, N. Lemaitre, M. Vilkman, M. Välimäki, S. Nordman, C. J. Brabec, F. C. Krebs, *Energy Environ. Sci.* **2014**, *7*, 2792.

[7]   M. J. Griffith, N. A. Cooling, B. Vaughan, D. C. Elkington, A. S. Hart, A. G. Lyons, S. Quereshi, W. J. Belcher, P. C. Dastoor, *IEEE J. Sel. Top. Quantum Electron.* **2016**, *22*, 4100714.

[8]   A. Gambhir, P. Sandwell, J. Nelson, *Sol. Energy Mater. Sol. Cells* **2016**, *156*, 49.

[9]   R. Zhang, M. Engholm, *Nanomaterials* **2018**, *8*, 1.

[10]   K. W. Seo, J.-Y. J. J. Y. J. Lee, J. Jo, C. Cho, J.-Y. J. J. Y. J. Lee, *Adv. Mater.* **2019**, *31*, 1902447.

[11]   H. Kang, S. Jung, S. Jeong, G. Kim, K. Lee, *Nat. Commun.* **2015**, *6*, 6503.

[12]   D. R. Sahu, J. L. Huang, *Appl. Surf. Sci.* **2006**, *253*, 915.

[13]   H. B. Lee, W. Y. Jin, M. M. Ovhal, N. Kumar, J. W. Kang, *J. Mater. Chem. C* **2019**, *7*, 1087.

[14]   S. Choi, S.-J. Kim, C. Fuentes-Hernandez, B. Kippelen, *Opt. Express* **2011**, *19*, A793.

[15] F. L. M. Sam, M. A. Razali, K. D. G. D. G. I. Jayawardena, C. A. Mills, L. J. Rozanski, M. J. Beliatis, S. R. P. Silva, *Org. Electron.* **2014**, *15*, 3492.

[16] F. L. M. Sam, C. A. Mills, L. J. Rozanski, S. R. P. Silva, *Laser Photonics Rev.* **2014**, *8*, 172.

[17] Y. Xia, X. M. Zhao, E. Kim, G. M. Whitesides, *Chem. Mater.* **1995**, *7*, 2332.

[18] C. Merian, X. Du, D. Hardt, H. AlQahtani, In *ASME International Mechanical Engineering Congress and Exposition, Proceedings (IMECE)*; American Society of Mechanical Engineers, 2015; Vol. 14–2015.

[19] M. Geissler, H. Schmid, A. Bietsch, B. Michel, E. Delamarche, *Langmuir* **2002**, *18*, 2374.

[20] J. Zou, H. L. Yip, S. K. Hau, A. K. Y. K.-Y. Jen, *Appl. Phys. Lett.* **2010**, *96*, 203301.

[21] T. Oishi, K. Koyama, S. Alam, M. Tanaka, J. C. Lee, *Hydrometallurgy* **2007**, *89*, 82.

[22] A. Alzate, M. E. López, C. Serna, *Waste Manag.* **2016**, *57*, 113.

[23] E. Georgiou, S. A. Choulis, F. Hermerschmidt, S. M. Pozov, I. Burgués-Ceballos, C. Christodoulou, G. Schider, S. Kreissl, R. Ward, E. J. W. List-Kratochvil, C. Boeffel, *Sol. RRL* **2018**, *2*, 1700192.

[24] L. Mao, Q. Chen, Y. Li, Y. Li, J. Cai, W. Su, S. Bai, Y. Jin, C. Q. Ma, Z. Cui, L. Chen, *Nano Energy* **2014**, *10*, 259.

[25] Y. Li, L. Mao, Y. Gao, P. Zhang, C. Li, C. Ma, Y. Tu, Z. Cui, L. Chen, *Sol. Energy Mater. Sol. Cells* **2013**, *113*, 85.

[26] X. Fan, W. Nie, H. Tsai, N. Wang, H. Huang, Y. Cheng, R. Wen, L. Ma, F. Yan, Y. Xia, *Adv. Sci.* **2019**, *6*.

[27] D. Qin, Y. Xia, G. M. Whitesides, *Nat. Protoc.* **2010**, *5*, 491.

[28] L. Wang, Y. Yao, X. Ma, C. Huang, Z. Liu, H. Yu, M. Wang, Q. Zhang, X. Li, S. Chen, W. Huang, *Org. Electron.* **2018**, *61*, 96.

[29] Y. Li, L. Meng, Y. Yang, G. Xu, Z. Hong, Q. Chen, J. You, G. Li, Y. Yang, Y. Li, *Nat. Commun.* **2016**, *7*, 10214.

[30] P. Bellchambers, M. Walker, S. Huband, A. Dirvanauskas, R. A. Hatton, *ChemNanoMat* **2019**, *5*, 619.

[31] P. Bellchambers, J. Lee, S. Varagnolo, H. Amari, M. Walker, R. A. Hatton, *Front. Mater.* **2018**, *5*, 71.

[32] C. Zhong, Y. M. Jiang, D. M. Sun, J. Gong, B. Deng, S. Cao, J. Li, *Chinese J. Phys.* **2009**, *47*, 253.

[33] P. Keil, D. Lützenkirchen-Hecht, R. Frahm, In *AIP Conference Proceedings*; 2007; Vol. 882, pp. 490–492.

[34] H. M. Stec, R. A. Hatton, *ACS Appl. Mater. Interfaces* **2012**, *4*, 6013.

[35] L. Lu, N. R. Tao, L. B. Wang, B. Z. Ding, K. Lu, *J. Appl. Phys.* **2001**, *89*, 6408.

[36] I. Platzman, R. Brener, H. Haick, R. Tannenbaum, *J. Phys. Chem. C* **2008**, *112*, 1101.

[37] M. C. Biesinger, *Surf. Interface Anal.* **2017**, *49*, 1325.

[38] J. Iijima, J. W. Lim, S. H. Hong, S. Suzuki, K. Mimura, M. Isshiki, *Appl. Surf. Sci.* **2006**, *253*, 2825.

[39] J. Shewchun, R. Singh, M. A. Green, *J. Appl. Phys.* **1977**, *48*, 765.

[40] J. Maserjian, *J. Vac. Sci. Technol.* **1974**, *11*, 996.

[41] M. Depas, B. Vermeire, P. W. Mertens, R. L. Van Meirhaeghe, M. M. Heyns, *Solid State Electron.* **1995**, *38*, 1465.

[42] A. Sundqvist, O. J. Sandberg, M. Nyman, J. H. Smått, R. Österbacka, *Adv. Energy Mater.* **2016**, *6*, 1.

[43] L. Zuo, J. Yao, H. Li, H. Chen, *Sol. Energy Mater. Sol. Cells* **2014**, *122*, 88.

[44] D. G. Castner, K. Hinds, D. W. Grainger, *Langmuir* **1996**, *12*, 5083.

[45]   H. S. Choi, Y. Kang, H. Lee, C. Lee, *Curr. Appl. Phys.* **2007**, *7*, 522.

[46]   S. Chen, L. Song, Z. Tao, X. Shao, Y. Huang, Q. Cui, X. Guo, *Org. Electron. physics, Mater. Appl.* **2014**, *15*, 3654.

[47]   E. Vitoratos, *Open J. Org. Polym. Mater.* **2012**, *02*, 7.

[48]   G. D. M. R. Dabera, M. Walker, A. M. Sanchez, H. J. Pereira, R. Beanland, R. A. Hatton, *Nat. Commun.* **2017**, *8*, 1894.

[49]   M. Janczarek, E. Kowalska, *Catalysts* **2017**, *7*.

[50]   K. Norrman, M. V Madsen, S. A. Gevorgyan, F. C. Krebs, *J. Am. Chem. Soc.* **2010**, *132*, 16883.

[51]   S. Holliday, R. S. Ashraf, A. Wadsworth, D. Baran, S. A. Yousaf, C. B. Nielsen, C. H. Tan, S. D. Dimitrov, Z. Shang, N. Gasparini, M. Alamoudi, F. Laquai, C. J. Brabec, A. Salleo, J. R. Durrant, I. McCulloch, *Nat. Commun.* **2016**, *7*, 1.

[52]   D. Baran, R. S. Ashraf, D. A. Hanifi, M. Abdelsamie, N. Gasparini, J. A. Röhr, S. Holliday, A. Wadsworth, S. Lockett, M. Neophytou, C. J. M. Emmott, J. Nelson, C. J. Brabec, A. Amassian, A. Salleo, T. Kirchartz, J. R. Durrant, I. McCulloch, *Nat. Mater.* **2017**, *16*, 363.

[53]   B. J. Tremolet de Villers, K. A. O'Hara, D. P. Ostrowski, P. H. Biddle, S. E. Shaheen, M. L. Chabinyc, D. C. Olson, N. Kopidakis, *Chem. Mater.* **2016**, *28*, 876.

[54]   N. Y. Doumon, M. V. Dryzhov, F. V. Houard, V. M. Le Corre, A. Rahimi Chatri, P. Christodoulis, L. J. A. Koster, *ACS Appl. Mater. Interfaces* **2019**, *11*, 8310.

[55]   Y. Xia, G. M. Whitesides, *Annu. Rev. Mater. Sci.* **1998**, *28*, 153.

[56]   H. Hagendorfer, K. Lienau, S. Nishiwaki, C. M. Fella, L. Kranz, A. R. Uhl, D. Jaeger, L. Luo, C. Gretener, S. Buecheler, Y. E. Romanyuk, A. N. Tiwari, *Adv. Mater.* **2014**, *26*, 632.

[57]   Y. H. Lin, S. R. Thomas, H. Faber, R. Li, M. A. McLachlan, P. A. Patsalas, T. D. Anthopoulos, *Adv. Electron. Mater.* **2016**, *2*, 1.

[58]   J. H. Lee, B. O. Park, *Mater. Sci. Eng. B Solid-State Mater. Adv. Technol.* **2004**,

106, 242.

[59] K. Ellmer, Past achievements and future challenges in the development of optically transparent electrodes. *Nat. Photonics* **2012**, *6*, 809–817.

[60] S. Jeong, S. Jung, H. Kang, D. Lee, S. Choi, S. Kim, B. Park, K. Yu, J. Lee, K. Lee, *Adv. Funct. Mater.* **2017**, *27*, 1.

[61] T. Gao, B. Wang, B. Ding, J. K. Lee, P. W. Leu, *Nano Lett.* **2014**, *14*, 2105.

[62] J. Yun, *Adv. Funct. Mater.* **2017**, *27*, 1606641.

[63] K. Sivaramakrishnan, T. L. Alford, *Appl. Phys. Lett.* **2009**, *94*, 2104.

[64] D. S. Ghosh, Q. Liu, P. Mantilla-Perez, T. L. Chen, V. Mkhitaryan, M. Huang, S. Garner, J. Martorell, V. Pruneri, *Adv. Funct. Mater.* **2015**, *25*, 7309.

[65] F. C. Krebs, N. Espinosa, M. Hösel, R. R. Søndergaard, M. Jørgensen, *Adv. Mater.* **2014**, *26*, 29.

[66] J. R. Davis, *Copper and Copper Alloys*; ASM International: Ohio, 2001.

[67] Nasdaq, Nasdaq: Commodity Prices.

[68] HKEX, London Metal Exchange.

[69] G. Zhao, S. M. Kim, S. G. Lee, T. S. Bae, C. W. Mun, S. Lee, H. Yu, G. H. Lee, H. S. Lee, M. Song, J. Yun, *Adv. Funct. Mater.* **2016**, *26*, 4180.

[70] O. S. Hutter, R. A. Hatton, *Adv. Mater.* **2015**, *27*, 326.

[71] H. J. Pereira, J. Reed, J. Lee, S. Varagnolo, G. D. M. R. Dabera, R. A. Hatton, *Adv. Funct. Mater.* **2018**, *28*, 1802893.

[72] J. H. Im, K. T. Kang, S. H. Lee, J. Y. Hwang, H. Kang, K. H. Cho, *Org. Electron.* **2016**, *33*, 116.

[73] L. Leandro, R. Malureanu, N. Rozlosnik, A. Lavrinenko, *ACS Appl. Mater. Interfaces* **2015**, *7*, 5797.

[74] I. P. Lopéz, L. Cattin, D.-T. Nguyen, M. Morsli, J. C. Bernède, *Thin Solid Films*

227

2012, *520*, 6419.

[75] N. Formica, D. S. Ghosh, A. Carrilero, T. L. Chen, R. E. Simpson, V. Pruneri, *ACS Appl. Mater. Interfaces* **2013**, *5*, 3048.

[76] J. Meiss, M. K. Riede, K. Leo, *J. Appl. Phys.* **2009**, *105*, 1.

[77] O. S. Hutter, H. M. Stec, R. A. Hatton, *Adv. Mater.* **2013**, *25*, 284.

[78] D. Yu, Y. Q. Yang, Z. Chen, Y. Tao, Y. F. Liu, *Opt. Commun.* **2016**, *362*, 43.

[79] A. Behrendt, C. Friedenberger, T. Gahlmann, S. Trost, T. Becker, K. Zilberberg, A. Polywka, P. Görrn, T. Riedl, *Adv. Mater.* **2015**, *27*, 5961.

[80] J. B. Kim, C. S. Kim, Y. S. Kim, Y.-L. Loo, *Appl. Phys. Lett.* **2009**, *95*, 183301.

[81] C. Zuo, L. Ding, *Small* **2015**, *11*, 5528.

[82] G. Zhou, L. Wang, J. C. Yang, *J. Appl. Phys.* **2005**, *97*, 063509.

[83] C. Gattinoni, A. Michaelides, *Surf. Sci. Rep.* **2015**, *70*, 424.

[84] Y.-R. Luo, *Comprehensive Handbook of Chemical Bond Energies*; CRC Press: Boca Raton, FL, 2007.

[85] W. Gao, H. Gong, J. He, A. Thomas, L. Chan, S. Li, *Mater. Lett.* **2001**, *51*, 78.

[86] M. O'Reilly, X. Jiang, J. T. Beechinor, S. Lynch, C. NíDheasuna, J. C. Patterson, G. M. Crean, *Appl. Surf. Sci.* **1995**, *91*, 152.

[87] J. Li, J. W. Mayer, E. G. Colgan, *J. Appl. Phys.* **1991**, *70*, 2820.

[88] M. C. Biesinger, L. W. M. Lau, A. R. Gerson, R. S. C. Smart, *Appl. Surf. Sci.* **2010**, *257*, 887.

[89] D. S. Ghosh, R. Betancur, T. L. Chen, V. Pruneri, J. Martorell, *Sol. Energy Mater. Sol. Cells* **2011**, *95*, 1228.

[90] W. A. Lanford, P. J. Ding, W. Wang, S. Hymes, S. P. Muraka, *Thin Solid Films* **1995**, *262*, 234.

[91] R. Liu, F. Zhang, C. Con, B. Cui, B. Sun, *Nanoscale Res. Lett.* **2013**, *8*, 155.

[92] B. Lesiak, A. Jablonski, J. Zemek, P. Jiricek, *Surf. Interface Anal.* **1998**, *26*, 400.

[93] M. A. Marcus, J. E. Bower, *J. Appl. Phys.* **1997**, *82*, 3821.

[94] S. Yu, G. Santoro, Y. Yao, D. Babonneau, M. Schwartzkopf, P. Zhang, S. K. Vayalil, P. Wessels, R. Döhrmann, M. Drescher, P. Müller-Buschbaum, S. V Roth, *J. Phys. Chem. C* **2015**, *119*, 4406.

[95] G. Kaune, M. A. Ruderer, E. Metwalli, W. Wang, S. Couet, K. Schlage, R. Röhlsberger, S. V Roth, P. Müller-Buschbaum, *ACS Appl. Mater. Interfaces* **2009**, *1*, 353.

[96] J. R. Levine, J. B. Cohen, Y. W. Chung, P. Georgopoulos, *J. Appl. Crystallogr.* **1989**, *22*, 528.

[97] T. L. Barr, *Surf. Interface Anal.* **1982**, *4*, 185.

[98] B. R. Strohmeier, *Surf. Interface Anal.* **1990**, *15*, 51.

[99] B. R. Strohmeier, D. M. Hercules, *J. Catal.* **1984**, *86*, 266.

[100] B. P. Payne, M. C. Biesinger, N. S. McIntyre, *J. Electron Spectros. Relat. Phenomena* **2009**, *175*, 55.

[101] B. P. Payne, A. P. Grosvenor, M. C. Biesinger, B. A. Kobe, N. S. McIntyre, *Surf. Interface Anal.* **2007**, *39*, 582.

[102] Y. Cudennec, A. Lecerf, *Solid State Sci.* **2003**, *5*, 1471.

[103] K. L. Chavez, D. W. Hess, *J. Electrochem. Soc.* **2001**, *148*, G640.

[104] H. J. Pereira, O. S. Hutter, G. D. M. R. Dabera, L. A. Rochford, R. A. Hatton, F. Flory, J. C. Bernéde, Y. Li, J. Hou, J. You, Y. Yang, F. von Wrochem, W. Wenzel, *Sustain. Energy Fuels* **2017**, *112*, 63505.

[105] J. Hun Park, W.-K. Kim, J. Seong Bae, D. Hee Lee, I. Hee Park, T. Woo Lee, Y. Chan Cho, J.-Y. Kim, S. Lee, C. Ryong Cho, S.-Y. Jeong, *Sci. Rep.* **2015**, *5*, 305.

[106] S. Lim, D. Han, H. Kim, S. Lee, S. Yoo, *Sol. Energy Mater. Sol. Cells* **2012**, *101*, 170.

[107] H. J. Pereira, R. A. Hatton, *Front. Mater.* **2019**, *6*, 228.

[108] F. Wiame, V. Maurice, P. Marcus, *Surf. Sci.* **2007**, *601*, 1193.

[109] T. K. S. Wong, S. Zhuk, S. Masudy-Panah, G. K. Dalapati, *Materials (Basel).* **2016**, *9*, 1.

[110] C. Zhang, D. Zhao, D. Gu, H. Kim, T. Ling, Y. K. R. Wu, L. J. Guo, *Adv. Mater.* **2014**, *26*, 5696.

[111] C. Y. Ho, M. W. Ackerman, K. Y. Wu, T. N. Havill, R. H. Bogaard, R. A. Matula, S. G. Oh, H. M. James, Electrical Resistivity of Ten Selected Binary Alloy Systems. *J. Phys. Chem. Ref. Data* **1983**, *12*, 183–322.

[112] J. Ilavsky, P. R. Jemian, *J. Appl. Crystallogr.* **2009**, *42*, 347.

[113] M. S. Wertheim, *Phys. Rev. Lett.* **1963**, *10*, 321.

[114] J. K. Percus, G. J. Yevick, *Phys. Rev.* **1958**, *110*, 1.

[115] E. Thiele, *J. Chem. Phys.* **1963**, *39*, 474.

6.7　Appendix
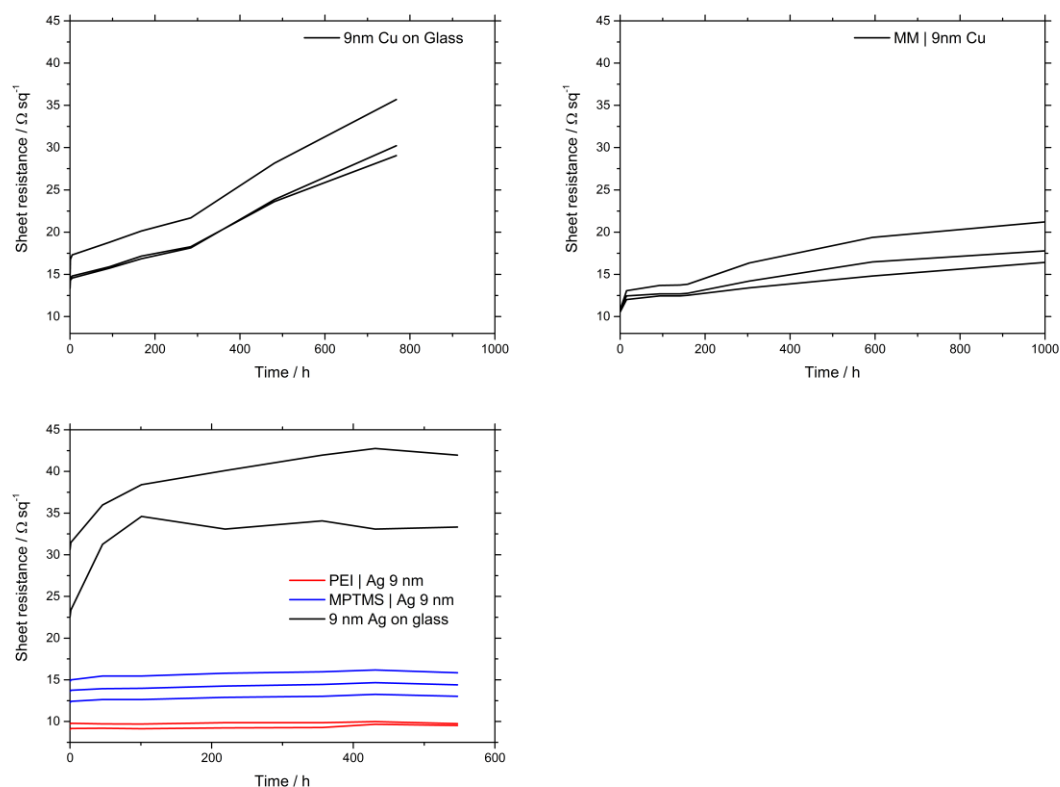
Figure A1: Graphs showing the change in sheet resistance with time exposed to ambient air for the five reference electrode structures given in Table 1.
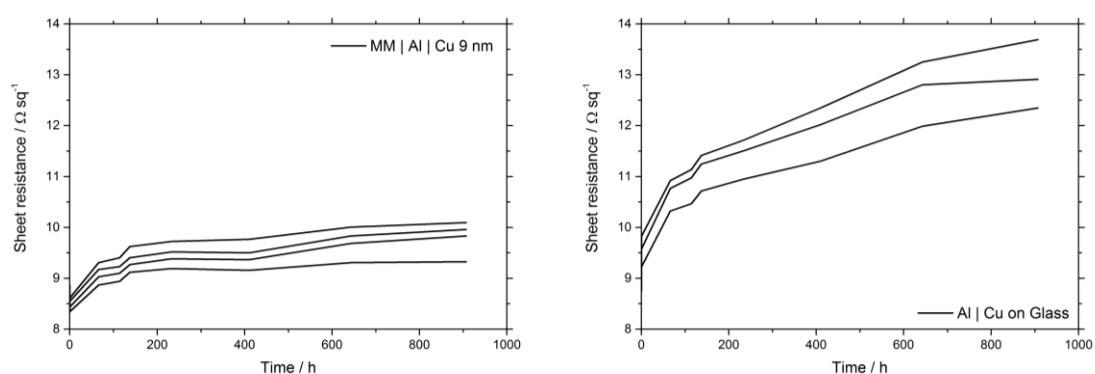
Figure A2: Graphs showing the change in sheet resistance with time exposed to ambient air for Al | Cu films fabricated with and without a mixed monolayer for adhesion (APTMS:MPTMS, 1:1) as in Table 1.
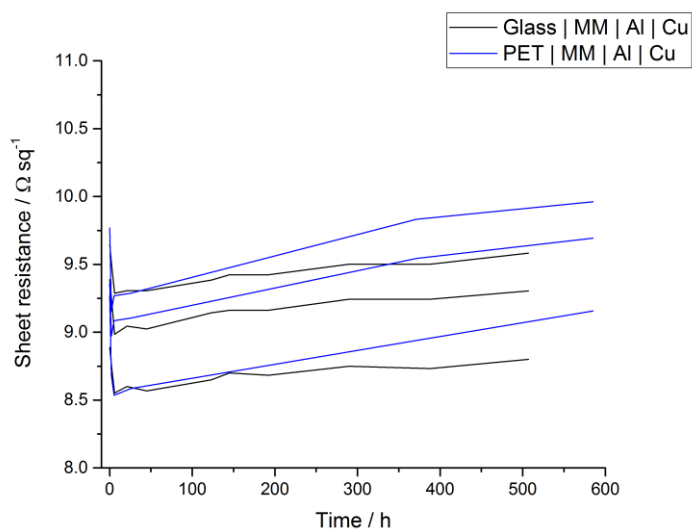
Figure A3: Evolution of sheet resistance with time exposed to air for 9 nm Cu films on glass (black) and PET (blue) modified with a mixed monolayer (MM) | 0.8 nm Al seed layer.

Table A1: The four sets of peak positions from the high resolution XPS study in Figure 15. Analysis was done using the CasaXPS software with a Shirley background fitting.

Cu 2p 3/2 – 0 hr oxidation		
Peak	**Position**	**Area**
1	932.70	186682.6

Cu 2p 3/2 – 400 hr oxidation		
Peak	**Position**	**Area**
1	932.45	30073.6
2	934.39	4547.6

3	935.39	4820.5

Cu LMM – 0 hr oxidation		
Peak	**Position**	**Area**
a	565.55	10061.2
b	567.08	4304.7
c	568.24	35334.9
d	569.66	8674.1
e	570.72	3145.2
f	572.41	18843.1

Cu LMM – 400 hr oxidation		
Peak	**Position**	**Area**
a	565.38	2302.8
b	566.84	579.2
c	567.98	5905.8
d	569.75	6316.6
e*	-	0

f	571.90	7341.2

*For 400 hr oxidation the small additional peak e, attributed to another transition state of the Cu LMM spectrum (alongside a, b, and f), was not necessary to achieve an effective fit. The increased intensity of peak d may make this difficult to assign with certainty.

7 An Evaluation of Evaporated Bilayer Cu/Sn and Cu/Zn films Used as an Electron-Selective Transparent Electrode in OPVs

7.1 Chapter Summary

In this chapter the possibility of passivating copper window electrodes towards oxidation in air with ultra-thin films of Sn and Zn is explored. Sn and Zn passivation layers were chosen because their oxidation products in air are n-type semiconductors with conduction band edges suitable for electrode extraction in OPVs. Sn layers with a thickness of ≥ 0.8 nm and Zn layers of ≥ 3 nm were found to be extremely effective at passivating an underlying Cu metal film. Cu | Zn 3 nm electrodes show virtually no oxidation of Cu after 6000 hours in air by XPS, and their integration into OPV devices is explored. Model devices are demonstrated with Cu 8 nm | Zn 3 nm metallic bilayer electrodes where the Zn layer both passivates the Cu and blocks hole extraction at the interface, improving device performance. We further demonstrate these electrodes can be fabricated and stored in air with integration to OPV devices < 2 weeks after evaporation to no consequence. The compatibility of passivated Cu-based electrodes with the previously developed microcontact printing process is latterly explored, whereby a sacrificial 2 nm Cu layer is found to improve dramatically the quality of the achievable pattern matching that achieved for high-purity Cu.

7.2 Introduction

As discussed, there is now wide recognition of the need for a new transparent electrode (TCE) matched to the processing requirements and strengths of organic photovoltaics (OPVs). It has been shown in the previous chapters of this thesis that Cu-based TCEs can simultaneously meet the requirements for flexibility, sheet resistance < 3 Ω sq^{-1} and transparency, with a raw material cost ~1% of comparable alternatives based on Ag.[4] In Chapter 4 this was achieved using microcontact printing to fabricate Cu grid electrodes with grid lines of < 2 μm width, < 25 μm inter-line distance and thickness of $40 - 120$ nm.

Cu has a similar conductivity to Ag but has a higher susceptibility to oxidation in air, forming a mixed oxide layer composed of the short-lived hydroxide $Cu(OH)_2$, Cu_2O and CuO. Despite progress with flexible encapsulants for OPVs, oxygen and moisture ingress is inevitable given sufficient time.[5,6] CuO and Cu_2O are both *p*-type semiconductors and their presence at the surface of the metal electrode is shown in Chapter 6 not to present a barrier to charge extraction in OPV devices at low thickness.[7,8] The reduced metal thickness does however degrade the sheet resistance of the electrode, leading to ohmic losses in OPV devices manifested as a degradation of the device fill factor.[3]

In Chapter 5 it is shown that an evaporated aluminium (Al) layer of just 0.8 nm thickness (4-5 atoms thickness) effectively passivates Cu films at room temperature, which is remarkable because the self-limiting native oxide thickness of Al is > 2 nm:[9,10] After more than two years in ambient air 9 nm thick Cu films with a 0.8 nm Al overlayer show no significant change in sheet resistance.[11] In Chapter 5 it was shown that the effectiveness of such a thin Al layer stems from the behaviour at the nanoscale: Firstly, upon condensation, the Al alloys with the underlying Cu to form an oversaturated alloy at the surface of the crystallites before spontaneously phase separating preferentially to the grain boundaries in the underlying polycrystalline Cu film, forming $Cu_xAl_yO_z$ plugs. These mixed $Cu_xAl_yO_z$ plugs block the ingress of oxygen along grain boundaries in the Cu film where it reacts to form copper oxides, increasing the contact resistance between grains. Secondly, the mixed overlayer prevents the egress of Cu$^+$ ions from the Cu bulk to the air-interface where a reaction occurs with adsorbed water to form CuO via the metastable hydroxide, $Cu(OH)_2$.[12] Additionally the Cu | Al bilayer electrode has a very low work function of 3.1 eV rising to 3.8 eV upon oxidation making it suitable as the

electron extracting electrode in OPVs.[10] Unfortunately HDT does not form SAMs on Cu | Al bilayer films with sufficiently low defect-density to act as an effective mask to a wet etchant, and so cannot be patterning using µ-CP to fabricate high-performance transparent electrodes using the method described in Chapter 4.

This chapter describes investigations aimed at exploring the potential of ultra-thin evaporated tin (Sn) and zinc (Zn) metal overlayers on Cu to protect the underlying Cu film from air-oxidation. Both Sn and Zn can be easily thermally evaporated and, similarly to Al, will oxidise readily in air and at ambient temperatures to form low work function oxides. The oxidation products of both metals are known to perform well as electron selective contacts for photovoltaic devices.[13,14] Indeed, Zn reduces the energy outlay as it can be evaporated at extremely low temperatures (180°C at 10^{-6} mBar). Unlike the case of Al_2O_3, the dominant oxide products of both Sn (SnO_2) and Zn (ZnO) are semiconductors, with accessible conduction bands for electron transport and so there is not the same constraint on film thickness.

7.3   Results and Discussion

Figure 1 is an exploded schematic of the Cu-based model electrode structure as-deposited (i.e. before air exposure) evaluated in this chapter. Due to the low metal thickness, changes in electrical resistance can be used to monitor the rate and extent of oxidation as a function of capping layer choice for oxide thicknesses in the range 0.5 – 5 nm.
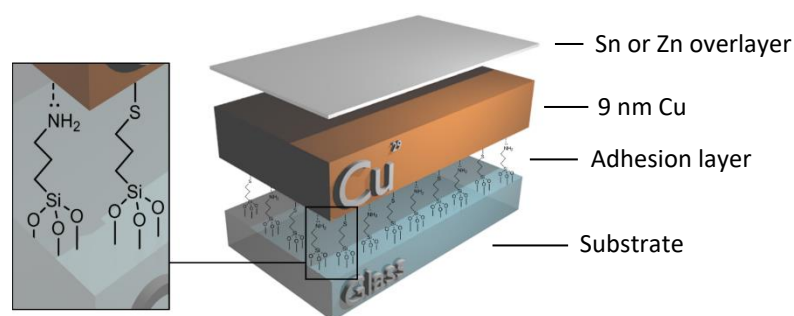
Figure 1: Schematic depiction of the electrode structures investigated in this chapter. The expansion (left) shows the mixed molecular adhesive layer used to enable the fabrication of a robust Cu film on glass or plastic substrates as described in previous chapters. Sn and

Zn overlayers of thickness 0.8 and 3 nm were investigated as barrier layers for the protection of metallic Cu.

7.3.1 *Thin film characterisation – Cu/Sn bilayers*

Figure 2 shows the evolution of the sheet resistance over time for a 9 nm Cu reference film (Blue) and 9 nm Cu films with Sn overlayers of 0.8 nm (Black) and 3 nm (Red). The lower thickness of 0.8 nm was chosen to allow a direct comparison to the effectiveness of a 0.8 nm Al overlayer as evaluated in Chapter 5. Both films with Sn overlayers have a starting sheet resistance 33% below that of the unprotected Cu 9 nm film (Pure-Cu: 10.8 ± 0.2, Cu | Sn 0.8 nm: 7.2 ± 0.1, Cu | Sn 3 nm: 7.1 ± 0.1 Ω sq^{-1}; Table 1), because the sheet resistance measurements are made in ambient air: It is shown in Chapter 5 that the initial oxide formation on pristine Cu is extremely rapid and results in a sharp initial increase in resistance attributed to oxidation of the grain boundaries between copper crystallites. It is notable that the starting sheet resistance of 9 nm Cu films with a 0.8 nm Sn overlayer is almost the same as that with a 3 nm Sn overlayer. The conductivity of Sn is only 15% that of Cu however, and so 3 nm of Sn is equivalent to 0.45 nm of additional Cu thickness which is within the range of certainty associated with Cu metal thickness: ± 5%. The contribution that the Sn overlayer makes to the conductance of the bilayer film is further reduced if the Sn layer is oxidized.

Figure 2 shows that a 0.8 nm Sn overlayer is remarkably effective at retarding oxidation of the underlying Cu and is equally effective as a much thicker 3 nm layer. Given that the conductivity of Sn is 15% that of Cu, to a good approximation its contribution to the film conductance can be ignored and the increase in sheet resistance interpreted in terms of an equivalent thickness of Cu converted to copper oxides. It is estimated from the sheet resistance increase after 5000 hours of air exposure that 1.4 nm of the initial 9 nm Cu has been oxidized. Since the sheet resistance of Cu films with 0.8 and 3 nm Sn overlayers is relatively stable after 300 hours in air, it is assumed that the majority of this oxide is formed in the first 300 hours. To the best of the authors knowledge, the native oxide thickness of Sn metal under ambient conditions is not well characterized; however, the low critical thickness of Sn ($\leq$ 0.8 nm) in order to passivate an underlying Cu layer is indicative of a mechanism similar to that of a 0.8 nm Al overlayer on Cu. It is postulated that, similarly to Al, Sn segregates to the grain boundaries and forms stable oxide 'plugs' which prevent degradation of the contact resistance

between grains. The high stability of Sn capped Cu electrodes in air, where the concentrations of H_2O and O_2 are far in excess of that experienced *in-situ* in an OPV devices since OPV devices are universally encapsulated to slow the ingress of these, bodes well for application in OPVs.
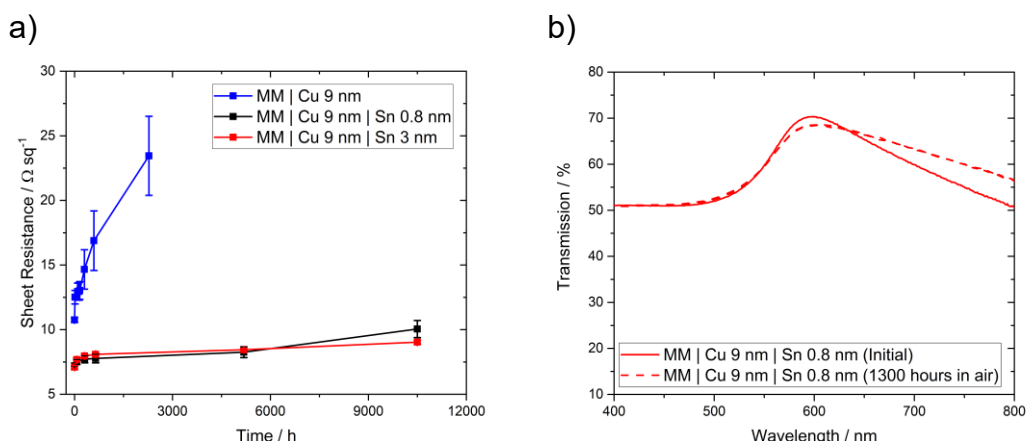

Figure 2: (a) Evolution of the sheet resistance for 9 nm Cu films supported on glass derivatized with an APTMS:MPTMS monolayer protected by overlayers, as in Figure , of 0.8 nm Sn (Black), 3 nm Sn (Red) or no overlayer (Blue). The temperature and humidity fluctuated in the range 18-30°C and 15-50% respectively during monitoring, first measurements were made after < 5 minutes in air. Tabulated initial and minimum sheet resistances are given in Table 1. (b) The Far-field transparency of MM | Cu | Sn 0.8 nm at 0 (Solid line) and 1300 hours (Dashed line) in air.

Table 1: Tabulated initial sheet resistances and minima sheet resistances for the electrodes in this work based around a 9 nm Cu film with evaporated Sn or Zn overlayers. Initial measurements were taken after < 5 minutes air exposure.

Electrode Structure	Full Structure	Initial Average Sheet Resistance ± Standard Deviation (Ω sq^{-1}) *(Champion)*	Minimum Average Sheet Resistance ± Standard Deviation (Ω sq^{-1}) *(Champion)*	Minimum Point (Hours)
MM | Cu	Glass | APTMS:MPTMS | 9 nm Cu	10.8 ± 0.2 *(10.5)*	10.8 ± 0.2 *(10.5)*	0
MM | Cu | Sn 0.8 nm	Glass | APTMS:MPTMS | 9 nm Cu | Sn 0.8 nm	7.2 ± 0.1 *(7.2)*	7.2 ± 0.1 *(7.2)*	0
MM | Cu | Sn 3 nm	Glass | APTMS:MPTMS | 9 nm Cu | Sn 3 nm	7.1 ± 0.1 *(7.0)*	7.1 ± 0.1 *(7.0)*	0
MM | Cu | Zn 0.8 nm	Glass | APTMS:MPTMS | 9 nm Cu | Zn 0.8 nm	7.7 ± 0.1 *(7.7)*	7.7 ± 0.1 *(7.7)*	0
MM | Cu | Zn 3 nm	Glass | APTMS:MPTMS | 9 nm Cu | Zn 3 nm	9.0 ± 0.2 *(8.7)*	8.6 ± 0.1 *(8.4)*	95

The small evolution of the transmission spectrum of the 9 nm Cu | 0.8 nm Sn film after an extended period in air (Figure 2 (b)) is consistent with the formation of a very thin oxide layer: The increasing transmission at longer wavelengths where reflection dominates is most sensitive to the formation of thin films of wide band gap materials such as SnO_2, CuO_2 or CuO. The observation of very little change in absorption at low wavelengths, the region associated with inter-band transitions in Cu metal, also supports the conclusion that little oxidation of the Cu film has occurred.

After 6000 hours of air exposure, XPS analysis of MM | Cu 9 nm | Sn 0.8 nm and MM | Cu 9 nm | Sn 3 nm electrodes was performed to determine the extent of oxidation. The Sn 3d region has two peaks with a spin-orbit separation of ~ 8 eV and an intensity ratio of 2:3, corresponding to Sn $3d_{3/2}$ and $3d_{5/2}$. The Sn $3d_{5/2}$ region for the MM | Cu | Sn 3 nm film, shown in Figure 3 (a), has peaks at 486.6 and 485.1 eV characteristic of SnO_2/SnO and Sn(0) respectively. The difference in binding energy between Sn 3d electrons in SnO and SnO_2 is approximately 0.1 eV and so too small to be resolved.[15] In contrast the MM | Cu | Sn 0.8 nm film spectra in Figure 3 (b) has no peak corresponding to Sn(0); all of the Sn metal has been oxidized to SnO/SnO_2. After 6000 hours in air, the presence of remaining metallic Sn for the film starting with a 3 nm Sn thickness indicates that either a self-limiting native oxide layer has been formed at the air interface or the rate of continuing oxidation is negligible. Importantly, since the sheet resistance of the Cu film with 0.8 nm Sn overlayer is equivalent to that with a 3 nm Sn thickness after 6000 hours exposure to air (Figure 2 (a)) this indicates that the passivation of the underlying Cu is related to the formation of a thin Sn oxide layer at the air-interface. After more than 10000 hours air exposure the Cu film with 0.8 nm Sn overlayer exhibits a small but significant increase in sheet resistance as compared to that with a 3 nm Sn thickness, which supports the formation of a self-limiting native Sn oxide layer at 3 nm starting thickness but not 0.8 nm.
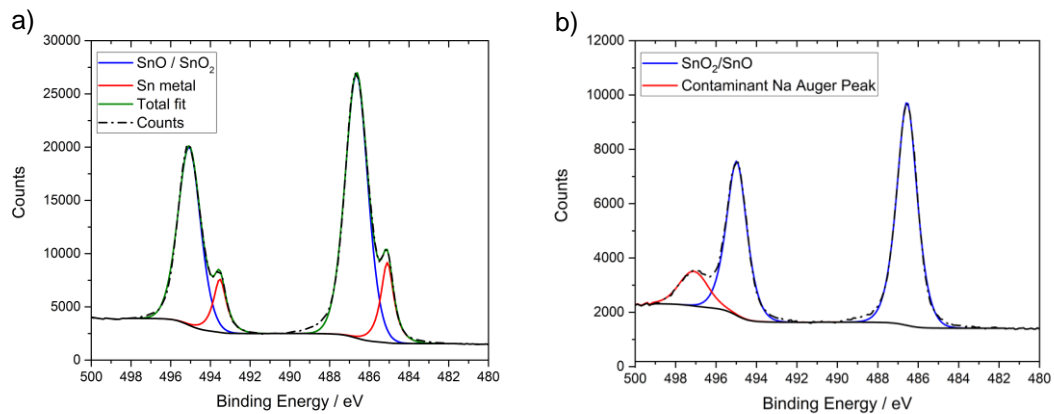

Figure 3: (a) Fitted XPS spectra of the Sn 3d region for a MM | Cu 9 nm | Sn 3 nm electrode exposed to ambient laboratory air for 6000 hours. (b) Fitted XPS spectra of the Sn 3d region for a MM | Cu 9 nm | Sn 0.8 nm electrode exposed to ambient laboratory air

for 6000 hours. The contaminant peak is confirmed as Na by the strong Na 1s peak at ~1071 eV in the survey spectrum.

The transmission spectra in Appendix, Figure A1 also reflect the difference between the 0.8 nm and 3 nm Sn overlayers because SnO_2 and SnO are wide band gap semiconductors, whereas Sn(0) absorbs light strongly degrading the film transmission. For metal grid electrode applications this parasitic absorption is not important but confirms the presence of Sn metal. Although the transparency of the MM | Cu 9 nm | Sn 3 nm electrode is too low for application as a transparent conductive electrode in OPVs, films of higher Cu thickness protected still by a 3 nm Sn overlayer could for example be patterned into opaque grid lines with transparent voids (as in Chapter 4) to overcome this.

Figure 4 shows the Cu 2p region of the XPS spectra of 9 nm Cu films with overlayers of (a) 0.8 nm Sn (b) 3 nm Sn. These are supported by the corresponding Cu Auger electron spectra, shown in Figure 5. The Auger electron spectra are complimentary to the Cu XPS spectra because the difference in binding energy between Cu^{1+} and Cu^0 in the Cu 2p region (Figure 4) is too small to be able to be resolved; Cu(0) 932.6 and Cu_2O 932.4 eV.[16] The Auger peaks confirm that the Cu_2O component obscured in the Cu 2p region follows the trend of the CuO and $Cu(OH)_2$ peaks identifiable in the 2p region: MM | Cu | Sn 0.8 nm shows the most Cu_2O characteristic (peaking at 916.8 eV)[16] with MM | Cu | Sn 3 nm lesser, although still present. To simplify the discussion, in the following discussion the 'Cu Oxide Components' will refer to the intensity of those peaks assigned to $Cu(OH)_2$ (935.4 eV) and CuO (934.4 eV) in the Cu 2p XPS spectra (Figure 4) and the 'Cu Metal Component' as the Cu(0)/Cu_2O peak at 933.7 eV.
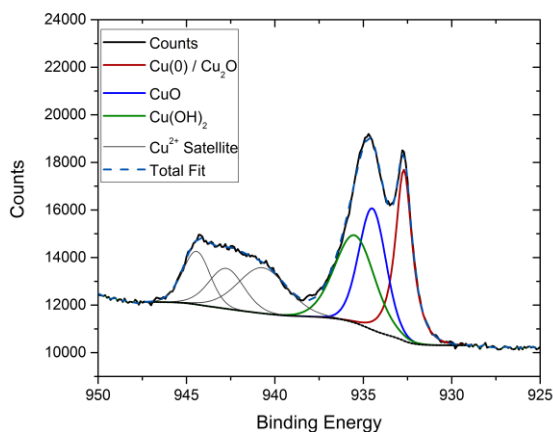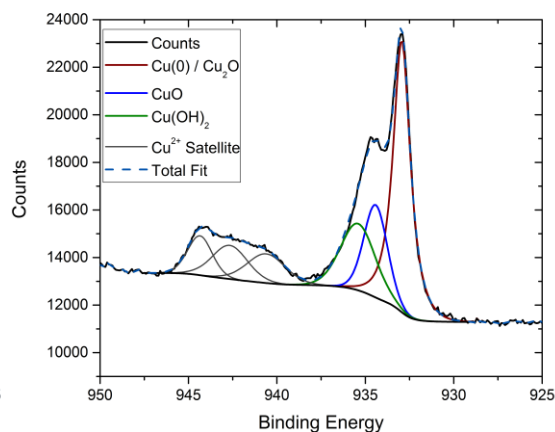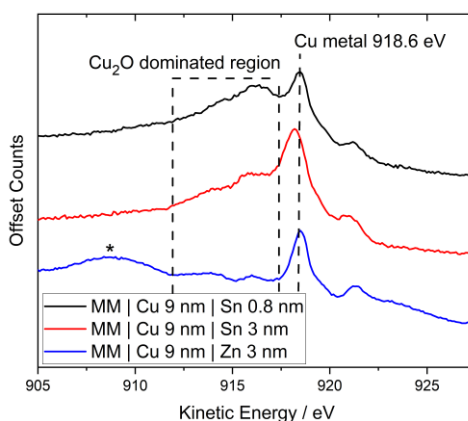
Figure 4: XPS spectra, unadjusted, of the fitted Cu 2p regions for two electrodes after 6000 hours in air. (a) MM | Cu 9 nm | Sn 0.8 nm, (b) MM | Cu 9 nm | Sn 3 nm.

Figure 5: Cu Auger Electron Spectra corresponding to the scans made in Figure 4 of MM | Cu | Sn 0.8 nm (Black), MM | Cu | Sn 3 nm (Red) and MM | Cu | Zn 3 nm (Blue) after 6000 hours in air. *Zn Auger Peak.

Most immediately notable from Figure 4 is there is significant Cu oxidation for both Sn thicknesses. A quantitative comparison is not made due to the high attenuation of the Cu signal anticipated by the thicker 3 nm Sn overlayer. It is however clear from the relative intensities of the Cu^0 and oxide peaks that the Cu film with a 0.8 nm Sn overlayer has a greater extent of Cu oxidation than that with a 3 nm Sn thickness. The increase in the

sheet resistance of 15% for both films over the same period (Figure 2) gives an estimated Cu thickness lost to oxide formation of 1.4 nm. Although the equal sheet resistance seems contradictory to the greater extent of Cu oxide in the XPS spectra for the Cu film with 0.8 nm Sn thickness, the oxidation at grain boundaries is expected to dominate the changes in sheet resistance. This difference is therefore indicative of effective passivation for both Sn thicknesses at the crucial grain boundaries, however the greater coverage of the 3 nm Sn overlayer prevents long-term oxidation of the crystallite surfaces. This effect can be seen after > 10000 hours air exposure by a small but significant increase in the sheet resistance of the MM | Cu 9 nm | Sn 0.8 nm film.

We postulate that the comparable effectiveness to passivate underlying Cu of the 0.8 nm Sn overlayer when compared to a 3 nm thickness, supported by the XPS spectra, is evidence of a similar behaviour to the Cu/0.8 nm Al system where Cu and Sn spontaneously segregate from an oversaturated alloy preferentially at grain boundaries as mixed oxide 'plugs'. This similar mechanism is supported by the phase diagram for the Cu-Sn system at room temperature:[17] There are very few stable single-phase regions and as such the driving force for segregation is high for most compositions.

### 7.3.2   *Thin film characterisation – Cu/Zn bilayers*

It is evident from Figure 6 that the sheet resistance of the MM | Cu | Zn 0.8 nm electrode is initially lower than the bare 9 nm Cu film, which is attributed to oxidation of the Zn overlayer before the onset of Cu oxidation. The long-term stability is poor however, being essentially the same as for a bare Cu film.
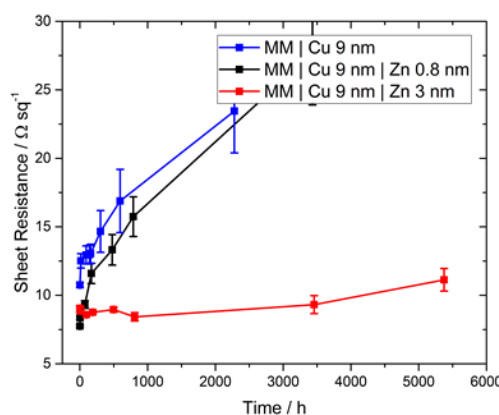
Figure 6: Evolution of the sheet resistance for 9 nm Cu films supported on glass derivatized with an APTMS:MPTMS monolayer protected by overlayers, as in Figure , of 0.8 nm Zn (Black), 3 nm Zn (Red) or no overlayer (Blue). The temperature and humidity fluctuated in the range 18-30°C and 15-50% respectively during monitoring, first measurements were made after < 5 minutes in air. Tabulated initial and minimum sheet resistances are given in Table 1.

Cu films with a 3 nm Zn overlayer exhibit a sustained reduction in the sheet resistance for the first 100 hours, like that previously observed for a Cu | 0.8 nm Al bilayer film in Chapter 5. In the Cu/Al bilayer system this is understood to be associated with dealloying from an oversaturated Cu/Al alloy. The greater thickness of the Cu alloy, the lower the thickness of the pure Cu which is by far the biggest contributor to the overall conductivity of the electrode. Unlike the Cu/Al system, no evidence for alloying is seen in the sheet resistance with a 0.8 nm Zn overlayer. This difference is believed to be caused by the relative rapidity of Zn oxidation even under the deposition conditions used here (base pressure $\leq 10^{-6}$ mBar): At room temperature clean Zn foil exposed to 7×10^{-7} Torr pressure of O_2 (UHV) was shown by Noothongkaew *et al.* to form a 1.5 nm thick ZnO overlayer after only 5 minutes.[18] Despite the propensity of Zn/Cu to alloy, the rapidity of this oxidation is believed to fix the Zn at the interface and reduce the degree of alloying. This is supported by the unexpectedly higher initial sheet resistance of MM | Cu 9 nm | Zn 3 nm (9.0 ± 0.2 Ω sq^{-1}) than MM | Cu 9 nm | Zn 0.8 nm (7.7 ± 0.1 Ω sq^{-1}) as the thicker Zn layer is expected to take longer to oxidise under vacuum and as such the window of opportunity to alloy with Cu is increased. Since alike the Al/Cu alloy, Zn/Cu alloys are of higher resistivity than pure-Cu this explains the higher sheet resistance.

The transparency of a MM | Cu 9 nm | Zn 3 nm electrode (Figure 7 (a)) is reduced as for a 3 nm Sn overlayer, although to a lesser extent possibly due to the higher reactivity of Zn and so faster conversion to the oxide. Unlike the Sn overlayer however, within the first 100 hours in ambient laboratory air the transparency of the electrode lost is largely recovered. This highlights a key difference between the two metal overlayers; unlike 3 nm Sn, the Auger electron spectrum shows that 3 nm Zn is rapidly oxidized to a ZnO overlayer (Figure 8) without any evidence for retention of metallic character. Since ZnO is a wide band-gap semiconductor (~ 3.4 eV), the average transmission recovery is consistent with the conversion of Zn to ZnO. A small side peak at ~990 eV in Figure 8 is possible evidence of a small presence of ZnS, a wide band gap compound formed by sulfurization in air. The passivation of Cu by a 3 nm Zn overlayer is also evident from the evolution of the transmission spectra after 100 and 3500 hours in air (Figure 7 (b)): The shape of the spectrum is typical of that for bare Cu and remains unchanged over time. For this comparison, since as discussed the transparency of films with a 3 nm overlayer improve over the first 100 hours exposure caused by the oxidation of Zn, the 100 hour scan is used as opposed to the initial scan (Figure 7 (a)).
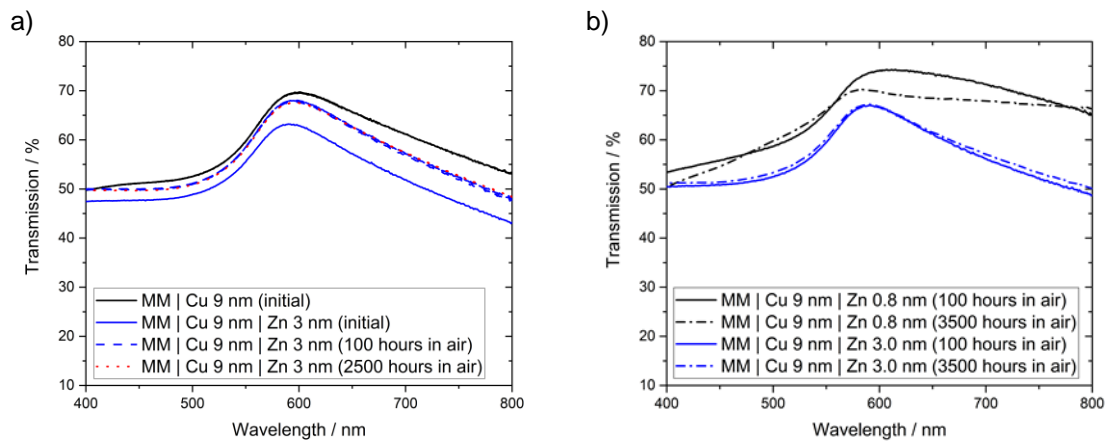

Figure 7: (a) The evolution of the far-field transparency of an MM | Cu 9 nm | Zn 3 nm film over time in ambient air. (b) Far-field transparency of MM | Cu 9 nm | Zn 0.8 nm (Black) and 3 nm (Blue) after 100 hours (Solid lines) and after 3500 hours in air (Dashed lines). 100 hours is used as a baseline due to the initial drop in sheet resistance attributed to the de-alloying of Zn above.
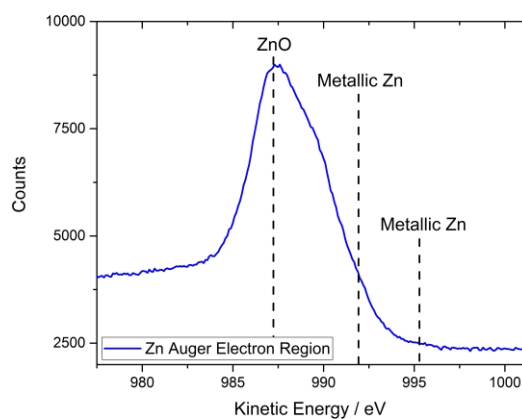
Figure 8: The Zn LMM Auger Electron spectrum of the same Cu | Zn 3 nm film from Figure 7 after 6000 hours in ambient laboratory air.

For application in OPVs it is important that the transparent electrode is stable to heating up to 200°C to enable subsequent air processing steps, such as ZnO sol-gel formation which requires 180°C heating in air. At 100°C (Figure 9, Red) an unprotected 9 nm Cu film in air is completely oxidized and changes color to yellow. Conversely, the Cu 9 nm film capped with a 3 nm Zn layer (Figure 9 (Black)) combines both morphological and oxidative stability, reflected in a stable sheet resistance, up to 250°C when heated in air. The implications of this important result to produce PEDOT:PSS-free Cu grid OPVs are discussed in the future work.
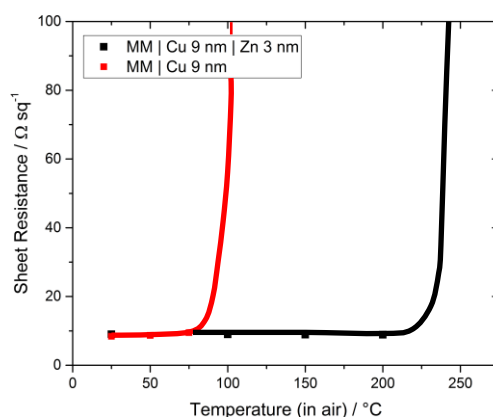
Figure 9: The evolution of sheet resistance with concurrent 15-minute heating steps for an unprotected MM | Cu 9 nm film (Red) and a protected MM | Cu 9 nm | Zn 3 nm film (Black). The added lines are to guide the eye only, both electrodes rise to > 500 Ω sq^{-1} at 100 and 250°C respectively.

Figure 10 shows the overlaid Zn 2p and Cu 2p XPS spectra of the same MM | Cu 9 nm | Zn 3 nm film after 6000 hours in air for take-off angles (θ) of 90, 30 and 15°. The mean free path (λ) for photoelectrons in the relevant energy range is approximately 2.5 nm for ZnO,[19] and so 95% of photoelectrons originate from a depth of 7.5, 5.0 and 2.5 nm for 90, 30 and 15° respectively (3 λ sin[θ]).

The Zn overlayer will increase in thickness when converted to ZnO due to the lower density of the oxide (Zn; 7.1 g/cm^3, ZnO; 5.6 g/cm^3), and so 3 nm of Zn^0 will convert to a ~ 4.7 nm ZnO layer. For a take-off angle of 90° and 30° it is expected to see significant Cu intensity even in the aged MM | Cu | Zn electrode (with 95% signal coming from the top 7.5 nm and 5 nm respectively), however at 15° very little intensity attributed to the underlying Cu is expected. In Figure 10, at 90° (~7.5 nm sampling depth) Zn and Cu are detected in the survey scan at an atomic ratio of 86:14. A low ratio of Cu intensity is expected despite that the sampling depth is greater than the ZnO thickness because the Cu intensity will be shielded from the detector by the ZnO overlayer. At both 30° (top ~5 nm) and 15° (top ~2.5 nm), at which depths it is not expected to probe the bulk Cu film, the atomic ratio stabilizes at 91:9 showing the presence of Cu mixed at small quantities evenly throughout the ZnO layer. At low atomic ratios, Zn is miscible with Cu and forms a solid solution at room temperature of a single phase.[20] As such this alloying may occur

in the early phases (prior to oxidation), or post-oxidation since the *in-situ* doping of ZnO nanoparticles by Cu is already well characterized.[21,22]
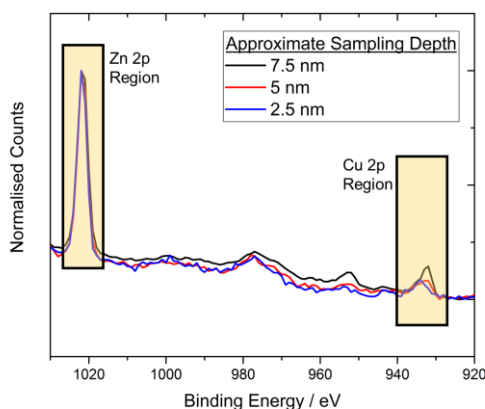
Figure 10: Three survey scans of an aged MM | Cu 9 nm | Zn 3 nm electrode after 6000 hours in air at take-off angles of 90° (Black), 30° (Red) and 15° (Blue). The spectra have been normalised to the Zn 2p peak at 1022 eV to aid comparison.

Figure 11 shows the Cu 2p region of the XPS spectra of 9 nm Cu films with a 3 nm Zn overlayer after 6000 hours air exposure. Cu films with a 0.8 nm Zn overlayer were not analysed because the sheet resistance stability in Figure 6 shows no passivation effect with this overlayer thickness. This is supported by the corresponding Cu Auger electron spectrum, shown alongside those for Sn in Figure 5. The Auger peaks confirm that the Cu_2O component obscured in the Cu 2p region is in agreement with those for CuO and $Cu(OH)_2$ peaks identifiable in the 2p region: There is no evidence for significant Cu_2O oxide in the Auger electron spectrum.
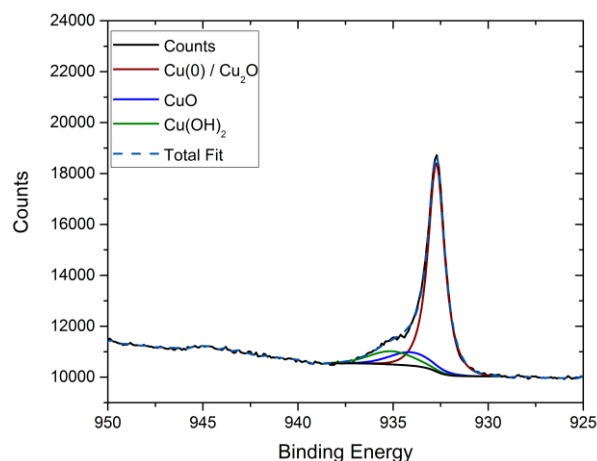
Figure 11: A fitted Cu 2p region by XPS of the electrode structure MM | Cu 9 nm | Zn 3 nm after 6000 hours air exposure. This is directly comparable to Figure 4.

Although some degree of alloying is also seen in the Cu/Zn system (Figure 10), the low total Cu intensity here as compared to the comparable Cu with Sn 3 nm overlayer shown earlier in Figure 4 is indicative of a lower degree of alloying, with greater Cu held in the bulk and shielded by the predominantly ZnO overlayer. This is proposed as an explanation for why the Cu | Zn 3 nm system is both the least stable to long-term changes in sheet resistance (Figure 6) and yet the lowest Cu oxide content, with very little oxide contribution in Figure 11: The mixed oxide systems (Cu/Al and Cu/Sn) appear to form stable native oxide layers where further oxidants cannot penetrate or penetrate only very slowly, however initial oxidation is necessary to achieve passivation. The Cu/Zn system however alloys only at very low concentrations and as such the overlayer behaves as ZnO which is known to not form a stable native oxide and continue oxidation steadily over time; oxygen species continue to diffuse through even bulk ZnO and, although slow, the further oxidation of Zn metal continues.[23]

The products of Zn air-oxidation are demonstrated in Figure 12 (a): The Zn LMM spectra of a 100 nm Zn film after 900 hours air exposure shows significant peaks assigned to metallic Zn (992 eV) and ZnO (987 eV) only, with no peaks relating to other oxidation products.[24] The evolution of the sheet resistance over time for a 100 nm Zn film grown on a 2 nm Cu seed layer (Zn adheres only very weakly to glass substrates compared to Cu, Figure 12 (b)) shows a beneficial process occurs over the first 50 hours reducing the

resistivity, before oxidation at a steady state where further Zn is continuously oxidized to ZnO. It is likely that this beneficial process is linked to changes in the polycrystalline structure of Zn and linked to the low melting point, as reported here Chapter 4 for thick Cu films, and that this process competes with the continuous oxidation of metal. The formation of ZnO at the surface of Zn metal in air raises the suitability for application in OPVs as an ETL: Nanoparticulate ZnO is already well established as the dominant ETL for flexible OPVs.[21,22,25–37] The continual nature of Zn oxidation indicated by Figure 12 (b) is important to note as it raises the possibility of tuning the thickness of Zn deposited to form an *in-situ* oxygen sink within OPVs: The inclusion of a thick Zn layer between the electrode and sensitive polymeric absorber layers may soak O_2 and H_2O offering protection to the adjacent materials.
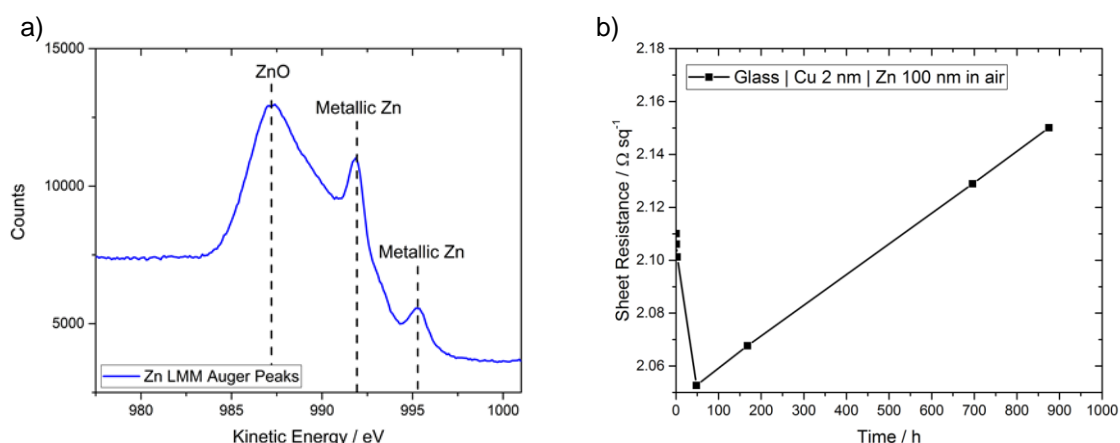

Figure 12: (a) Auger LMM excitation spectra of an air-exposed 100 nm Zn film with dashed lines to direct the eye to those features typical of ZnO (987 eV) and metallic Zn (992, 995 eV). (b) Evolution of the sheet resistance of the same film in air over time. The temperature and humidity fluctuated in the range 18-30°C and 15-50% respectively during monitoring.

7.3.3 Model OPV devices – Cu/Zn bilayer

The photoelectron spectroscopy analysis shows that a 3 nm Zn layer on Cu is entirely converted to ZnO within 100 hours exposure to air and is doped with Cu. ZnO is already widely used for the selective extraction of electrons in OPVs, although it is almost always deposited in the form of ZnO nanoparticles or a film on organo-zinc compound that is converted to ZnO by heating in air. It was therefore of interest to evaluate if ZnO formed by air oxidation of the metal could serve as an electron extracting layer in the model OPV device with structure: Cu | Zn 3 nm | ITIC/PBDB-T | MoO₃ | Al (

Figure **13**). Throughout this section, the thicknesses of each layer were not optimized and so the current density and PCE are not the maximum achievable. The device fill-factor is dominated by the resistances within the device structure however, and as such is a good measure of the effectiveness of the Zn overlayer as an ETL.
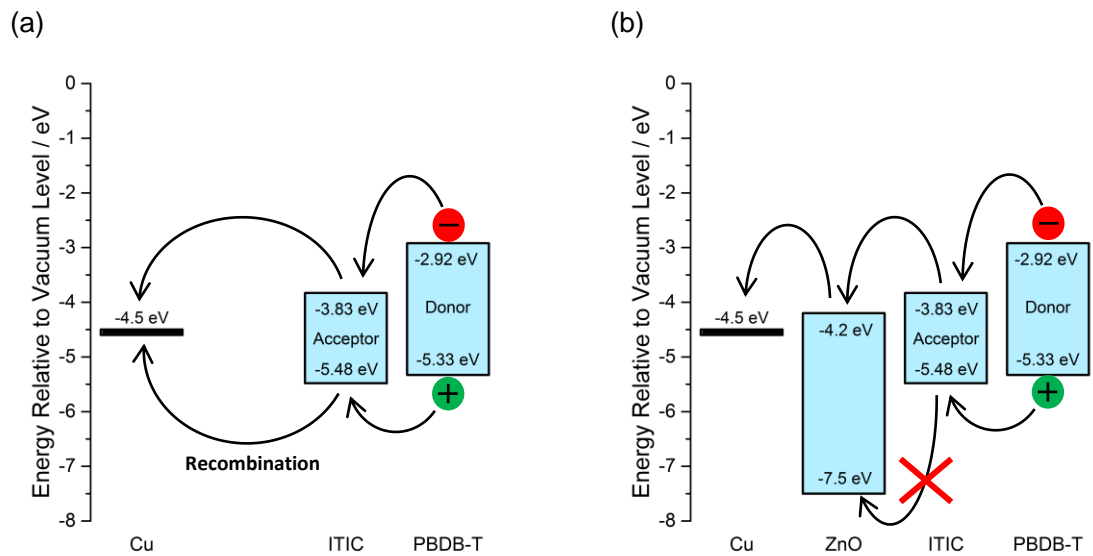

Figure 13: Flat band energy level diagram for the electron-extracting structure used here (Cu,[10] ZnO,[38] ITIC,[39] PBDB-T,[35]) (a) without and (b) with an ideal ZnO interfacial layer to block recombination.

It is anticipated that significant oxidation of the 3 nm Zn metal layer will occur even within the inert (< 2 ppm O_2/H_2O) environment of the glovebox.[18] To understand whether the selectivity of Cu electrodes capped with a 3 nm Zn layer evolves with increasing oxidation-pressure, model OPVs were fabricated with the structure Cu | Zn 3 nm | ITIC/PBDB-T | MoO_3 | Al. Half of the electrodes were annealed at 120°C in air to simulate long-term ambient oxidation and half were incorporated directly upon fabrication with no intentional oxidation (Figure 14, Appendix; Table A1). The champion device fill-factor between annealed and non-annealed electrodes is similar at 0.57 and 0.55 respectively, however the variation is much higher for the non-annealed electrodes which is attributed to heterogeneous oxidation of the Zn metal layer. The similar series resistance evident from Figure 14 shows that incomplete oxidation of the Zn metal layer does not block electron extraction to the underlying Cu. The lower champion performance (PCE: 4.79 *vs* 2.94%) of the non-annealed electrode is largely caused by the loss in open-circuit voltage. It is evident from the dark current response in Figure 14 that this lower voltage is caused by an earlier onset of forward current injection. It is possible that this lower barrier to current injection in forward bias results from the tunnelling of holes across the ZnO layer at voltages > 0.7 V, facilitated by the incomplete oxidation of Zn forming only a thin ZnO layer (1 – 2 nm) in the non-annealed sample, and that this may be improved by *in-situ* ageing.
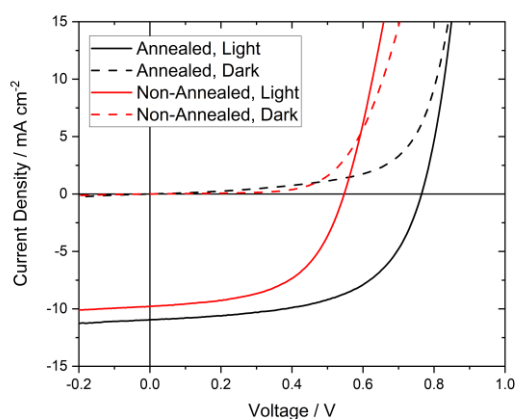
Figure 14: Champion device characteristics for model OPV devices on MM | Cu | Zn 3 nm electrodes where half are heated in air before processing (Black lines) and half held under N_2 (Red lines). Electrode | PBDB-T/ITIC | MoO_3 | Al.

The open circuit voltage can be further improved by the inclusion of an additional ZnO-nanoparticle interlayer, from 0.71 ± 0.06 to 0.82 ± 0.02 V (Appendix, Table A1), shown in Figure 15. The addition of the ZnO-nanoparticle layer also improves the champion fill-factor from 0.57 to 0.67. In combination this suggests that 3 nm of Zn, equivalent to a ~ 5 nm ideal ZnO layer, is below the optimal thickness for this design to block hole current through the device. The lower current for the non-optimised Cu electrode device is a function of the lower transparency of the Cu electrode compared to ITO-coated glass.
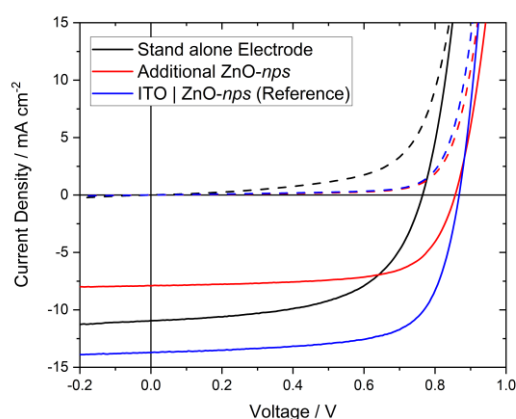
Figure 15: Champion device characteristics for model OPV devices on pre-annealed MM | Cu | Zn 3 nm electrodes with the structure Electrode | Optional ZnO-nanoparticle layer | PBDB-T/ITIC | MoO$_3$ | Al.

In Chapter 6, the tolerance of OPVs based upon an unprotected 8 nm Cu electrode to oxidation at the interface was assessed: Unexpectedly, the presence of a ~ 3 nm copper oxide layer appears to have no significant effect upon device performance for an unprotected Cu electrode (Champion PCE 6.51 *vs* 6.78% for a pristine Cu electrode). The dominant factor affecting device performance was shown to be the remaining thickness of the underlying Cu metal film, the degradation of which directly increases the series resistance. Since after 6000 hours of air exposure, the Cu 2p XPS spectrum in Figure 11 reveals no significant copper oxide layer, a comparable experiment was designed to assess the influence of a 3 nm Zn overlayer on the shelf-life of Cu based electrodes; OPV devices were fabricated using MM | Cu 9 nm | Zn 3 nm electrodes that had been exposed to
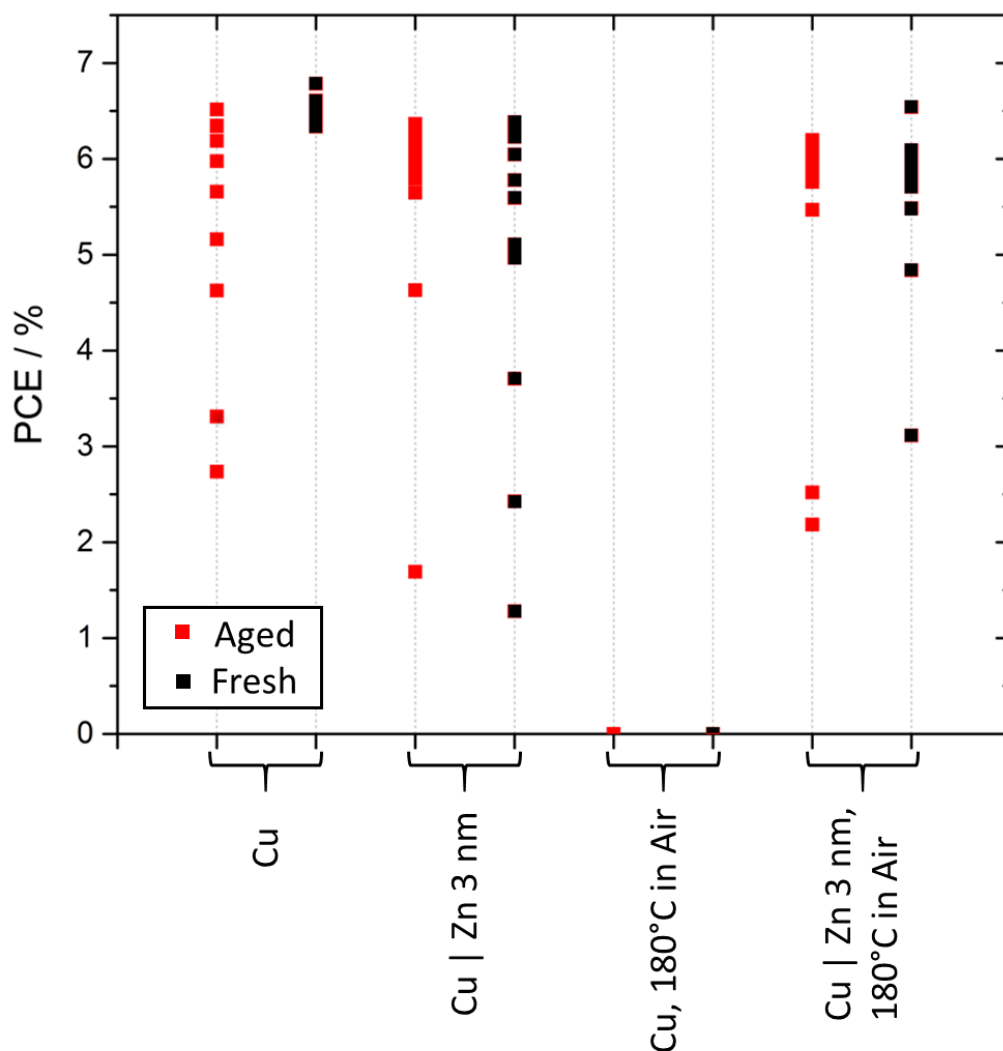
ambient laboratory air for 2 weeks (336 hours, Table 2). As expected, the device performance in Figure 16 was not impacted by the air-exposure of the electrode.

Table 2: Tabulated device data for the device structure: Electrode | ZnO | PBDB-T/ITIC | MoO$_3$ | Al. Data is presented as the mean of 6 - 18 devices ± Standard Deviation (Champion). One third of the MM | Cu 8 nm | Zn 3 nm electrodes were aged in ambient laboratory air for 2 weeks before building the device and one third again were annealed at 180°C in air for 15 minutes.

Electrode	Aged / Fresh	Annealed	J_{sc} / mA cm^{-2}	V_{oc} / V	FF	PCE / %
MM	Cu 8 nm	Zn 3 nm	Aged	No	10.41 ± 0.26 (10.61)	0.79 ± 0.08 (0.83)	0.65 ± 0.13 (0.72)	5.48 ± 1.34 (6.37)
MM	Cu 8 nm	Zn 3 nm	Fresh	No	10.64 ± 0.23 (10.98)	0.74 ± 0.16 (0.82)	0.60 ± 0.12 (0.71)	4.89 ± 1.71 (6.38)
MM	Cu 8 nm	Zn 3 nm	Fresh	180°C, Air	9.83 ± 0.85 (11.14)	0.84 ± 0.02 (0.84)	0.67 ± 0.07 (0.70)	5.54 ± 0.96 (6.54)

To further test the resilience of the Cu electrodes protected by a 3 nm Zn overlayer to oxidation, OPV devices were fabricated with an identical structure however the electrode was heated to 180°C in air. For an unprotected MM | Cu 8 nm electrode this completely oxidized the film and as a result the OPV devices did not function (Appendix, Table A2). With the inclusion of a Zn overlayer however, the OPV devices after electrode annealing in air performed equal to or better than the fresh or air-exposed electrodes (Table 2, Figure 16). This important result demonstrates not only the near-complete passivation of the underlying Cu electrode by a 3 nm Zn overlayer, but importantly also enables air-processing steps involving annealing at 180°C not possible with pure-Cu electrodes. After long-term storage in N$_2$, the MM | Cu | Zn 3 nm devices show a small improvement in

V_{oc} (Appendix, Figure A3), it is postulated this could be related to further doping of the two ZnO overlayers by Cu.


Figure 16: Device PCE data for the device structure: Electrode | ZnO | PBDB-T/ITIC | MoO₃ | Al (Average ± Standard Deviation (Champion)). Half of each electrode type (MM | Cu 8 nm or MM | Cu 8 nm | Zn 3 nm) were aged in ambient laboratory air (Red) for 2 weeks before building the device and half again of each were then annealed at 180°C in air for 15 minutes.

### 7.3.4   *Compatibility with microcontact printing*

The average transparency of the Cu/Zn electrode, ~ 60%, is too low for high-performance OPVs and so it was of interest to explore the compatibility with existing methods of increasing the transparency. To improve the transparency these electrodes could be patterned with an array of small apertures such as has been demonstrated previously in Chapter 5, at the cost of the resistivity of the film. Much higher transparency could be achieved without compromising on the resistivity by patterning thicker Cu | Zn electrodes into a grid structure by microcontact printing (μ-CP) like that in Chapter 4. Hexadecanethiol (HDT) is an excellent molecular resist for μ-CP on Cu with extremely short contact times. The defect-density of this monolayer has previously been found to be dependent on many factors most notably presence of a Cu oxide at the interface and is exaggerated in the final pattern since these defects can allow the continual penetration of the etchant.

Alkanethiolate molecules are reported to bind strongly from solution to stoichiometric ZnO,[40] and so Cu 40 nm | Zn 3 nm films were printed in air with a grid pattern of HDT (2 mM ink) and etched in aqueous APS (Figure 17 (a)) with varying contact time and etching time. Unfortunately, it did not prove possible to achieve a patterned grid structure of any description on the Cu 40 nm | Zn 3 nm film, with only indistinct patterns remaining, showing only a slight difference in etching rate between the stamped and unstamped regions. It is tentatively suggested that the printed HDT layer was not sufficiently compact to block the APS etchant, although this hypothesis was not tested.
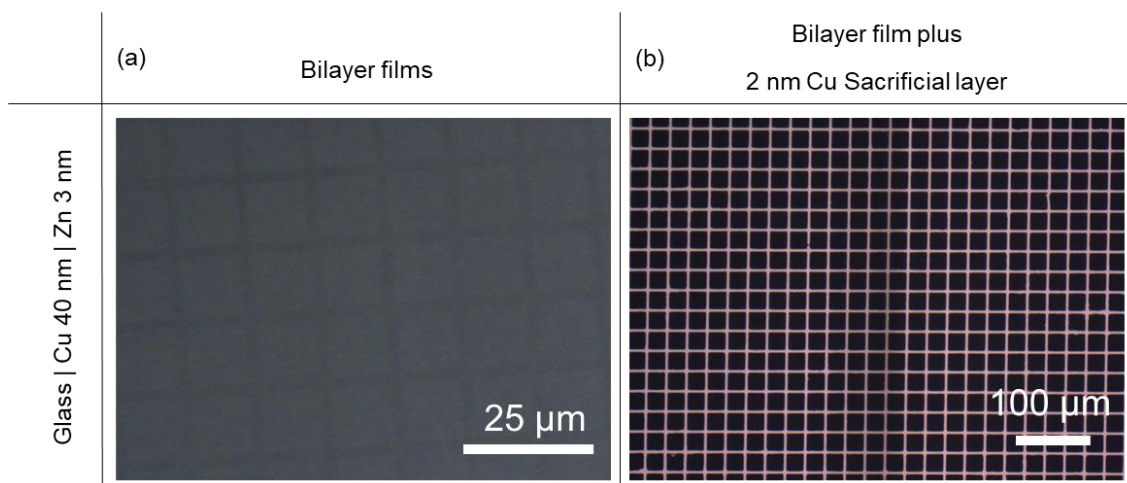
Figure 17: Optical microscope images of films after stamping with HDT and etching in ammonium persulfate (APS). (Left) Champion first attempt at patterning Cu 40 nm | Zn 3 nm films with a thin air-exposed Zn overlayer. (Right) Representative image of the grid structures resultant from printing onto an added 2 nm sacrificial Cu overlayer (Cu 40 nm | Zn 3 nm | Cu 2 nm).

To circumvent this problem, a 'sacrificial' 2 nm Cu overlayer was deposited onto the 3 nm Zn layer without breaking vacuum to produce a triple-layer Cu | Zn (3 nm) | Cu (2 nm) electrode to interface with the thiol binding groups of HDT. This approach proved effective (Figure 17 (b)), however when etching the Cu | Zn 3 nm | Cu 2 nm system particulate debris remained significant within the apertures for much longer during etching. Whilst it was possible to remove using longer etching times or higher APS concentrations, this risked exaggerating damage to the masked grid lines. At higher Cu thickness (120 nm, Figure 18) the balance between etching cleanly and damaging the Cu grid lines was hard to achieve. This is similar to the effect previously seen when etching Cu | Al bilayer electrodes using a thick polymer mask patterned by photolithography, where particles remained in the apertures for samples with Al (Appendix, Figure A4).
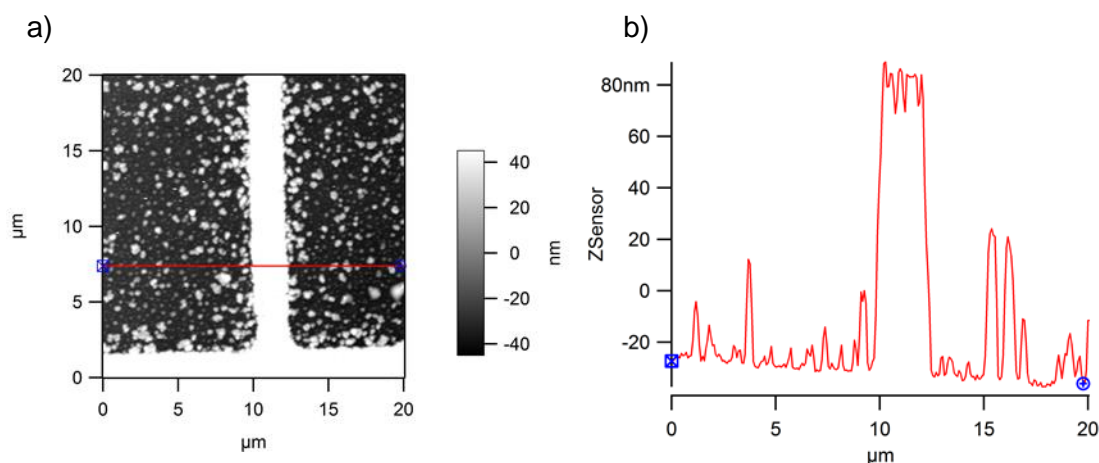
Figure 18: (a) AFM image and (b) cross-section of a 120 nm thick Cu grid with 3 nm metallic Zn overlayer where metal particles remain in the voids. A 2 nm sacrificial Cu layer was used to alloy binding of a thiol mask as described in-text.

An additional potential drawback of the 3 nm Zn | 2 nm Cu passivation layer is the possibility that the Zn layer is etched away during further processing. The 2 nm Cu overlayer has been described as a 'sacrificial' layer for two reasons: This layer is expected to oxidise when exposed to air and that typical processing established here for Cu grid electrodes applied in OPV devices involves removing the mask using a UV/O$_3$ treatment followed by washing with acetic acid to improve the wetting of PEDOT:PSS (Chapter 4). This treatment would be expected to oxidise the upper Cu layers, which are then selectively removed by an acetic acid rinse. There was concern that this processing may also remove the thin Zn/ZnO layer rendering the underlying Cu vulnerable to oxidation. Confirming this using energy-dispersive X-ray spectroscopy (EDAX) is not straightforward due to overlap in the common peaks, and so X-ray fluorescence (XRF) was used to quantify a Cu 120 nm | Zn 3 nm | Cu 2 nm film before and after a 10-minute UV/O$_3$ treatment and acetic acid rinse (Figure 19). The Cu peak remained stable as the removal of the 2 nm Cu overlayer would not be significant, and the strong Zn contribution remaining post-treatment (Figure 19 (b)) shows significant remaining ZnO after processing. The XRF intensity associated with Zn is reduced after processing with UV/O$_3$ and acetic acid indicating partial removal, which may present a problem if this undermines the stability of the Cu to air oxidation. The stability of the remaining grid electrode after such processing remains further work.
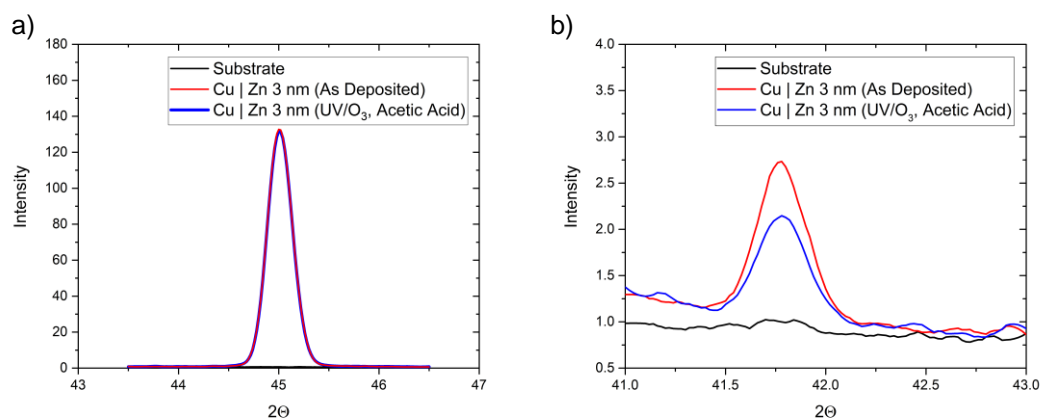
Figure 19: XRF peaks before (Red) and after (Blue) a 10-minute UV/O$_3$ treatment and acetic acid treatment for a Cu 120 nm | Zn 3 nm | Cu 2 nm film. (a) Copper region. (b) Zinc region.

7.4   Future work

Although not an avenue of further investigation in this work, it was hoped during the initial investigation of Cu | Al electrodes by Hutter *et al.* that the thin Al layer may act as an *in-situ* desiccant within OPV devices, scavenging moisture and oxygen which otherwise will oxidise the sensitive polymer donor/acceptor materials.[10,41] The greater bulk and reactivity of Zn or Sn metals available may further this concept creating a greater oxidant buffer parallel to the sensitive polymeric OPV layers, the oxidation of which leads invariably to the deterioration of device performance.[42,43].

Further device fabrication should also follow this chapter in order optimise the thickness of the Zn overlayer utilised and assess the functionality of patterned Cu | Zn electrodes in OPV. It was postulated earlier that a thicker Zn overlayer may increase the barrier to reverse current flow, improving the V_{oc} in OPV devices and negating the requirement for an additional hole-blocking layer. A comparison of the effectiveness of evaporated Sn overlayers to Zn within OPVs to replace the hole-blocking layer should also be made.

Significantly better-quality grid electrodes were achieved when printing HDT to a Cu 40 nm | Sn 0.8 nm film than a Cu | 40 nm | Zn 3 nm film shown in Figure 23. The thinner overlayer, and the lower reactivity of Sn, may improve the binding of the mask and as such distinct patterns can be achieved in the metal.
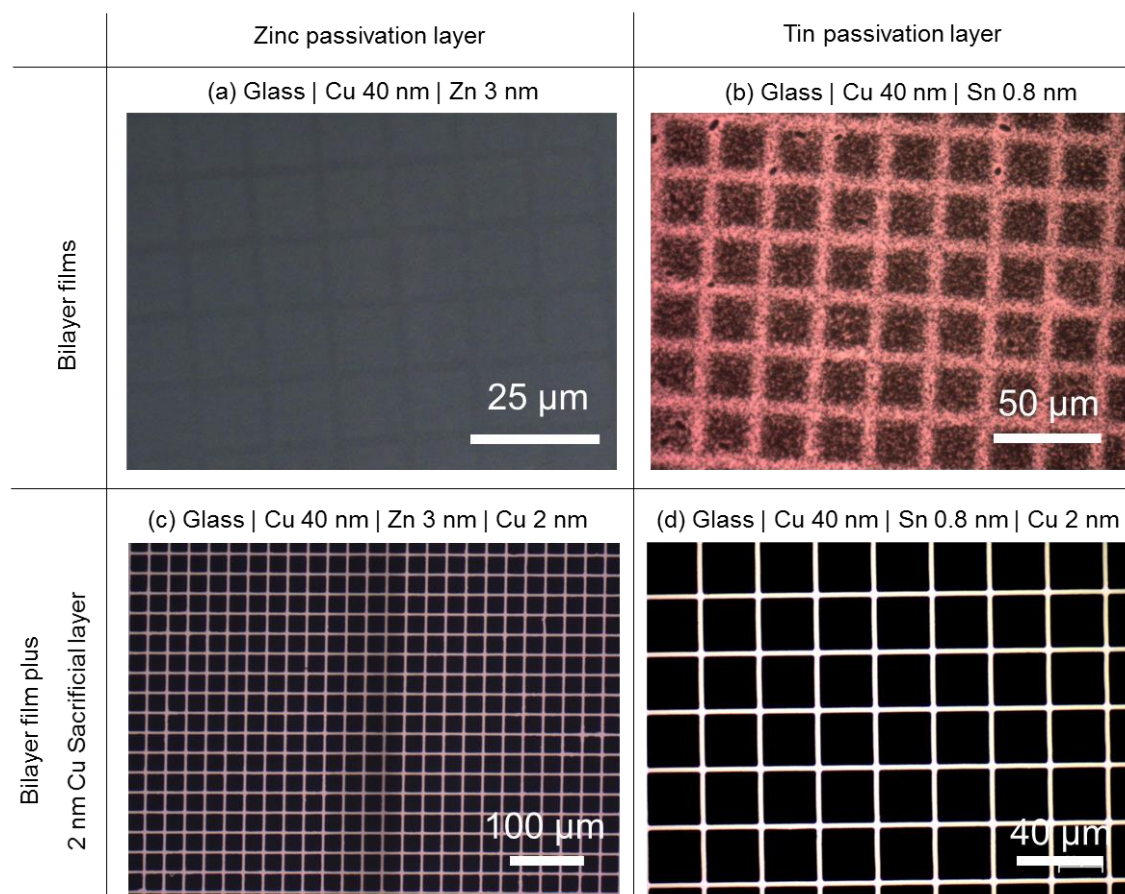
Figure 20: Optical microscope images of the labelled films after stamping with HDT and etching in ammonium persulfate (APS). (Upper) Champion first attempts at patterning films with a thin metal oxide overlayer. (Lower) Representative images of the grid structures resultant from printing onto a 2 nm sacrificial Cu overlayer.

Thiols only bind weakly to ZnO, as compared for example to phosphonic acids,[40] and it is evident that the density of defects will as such be very high on ZnO as compared to pristine Cu. In Figure 21 HDT was compared to a octadecylphosphonic acid ink using the same PDMS stamps, following the procedure optimised for Al.[44] This resulted in significantly improved metallic grids than the thiol showing much improved binding. These grids are not conductive however due to the number of line breaks and defects, and so not applicable as a TCE in OPVs, although further optimisation may achieve sufficient selectivity.
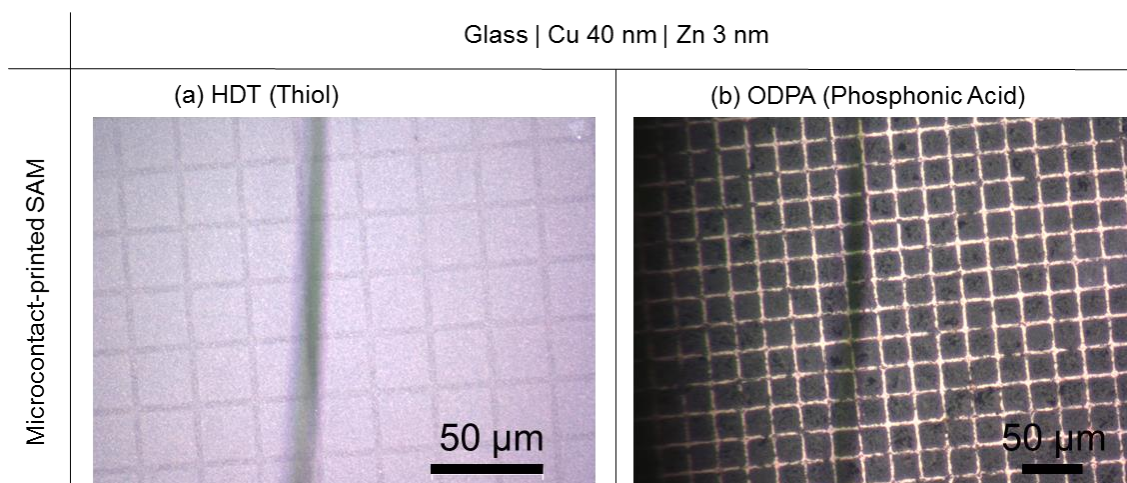
Figure 21: Optical microscope images comparing the resultant patterning of a Cu 40 nm | Zn 3 nm air exposed film by microcontact printing with (a) HDT (thiol head group) or (b) ODPA (phosphonic acid head group) and etching with APS.

There are multiple other routes in the literature to improve the quality of the pattern produced here on Cu 40 nm | Sn 0.8 nm: Octanol can be used to 'heal' defects in the monolayer by inserting between two surface bound molecules, or a large-molecule based etchant can be chosen which cannot penetrate individual defects in the monolayer.[45] As earlier, to the Cu | Sn 0.8 nm films 2 nm of additional Cu was subsequently evaporated to interface with HDT. Experientially the etching of the Cu | Sn 0.8 nm system was simpler than the Cu | Zn 3 nm system: Due to the better etching of $Sn/SnO_2/SnO$ by APS or the thinner overlayer, clean grids were easily produced without particulate metal left within the voids resulting in an electrode with 14.9 Ω sq^{-1} ($\leq$ 40 nm Cu alone) and exceptional 86.3% average transparency (Figure 23, Figure 22, Figure 23): performance equal to or greater than that achieved on pure-Cu films.
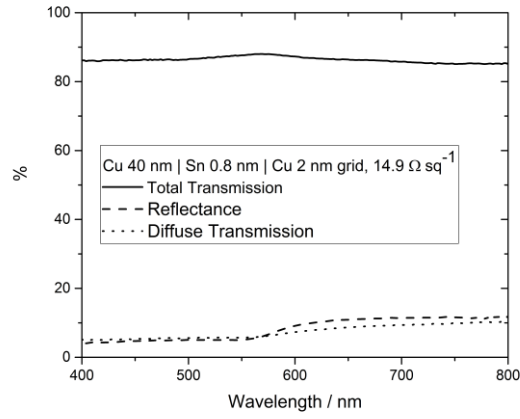
Figure 22: Total transmission (Solid line), reflectance (Dashed line) and diffuse transmission (Dotted line) for a Cu 40 nm | Sn 0.8 nm | Cu 2 nm grid electrode (14.9 Ω sq^{-1}**).**
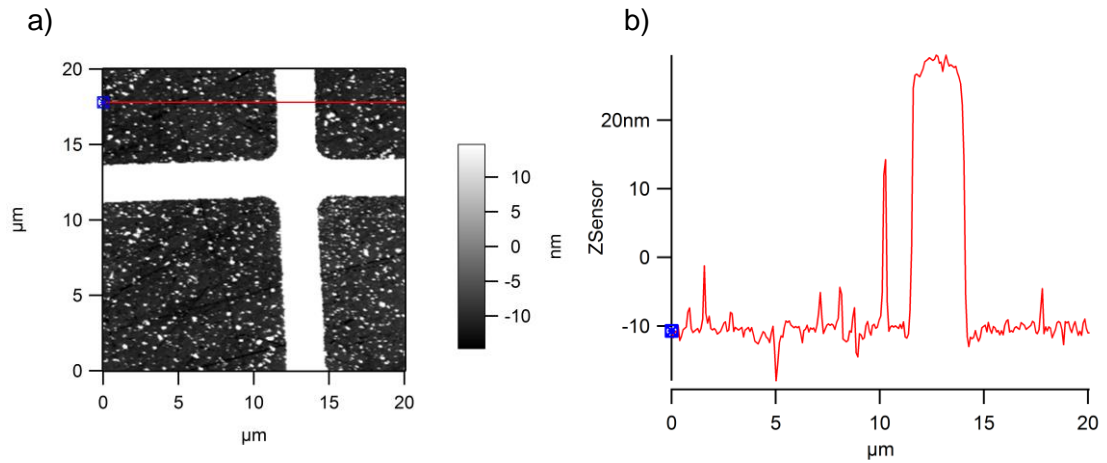
Figure 23: (a) AFM image and (b) cross-section of a 40 nm Cu | Sn 0.8 nm | Cu 2 nm grid electrode produced by microcontact printing a HDT mask and etching with APS.

7.5 Conclusion

Both Sn and Zn evaporated metallic overlayers have been shown here to dramatically supress the oxidation of Cu films exposed to air, with a champion < 15% sheet resistance rise after 5000 hours in air. Using XPS we have elucidated that Sn, like Al is already known to, forms an alloy during deposition together with Cu which allows an extremely thin layer (0.8 nm) to provide disproportionate passivation to the underlying film although some oxidation is observed. Zn overlayers however are shown not to alloy strongly with Cu but form a ZnO overlayer: this recovers the reduced transparency as compared to Sn and Al and XPS shows no significant Cu oxidation. This also promises the development of a simultaneous Zn oxygen sink, ETL and passivating layer for Cu electrodes in OPVs as evaporated Cu | Zn bilayer electrodes effectively act as an electron selective electrode. A route to the compatibility of oxidised metal overlayers with the established microcontact printing of fine Cu grids is then developed.

7.6 Experimental

Electrode preparation

Glass microscope slides (7525 M, J. Melvin Freed Brand) or polyethylene terephthalate (PET) substrates were ultra-sonically agitated for 15 minutes each in diluted surfactant (Hellmanex III, Hellma Analytics), deionised water and propan-2-ol (AnalaR, VWR). These substrates were then UV/O$_3$ treated for 15 minutes immediately prior to use. Where stated, these slides were transferred to a desiccator and held at approx. 50 mBar for 4 hours with an open vial of mixed APTMS/MPTMS. All substrates were then transferred to the evaporator for Cu, Sn or Zn deposition using a base pressure of < 5 ×10^{-8} mbar unless stated. Cu, Sn and Zn were evaporated at 1 Å s^{-1}. Zn evaporates at relatively low temperature (< 200°C) and so was evaporated from the organic (LTE) sources. Thicknesses were calibrated using an Asylum Research MFP-3D AFM and monitored using quartz-crystal microbalances. Masks were exchanged where required by a series of transfer arms without breaking the vacuum. During metal deposition, the chamber pressure rose to approximately 5×10^{-7} mbar**.**

OPV Devices

The planar electrodes as described and together with ITO reference electrodes (Washed and UV/O$_3$ treated. Glass, Thin Film Devices. PEN, Diamond Coatings) were transferred into a N$_2$ filled glovebox with < 2 ppm O$_2$ and H$_2$O, 25 nm of ZnO was deposited by spin

coating (Aluminum-doped zinc oxide ink for spin coating/slot-die coating, Sigma Aldrich, 5000 rpm, filtered) followed by the bulk heterojunction. For the PBDB-T/ITIC (Ossila) devices solutions were prepared in anhydrous chlorobenzene and 0.5% 1,8-diiodooctane (DIO) at a 1:1 wt% (20 mg per mL), spin cast at 2500 rpm and annealed at 120°C for 15 minutes. All devices were loaded into the thermal evaporator and held under vacuum overnight. 6 nm MoO_3 was then evaporated at 0.2 Å s^{-1} before the devices were transferred under vacuum to the pixel mask and 150 nm Al was evaporated at 1 Å s^{-1}. These devices were tested unencapsulated under 1 sun illumination in an N_2 atmosphere (< 2 ppm O_2, H_2O) through a calibrated shadow mask for the small area devices.

X-ray Fluorescence (XRF)

The XRF was undertaken on a Rigaku Primus IV Wavelength Dispersive X-ray Fluorescence (WDXRF) system with a 4kW tube. Samples were mounted under a 20mm mask and measured under vacuum using a Qualitative scan of the Cu, Zn Ka peaks, with a LiF 200 crystal and the Si Ka peak with a PETH synthetic crystal. Other elements were not measured. The counting time was chosen to ensure sufficient counting statistics in the peaks and the total measurement time was 4 minutes per sample. The tube power was kept at 3kW to avoid excessive heat load on the samples. The software uses a fundamental parameters model, using sensitivity data for each element measured in the factory, to model the sample matrix and estimate the composition – summing to 100% the amount of Cu, Zn and Si.

7.7   References

[1]   H. Lu, X. Ren, D. Ouyang, W. C. H. Choy, *Small* **2018**, *14*, 1703140.

[2]   M. W. Rowell, M. D. McGehee, *Energy Environ. Sci.* **2011**, *4*, 131.

[3]   D. A. Jacobs, K. R. Catchpole, F. J. Beck, T. P. White, *J. Mater. Chem. A* **2016**, *4*, 4490.

[4]   HKEX, "London Metal Exchange," can be found under http://www.lme.com/, **n.d.**

[5]   D. Yu, Y. Q. Yang, Z. Chen, Y. Tao, Y. F. Liu, *Opt. Commun.* **2016**, *362*, 43.

[6]   E. Georgiou, S. A. Choulis, F. Hermerschmidt, S. M. Pozov, I. Burgués-Ceballos, C. Christodoulou, G. Schider, S. Kreissl, R. Ward, E. J. W. List-Kratochvil, C. Boeffel, *Sol. RRL* **2018**, *2*, 1700192.

[7]   T. K. S. Wong, S. Zhuk, S. Masudy-Panah, G. K. Dalapati, *Materials (Basel).* **2016**, *9*, 1.

[8]   M. Nolan, S. D. Elliott, *Phys. Chem. Chem. Phys.* **2006**, *8*, 5350.

[9]   J. Evertsson, F. Bertram, F. Zhang, L. Rullik, L. R. Merte, M. Shipilin, M. Soldemo, S. Ahmadi, N. Vinogradov, F. Carlà, J. Weissenrieder, M. Göthelid, J. Pan, A. Mikkelsen, J. O. Nilsson, E. Lundgren, *Appl. Surf. Sci.* **2015**, *349*, 826.

[10]   O. S. Hutter, H. M. Stec, R. A. Hatton, *Adv. Mater.* **2013**, *25*, 284.

[11]   P. Bellchambers, J. Lee, S. Varagnolo, H. Amari, M. Walker, R. A. Hatton, *Front. Mater.* **2018**, *5*, 71.

[12]   I. Platzman, R. Brener, H. Haick, R. Tannenbaum, *J. Phys. Chem. C* **2008**, *112*, 1101.

[13]   C. A. Vincent, *J. Electrochem. Soc.* **1972**, *119*, 515.

[14]   J. H. Lee, B. O. Park, *Mater. Sci. Eng. B Solid-State Mater. Adv. Technol.* **2004**, *106*, 242.

[15]   P. A. Grutsch, M. V. Zeller, T. P. Fehlner, *Inorg. Chem.* **1973**, *12*, 1431.

[16]   M. C. Biesinger, *Surf. Interface Anal.* **2017**, *49*, 1325.

[17]   S. Fürtauer, D. Li, D. Cupid, H. Flandorfer, *Intermetallics* **2013**, *34*, 142.

[18]   S. Noothongkaew, H. Nakajima, A. Tong-On, W. Meevasana, P. Songsiriritthigul, *Appl. Surf. Sci.* **2012**, *258*, 1955.

[19]   L. G. Mar, P. Y. Timbrell, R. N. Lamb, *Thin Solid Films* **1993**, *223*, 341.

[20]   P. Kejzlar, J. Machuta, I. Nová, *Manuf. Technol.* **2017**, *17*, 44.

[21]   H. J. Pereira, J. Reed, J. Lee, S. Varagnolo, G. D. M. R. Dabera, R. A. Hatton, *Adv. Funct. Mater.* **2018**, *28*, 1802893.

[22]   H. J. Pereira, R. A. Hatton, *Front. Mater.* **2019**, *6*, 228.

[23]   Y. Chen, P. Schneider, A. Erbe, *Phys. Status Solidi Appl. Mater. Sci.* **2012**, *209*, 846.

[24]   C. R. Brundle, R. I. Bickley, *J. Chem. Soc., Faraday Trans. 2* **1979**, *75*, 1030.

[25]   E. Lee, J. Ahn, H. C. Kwon, S. Ma, K. Kim, S. Yun, J. Moon, *Adv. Energy Mater.* **2018**, *8*, 1702182.

[26]   M. Bauch, T. Dimopoulos, *Mater. Des.* **2016**, *104*, 37.

[27]   J. Hun Park, W.-K. Kim, J. Seong Bae, D. Hee Lee, I. Hee Park, T. Woo Lee, Y. Chan Cho, J.-Y. Kim, S. Lee, C. Ryong Cho, S.-Y. Jeong, *Sci. Rep.* **2015**, *5*, 305.

[28]   J. Lee, M. Walker, S. Varagnolo, S. Huband, R. A. Hatton, *ACS Appl. Energy Mater.* **2019**, *2*, 5198.

[29]   K. Zhang, C. Zhong, S. Liu, C. Mu, Z. Li, H. Yan, F. Huang, Y. Cao, *ACS Appl. Mater. Interfaces* **2014**, 1.

[30]   X. Liu, H. Q. Wang, Y. Li, Z. Gui, S. Ming, K. Usman, W. Zhang, J. Fang, *Adv. Sci.* **2017**, *4*, 1700053.

[31]   C. A. Polyzoidis, C. Kapnopoulos, E. D. Mekeridis, L. Tzounis, S. Tsimikli, C. Gravalidis, A. Laskarakis, S. Logothetidis, in *Mater. Today Proc.*, **2016**, pp. 758–771.

[32]   N. Seob Baek, A. K.-Y. Jen, *Artic. Appl. Phys. Lett.* **2008**, DOI

10.1063/1.2919524.

[33] A. Khan, V. H. Nguyen, D. Muñoz-Rojas, S. Aghazadehchors, C. Jiménez, N. D. Nguyen, D. Bellet, *ACS Appl. Mater. Interfaces* **2018**, *10*, 19208.

[34] Y. Won, A. Kim, D. Lee, W. Yang, K. Woo, S. Jeong, J. Moon, *NPG Asia Mater.* **2014**, *6*, DOI 10.1038/am.2014.36.

[35] W. Zhao, D. Qian, S. Zhang, S. Li, O. Inganäs, F. Gao, J. Hou, *Adv. Mater.* **2016**, *28*, 4734.

[36] Z. He, C. Zhong, S. Su, M. Xu, H. Wu, Y. Cao, A. K. K. A. Kyaw, D. D. H. Wang, V. Gupta, J. Zhang, S. Chand, G. C. Bazan, A. J. Heeger, *Nat. Photonics* **2013**, *25*, 593.

[37] J. Zou, C. Z. Li, C. Y. Chang, H. L. Yip, A. K. Y. Jen, *Adv. Mater.* **2014**, *26*, 3618.

[38] J. C. Wang, W. T. Weng, M. Y. Tsai, M. K. Lee, S. F. Horng, T. P. Perng, C. C. Kei, C. C. Yu, H. F. Meng, *J. Mater. Chem.* **2010**, *20*, 862.

[39] H. Bin, Z.-G. Zhang, L. Gao, S. Chen, L. Zhong, L. Xue, C. Yang, Y. Li, *J. Am. Chem. Soc.* **2016**, *138*, 4657.

[40] C. L. Perkins, *J. Phys. Chem. C* **2009**, *113*, 18276.

[41] Y. Matsuo, A. Ozu, N. Obata, N. Fukuda, H. Tanaka, E. Nakamura, *Chem. Commun.* **2012**, *48*, 3878.

[42] M. Jørgensen, K. Norrman, F. C. Krebs, *Sol. Energy Mater. Sol. Cells* **2008**, *92*, 686.

[43] F. C. Krebs, K. Norrman, *Prog. Photovoltaics Res. Appl.* **2007**, *15*, 697.

[44] C. Merian, X. Du, D. Hardt, H. AlQahtani, in *ASME Int. Mech. Eng. Congr. Expo. Proc.*, American Society Of Mechanical Engineers, **2015**.

[45] M. Geissler, H. Schmid, A. Bietsch, B. Michel, E. Delamarche, *Langmuir* **2002**, *18*, 2374.

7.8   Appendix
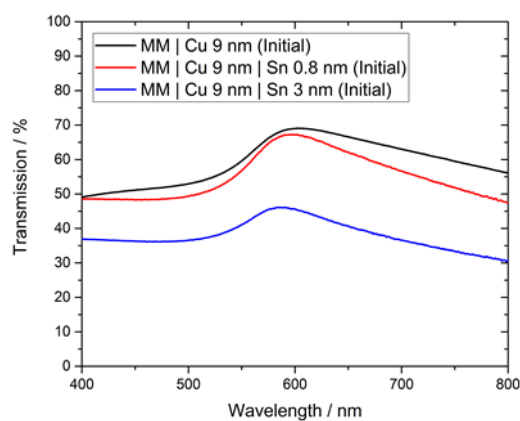
Figure A1: Far-field transparency of three 9 nm Cu electrodes using a mixed APTMS:MPTMS seed layer on glass. Without overlayer (Black), with 0.8 nm Sn (Red) and 3 nm Sn (Blue). Referenced against glass to subtract reflection at the air/glass interface which would be negated by an anti-reflective coating on PV modules.

Table A1: Tabulated performances of model OPV devices of the structure Electrode | optional (additional) ZnO layer | PBDB-T/ITIC | MoO$_3$ | Al. Data is presented as the mean of 6 - 18 devices ± Standard Deviation (Champion).

Electrode	Additional ZnO ETL by spin coating	J$_{sc}$ / mA cm^{-2}	V$_{oc}$ / V	FF	PCE / %
ITO	Yes	13.59 ± 0.50 (13.72)	0.86 ± 0.01 (0.87)	0.65 ± 0.05 (0.69)	7.58 ± 0.66 (8.21)
ITO	No	11.38 ± 2.35 (13.57)	0.09 ± 0.02 (0.11)	0.28 ± 0.01 (0.29)	0.32 ± 0.13 (0.44)
MM | Cu | Zn 3 nm (Annealed)	Yes	6.98 ± 1.06 (7.90)	0.82 ± 0.02 (0.86)	0.58 ± 0.07 (0.67)	3.40 ± 0.87 (4.56)
MM | Cu | Zn 3 nm (Annealed)	No	10.53 ± 0.34 (10.95)	0.71 ± 0.06 (0.76)	0.56 ± 0.11 (0.57)	4.14 ± 0.81 (4.79)
MM | Cu | Zn 3 nm (Non-Annealed)	Yes	6.43 ± 0.86 (7.19)	0.78 ± 0.05 (0.82)	0.49 ± 0.06 (0.58)	2.49 ± 0.68 (3.43)
MM | Cu | Zn 3 nm (Non-Annealed)	No	7.08 ± 2.35 (9.79)	0.45 ± 0.10 (0.55)	0.47 ± 0.09 (0.55)	1.67 ± 0.95 (2.94)

Table A2: Tabulated performances of model OPV devices of the structure MM | Cu 8 nm | ZnO-nanoparticle layer | PBDB-T/ITIC | MoO_3 | Al. Half of the electrodes were exposed to ambient laboratory air for 336 hours before device fabrication, and half were annealed at 180°C in air. Data is presented as the mean of 6 - 18 devices ± Standard Deviation (Champion).

Electrode	Aged / Fresh	Annealed	J_{sc} / mA cm^{-2}	V_{oc} / V	FF	PCE / %
MM | Cu 8 nm	Aged	No	10.16 ± 1.00 (11.05)	0.81 ± 0.03 (0.82)	0.64 ± 0.13 (0.72)	5.29 ± 1.33 (6.51)
MM | Cu 8 nm	Fresh	No	11.46 ± 0.21 (11.63)	0.83 ± 0.00 (0.83)	0.69 ± 0.01 (0.71)	6.54 ± 0.16 (6.78)
MM | Cu 8 nm	Fresh	180°C, Air	0.00 ± 0.00 (0.00)	0.41 ± 0.04 (0.46)	0.35 ± 0.05 (0.40)	0.00 ± 0.00 (0.00)
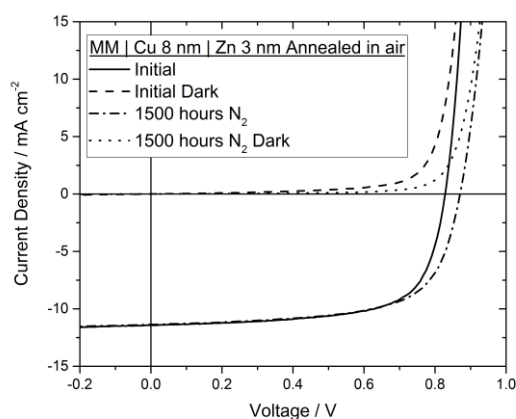
Figure A3: A representative device of the structure MM | Cu 8 nm | Zn 3 nm | ZnO | PBDB-T/ITIC | MoO_3 | Al showing the improvement of the structure stored under N_2 atmosphere.
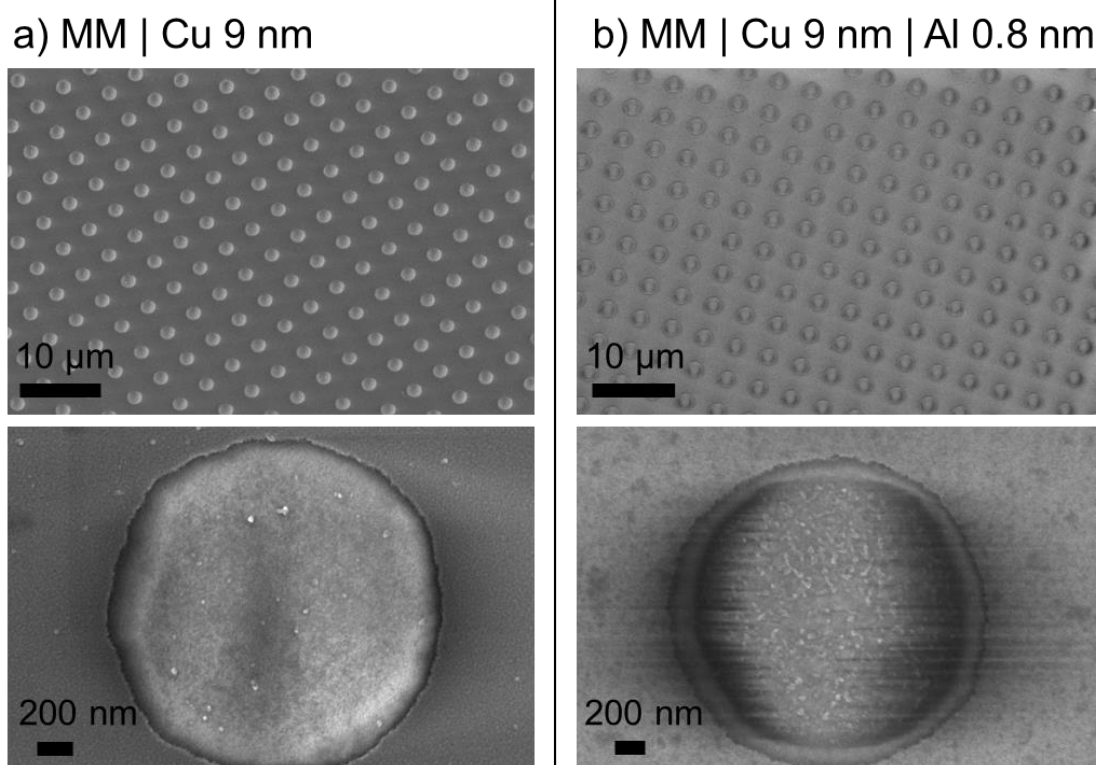
Figure A4: SEM images comparing the size and uniformity of the patterned electrodes produced using a conventional photolithography method and etched using ammonium persulfate solution. At high resolution, when imaging (b) MM | Cu | Al aperture, it can be seen that the etchant does not cleanly remove the oxidised Al and this debris remains within the aperture which may still affect the transparency of the patterned film, especially at > 600 nm. The interference seen, especially at high magnification, is caused by charging of the non-conductive glass substrate.